Design and Fabrication of Microstructured

and Switchable Biological Surfaces

by

Chun L. Yeung

A thesis submitted to
The University of Birmingham
for the degree of
DOCTOR OF PHILOSOPHY

School of Chemistry
College of Physical Sciences and Engineering
The University of Birmingham
April 2011

This thesis is dedicated to my parents, Pui Miu Ng and Yau Ho Yeung, who have sacrificed everything in their life to support my academic career. I could have never come this far without you two!

Abstract

The research presented in this thesis explores the design and fabrication of microstructured and switchable biological surfaces, which may have potential applications of nanobiotechnology. The thesis focuses on the fabrication of biological surfaces which can be controlled via external stimuli.

Chapter 1 - Introduction to Nanobiotechnology - presents an introduction to the background of this research including the role of self-assembled monolayers (SAMs) in nanobiotechnology, microstructure fabrication techniques, stimuli responsive surfaces and cell migration.

Chapter 2 - Surface characterisation techniques - presents surface characterisation techniques employed throughout this research.

Chapter 3 - Study of Arp2/3 complex activity in filopodia of spreading cells using patterned biological surfaces - presents the fabrication and characterisation of patterned biological (fibronectin) surfaces using patterning technology (microcontact printing) and several surface analytical techniques. This study explores the role of filopodia in the spreading of Mouse Embryonic fibroblast (MEF) cells and the function of Arp2/3 complex in this process. The results demonstrated that filopodia, produced by MEF cells interacted with the patterned fibronectin surface and guided lamellipodia protrusion. Arp2/3 complex, which is absent on the

filopodia adhesion site, does not facilitate in the adhesion of filopodia on the fibronectin surface.

Chapter 4 - Tuning specific biomolecular interactions using electro-switchable oligopeptide surfaces - presents the fabrication of responsive surfaces that rely on electro-switchable peptides to control biomolecular interactions on gold surfaces. This system is based upon the conformational switching of positively charged oligolysine peptides that are tethered to a gold surface. The bioactive molecular moieties (biotin) terminates on the oligolysines can be reversibly exposed (bio-active state) or concealed (bio-inactive state) on demand, as a function of surface potential.

Chapter 5 - Experimental procedures, protocols and synthesis - describes the experimental techniques used during the investigations performed throughout the work described in this thesis. Experimental protocols and data analysis by various equipment are described.

Acknowledgements

There are many people I would like to thank for their help and support during the 3 years of my research and the writing up of this thesis.

First of all, I would like to thank Dr. Paula M. Mendes for her guidance, support and training throughout my course. Her passion, enthusiasm and beliefs on research have lead me to become a different person by changing my perspective and standard in research and in life. Her strong belief in my work and me has been my moral support when progress was slow. The second person who I would like to thank is Professor Jon A. Preece for allowing me to undertake my PhD studies in his group. His support, guidance, and encouragement have been key for my success for the last 3 years. His teaching, not just academically, but also in life, has armed me with crucial skills and experience that I will need to continue my career in research. I really could not have completed this course without my two supervisors.

Many thanks must also go to members of the Preece and Mendes group past and present, namely Dr. Parvez Iqbal, Dr. James Bowen, Dr. Simon Leigh, Dr. Christopher Hamlett, Dr. Yue Long, Scott Charlesworth, Rachel Manton, Marzena Allen, Cait Costello, Oliver Curnick, Minhaj Lashkor, and Alice Pranzetti. Their friendship, advice and support helped me sail through my PhD.

Contents

Chapter 2: Surface characterisation techniques

Chapter 3: Study of Arp2/3 complex activity in filopodia of spreading cells using patterned biological surfaces

Chapter 4: Tuning specific biomolecular interactions using electro-switchable oligopeptide surfaces

Chapter 5: Experimental procedures, synthesis and equipments

Chapter 6 Conclusions and Future work

List of Common Acronyms Used

AFM	Atomic force microscopy
BSA	Bovine serum albumin
CA	Contact angle goniometry
µCP	Microcontact printing
CD	Cyclodextrin
CV	Cyclic voltammetry
DPN	Dip-pen nanolithography
EBL	Electron beam lithography
ECM	Extracellular matrix
FM	Fluorescence microscopy
MEF	Mouse embryonic fibroblast
MHA	16-mercaptohexadecanoic acid
ITO	Indium tin oxide
OC	Open circuit
ODTMS	Octadecyltrimethoxysilane
OEG	Oligo(ethylene glycol)
OF	ODTMS fibronectin substrate
OTS	Octadecyltrichlorosilane
PBS	Phosphate buffer solution
PDMS	Poly(dimethoxysilane)
PEG	Poly(ethylene glycol)
PF	PDMS fibronectin substrate
SA	Streptavidin
SAMs	Self-assembled monolayers
SCE	Standard calomel electrode
SPR	Surface plasmon resonance spectroscopy
XPS	X-ray photoelectron spectroscopy

Chapter 1

Introduction to Nanobiotechnology

Chapter 1 is reproduced in parts from an article entitled:

"Bio-nanopatterning of surfaces" by Paula M. Mendes, Chun L. Yeung, Jon A. Preece.

Nanoscale Research Letters, **2007**, *2*, 373-384

Abstract: *Nanobiotechnology is a field that incorporates many disciplines of science including chemistry, biology, physics and engineering. In this chapter, we will examine the motivation behind the development of biological surfaces, and the development of switchable biological surfaces. This chapter will review various aspects of self-assembled monolayers (SAMs), fabrication of biocompatible surfaces, stimuli responsive surfaces and conclude with a description of cell migration and cell motility on surfaces.*

1.0 Introduction

Just as biology is offering inspiration and components to nanotechnology,[1, 2] nanotechnology is providing new tools and technological platforms to measure, understand and control biological systems.[3-6] Nanobiotechnology[7] is the application of nanotechnology and nanoscience into the field of biological sciences. This area of science focuses on making molecular scale-mechanics by imitating biological systems,[3] or by building tools to study natural phenomena occurring in biological systems on the nanometre scale.[8]

Nanobiotechnology uses micro- and nano- scale science and technology in combination with the knowledge and techniques used in biological studies to manipulate molecular, genetic, and cellular processes.[4-7] This approach has afforded a platform for scientists to generate new tools that are fundamentally important in discovering new life sciences processes. In addition, it is expected to create innovative ideas and products, whilst acting as a pivotal role in various biological applications at the same time. These applications include drug delivery and gene therapy,[9] molecular imaging,[10] biomarkers[11] and biosensors.[12] Targeting specific drug therapies for early diagnosis of disease is a priority in research where nanotechnology may play an important role.[13]

Over the past few years,[3] the study of biological surfaces has provided a platform to investigate how cells probe and interact with their surroundings environments.[4, 14, 15] Using bottom-up[16] and top-down[17] approaches, scientists can create nano scale surfaces with specific functionalities which provide a platform to conduct various research in the fields of medicine,[9] bioengineering,[12] and in the life sciences.[11]

One of the techniques that nanobiotechnology focuses on is the bio-nanopatterning of surfaces. Bio-nanopatterning[7, 18-20] of surfaces has been of growing interest in recent years, from both scientific and technological points of view. Such artificial biological surfaces can be tremendously useful in diverse biological and medical applications, including nanobiochips,[21] nanobiosensors,[22] and fundamental studies of cell biology.[23] Biomolecule nanoarray technology not only offers the rewards of smaller biochips with more reaction sites, but also smaller test volume and potentially higher sensitivity and throughput screening for molecular diagnostics.[24] With the advent of DNA hybridisation nanoarrays comes the remarkable ability

to rapidly and effectively monitor the expression of thousands of genes used in the diagnosis and treatment of disease.[7] In comparison to DNA nanoarrays, protein nanoarrays offer the possibility of developing a rapid global analysis of an entire proteome, leading to protein-based diagnostics and therapeutics.[7, 18] Another area that will profit from this novel platform technology, thanks to its flexibility in terms of pattern shape/geometry, is the study of cell adhesion and motility.[14]

This broad range of biological and medical applications presents many challenging materials-design concepts.[20-22, 25] Prominent among these challenges is the need for:

1) Spatially positioning biomolecules on a substrate with nanoscale resolution, whilst retaining their native biological structures and functions.[21]

2) High bimolecular resistivity by the other regions of the substrate.[26]

The past few years has witnessed the advent of several promising strategic methodologies for the aforementioned needs, which are due primarily to the important advances in nanofabrication technology. Further details on nanofabrication technologies will be discussed in more details in **section 1.2**.

1.1 Bottom-up approach

The bottom-up approach[16] affords structures that are made atom-by-atom, or more commonly molecule-by-molecule, utilising covalent, ionic, metallic or non-covalent bonds (i.e. van der Waals forces, dipole-dipole interactions). This approach produces nanostructures from a molecular level using, for instance, supramolecular chemistry[27] and self-assembly.[28]

1.1.1 Self-assembly

The term self-assembly can be referred to as the spontaneous formation of discrete nanometre-sized units from simpler subunits of building blocks.[29] During the self-assembly process, the constituent subunits such as atoms, molecules, biological structures combine to form a secondary and more complex structure. There are two types of self-assembly, intramolecular self-assembly and intermolecular self-assembly.[30]

Intramolecular self-assembling systems often comprise complex polymers with the ability to assemble from the random coil conformation into a well-defined stable structure. Examples would be protein folding[31] in aggregation to give functioning nanostructures such as enzymes. Intermolecular self-assembly[32] is the formation of supramolecular assemblies such as the formation of a micelle by surfactant molecules in solution.

Self-assembly is increasingly powerful for the bottom-up fabrication of nanoscale structures.[33] This technique provides a vast potential in the fields of biology and medicine. Molecules are used as building blocks for the design of biomolecule carriers, for biorecognition assays,[17] as coating for implants[34] and as surface agents for changing cell and bacteria adhesion to surfaces.[17, 34, 35] It is important to understand the interactions involved during the self-assembly process. Much work has been focused upon the self-assembly of organic monolayers on metal surfaces to fabricate self-assembled monolayers (SAMs).

1.1.2 Self-assembled monolayers (SAMs)

Self-assembled monolayers (SAMs) are formed spontaneously by the adsorption of an active surfactant (from liquid, or vapour) onto a solid surface in which intermolecular forces play a

crucial role. The properties of a SAM (thickness, structure, surface energy, stability) can be easily controlled and specific functionalities[8] can also be introduced into the surfactant building blocks. SAMs of alkanethiols on gold[36] and triethoxysilanes on silicon dioxide (SiO_2)[37] are examples of two widely used systems to modify the surface properties of metallic and inorganic substrates, respectively. Each of the surfactant molecules that constitute the building blocks of the system can be divided into three parts, the head group (surface linking group), the backbone and the terminal (active) group (**figure 1.1**).

Terminal group (Biotin, NH_3^+, COO^-, progesterone)

Backbone (Oligolysine, hydrocarbon chain)

Head group (thiol, organosilane)
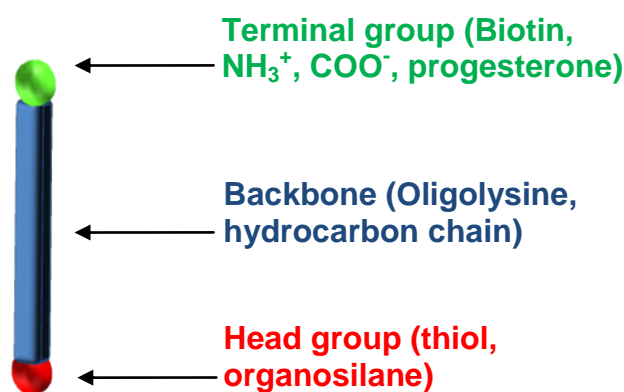
Figure 1.1 Schematic representation of a surfactant molecule.

The head group guides the physis and/or chemisorption onto the surface. The interaction between the hydrocarbon backbones via intermolecular interactions ensures an efficient packing of the surfactant in the monolayer and leads to a dense monolayer. The terminal group provides the desired physiochemical properties of the newly formed interface, and provides an anchor point for further surface modification such as the attachment of biomolecules[17] and the formation of nanostructures.[17, 38]

SAMs can be studied and characterised by various surface analytical techniques, including atomic force microscopy, X-ray photoelectron spectroscopy, ellipsometry and contact angle

goniometry. Readers can find a detailed discussion of these techniques in **chapter 2** of this thesis.

1.1.2.1 Thiol based SAMs

Thiols SAMs on gold[39] have attracted much attention. The surface stability is due to the strength of the S-Au bond and the van der Waals interactions between the backbones of the surfactant. These molecules exhibit molecular order and are stable at ambient conditions. The most studied SAMs are the alkanethiols SAMs on a clean gold (111) (Au) surface.[38] Gold does not form a stable oxide film[40] on its surface, therefore, it is easier to handle under ambient conditions. In this chapter, we will focus the discussion on the alkanethiols SAMs on gold substrates.

A thiol molecule consists of three parts: (i) the sulfur head group forms a strong, covalent bond with the gold substrate, (ii) the hydrocarbon chain acts as the backbone of the molecule and stabilizes the SAM through van der Waals interactions, and (iii) the terminal group, which can have different functionalities, leads to different physiochemical properties of the surface. For example, by changing the terminal group from CH_3 to COOH, the surface can change from a hydrophobic, anti-adherent surface into a hydrophilic surface with good metal ion and protein binding properties.[41]

Self-assembly of thiols on gold is easy to achieve and can be carried out from vapours and solutions, the latter one being the most popular due to simplicity and accessibility in most laboratories.[38] The thiol adsorption concentration normally lies within the range of 10-1000 μM.

Using dodecanethiol (DDT) SAM on gold as an example, a SAM is formed by initial physisorption of the surfactant deposited onto the surface from the solution phase (**process 1**, **figure 1.2**), followed by the chemisorption of the thiol head group affording Au-S bond (**process 2**, **figure 1.2**). Chemisorption is an exothermic process that allows relatively strong molecular-substrate interactions ($\sim$209 kJ mol^{-1}), and can result in pinning of the surfactant head group to a specific surface site through a thiolate bond. The molecules that have already adsorbed on to the surface organize into island structures (**process 3**, **figure 1.2**) by van der Waals forces between the alkyl chains ($\sim$4-8 kJ mol^{-1} per methylene groups), eventually leading to the formation of monolayers (**process 4**, **figure 1.2**) as the island coalesce.
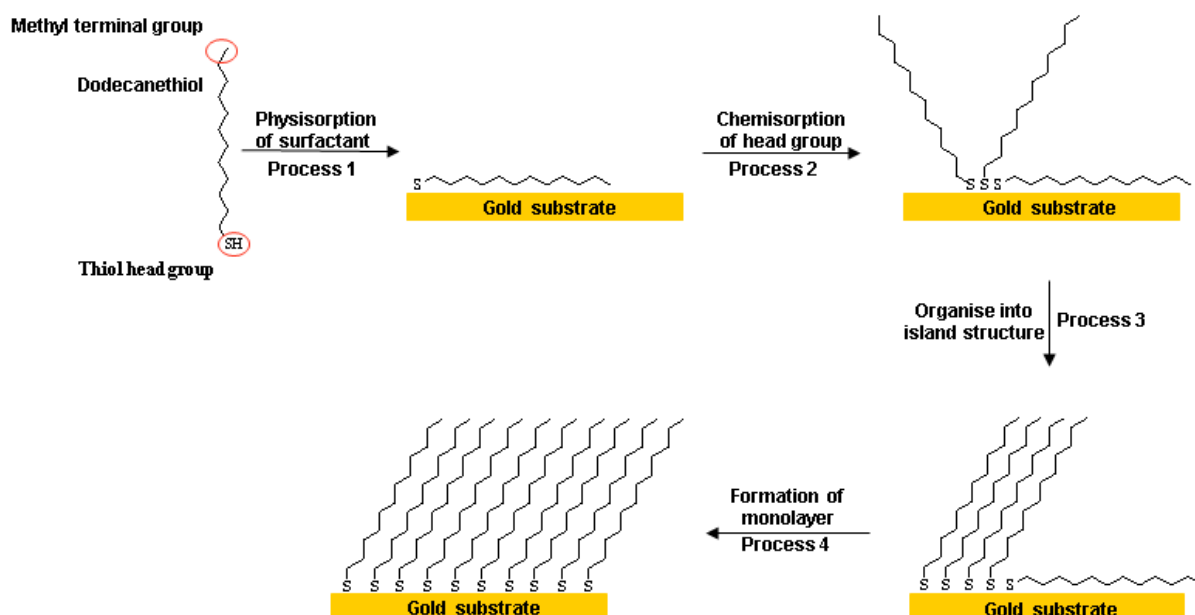
Figure 1.2 An overall schematic diagram of the formation of DDT SAMs on Au.

The adsorption process, including physisorption and chemisorption of alkanethiols on gold can be written as the following reactions:

$$CH_3(CH_2)_nSH + Au \rightarrow (CH_3(CH_2)_nSH)_{phys}Au \qquad (1)$$

$$(CH_3(CH_2)_nSH)_{phys}Au \rightarrow CH_3(CH_2)_nS\text{-}Au + 1/2H_2 \qquad (2)$$
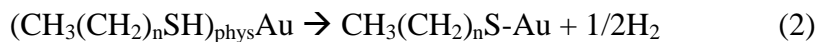
Reaction 1 corresponds to the physisorption of alkanethiols on a gold surface (**process 1**, **figure 1.2**), whereas, reaction 2 illustrates the chemisorption process (**process 2**, **figure 1.2**). The chemisorption mechanism of reaction 2 is not completely understood: it has been assumed that the reaction occurs via oxidative adsorption of the alkanethiol RS-H bond to the metallic gold surface.[28] Further, it is unknown whether the mechanism involves an ion, a radical or another species. The exact theory on the process of the thiol hydrogen atom adsorption on the surface remains a question yet to be answered.[42,43]

The most widely accepted hypothesis[43] is that hydrogen atoms react and generate H_2, as shown in reaction 2. The support for this claim has been verified by results obtained from the self-assembly of nitroaromatic thiols on gold surfaces prepared by vacuum vapour deposition,[43] where a partial reduction of terminal nitro group to amino groups during SAM formation was observed. The reduction is due to the release of atomic hydrogen by cleaving the S-H bonds during the formation of thiolates. Therefore, reaction 2 seems to be applicable for the chemisorption of alkanethiols on gold surfaces.

After addressing the chemisorption reaction, we will now focus on the monolayer formation of the surface. Studies show that chemisorption of surfactants of thiol molecules is easier at the defect sites (step edges) on the gold surface, where preferred nucleation of islands containing lying down molecule takes place (**process 3, figure 1.2**).[44] After nucleation, the island grows, and increases the surface coverage of the thiolate species across the gold surface forming a monolayer (**process 4, figure 1.2**).[45] The completion of this process can take

several hours, depending on the nature of the backbone. Wu *et al.*[46] have reported that shorter chain alkanethiols adsorb faster than those with longer chains. The faster adsorption rate might be due to the higher mobility of the shorter alkanethiol chain towards the surface. They have also reported that terminal groups such as porphyrin, which is bulky and electron rich, could decrease the adsorption rate due to steric hindrance and electrostatic repulsion between alkanethiols.[46]

The ordering of the alkanethiol monolayer on the surface has been studied by IR spectroscopy.[47] From the analysis of the CH_2 and CH_3 stretching modes, it was found that at room temperature, alkanethiols form densely packed, crystalline monolayers with chains mainly adopting an all-*trans* configuration with very few *gauche* conformations to the outermost alkyl unit. Although, clean, freshly prepared gold substrates produce the best quality SAMs, the adsorption of most alkanethiols to gold is sufficiently strong to displace weakly adsorbed contaminants on the surface.

Studies have shown that SAMs with an alkyl chain containing 12 or more methylene groups form well ordered dense monolayers on Au (111) surfaces.[48] **Figure 1.3** shows the arrangement of the gold (Au) atoms of the (111) surface. The thiols (red circle) are believed to attach to the three-fold hollow sites of the gold surface that are arranged in a hexagonal relationship with respect to each other as demonstrated by the black lines connecting six of them.[40] The thiol loses a hydrogen atom in the process, forming a $(\sqrt{3} \times \sqrt{3})R30^o$ overlayer structure.
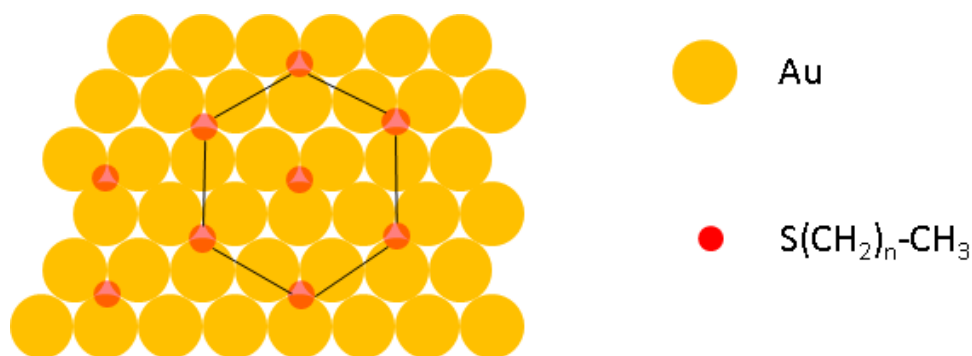
Figure 1.3 A schematic model of ($\sqrt{3}$ x $\sqrt{3}$)R30^o overlay structure formed by alkanethiol SAMs on a Au (111) surface.

The distance between each pinning site is about 0.497 nm, resulting in an area of each molecule of 0.214 nm^2.[28] Since the van der Waals diameter of the alkanethiol (0.46 nm) is too small to occupy that area, the chains tilts, forming an angle (α) approximately 30°-35° to the surface normal (**figure 1.4**).[28, 49] Depending on the chain length and the terminating group, various super-lattice structures are superimposed on the ($\sqrt{3}$ x $\sqrt{3}$)R30^o overlay structure. The tilt angle (α) plays the most important role in SAMs formation as it provides the parameter to maximise the van der Waals chain-chain interactions, leading to effective close packed monolayers.[28]
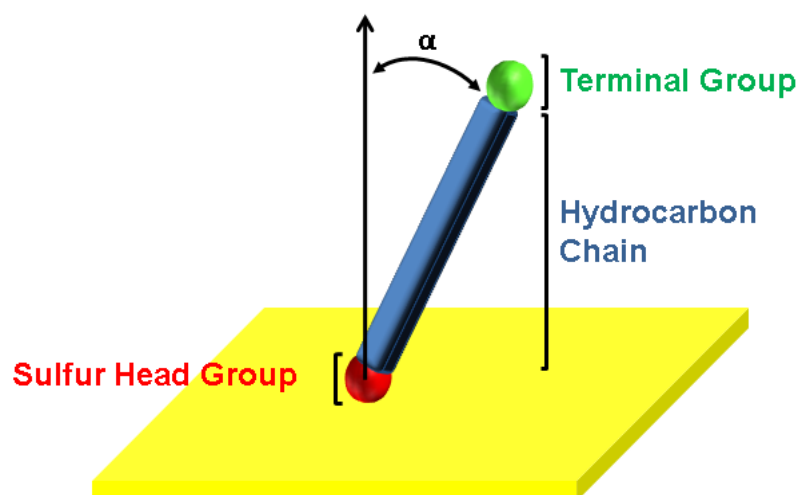
Figure 1.4 A cartoon representation of a thiol adsorbed on a Au (111) surface.

1.1.2.2 Organosilane based SAMs

Organosilane SAMs on a silicon oxide surface[50] provides more application potentials than the alkanethiol SAMs on a gold surface, since silicon is widely used in micro-electronics industry.[51] The process for organosilane SAM formation on silica is more complicated than alkanethiol SAMs formation on gold.

The mechanism of organosilane SAM formation is not fully understood. Studies[52, 53] using octadecyltrichlorosilane (OTS) suggests the following steps.

1) Initially, the OTS molecules are hydrolysed and form silanols (**process 1**, **figure 1.5**).[52]

2) The silanols adsorb on the substrate surface (**process 2**, **figure 1.5**).

3) The silanols condense to form islands of polysiloxanes. (**process 3**, **figure 1.5**).[52, 54]

4) With increasing surface coverage, these islands grow laterally and combine (cross-linking) with other aggregates until a complete monolayer is formed (**process 4**, **figure 1.5**).[54]

Figure 1.5 An overall schematic diagram of the formation of organosilane SAMs on silicon.

1.1.3 SAMs defects

In many schemes found in the literature especially in those with nano-technological applications, SAMs on gold are always presented as perfect monolayers, with molecules in a closed packed configuration as shown in **figure 1.2**. However, this representation only shows an ideal formation of SAMs and the reader should be made aware of several defects[38] that SAMs possess and its impact on potential applications.

Molecular defects are present even in well-ordered, crystalline alkanethiolate domains. These defects can either be a small number of missing molecules known as **pin hole** defects (**figure 1.6a**) or regions where the molecular chains have a certain degree of disorder. The **disorder**

defect normally refers to regions of monolayer that have hydrocarbon chains which are not fully extended (**figure 1.6b**) with gauche conformation.[38] On the other hand, the molecular layer can adopt a number of symmetry equivalents to different regions on the gold lattice. Under growth conditions, various domains nucleate, grow, and coalesce with respect to the gold surface. The domains are separated by boundaries on the surface which causes a defective region in a SAM known as a **domain** defect (**figure 1.6c**). The domain defect is either caused by the adjacent domains of different lattices or two domains of the same ordered lattice but with different orientation on the surface.
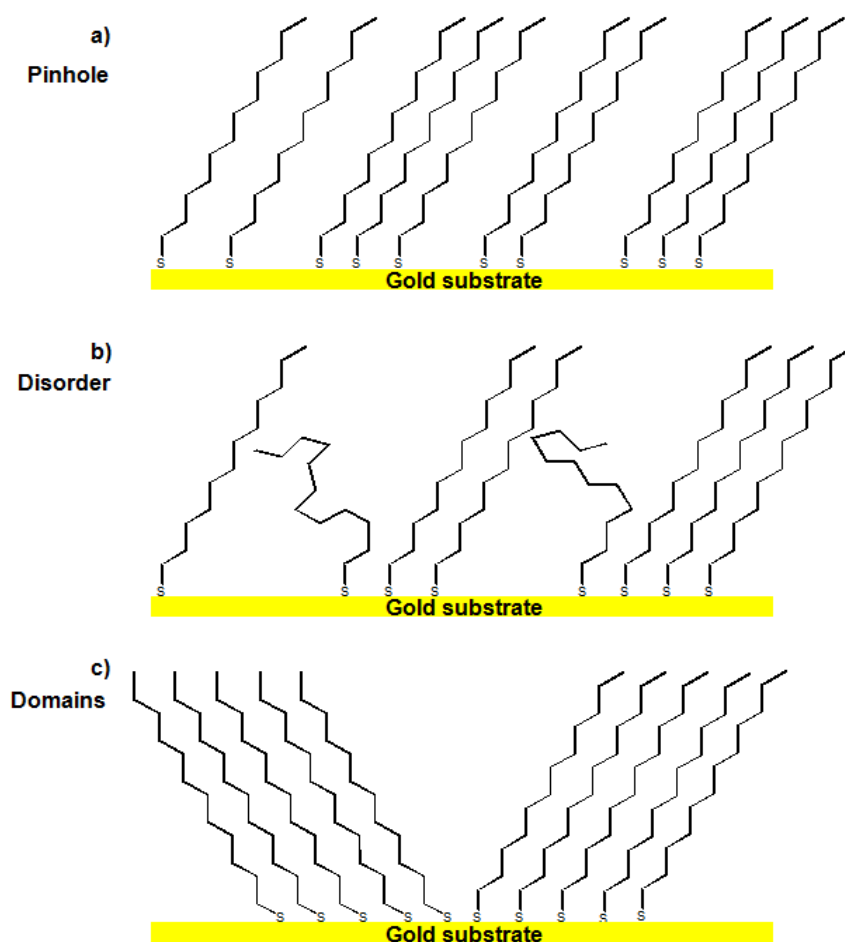
Figure 1.6 Illustration of possible SAM defects.

1.1.4 Mixed SAMs

In addition to uniform monolayers formed by using a single thiol compound, mixed SAMs are increasingly used for the immobilization of biomolecules and employed widely in the field of biosensors.[55] The purpose of creating a mix of thiols in a monolayer is to create a greater spatial distribution between the thiol molecules.[56]

In principle, the molar ratio of different thiols in a mixed SAM is the same as their original molar ratio in the solution used in SAMs formation.[57] Hence, if the mixture of two thiols compounds does not show phase segregation, we can assume that the two thiols compounds randomly adsorb onto the surface.[58] However, as reported in the literature,[59] the ratio of two components in solution are rarely identical from that in the SAM, due to the preferential adsorption of one of the components, hence more surface characterization is needed to determine the exact surface coverage of the mixed SAMs.

Mixed SAMs offer the potential to mix an ω-substituted alkanethiol with short chain non-substituted thiols resulting in a reduction of steric hindrance for anchor molecules such as proteins (**figure 1.7a-c**) to attach onto the surface. **Figure 1.7a** shows a pure SAM layer with the same chain length causes severe steric hindrance to anchor molecules. In **figure 1.7b**, mixed SAMs with space between reactive groups illustrated by green triangle causes less steric hindrance. Furthermore, mixed SAMs with different chain lengths and space between reactive groups as shown in **figure 1.7c**, provide much reduced steric hindrance surface for the anchoring of molecules.
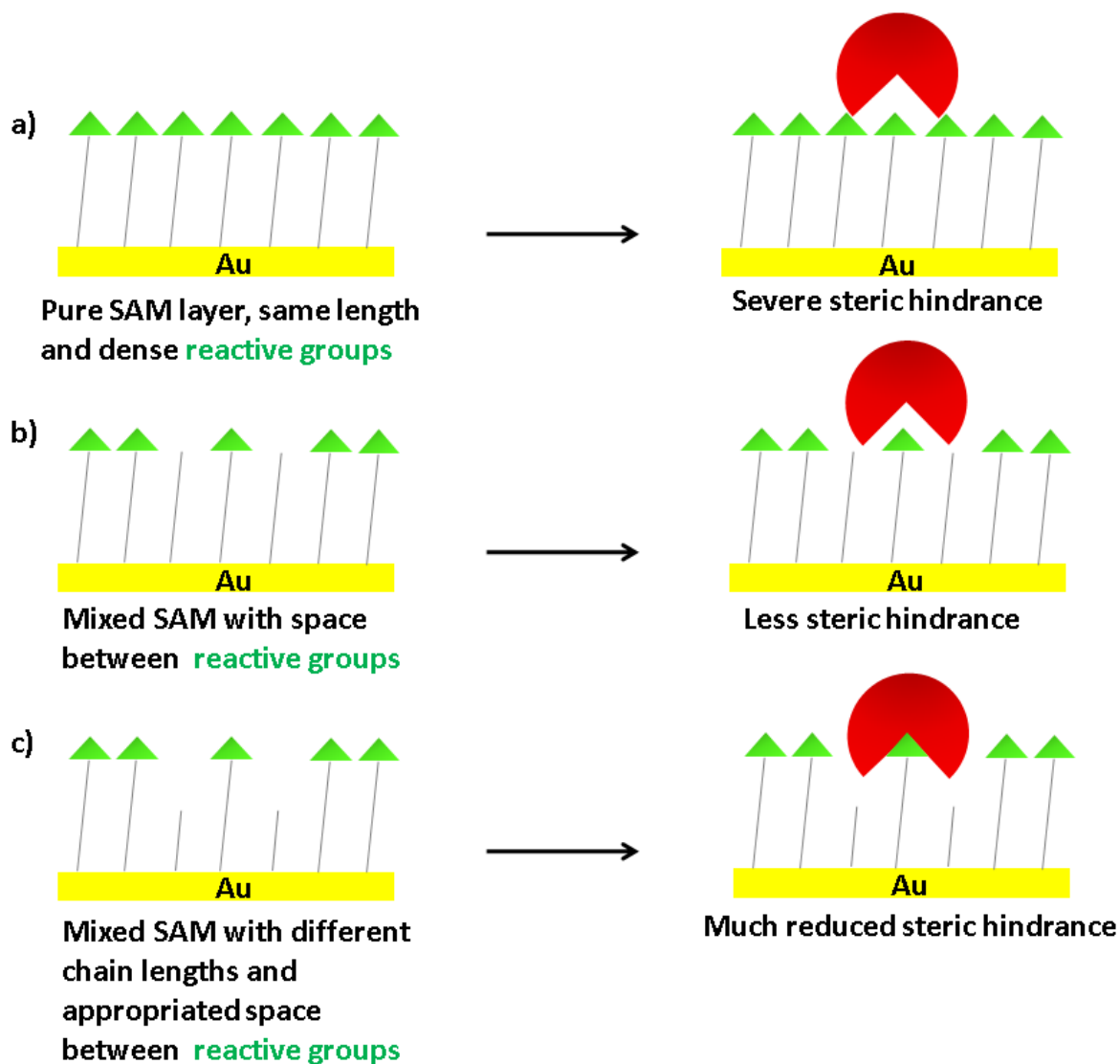
Figure 1.7 A schematic illustration of different SAMs layers: **a)** A pure SAM containing surfactants with the same chain length and dense reactive groups leads to **severe** steric hindrance. **b)** A mixed SAM containing surfactants with similar chain lengths and limited spaces between reactive groups results in **less** steric hindrance. **c)** A mixed SAM containing surfactants with different chain lengths and appropriated spaces between reactive groups – **much reduced** steric hindrance.

1.2 Applications of SAMs

SAMs have a rather large range of applications including organic semiconductors for applications in organic electronics,[60] generation of biocompatible surfaces,[38] anchoring proteins to surfaces,[61] and deposition of metal organic frameworks on SAMs surfaces.[62] Among these, the generation of biocompatible surfaces will be discussed in detail in this report.

1.2.1 Generation of biocompatible surfaces

The generation of biocompatible surfaces with specific designed functionalities is pivotal for biological[6] and medical applications.[9] Proteins are macromolecules produced by living organisms that are employed for a variety of processes, from catalysis of biochemical processes to forming structured motifs in cells.[4] Many of these processes occur at biological interfaces. Thus, the interaction of proteins with a surface is an important subject that is worth exploring. Proteins can adsorb onto a surface in two ways.

i) Non-specific adsorption, which involves the physisorption of biomolecules onto the surface.

ii) Specific interaction of proteins selectively binding to a chemical/biochemical moiety exposed at the surface without causing protein conformational change.

1.2.2 Protein inert surfaces

In general, proteins adhere to many surfaces in a non-specific fashion. Therefore, one of the most important and most fundamental problems in connection with protein-surface interactions is the generation of protein inert surfaces.

Surface Plasmon Resonance Spectroscopy (SPR) (further discussion of SPR can be found in **chapter 2**) allows for fundamental investigations of the interactions of proteins to the surfaces. Recently, a study[63] showed the results of corresponding measurements for the interaction of a protein (Streptavidin (SA)) with a CH_3-terminated SAM surface. SPR data revealed a strong interaction of the proteins with this hydrophobic surface. As soon as the protein containing buffer comes into contact with the CH_3-terminated SAM surface, there is a strong increase in signal as shown in **figure 1.8**.
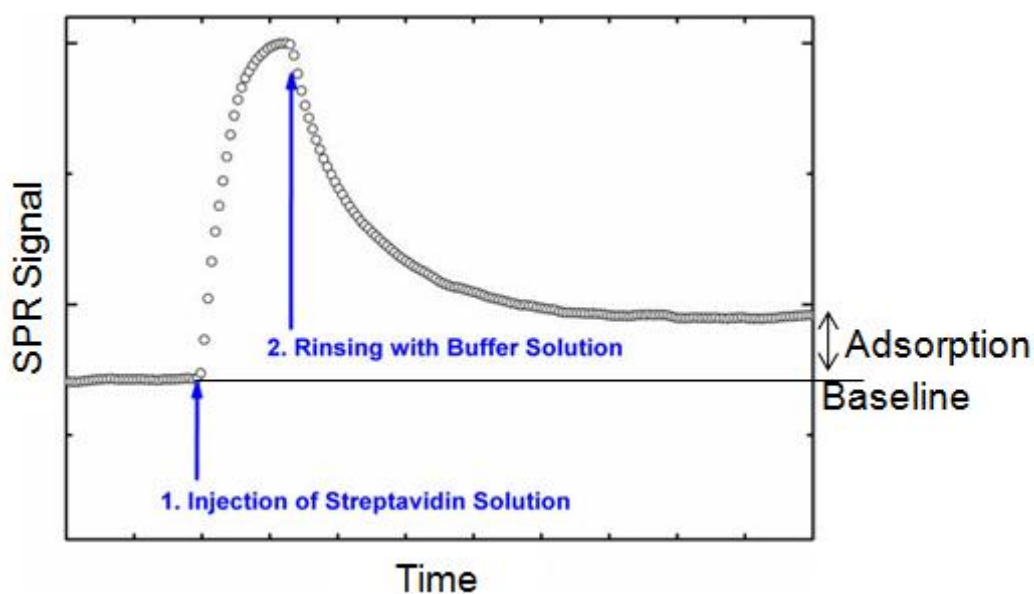
Figure 1.8 These SPR data show the adsorption of a protein on a CH_3-terminated SAM surface.[63] Prior to the time point marked with 1, the surface is in contact with pure buffer solution. The SPR signal is constant. At the time point 1, a solution of the protein is flushed to the cell and there is a strong increase in signal intensity. At time point 2, when the surface is washed with pure buffer solution, the strong signal decreases again but does not drop to the basic level that was present prior to the injection of protein, indicating an irreversible binding of the protein to this hydrophobic surface.

Typically, protein binds to a surface non-specifically as shown in the above example; this causes protein to unfold and the protein is denatured and loses its biochemical functionality. In the last decade, intensive investigations have taken place to search for bio-inert surfaces which do not promote non-specific protein binding and denaturation of the protein. The oligo(ethylene glycol) (OEG) terminated surfaces have demonstrated[64] to be the most effective in preventing non-specific adsorption of proteins. As shown in **figure 1.9**, SA employed in this study does not adsorb onto the OEG-terminated surface.
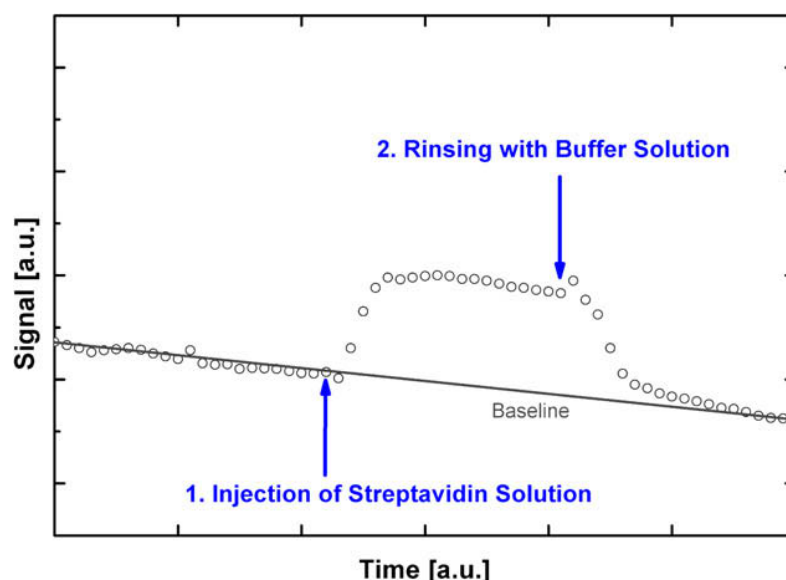
Figure 1.9 SA was brought in contact with an OEG-terminated surface. Unlike the CH_3-terminated SAM surface as shown in **figure 1.8**, the signal increases when SA was flushed onto the surface as seen in time point 1, but drops back to the baseline after rinsing with the buffer solution (time point 2). These measurements prove that SA does not adsorb onto an OEG-terminated surface.

Being able to prevent non-specific adsorption of proteins onto solid surfaces is only half of the story; what is also important is to generate a surface that proteins can specifically bind onto without losing their biochemical function.

1.2.3 Specific protein adsorption onto surfaces

The anchoring of proteins to artificial surfaces so that they can retain their functionality is crucial for systematic studies in protein affinity at surfaces. Much of the work in the literature employs a very well studied biological system, SA and biotin, due to the high binding affinity.[65] The SA protein exhibits a total of four binding pockets for biotin as shown in **figure 1.10**. The bond is relatively strong, with a dissociation constant of 10^{-15} M.[66] The binding of the biotin molecule to SA is irreversible under physiological conditions, thus, making this interaction between SA and biotin molecule an ideal candidate for studies of specific protein adsorption on a solid surface.
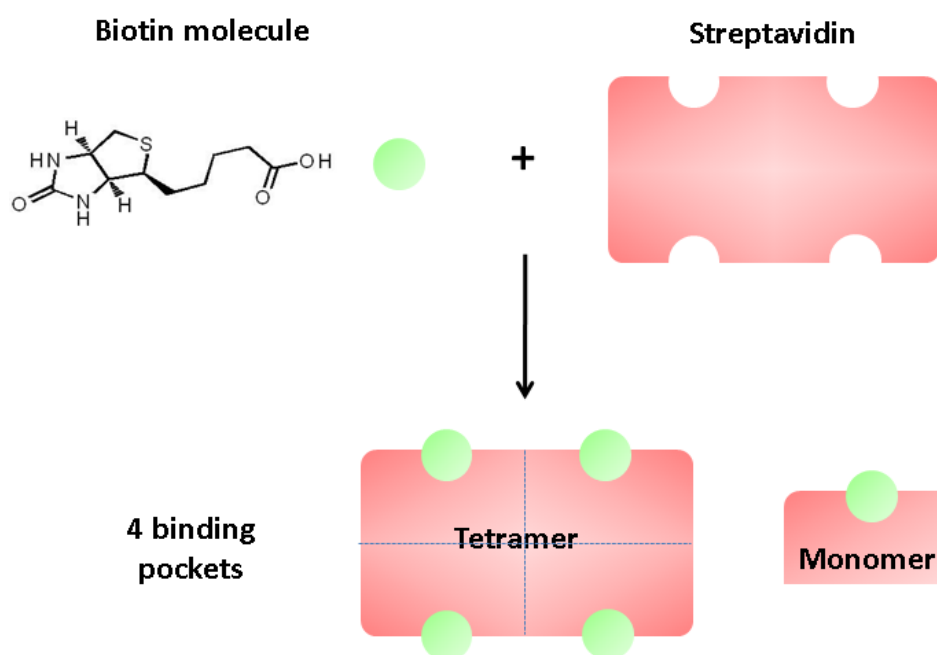
Figure 1.10 Schematic structure of the streptavidin protein consisting of four subunits. Each subunit possesses a binding pocket for the biotin molecule.

This interaction can be exploited for anchoring the SA protein to a surface by generating a biotin-terminated surface as shown schematically in **figure 1.11**.
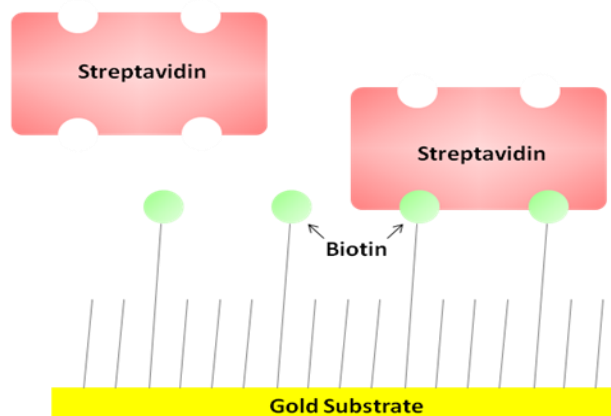
Figure 1.11 Schematic drawing illustrating the specific binding of streptavidin onto a biotinylated surface. By binding the biotin functions to the binding pockets of streptavidin, secure anchorage of streptavidin onto the gold surface is achieved.

Figure 1.12 shows an example[67] where the biotin has been patterned onto a surface using microcontact printing (More detail discussion of microcontact printing can be found in **section 1.2.5.2**). Fluorescently labelled SA was introduced onto the patterned biotinylated surface, and the fluorescence image clearly shows that SA binds only to those parts of the organic surface where the biotinylated surface is exposed. The darker squares are covered by an OEG group, which inhibits SA non-specific binding.
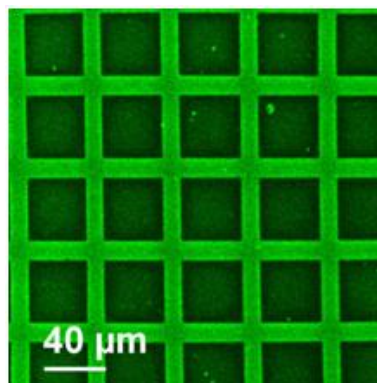
Figure 1.12 Fluorescence microscopy image of a SAM prepared by microcontact printing. The stripes consist of a mixture of 25 mol% biotin thiol and 75 mol% OH-terminated thiol. The square is OEG-terminated thiol. The SAM has been immersed in a 100 nM fluorescence-labelled SA solution. This protein only binds at the biotin-terminated parts of the surface as can be seen by the fluorescence signal.

SA cannot perform any biochemical transformation; the main reason for SA binding onto a surface is to act as a linker for the further anchoring of other proteins.[61] SA has further biotin binding pockets, and thus proteins furnished with a biotin anchor may be anchored to surface bound SA, generating a second layer of proteins on the surface. With regard to this approach, the biotin density on the organic surface should not be too high because if the packing density becomes too high, the density will sterically hinder the binding of SA on the surface. It is therefore necessary to dilute the biotin terminated organothiols to achieve the optimal surface concentration between 5% and 10% as shown by the SPR data in **figure 1.13**[61]. As can be seen, maximum adsorption occurs at the concentration at approximately 5% biotin thiol on the surface. For higher surface biotin concentration, a slight decrease in the quantities of anchored SA is observed.
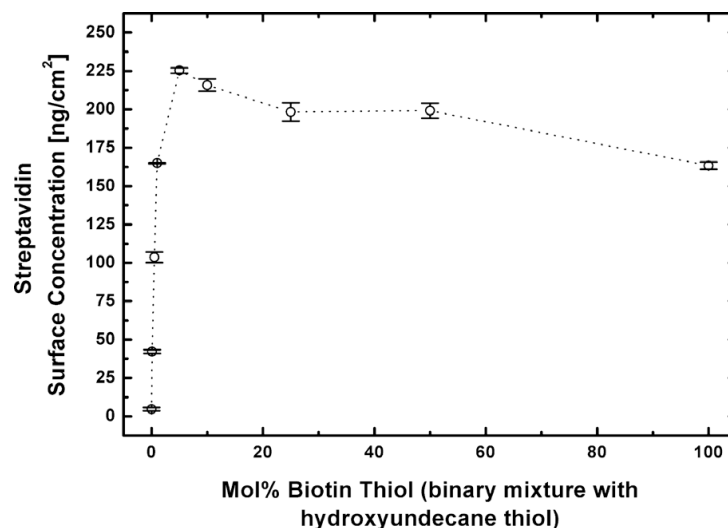
Figure 1.13 The quantity of SA molecules anchored to a biotin-functionalized based on the mol% of biotin thiol on the surface.

As mentioned previously, further biotin-labelled materials may be bound after the deposition of an SA layer, since SA has a total of four binding pockets for biotin. Thus, biotinylated bHRP protein has been absorbed (**figure 1.14**).[61] The bHRP protein retains its biochemical function after binding to the SA, with an activity only slightly lower compared to that in the natural biological environment.
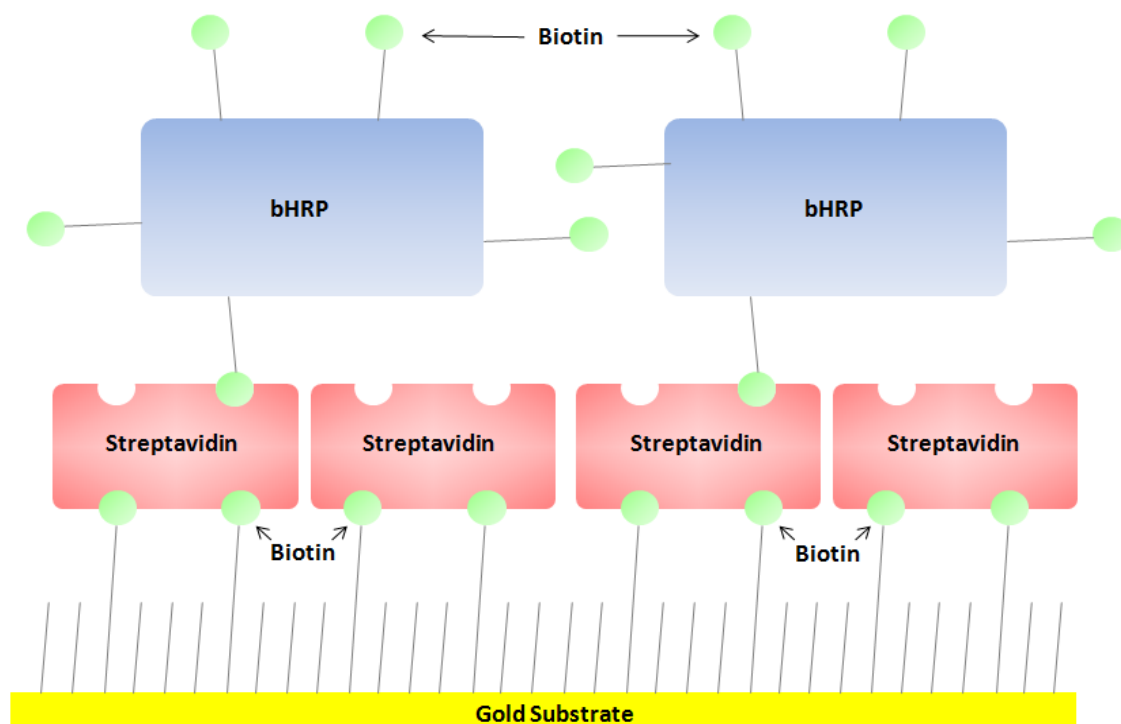
Figure 1.14 A cartoon representation to demonstrate how bHRP functionalized with biotin can specifically be anchored on a surface. SA is first chemically bound onto the biotinylated surface, and subsequently, the biotin residues of the labelled bHRP can bind to the remaining vacant binding pockets on the SA.

1.2.4 Organic surfaces and electrochemistry

The poor conductivity of organic materials creates problems in the electrochemical characterization of organic surfaces. Model organic surfaces prepared by the self-assembly of organothiols on gold substrates offer a convenient way to overcome these limitations. The presence of a well-defined layer of organic molecules on a metal substrate allows the electrical properties of the organic layer to be measured; therefore, the electrochemical characterisation of organic material is possible.

1.2.4.1 Electrochemical tools to characterize and modify SAMs

Electrochemical techniques are highly sensitive to nanometre scale monolayer defects that are difficult to discern using scanning techniques.[68] Pinhole defects can be detected using electrochemical methods[69] and ferrocene alkanethiols have been used to electrochemically label fast exchange defect sites.[68] Cyclic voltammetry (CV) can be used to electrochemically distinguish collapsed sites from pinhole defects using a ferrocene label.[70]

CV is often used to interrogate the structure and dynamics of SAMs. A disordered SAM allows an electrolyte to approach the electrode surface leading to a capacitive current.[71] In one of the first SAM electron transfer studies,[72] the capacitance of hydroxyalkane thiol SAMs of varying chain lengths (from 2 to 16 methylene units) was examined. CV revealed that the capacitance decreased as the number of methylene units increased, with capacitances ranging from 12.6 $\mu F/cm^2$ for 2 methylene units and 1.36 $\mu F/cm^2$ for 16 methylene units. This result suggested that thicker monolayers (16 methylene units) form a better insulating barrier between the gold surface and the redox species in the solution.

An example of controlling SAMs properties has been demonstrated by provided Mendes *et al*. (**figure 1.15**).[17] By employing electrochemical reactions, surface terminal groups (NO_2) in the SAM of 4-nitrothiolphenol on a gold surface can be electrochemically reduced to amino groups (NH_2) by applying a negative potential between the surface (working electrode) and the counter electrode in the presence of an electrolyte. By employing a bifunctional linker, proteins were able to bind onto the amino-terminated regions.
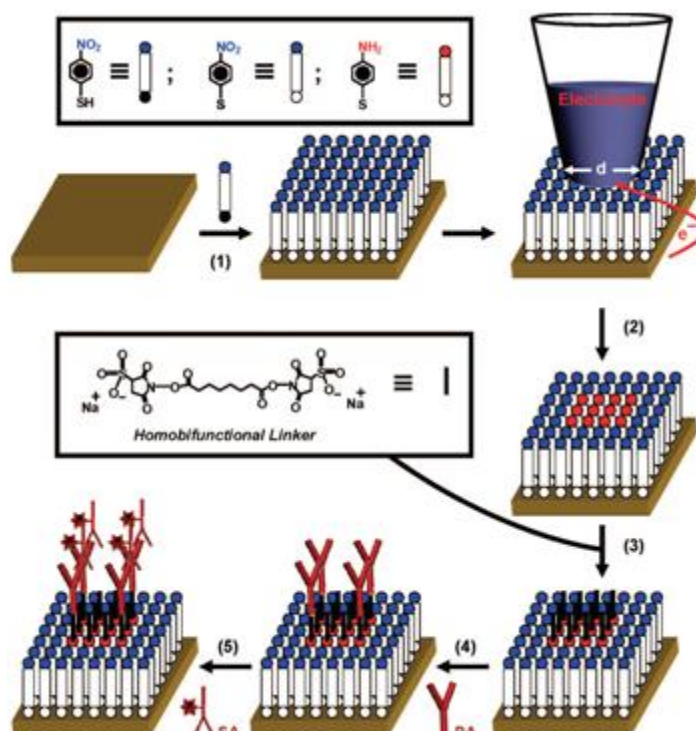
Figure 1.15 Schematic illustration of the electrochemical conversion of NO_2 terminal group to NH_2 terminal group, which can be employed for the attachment of functional linkers and subsequently, the immobilisation of antibodies (primary (PA) and secondary (SA)) on the surface.[16]

The first CV scan used 0.1M KCl (9:1 EtOH/ UHP water) as an electrolyte to check the characteristic CV peak that the NO_2 terminal group exhibit (**blue** curve of **figure 1.16**). The second scan was carried out using 0.1M KCl aqueous solution to ensure plenty of H^+ ions for the complete electrochemical reduction of NO_2 terminal group to NH_2 terminal group. The final scan observes the disappearance of the NO_2 peak (**red** curve of **figure 1.16**) using 0.1M KCl (9:1 EtOH/ UHP water) as the electrolyte.
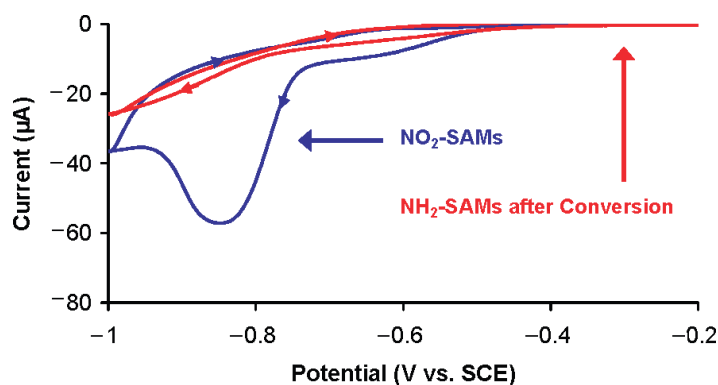
Figure 1.16 CV (**blue** curve) of a SAM of 4-nitrothiophenol, the reduction of NO_2 to NH_2 groups appears as a pronounced peak at around - 0.85 V. CV (**red** curve) of the SAM of 4-nitrothiophenol after the reductive scan.[16]

1.2.5 Patterning of organic surfaces using top down approach techniques

A very important application of thin films deposited on solid substrates has been their use as photoresists[73] or electron beam resists in high-resolution lithography.[74, 75] Surfactants can also be employed as the "ink" for dip-pen nanolithography and microcontact printing techniques to create patterned structures on surfaces. These techniques are tremendously important in the field of fabrication of nanostructured surfaces. Herein, a brief description of such techniques will be provided.

1.2.5.1 Photolithography

Photolithography[73] is a lithographic process which uses radiation passing through a mask to initiate chemical reactions on a resist (typically, an organic polymer) coated on a substrate (typically, SiO_2). The resist either fragments (positive tone) or cross-links (negative tone), and is soluble, or not soluble, in a developing agent, respectively. After development, the remaining resist acts as a barrier to an etching medium, that transfers the pattern to a substrate.

Figure 1.17 shows the general process of photolithography followed by etching to afford 3D structures.
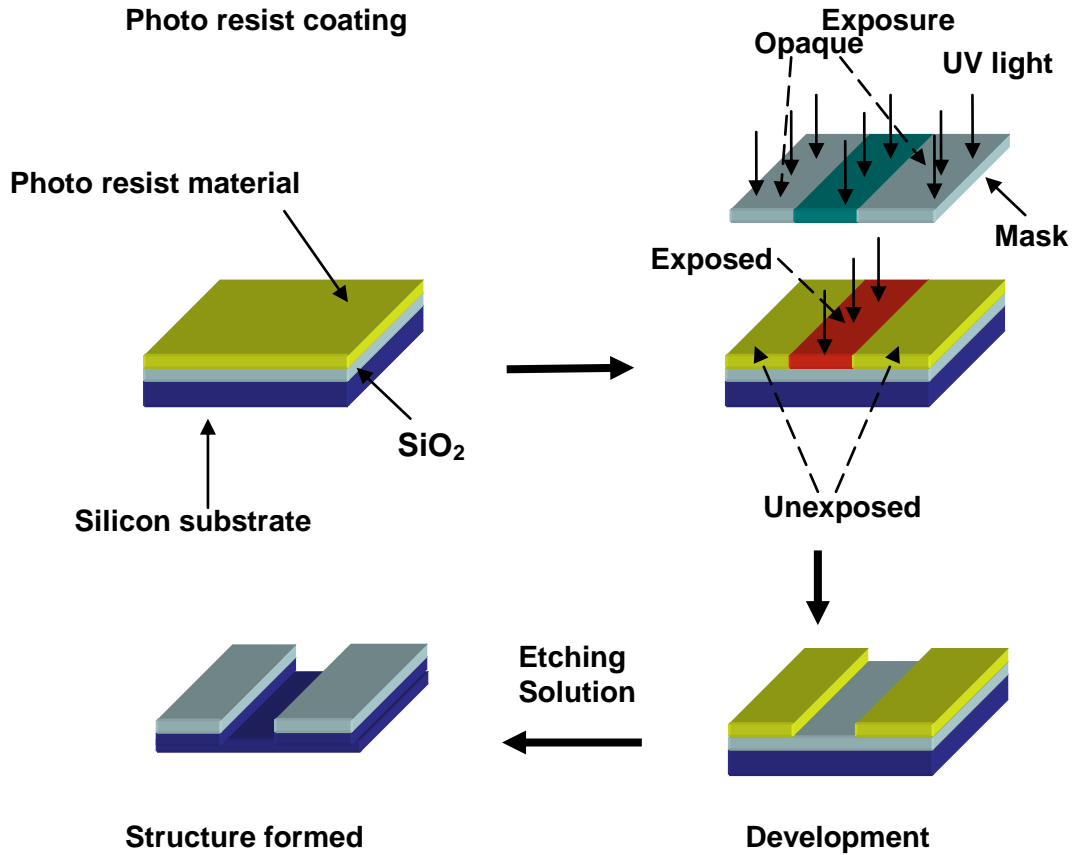
Figure 1.17 Schematic demonstrating the photolithography process (positive tone).

1.2.5.1.1 Limitations to Photolithography

There are limitations to photolithography. To decrease the size of the pattern, smaller mask features are required, but this will result in increased diffraction of the image.[76] This problem, in principle, can be overcome by using shorter wavelength light and utilizing constructive and destructive interference of the diffracted light.[77] However, the energy of the radiation will increase as wavelength decreases and damage the optics, mask, and substrate. With this difficulty in mind, a number of methodologies such as redox control,[78] conductive AFM,[79] scanning-near field photolithography,[80] nanoshaving,[81] nanografting,[82] dip pen

nanolithography,[83] electron beam lithography[84] and stamping techniques, such as imprint lithography,[85, 86] nanocontact printing[87] have been utilised for generating nanoscale features of biomolecules on surface.

1.2.5.2 Microcontact printing (µCP)

Apart from using self-assembled monolayers in the field of nanofabrication, microcontact printing is another technique that greatly contributes towards the advancement of molecular surfaces. The microcontact printing process (**figure 1.18**)[88, 89] involves the fabrication of polydimethoxysiloxane (PDMS) stamps by depositing a monomeric precursor over a silicon master and subsequently curing it (**step a**, **figure 1.18**). The stamp is then peeled from the master, wipped with a cotton wool and dipped in the surfactant solution (**steps b** and **c**). The stamp is removed from the surfactant solution (step **d**), leaving an "ink" of surfactant on the patterned PDMS stamp surface. The stamp is then brought into conformal contact with the substrate (**step e**), which can range from metals to oxide layers. The ink is transferred to the substrate where it forms a patterned surface (**step f**). A significant advantage of μCP compared to serial techniques such as dip-pen lithography[90] is that large areas can be micropatterned rapidly. Furthermore, as opposed to the parallel conventional photolithographic process, μCP is not diffraction limited and it is possible to nanopattern surfaces.[87, 91]
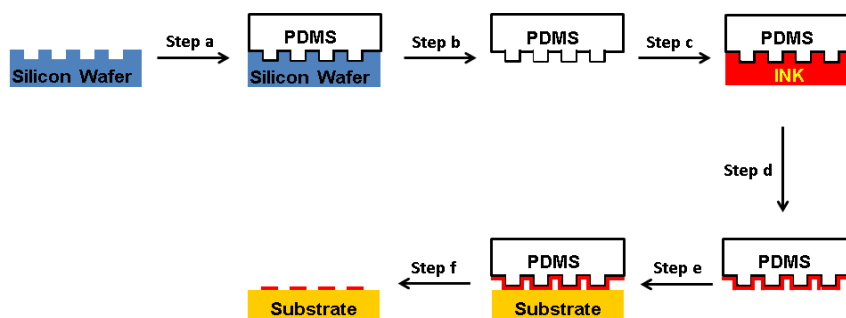
Figure 1.18 The microcontact printing process.

1.2.5.3 Nanocontact printing

Microcontact printing (μCP) is widely used for generating micropatterns of nanomaterials such as organic molecules and biomolecules[92-96] over large surface areas ($>$ cm^2). Since μCP is carried out under ambient conditions, different biomolecules have been directly transferred onto a variety of substrates while retaining their biological activity.[92-96]

More recently, a μCP concept has been extended to nano-scale dimensions, a process referred to as nanocontact printing (nCP).[97-99] Features as small as 40 nm can now be fabricated using this process.[98] Nanocontact printing has been achieved by decreasing the feature sizes in the PDMS stamp and diluting the nanomaterial "ink" concentrations,[99] utilising special variants of PDMS stamps[97, 98] or employing new polymeric stamp materials.[100] Another important factor for obtaining high-resolution prints at the 100 nm level relates to the different kind of "ink" utilised. In this context, biomolecules are attractive nanocontact printing inks, since their high molecular weight prevents diffusion during the printing step, resulting in high-resolution features.[85]

By diluting the protein solution and decreasing the feature size of the PDMS stamp, patterns of immunoglobulin (IgG) and green fluorescent proteins with 100 nm wide lines have been generated on glass substrates.[99] A composite PDMS stamp, cast from V-shaped gratings used for AFM tip characterisation, was also used to print lines of titin multimer proteins on a silicon surface with widths less than 70 nm (**figure 1.19**).[98] The stamp design was based on a two layer stamp that uses a thick film of standard soft PDMS (Sylgard 184 PDMS) to support a thin stiff layer of hard PDMS.[97] The hard PDMS layer improved the mechanical stability of the features on the stamp, reducing sidewall buckling and unwanted sagging from the relief

features.[97, 98] New polyolefin elastomer stamps were also exploited for creating fibrinogen protein nanostructures on glass surfaces.[100] The higher stiffness of these stamps allowed 100 nm wide lines of fibrinogen to be fabricated with superior quality than those resulting from PDMS stamps.[100]
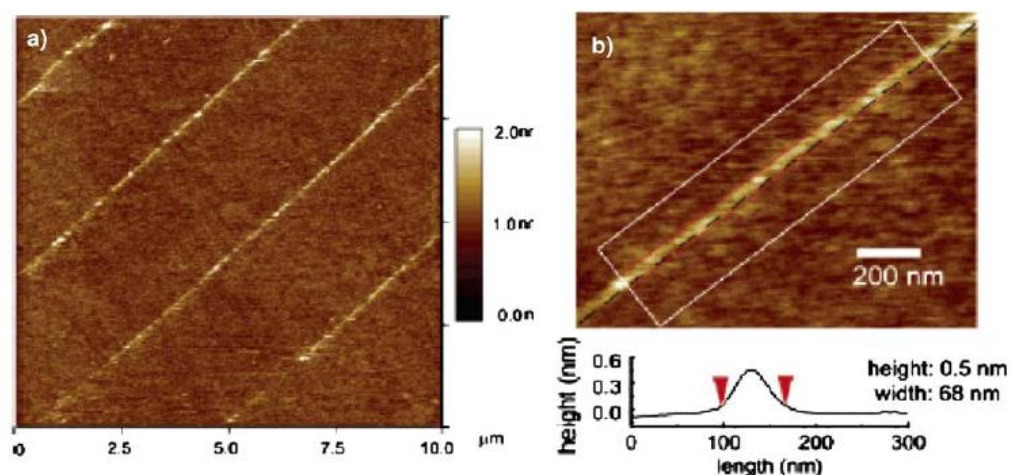
Figure 1.19 AFM tapping mode images of nanocontact printed titin multimer protein lines on a silicon surface **a**) at large scale and **b**) at high resolution with height profile cross section below.[98]

1.2.5.4 Dip-pen nanolithography

Dip-pen nanolithography[83] (DPN) is a scanning probe nanopatterning technique in which an AFM tip is used to deliver molecular and nanoscale materials directly to nanoscopic regions of a substrate. The deposition process involves the inking of an AFM tip with the molecular or nanoscale material, which is then transferred to the substrate by bringing the AFM tip in contact with the substrate surface. Once in contact with the surface, the AFM tip can be either removed from the surface to form dots of the material, or scanned across the surface before being removed, resulting in line patterns. The inked AFM tip is most commonly scanned across the substrate in contact mode, however, there have been reports of the AFM tip being

scanned in tapping mode.[90, 101] Although the exact tip-substrate transport mechanism remains unclear, there is some evidence that the ink transport from the tip is mediated by a water meniscus that forms between the tip and the surface under atmospheric conditions.[83, 102-104] Among other factors, water meniscus properties, the tip geometry, the chemical nature of the ink and substrate, substrate morphology, tip-substrate contact time and writing rate have been demonstrated[83, 104-110] to affect the resolution of the patterns. Early results showed that DPN could be used to pattern alkanethiol SAMs onto gold surfaces with dot features as small as 15 nm.[105] Each dot was formed by holding a 16-mercaptohexadecanoic acid (MHA)-coated tip in contact (relative humidity 23%) with the gold surface for 10 s.

Parallel probe arrays, which have previously been investigated for use in data storage,[111] have allowed DPN to develop into a parallel process.[105, 112-117] The use of tip arrays has been shown to be a technique that can pattern over square centimetres,[112, 118] while still retaining nanoscale control of the features. For instance, a 55,000-pen, two-dimensional array has been fabricated[118] that allowed the reproduction of the face of Thomas Jefferson, from a 2005 US five-cent coin, 55,000 times with nanoscale resolution. Perhaps more significantly, approximately 4.7×10^8 nanofeatures were used to generate the replicas, and the total time required to perform this fabrication was less than 30 min. This example of nanostructures formed by DPN using parallel probes highlights the potential of DPN as a high-throughput, commercial technique for applications in the fabrication of bioarrays.

Since DPN offers the ability to routinely patterning in the sub-100 nm regime under ambient conditions, which is critical for patterning biologically active molecules, several different

approaches have been investigated for bionanopatterning of surfaces using this technique.[119, 120, 121]

1.2.5.5 Electron Beam Lithography

Electron-beam lithography (EBL) is a well developed and optimised technique for semiconductor fabrication.[76] The resolution of EBL is not limited by the focus of the beam (<1 nm), but by the size of the molecules in the resists and secondary electron processes,[74] such as electron scattering and proximity effects. EBL is capable of producing features down to 5 nm in electron-sensitive resists such as SAMs.[74] Although electron-beam technology still has throughput issues, important advances have been made in the development of parallel techniques/tools such as projection e-beam lithography[122, 123] and multibeam sources.[124, 125]

Electron-beam lithography has been exploited to create biological nanostructures by first patterning a pre-formed homogeneous film, and subsequently attaching the biomolecules of interest. Building on well-known sensitivity of SAMs to electron irradiation,[126] thiolates SAMs on gold have been selectively removed by EBL and the exposed areas used for creating bioactive templates.[127, 128] For example, PEG monolayers on gold were patterned using an electron-beam to create biomolecular features with dimensions of about 40 nm.[128] Depending on the electron beam dose used, the SAM was removed from the gold surface or some carbonaceous material was deposited on the surface (i.e. contamination writing). Both patterned surfaces were shown to immobilise neutravidin-coated 40 nm FluoSpheres with high selectivity.[128] A similar electron-beam strategy was also applied to silane SAMs on Si/SiO_2 to create 250 nm patterns of DNA on these substrates.[129]

SiO$_2$ coated metal-oxide nanopatterns have also been formed which can subsequently direct the immobilisation of biomolecules.[130, 131] Indium-tin oxide (ITO)-glass substrates were coated with a thin layer of SiO$_2$, which was then electron-beam patterned to expose nanoregions of the underlying ITO. Dodecylphosphate, to which proteins can bind, was selectively adsorbed on the ITO nanostructures, whereas poly-L-lysine-g-poly(ethylene glycol) was used to passivate the surrounding SiO$_2$ regions against protein adsorption.[131] Fluorescently labelled streptavidin was shown to specifically adsorb to the hydrophobic ITO/dodecylphosphate nanopatterned surfaces (140 nm).[131]

By combining EBL with a lift-off technique, metal nanoarrays have been created for immobilising proteins on Si/SiO$_2$ surfaces.[132, 133] For instance, gold arrays (1 µm to 45 nm in width) were generated for selective immobilisation of disulfide-containing 2,4-dinitrophenylcaproate (DNP-cap) ligands.[132] The ligand patterned surfaces were shown not only to bind with high specificity to anti-DNP immunoglobulin E (IgE), but also to induce specific cellular responses when incubated with rat basophilic leukaemia mast cells.[132] PMMA (poly(methyl methacrylate)), which is widely used as a lithographic positive resist, has been exploited in conjunction with EBL for immobilising IgG[134] and collagen proteins[135] on Si/SiO$_2$ substrates. Collagen was forced to align and assemble into continuous bundles by the anisotropic dimensions of the electron-beam nanoscale patterns (30–90 nm).[135]

Electron-beam lithography has also been carried out to activate porous silicon[136] and polycaprolactone[137] films for further biomolecule immobilisation. Exposure of the electron-beam irradiated polycaprolactone surfaces to an acrylic acid solution in the presence of Mohr's salt led to a graft polymerisation of the acrylic acid on to the polymer surface.[137] A

three-step peptide immobilisation process was then used to immobilise a cysteine-terminated RGD containing peptide onto the grafted surface. EBL has also been exploited to locally crosslink amine-terminated poly(ethylene glycol) films to create hydrogel nanoarrays with 200 nm features on silicon substrates.[138] Two different BSA hydrogel nanoarray pads with lateral dimension of 5 µm by 5 µm on the same substrate were further employed to immobilise two different proteins, fibronectin and laminin, via a photoactivated heterobifunctional crosslinker (sulfosuccinimidyl-6-(40-azido-20-nitrophenylamino) hexanoate).[138]

A particularly attractive feature of using EBL for nanopatterning biomolecules is its compatibility with standard microfabrication techniques developed in the semiconductor industry, allowing the diverse functions of biomolecules to be easily integrated into, for example, bionanoelectromechanical systems (bioNEMS) and sensor devices.[139] However, the principal drawback is that electron-beam modification occurs under ultra-high vacuum conditions, limiting the potential of this technique for multicomponent biomolecule nanopatterning.

1.3 Stimuli responsive surfaces

Surfaces whose properties can be modulated by external stimuli such as electrical,[140] photochemical,[141] chemical and biochemical[142] are known as stimuli responsive surfaces, or "smart surfaces". These switching surfaces have attracted substantial attention over the last few years and this surface technology can be applied in a wide range of applications. [8, 140]

Stimuli responsive surfaces play an important role in the development of substrates that can regulate biological functions in response to external stimuli, and as a result, these substrates can act as a platform for the study of biological systems. Surfaces that can modulate biomolecular activity,[143-145] protein immobilisation,[8, 17, 146] and cell adhesion and migration[27, 147-149] on surfaces can be extremely useful in biological and medical applications. For example, surfaces that can generate and control the regulatory signals to a cell provide an excellent tool for the study of cell behaviour. Cells adhere to and interact with the extracellular environment by either specialised cell-to-cell or cell-to-extracellular matrix (ECM) contacts.[150] The ECM is a highly hydrated network containing three components, (i) the fibrous elements such as collagens, (ii) space filling modules such as proteoglycans and (iii) adhesive glycoproteins such as fibronectin.[150] Cells interact with ECM via a transmembrane receptor protein (integrin),[151] which transmits information across the cell's membrane and is responsible for regulating cell adhesion and migration.[14, 152] Integrin will be discussed further in **section 1.4**. Cell-to-ECM interactions are complicated.[153] In order to understand the complex cell responses to their surrounding physiological microenvironments, artificial microenvironments[154] are needed to understand these interactions. Thus, surfaces mimicking the functions of the natural ECM provide an ideal platform for cell behaviour studies in which cells sense, integrate and respond to changes to their surrounding environments. The advantage of these ECM surfaces is the ability to retain their biological functionality, and at the same time, reduce the complexity that cell studies performed *in vivo* environments. ECM models also have an impact in the field of tissue engineering regeneration.[155] For example, ECM materials provide a platform on which cell-trigger remodelling[156] can occur, thus, when placed at tissue defected sites, these materials can facilitate the regeneration process.

Stimuli responsive surfaces also have the potential to be developed into sophisticated biosensors. These surfaces can translate bio-recognition events on surfaces into measurable electronic[157] or opto-electroic[158] signals. The ability to manipulate biomolecular activity on surfaces can result in developing sensitive, re-usable and real time biosensors.[157-160] The development of the biotechnology and pharmaceutical industry, especially in the field of recombinant proteins (i.e. insulin production), has led to the development of highly functional microfluidic, bioanalysis and bioseparation systems.[161-164]

In order to fulfil the need of such sophisticated systems, applications that can modulate surface bioactivity based on external stimuli (electrical, photochemical, chemical and temperature) have been fabricated (**figure 1.20**).
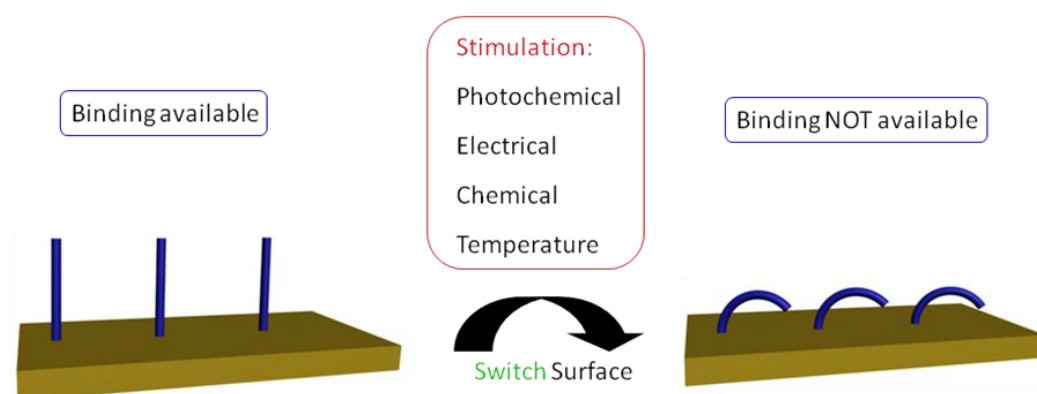
Figure 1.20 Schematic illustration of the range of stimuli that can be used to modulate bioactivity on surfaces based on SAMs.

1.3.1 Electrically responsive surfaces

SAMs containing various electroactive groups have been employed as switchable surfaces to modulate the interactions of peptides,[17, 27, 147, 165-167] DNA,[78, 168] proteins[17] and cells[27, 147, 165-167] to surfaces. Thiol based SAMs were employed electrochemically to release the immobilised proteins from selected micropatterned gold electrodes.[169] The thiolate bond formed between

the SAM and the gold surface can be electrochemically reduced to form thiols at a negative potential of - 1.5 V, thus, the surfactant can be displaced from the surface along with proteins that were immobilised on the SAMs surface. These systems[17, 169] provide a platform to control the adsorption and desorption of protein or protein mixtures, potentially on the nanometre scale using electrically addressable nanoscale electrodes.

SAMs[165-167, 170] with specifically designed electroactive groups on gold surfaces have been employed to modify the surface functionalities in response to an applied potential. The electroactive monolayers were able to switch the peptide ligand activities on and off, influencing the cell attachment behaviours.[27] Electroactive functionalised surfaces based on the hydroquinone-benzoquinone redox couple have provided real-time control over the molecular interactions between the surface and the RGD peptide. This switching property was based on the application of a positive potential on the *O*-silyl hydroquinone moiety that linked to the RGD peptides (E*-RGD) (**figure 1.21**). The hydroquinone moiety oxidised to benzoquinone, resulting in the silyl ether being hydrolysed and subsequently, the RGD peptide released from the surface. The resulting benzoquinone-terminated SAMs were further reacted with a second ligand diene-tagged RGD peptide (RGD-Cp) by Diels-Alder reaction as shown in **figure 1.21**.
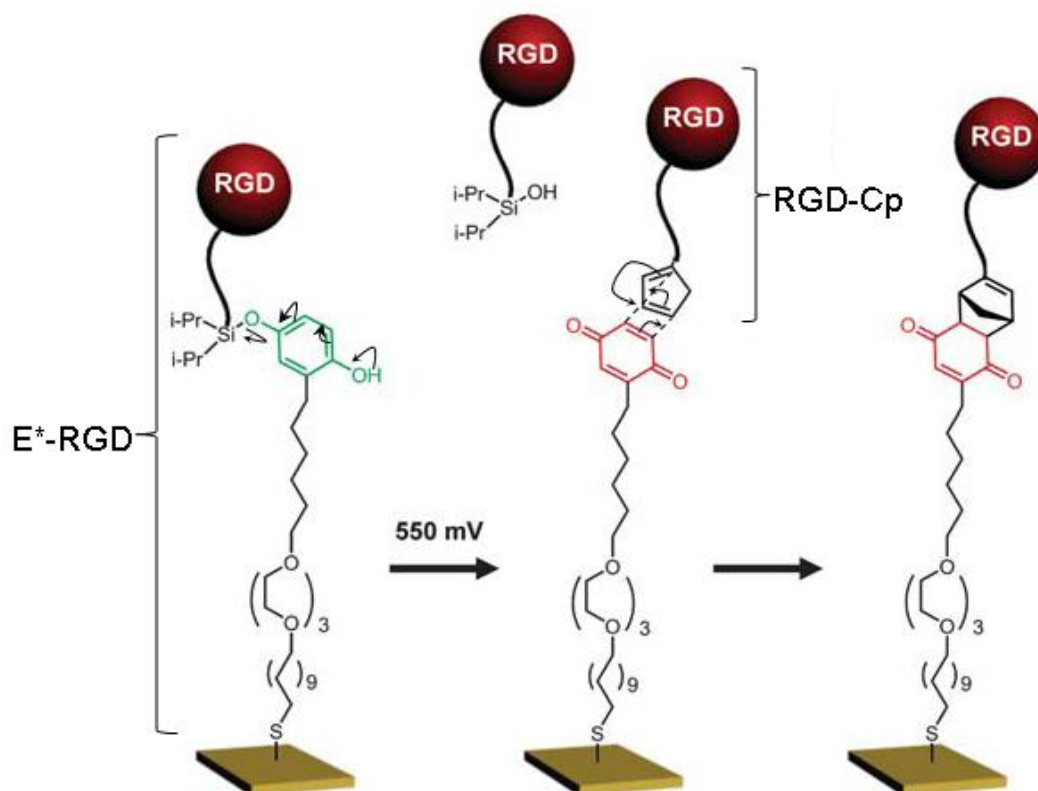
Figure 1.21 The release of the RGD peptide from *O*-silyl hydroquinone monolayer (E*-RGD) by electrochemical oxidation followed by the attachment of second ligand, diene-tagged RGD peptide (RGD-Cp) by Diels Alder reaction.

In order to demonstrate that dynamic substrates can be used as cell receptors on surfaces, a circular pattern of hexadecanethiol monolayer was printed onto the surface using the microcontact printing technique, with the intervening region backfilled with RGD peptide ligands that were tethered to the surface *O*-silyl hydroquinone groups (E*-RGD) (**figure 1.22**). Subsequently, the surface was treated with an ECM protein, fibronectin, which specifically adsorbed onto the hexadecanethiol circular regions. The introduction of 3T3 fibroblast cells adhering onto the surface leads to the attachments and the growth of cells evenly across the fibronectin and the RGD peptide regions (**figure 1.22a**). Upon the application of a positive electrical potential, the hydroquinone group was oxidised and converted to the benzoquinone

group, resulting in the release of cells from RGD regions (**figure 1.22b**). Subsequent attachment of a second ligand diene-tagged RGD peptide (RGD-Cp) onto the benzoquinone region has resulted in the cell migration from fibronectin regions back onto the RGD regions as shown in **figure 1.22c**.

Figure 1.22 Demonstration of dynamic substrates that contain 2 properties: i) the release of RGD ligand, and thus release of cells. ii) the immobilisation of a second RGD ligand leading to cell growth and migration on the surface. a) Swiss 3T3 fibroblast cells adhered and spread evenly over the entire substrate. b) An electrical potential of 550 mV was applied to the substrate for 5 min, and the substrate was incubated for 4 h. Cells were efficiently released only from the region of RGD peptide ligands that were tethered to the surface of *O*-silyl hydroquinone groups (E*-RGD). c) The attachment of second ligand diene-tagged RGD peptide (RGD-Cp) onto the benzoquinone region resulted in the cell migration from fibronectin (circular) regions back onto the RGD regions. After 24 hours, cells were distributed evenly across the whole surface.[27]

A similar approach was used to design surfaces that display two independent dynamic functions for controlling cell adhesion.[147] By patterning the surface with two different electroactive moieties (*O*-silyl hydroquinone and benzoquinone) that release the RGD peptide in response to either oxidative (+ 650 mV) (**figure 1.23 a→b and c→d**) or reductive (- 650 mV) (**figure 1.23 a→c and b→d**) potentials, it was possible to trigger the release of 3T3 fibroblasts cells from surfaces. These studies[27, 147, 166, 167] have demonstrated that applying electrical potentials to the surfaces does not seem to be harmful towards any cells adhered to the surface and is compatible in cell culture environments. Therefore, the electroactive monolayer can be specifically tuned to control the adhesion of different cells *in situ* and in real time.
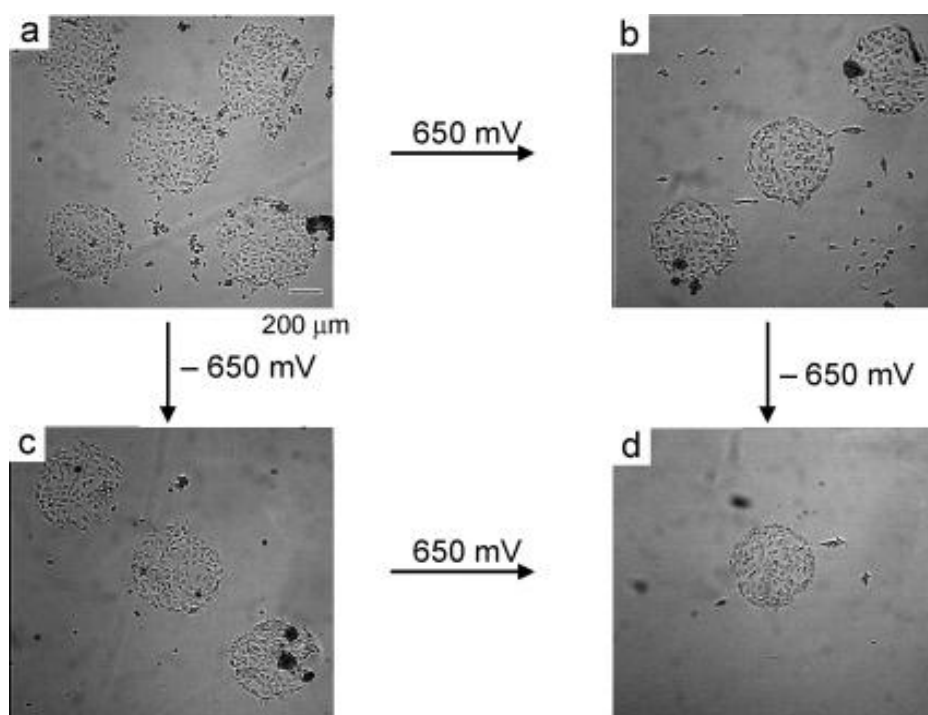
Figure 1.23 Electrochemical control of cell adhesion on RGD patterned gold surface. Upon the application of an electrical potential of 650 mV, cells were released from the electroactive *O*-silyl hydroquinone regions (a→b and c→d). Whereas the application of – 650 mV released the cells from benzoquinone regions of the substrate. (a→c and b→d).

Redox-active rotaxane SAMs[171] have also been employed to establish electrical communication between the electrode surface and the redox-centre of enzymes. Since the spatial separation between the electrode (conductive) surface and the enzyme prevent the direct electrical communication, enzymes need to be properly aligned with the electrode surface with redox relay units in between to act as an electron mediator.[172] A tetracationic macrocycle on a molecular wire has been employed as the charge transport track for wiring the enzyme apo-glucose oxidase (apo-GOx). The electron acceptor cyclobis(paraquat-*p*-phenylene) macrocycle was threaded onto a molecular wire that included a diiminobenzene π-donor site with the flavin adenine dinucleotide (FAD) cofactor acting as a stopper for the macrocyle and anchor/activation point for apo-GOx as shown in **figure 1.24**. The attachment of apo-GOx onto the FAD cofactor causes an electron transfer from the enzyme to the surface via the redox active rotaxane molecular wire, resulting in an electrically contacted biocatalytic system.
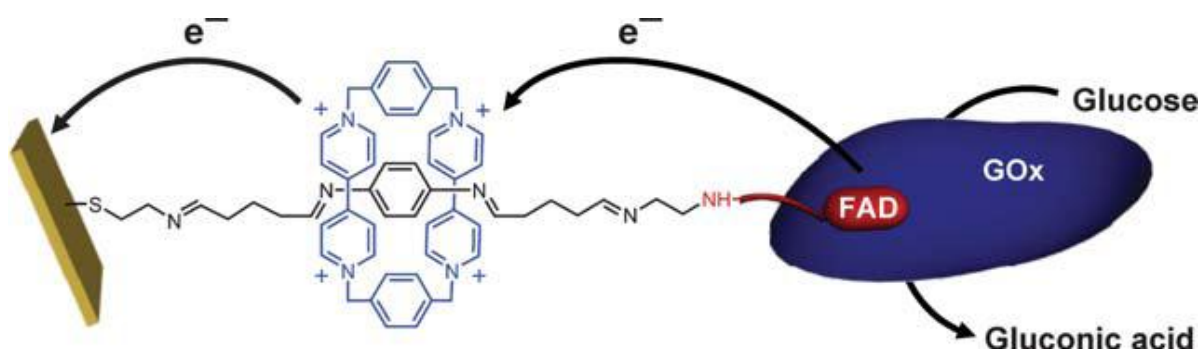
Figure 1.24 apo-GOx attached onto the FAD cofactor leading to electron transfer via the redox active rotaxane molecular wire.[172]

1.3.1.1 Low density SAMs (LD-SAMs)

Switching of surface properties of high density monolayers has been demonstrated by simply changing the electrical potential on a gold surface resulting in the desorption of surfactants

from the electrode surface.[173, 174] Other studies[175, 176] have illustrated that the chemical properties of electroactive monolayers can be modified by a simple redox reaction. However, the desorption approach requires the oxidation of the thiolate groups and the reversibility may prove difficult. Similarly, the redox approach may have its steric limitations[177, 178] when biomolecules adhere onto the surface. Therefore, low density SAMs (LD-SAMs) on gold may be the answer to these limitations.

LD-SAMs allow the exploration of conformational transitions due to their reduced constraints. Therefore, changes in the surface properties may be attained without affecting the chemical composition on the surface. This reduced steric constraint property is particularly interesting in the field of biosensors, as LD-SAMs allow the control of protein adsorption and release under electrical modulations.[8, 146] These surfaces enable the molecular conformational changes of surface confined molecules by providing sufficient distance between each active surfactant. One of the strategies employed in this method is the assembly of molecules with bulky groups, which can be removed by hydrolysis after the monolayer formation. Thus, creating a dense monolayer in respect of head groups, but exhibiting lower density in terms of alkyl chain coverage (**figure 1.25a**).[179] Another example demonstrated by Liu *et al*.[146] utilises a pre-formed inclusion complexes of cyclodextrin (CD) wrapped alkanethiolate on gold to create sufficient spacing between each molecules. The removal of non-covalently bound CD space filling group from the anchored inclusion complex on the thiolate creates a low density 16-mercaptohexadecanoic acid (MHA) monolayer (**figure 1.25b**). Loosely packed carboxylate terminated SAMs were shown to induce dynamic changes of surface properties, such as wettability and charges in response to an external electrical potential.
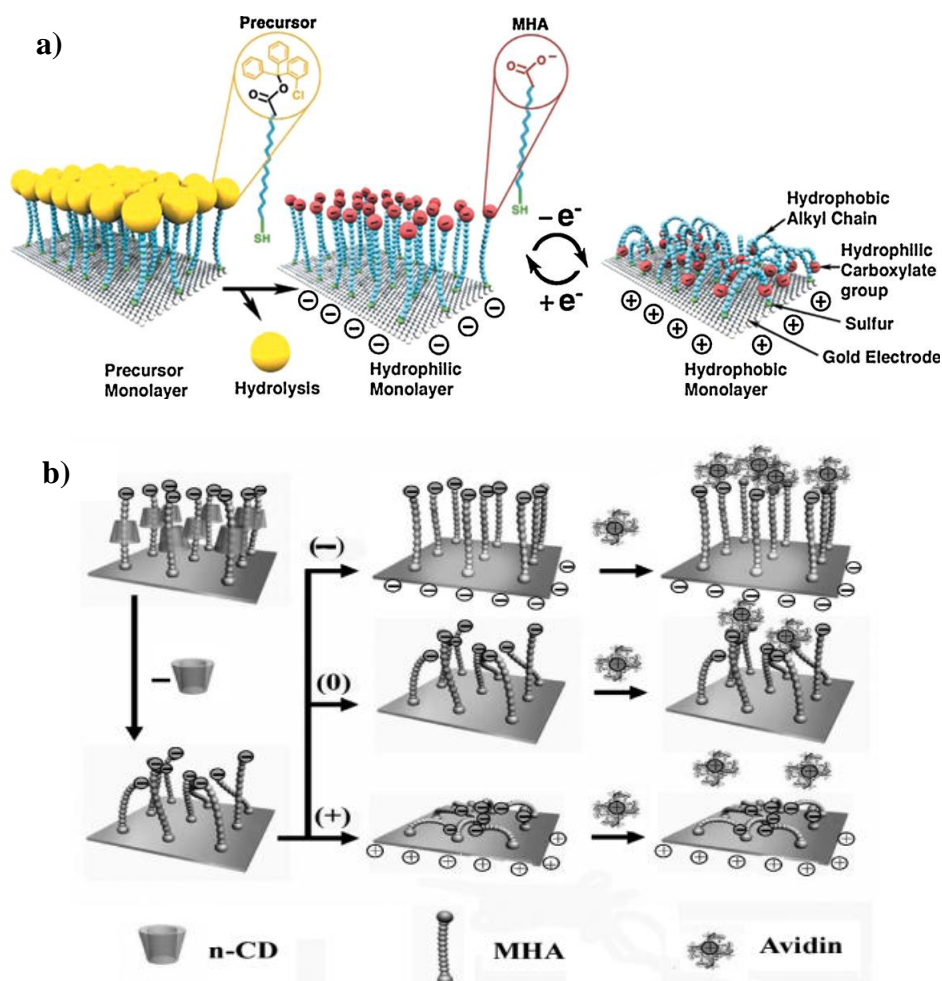
Figure 1.25 a) Schematic showing the LD-SAMs using bulky head groups to create a monolayer that can be switched between hydrophilic and hydrophobic states based on electrical potential applications.[179] **b)** An illustration of the fabrication of LD-SAMs using CD complexes, follow by the transition of anchored MHA at an applied potential and subsequent protein assembly.[146]

The changes in surface properties are due to the electrostatic interaction between the ionised terminal group and the potential on the gold surface. When a negative potential is applied on the surface, the hydrophilic negatively charged carboxylate terminal groups are electrostatically repelled from the surface leading to a straight chain "trans" conformation.

Whereas, upon the application of positive potential on the surface, the ionised terminal groups experience an electrostatic attractive force resulting in the the ion being attracted towards the surface leading to "gauche" conformations within the hydrophobic alkyl chains.

LD-SAMs have been integrated in microfluidic chips to reversibly control the adhesion of two proteins, avidin and streptavidin (**figure 1.26**).[179] The application of a negative potential on the surface repels and exposes the negatively charged carboxylate group on the surface, resulting in capturing positively charged avidin (**figure 1.26a**). Upon the application of a positive potential, the carboxylate terminal groups are attracted towards the surface, resulting in avidin released from the surface (**figure 1.26b**). In contrast, positively charged ammonium groups are repelled and exposed from the surface when positive potentials are applied onto the surface, resulting in the adhesion of negatively charged streptavidin (**figure 1.26c**). When the applied potential switches from positive to negative, the ammonium groups are attracted towards the surface, resulting in streptavidin released from the surface (**figure 1.26d**). These LD-SAMs can potentially be very useful in the separation of a target protein from a complex protein mixture using specific terminating groups as the anchor (capture) point on the surface.
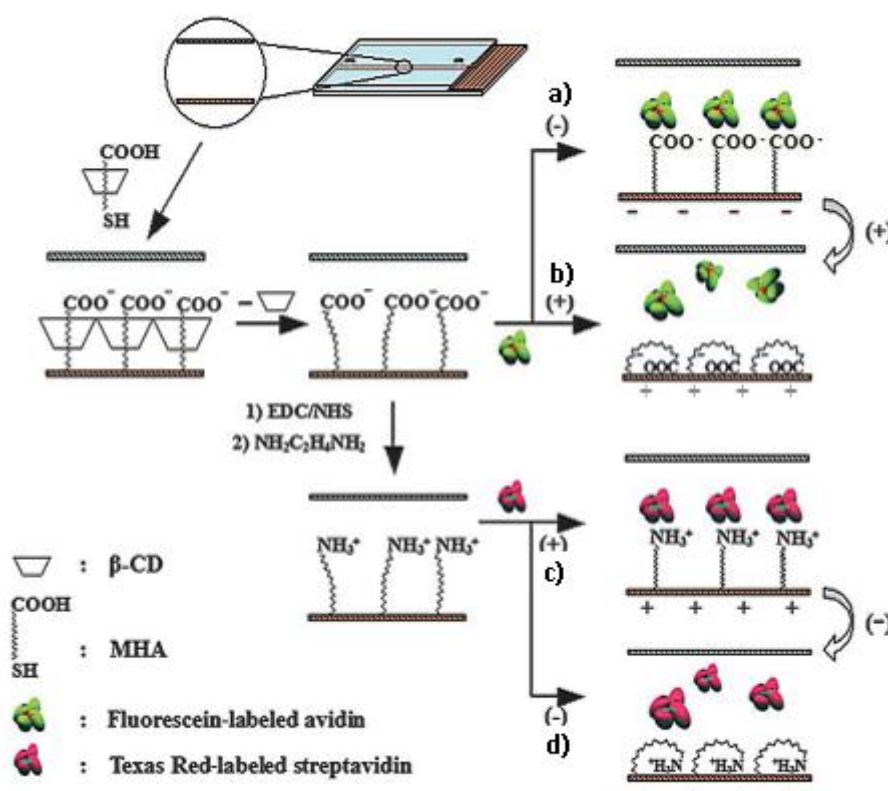
Figure 1.26 Illustration of LD-SAMs on microfluidic chips to control the adhesion and release of avidin and streptavidin upon the application of electrical potentials.[8] **a)** The application of a negative potential on the surface causes the carboxylate group electrostatically repelled from the surface, leading to the capture of positively charged avidin. **b)** Whereas, switching of potential from negative to positive on the surface attracted the carboxylate group towards the surface, causing the release of avidin from the surface. **c)** The application of positive potential on surface causes the ammonium groups to electrostatically repel from the surface, leading to the captured of negatively charged streptavidin. **d)** The switching of potential from positive to negative causes the ammonium groups to attract towards the surface, resulting in the release of negatively charged streptavidin.

1.3.1.2 Switchable DNA SAMs

DNA SAMs tethered onto an electrode surface have also been employed as switchable surfaces (**figure 1.27**). On application of an electrical potential, DNA SAMs[180-186] have exhibited switching properties by modulating the structural conformations on metal surfaces. They are capable of producing reversible, well-defined nanometre scale motions under reverse electrical potentials. DNA is polyanionic due to the phosphate groups in the backbone, thus, DNA molecules tethered to a conductive surface can be driven away from, or pulled towards the surface depending on the surface electrical potentials applied.[180, 181, 186] Upon the application of a negative electrical potential, the DNA molecules adopt a straight chain conformation, whereas, applying positive potential causes the molecule to tilt and lay flat on the surface. By coupling fluorophores on the surface bound DNA, the change of fluorescence can be observed as a function of applied potential to the surface as shown in **figure 1.27.**[186]
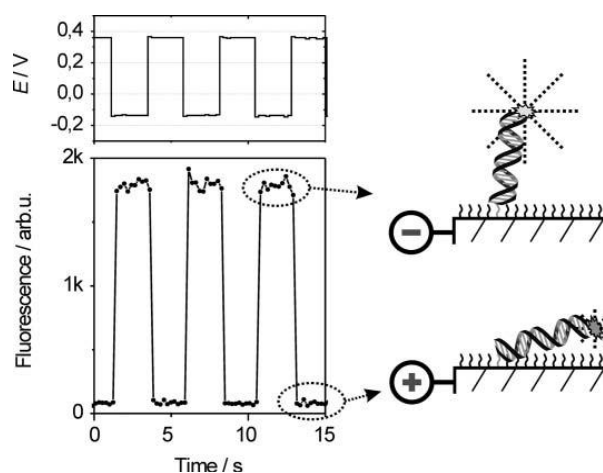
Figure 1.27 Alternating potentials applied on the electrically switchable DNA surface. On applying a negative potential, DNA strand repelled from the surface, causing a fluorescence response, whereas, a positive potential forces the DNA tilted towards the surface resulting the quenching of the fluorescence.[186]

The manipulation of surface bound DNA molecules is an excellent technique to detect the non-labelled target oligonucleotide (target DNA). Single stranded oligonucleotides are labelled with Cy3 fluorophores on one end, and at the other, are modified with thiol linkers, to operate as the probe on the gold surface for non-labelled target DNA. As mentioned above, the detection method depends on the orientation and the extension of the DNA molecule on the surface. When the surface potential is positive, the DNA probe adopts a tilted conformation, quenching the fluorescence of the Cy3 dye. In contrast, a negative potential drives the DNA probe away from surface, resulting in a stronger fluorescence signal, the alternating potential applied on the DNA surface has been shown in **figure 1.28a**.[186] The hybridization of the non-labelled target DNA onto the surface bound Cy3 labelled single stranded probe resulted in the amplified fluorescence signals (**figure 1.28b**).[183] **Figure 1.28c** illustrates that the surface bound Cy3 labelled single stranded (24 complementary sequence nucleotides, red data point) DNA probe has relatively low fluorescence intensity due to the partial alignment with the applied electric field on the surface. Whereas, the hybridization of the target DNA with the surface probe (48 complementary nucleotides, blue data point), resulted in amplified fluorescence signals due to the lower flexibility of the double stranded DNA.[183] Electrically switchable DNA surfaces allow real time detection of target DNA with high sensitivity. The information obtained using this technique can be used to control, monitor and characterise the binding event in real time.

Figure 1.28 Electrical switching and hybridization of DNA layers. **a)** The alternating potential applied on the DNA surface. **b)** The fluorescence emission of the Cy3 labelled DNA layer, showing the injection of (arrow) complementary target DNA that hybridize the surface bound Cy3 labelled single stranded probe resulted in an amplified fluorescence signals. **c)** The hybridization of target DNA with the 24 completer sequence nucleotides (**red** data point) to form the 48 completer sequence nucleotides (**blue** data point) resulted in amplified fluorescence signals. 24 non-completer sequence nucleotides (**black** data point) act as a control and exhibits negligible binding affinity.[183]

1.3.2 Photo-responsive surfaces

Switchable surfaces can also be modulated using light (photons). Instead of performing redox reactions on surface terminal groups, molecules are designed to exhibit conformational change when exposed to UV light that leads to a change in surface bio-activity. Azobenzene units exhibit a photo-switching effect by undergoing a *trans-* to *cis*-isomerization. These changes in azobenzene SAMs' molecular shape and orientation has an impact on surface properties.[141, 187]

SAM porosity can be controlled by taking advantage of the reversible photoisomerization of azobenzene. The ferrocenylazobenzene functionality has been attached to an ITO electrode in a variety of ways.[141, 188, 189] Upon UV irradiation, the interfacial barrier (monolayer) between the solution and ITO surface become more compact. For a loosely packed SAM with a terminal ferrocene and azobenzene group on ITO, the Laviron approach[190] was used to determine the standard rate constant (k_s) for the surface immobilised redox species before and after UV irradiation of the surface.[141] The decrease in k_s is attributed to the change in the microenvironment around the ferrocene moiety in the SAM corresponding to the *trans* to *cis* photoisomerization of the azobenzene N=N as shown in **figure 1.29**.
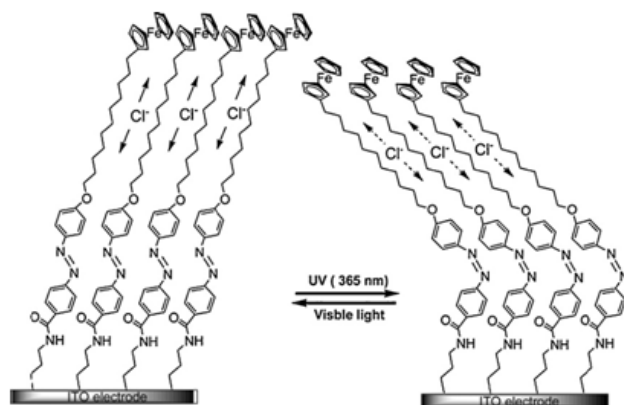
Figure 1.29 Photoisomerization of azobenzene changes in SAM packing due to *trans* to *cis* isomerization.[141]

Recently, Hayashi *et al.*[191] used a photoresponsive peptide with an azobenzene backbone and its RNA binding aptamer to develop an in-*vitro* selection method for RNA-ligand pairs. The ability to photo-regulate the binding of the RNA aptamer as a result of structural changes (*trans* to *cis* conformation) in azobenzene has potential applications in the modulation of gene expression. The photoresponsive peptide is comprised of Lysine-Arginine-azobenzene-Arginine (KRAzR). When covalently bound to a carboxylate terminated gold surface, the

peptide demonstrated a photoresponsive binding to its target RNA that could be switched "off" by exposing the surface to UV light (**figure 1.30**).
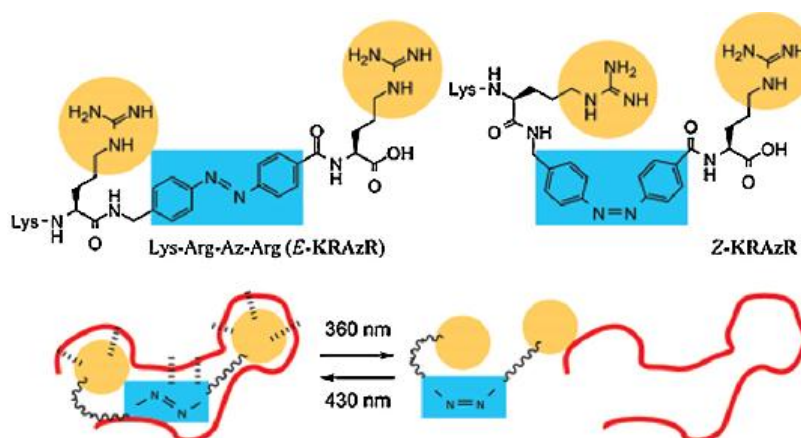
Figure 1.30 The *trans-cis* isomerization of photoactive peptide (KRAzR) controls the binding of target RNA aptamers (Red line). The binding is caused by the hydrogen bonding to the guanidinium group and the hydrophobic interactions to azobenzene group (dash line).[191]

1.3.3 Chemical or biochemical responsive surfaces

Responsive surfaces that respond to external chemical or biochemical stimuli provide a wide range of application potentials including biological sensors, bioadhesive surfaces and delivery systems with controlled release capabilities. The development of the electrochemical DNA (E-DNA) sensor[157, 160, 192] is a prime example of such responsive surfaces. The detection mechanism of an E-DNA sensor is based on the alteration of the electron transfer properties based on the structural rearrangement on the surface caused by the target hybridization.

An E-DNA sensor employs a surface bound DNA stem loop labelled with an electroactive group as a detector (**figure 1.31**).[160] In the absence of a target, the stem loop holds the electroactive ferrocene group close to the surface causing a high Faradaic current. In contrast, the presence of the target molecule causes the hybridization of the stem loop that forms a

thermodynamically more stable, rigid rod-like target sensor duplex. This conformation increases the distance between ferrocene group and the surface, and as a result, the current is less. The reduction in current can be employed to determine the presence and concentration of target molecules. This approach generates an "off" signal since we observe a lower current as the targets binds onto the DNA loop.
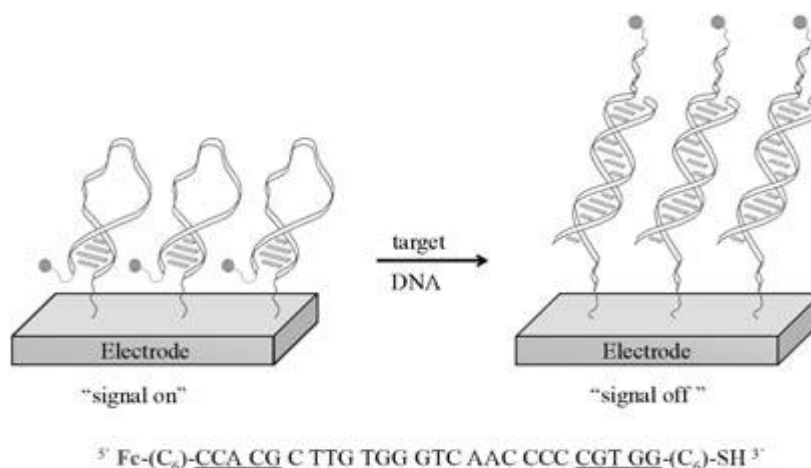
^{5} Fe-(C$_6$)-CCA CG C TTG TGG GTC AAC CCC CGT GG-(C$_6$)-SH ^{3}

Figure 1.31 Signal-off E-DNA sensor based on the surface bound DNA stem loop with a ferrocene electroactive reporter.[160] In the presence of the target DNA molecule, the distance between the ferrocene and the surface increases, causing a drop of current.

Using a similar approach (**figure 1.32**), this sensing technique has been applied to generate an "on" signal upon recognition of the target DNA molecule.[193] Using a surface bound, ferrocene labelled oligodeoxynucleotide (**blue strand**) - poly(ethylene glycol) (**red linker**) - oligodeoxynucleotide (**blue strand**) triblock molecules as the probe, the DNA molecules (**green strand**) are introduced onto the surface causing the hybridization of the top and the bottom oligodeoxynucleotide, forcing the terminally linked ferrocene tag to come into proximity of the surface to generate an electrochemical signal.
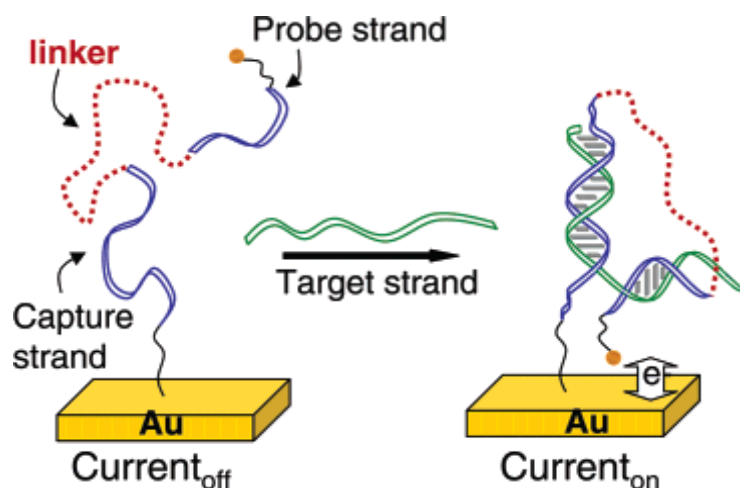
Figure 1.32 Signal-On E-DNA sensor based on the triblock molecule.[193] In the presence of a target DNA strand, the ferrocene group move into proximity with the surface, causing an increase in electrical current.

Xiao *et al*.,[194] have developed an E-DNA sensor based on the conformational change of the methylene blue (MeB)-modified duplex DNA that occurs after the target DNA strand displaces one of the original DNA strands on the surface (**figure 1.33**). In the absence of the target DNA molecule, the duplex DNA forces the electroactive methyl blue group away from the surface, limiting the electrical current. With the introduction of the target DNA onto the surface strand, the single strand containing the MeB group is liberated, resulting in an increase in the efficiency of the electron transfer between the MeB and the surface.
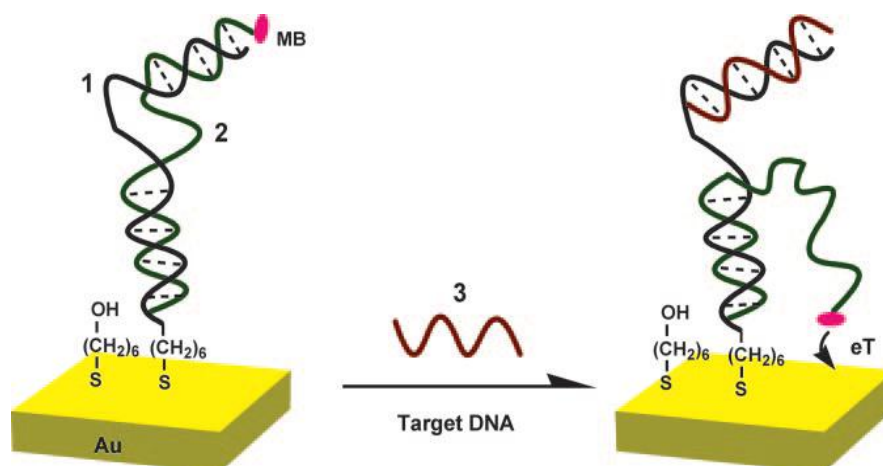
Figure 1.33 Signal-On E-DNA sensor using target DNA to liberate the MeB group, causing an increase in the electrical signal.[194]

1.4 Cell migration and cell motility

Cell migration is a process in which cells moves from one area of the body to another. One well known example of such cell migration is the spread of tumour cells, metastasis. The spread of tumour cells does not require external energy for the movement, rather, the cell utilises internal chemical energy in order to generate movement of the cell, and this is known as cell motility.[147, 153] Motility occurs both at the tissue and cellular levels. It occurs among cell types such as flagellated bacteria and motile sperm which require a cellular limb for propulsion to generate movement. One example of motility at the cellular level is the amoeboid movement.[156]

1.4.1 Amoeboid movement

Amoeboid movement[156] is a term uses to describe cells that are capable of a "crawling" movement. Several different processes (**figure 1.34**) are involved in cell crawling, including:

1) **Cell protrusion** - the leading edge of the cell forms protrusions that extend in the direction of travel.

2) **Attachment** - these protrusions can adhere to the substrate, or they can be pulled upward and back towards the cell body. When the protrusions adhere, they provide anchorage points for actin filaments.

3) **De-adhesion** - the trailing edge of the cell detaches itself from the surface.

4) **Contractile activities** - tension on actin filaments can then cause the rest of the cell to pull forward.
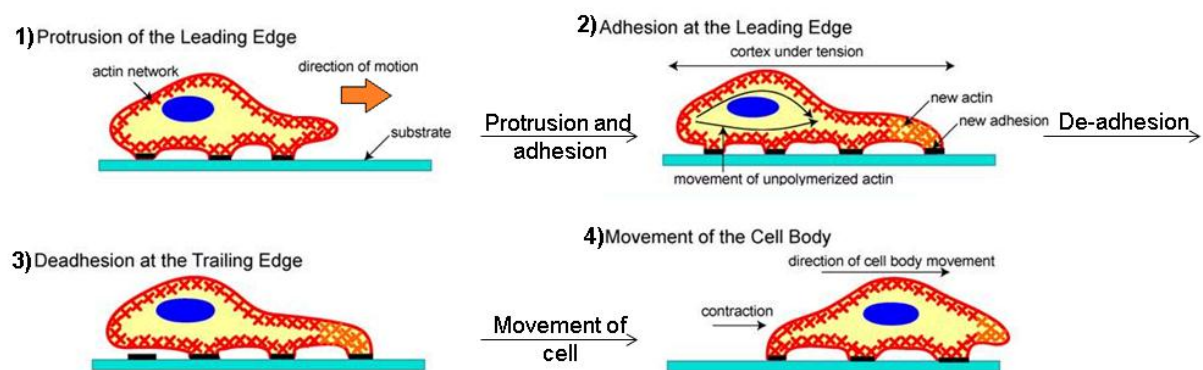
Figure 1.34 Schematic representations of the steps of cell crawling.[154]

This type of movement is normally accompanied by the protrusions of cytoplasm. There are several forms of cell protrusions, including the lamellipodia and filopodia.[154]

1.4.2 Lamellipodia and filopodia

Lamellipodia and filopodia are actin filaments with different types of architecture. Actin filaments are present in all types of cell protrusions. They are organised in a variety of different states depending on the presence of different actin-binding proteins.[153] Lamellipodia are actin filaments that cross-link into a gel form at the front of the cell (where protrusion occurs). The extension of cytoplasm (cell membrane) could be recognised as a form of such protrusions.[156] Parallel actin bundles that are found at the leading edge of lamellipodia are known as the filopodia.[195] The filopodia take the form of thin and pointed structures as shown

in **figure 1.35**. The main role of the filopodia is acting as a probe for the cell to detect possible attachment site with the surrounding environment as will be further explained in **section 1.4.3**.
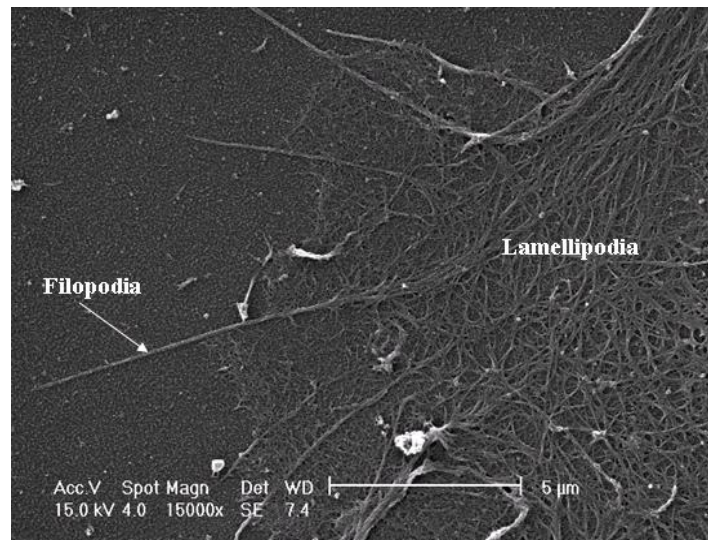
Figure 1.35 Scanning Electron Microscopy image of a Mouse Embryo Fibroblasts (MEF) cell in migratory stage.[153]

1.4.3 Cell attachment

Membrane protrusions[153] are normally associated with cell movement. New sites of attachment must be formed at the front of the cell and contacts from the rear must be broken. However, some membrane protrusions do not result in movement on the surface due to the strong interactions of the cells with the surface. The cell membrane will still protrude. Nevertheless the cell will remain at the same position and spread itself onto the surface.

Cell attachment[153] depends on a delicate interplay between the cell and its surrounding matrix, namely extracellular matrix (ECM). The interaction between the cell and ECM are primarily mediated by integrins. Integrins attached to the ECM through a complex linkage consisting of talin, vinculin and α-actinin. α-Actinin binds to the actin filament, talin binds to the membrane of integrin, and vinculin acts as a linkage between α -actinin and talin (**figure 1.36**).

Engagement of transmembrane integrin receptors and their clustering proteins leads to the formation of focal adhesions where integrins link to intracellular cytoskeletal complexes and bundles of actin filaments (lamellipodia and filopodia). These complexes not only serve to connect the cytoskeleton to the matrix, but also serve as a framework for the association of signalling proteins that regulate signal transduction pathways leading to integrin-induced changes in behaviour.
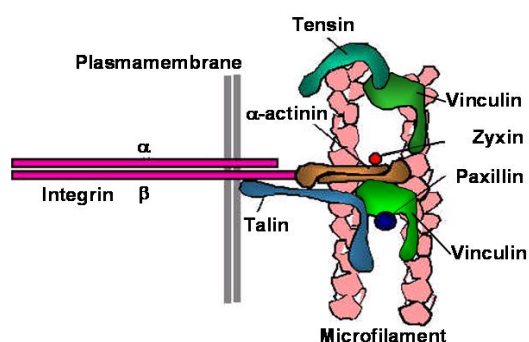
Figure 1.36 Diagram to show the attachment of actin filament with extracellular matrix through an integrin complex.[153]

1.5 Concluding remarks

Over the past decade, the advancement in SAMs fabrication has led to the development of switchable biological surfaces where the surface can interact with bio-molecules such as peptides, DNA and proteins. To date, external stimuli such as electrical, optical, chemical and biochemical stimulus have been employed to control the surfactant orientation, resulting in the control of surface bio-functionalities. Albeit, there are advancements in this field, specific bio-recognition switchable surface remains a challenge to be conquered.

1.6 PhD Aims

Herein, the aim of my PhD degree is to design and fabricate novel biological surfaces for medical and biological applications, which has the ability to selectively control the interaction between the surface and the surrounded biological environments. The project will concentrate on the development of:

i)   Fabrication of micro-patterned biological surfaces to create an extracellular matrix (ECM) model for the study of cell migration and cell motility. This study can be summarized into 3 steps.

Step 1) Fabrication of patterned fibronectin surface on hydrophobic surfaces using microcontact printing.

Step 2) Backfilling of bovine serum albumin (BSA) between fibronectin lines.

Step 3) Introduction of mouse embryonic fibroblast (MEF) cells onto the patterned fibronectin surfaces.
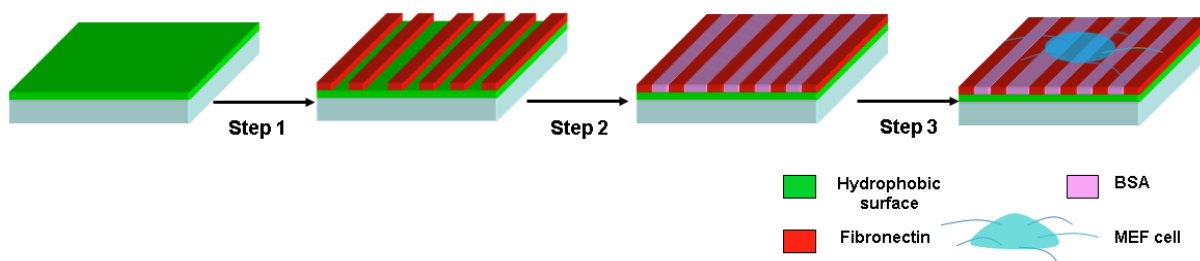
Figure 1.37 Schematic representations showing the fabrication of micro-patterned biological surfaces.

ii) The development of switchable biological surfaces that rely on electro-switchable peptides to control the bioactivity on gold surfaces upon the application of an external electrical stimulus.

Upon the application of a positive potential on the surface, the peptide adopts a "trans" configuration where the biotin is exposed and binds to the fluorescently labelled neutravidin (**figure 1.38 a→b**). The application of a negative potential drives the peptide to adopt a "gauche" configuration where the biotin is concealed, hence, neutravidin cannot bind to the surface (**figure 1.38 c→d**).
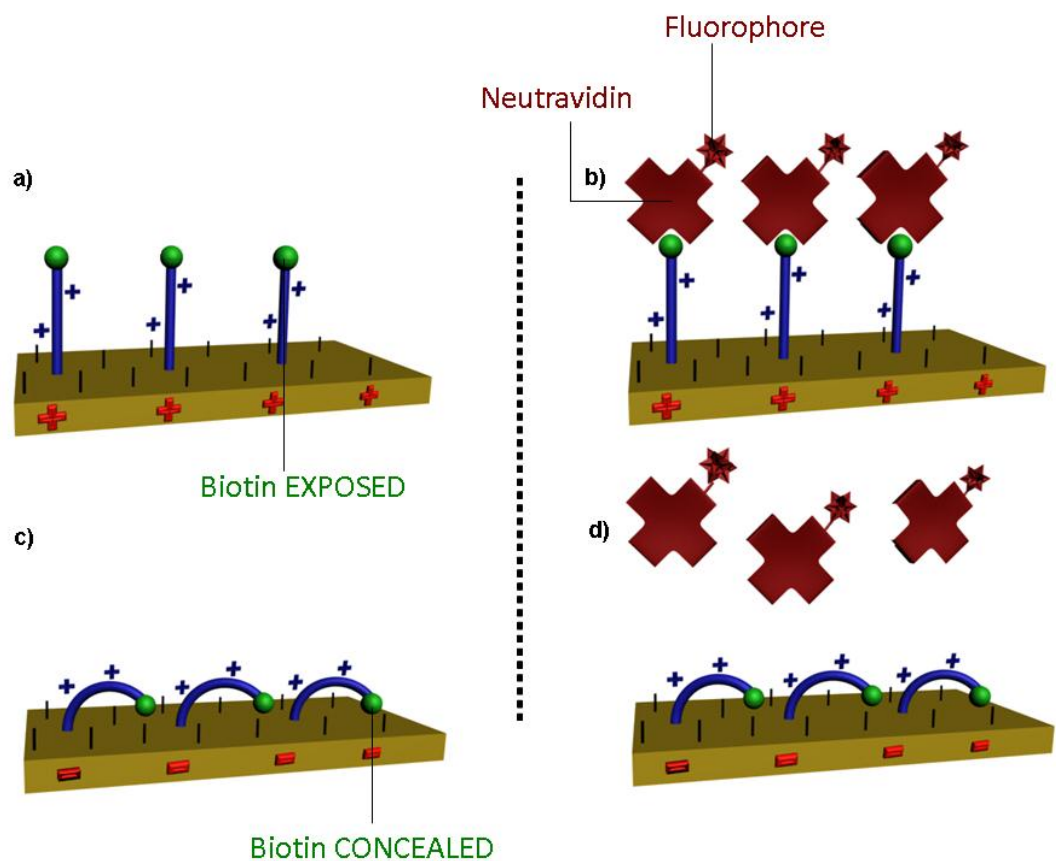
Figure 1.38 Schematic representations showing the electro-switchable biological surfaces.

Chapter 2

Surface Characterisation Techniques

Abstract: *In this chapter, various techniques for surface characterisation are reviewed. This chapter examines techniques available for the evaluation of surface treatments to ensure optimum surface properties. Techniques such as atomic force microscopy (for surface roughness and topography), contact angle (for wettability), ellipsometry (for surface thickness), X-ray photoelectron spectroscopy (for surface elemental composition), and cyclic voltammetry (for surface chemistry and stability) are employed to characterize the prepared surfaces. Other techniques, such as fluorescence microscopy (for surface fluorescence intensity) and surface plasmon resonance (for real time binding events on surface) are also utilized to study the binding events of fluorescent biomolecules onto surfaces.*

2.0 Surface characterisation techniques (Figure 2.1)

Atomic force microscopy (AFM),[196] fluorescence microscopy (FM),[197] X-ray photoelectron spectroscopy (XPS),[198] ellipsometry,[40] contact angle goniometry (CA),[40] cyclic voltammetry (CV)[199] and surface plasmon resonance (SPR)[200] are surface characterisation techniques employed in these studies. AFM is used in the determination of surface topography, whereas, FM is employed to study the fluorescence intensity of the surface. The surface elemental composition and surface thickness are studied using XPS and ellipsometry, respectively. In

addition, CA is used to evaluate the surface wettability and CV to study the stability of the SAM surface. Furthermore, SPR is used for real time binding studies on gold surfaces.
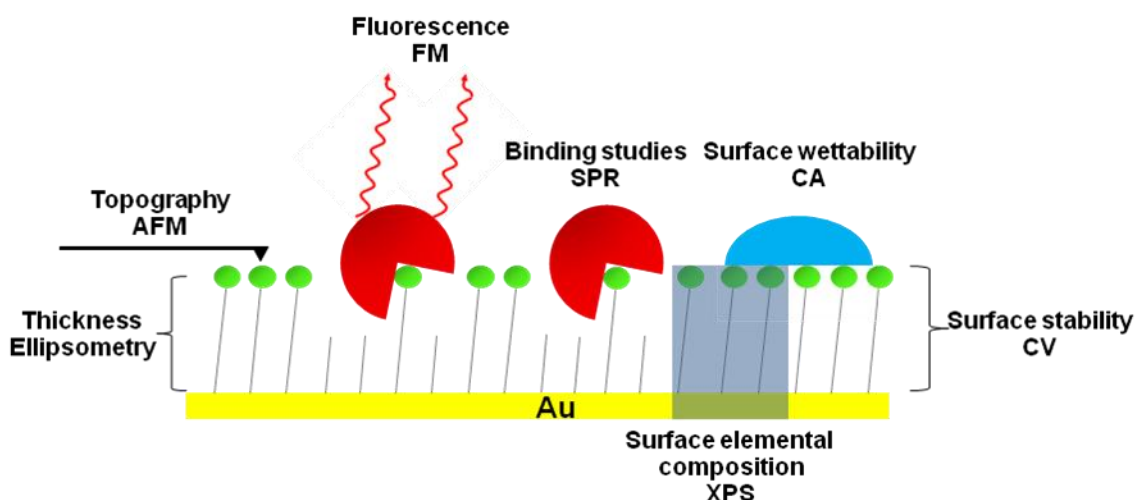
Figure 2.1 Cartoon representation of each characterization technique involved in the surface characterization in this thesis.

2.1 Atomic force microscopy (AFM)

AFM was developed by G. Binnig *et al*. (1986)[196] as an improvement of scanning tunnelling microscopy (STM),[201, 202] a technique which analyses conductive and semi-conductive surfaces. AFM, unlike STM, has the capability of analysing both conductive and insulating surfaces. This dual ability equips AFM with a wide range of applications including: the analysis of surface topography,[203] imaging biological systems in physiological environments[204] and the study[205] of the surface's electrostatic, adhesive and magnetic properties.

The substrate surface is loaded onto a piezoelectric crystal tube. On applying a potential, the crystal expands or contracts in the z plane, which manoeuvres the sample to or from the cantilever tip as the sample is rastered in the x-y plane.

The cantilever deflection is monitored by a reflected laser beam from the back of the cantilever onto a 4 quadrant photodiode as shown in **figure 2.2**. The laser is first adjusted to the zero point on the detector. As the cantilever scans across the surface, any structures encountered on the surface will change the position of the laser beam in relation to the zero point (**figure 2.2**, green and red laser). This difference in laser position is recorded and processed by the computer software to provide an image. The feedback mechanism acts as the safety measure to avoid the cantilever crashing onto the surface and damaging it when the tip approaches the substrate.
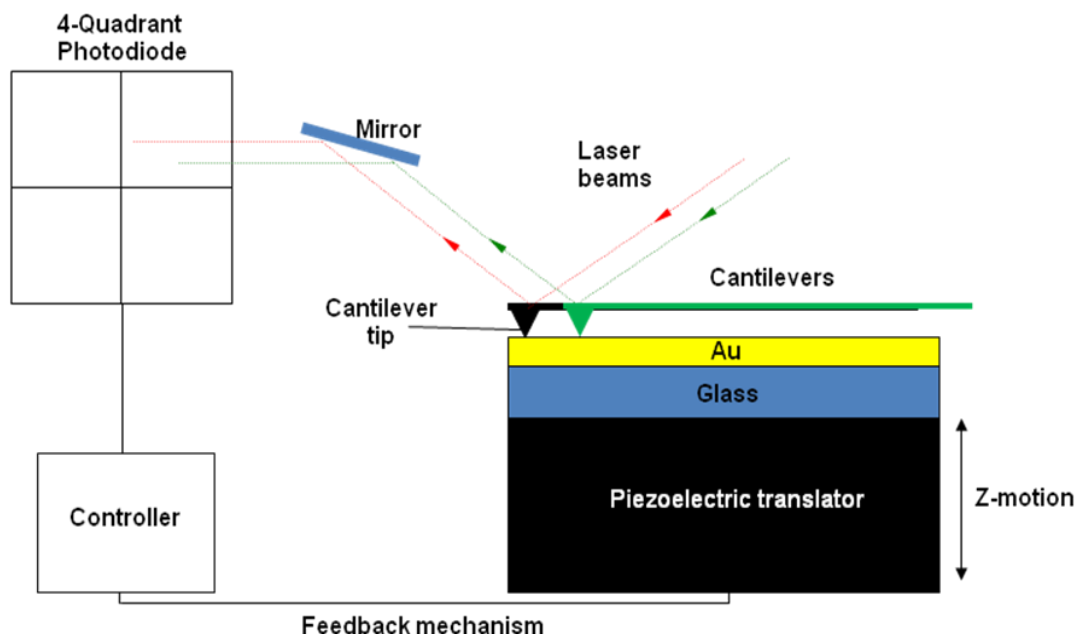
Figure 2.2 A cartoon representation of the AFM.[205]

There are two operations modes in AFM: contact mode and tapping mode.

1) In contact mode,[206] a tiny attractive force (10^{-7} N)[207] is exerted onto the AFM tip when brought into contact with the surface due to the interaction between the tip and surface atoms. As the AFM tip scans across the surface, it experiences either a repulsive (10^{-8} N)[207] or an

attractive force that leads to the cantilever being repelled from or attracted to the surface. The repulsive force originates from the nuclear repulsion between the AFM tip and the surface. The attractive force arises from the chemical bonding through the electron nuclear attraction between the tip and the surface. The contact mode AFM can provide atomic resolution of surfaces and molecular detail of physisorbed or chemisorbed molecules.[208]

2) In tapping mode,[209] delicate samples, such as biological samples, that are prone to damage by the contact mode are imaged by an alternative imaging mode, the tapping mode. The tapping mode is a "non-contact mode" where the tip is held tens to hundreds of angstroms (~20 nm)[209] above the surface with no physical contact. The forces measured are electrostatic or magnetic, which are weaker than forces measured in contact mode. In order to enhance the signal, the tip vibrates close to its resonant frequency with a set amplitude, "tapping". The force between the tip and the sample can affect the amplitude of the tip cantilever oscillation, therefore, as the tip scans across the surface, fixed oscillation amplitude is maintained via an electronic feedback control loop. This in turn produces a 3D image of the surface topography as a function of height, lateral position and phase images.[204, 210] The phase image is especially useful, as shown by Servoli *et al.*[204] when imaging biological surfaces. They use phase contrast images to show the protein distribution on SAMs and the phase-shift provides information on protein conformation.

2.2 Fluorescence microscopy

Fluorescence microscopy detects the energy that is emitted from a sample when irradiated by light at a specific wavelength. Samples can either fluoresce naturally, such as chlorophyll, or be chemically altered by attaching fluorescent molecules.[197] The basic task of the fluorescence

microscope is to irradiate samples with excitation light (I_0) and then spatially detect the emitted light (I_1). The microscope is fitted with a dichroic beam splitter and an emission filter, to filter all undesired radiation and allows only the desired wavelength that matches the fluorescing material to pass through to the detector (**figure 2.3**).
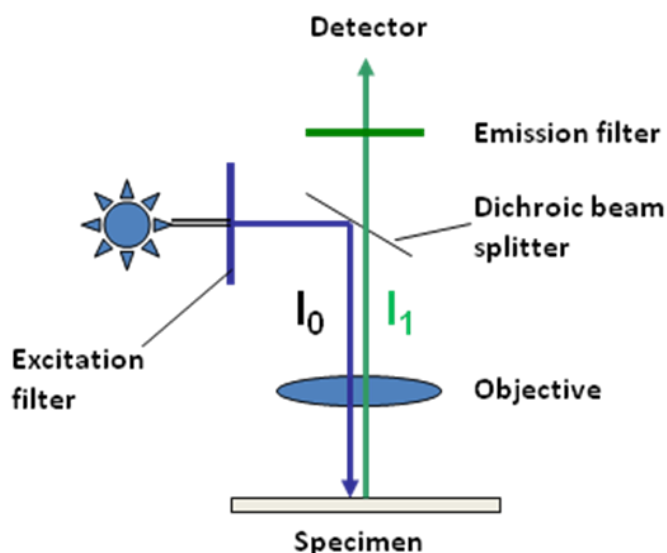
Figure 2.3 Schematic representation of the basic function of a fluorescence microscope.

Fluorescence spectral data are generally presented as emission spectra. A fluorescence emission spectrum is a plot of the fluorescence intensity versus wavelength or wavenumber. Two typical fluorescence emission spectra are shown in **figure 2.4**. Emission spectra vary widely and are dependent upon the chemical structure of the fluorophore and the solvent in which it is dissolved. The spectra of some compounds, such as perylene, show significant structure due to the individual vibrational energy levels of the ground and excited states. Other compounds, such as quinine, show spectra devoid of vibrational structure.
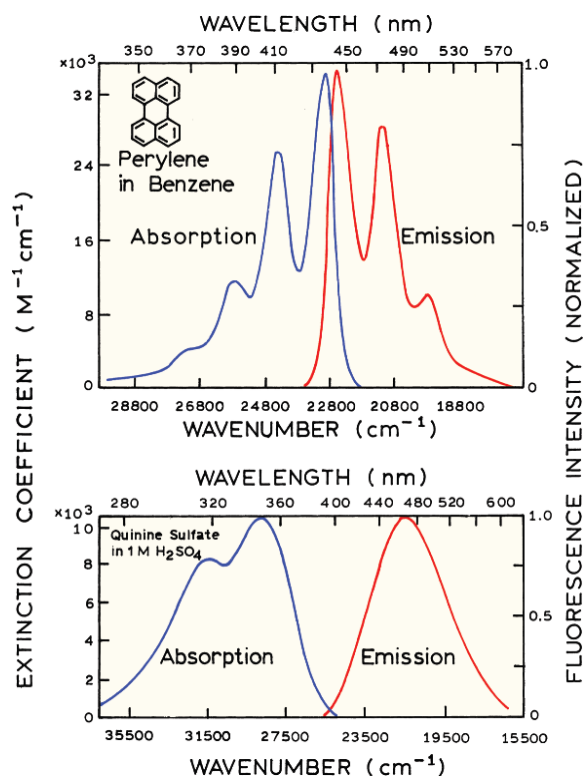
Figure 2.4 Absorption and fluorescence emission spectra of perylene and quinine.[211]

The process that occurs between the absorption and emission of light is normally presented using a Jablonski diagram[197] (**figure 2.5**). The singlet ground, first and second electronic states are represented as S_0, S_1, and S_2, respectively. At each of these electronic energy levels (S_0, S_1, and S_2), the fluorophores can exist in a number of vibrational energy levels, represented by 0, 1, 2. The energy spacing between the various vibrational energy levels is illustrated by the emission spectrum of perylene as shown in **figure 2.4**. The individual emission maxima (and hence vibrational energy levels) are about 1500 cm^{-1} apart.

At room temperature, the background thermal energy is not adequate to significantly populate the excited vibrational states due to the large energy difference between the S_0 and S_1 excited states. Since the absorption and emission occur mostly from molecules with the lowest

vibrational energy, light has been employed to induce fluorescence on the surface. The transitions between states are presented as vertical lines to illustrate the light absorption.

Following the light absorption, a fluorophore is usually excited to higher vibrational level of either S_1 or S_2. The molecules then rapidly relax to the lowest vibrational level of S_1, and this process is termed internal conversion and generally occurs within 10^{-12} s or less. Since fluorescence lifetimes are typically near 10^{-8} s, internal conversion is generally complete prior to emission. Hence, fluorescence emission happens from a thermally equilibrated excited state, which is the lowest energy vibrational state of S_1. When electrons relaxes from the S_1 vibrational state to the original ground state S_0 level, the energy is emitted as fluorescence light (**figure 2.5**).[197]
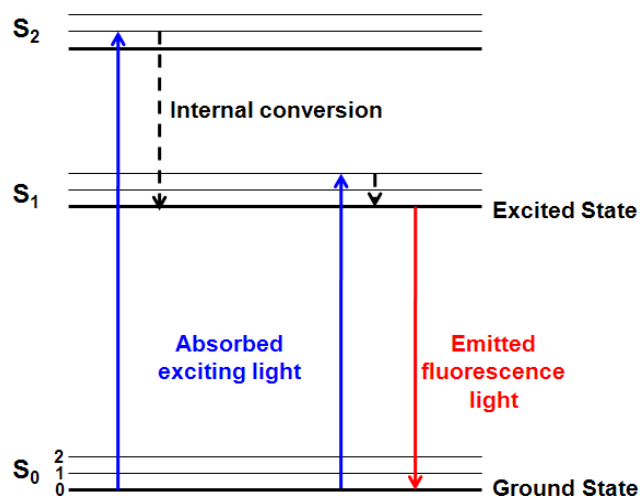
Figure 2.5 Jablonski diagram of the generation of fluorescence light.

2.3 X-Ray photoelectron spectroscopy (XPS)

X-ray photoelectron spectroscopy is a technique used for the determination of the elemental composition on a surface by irradiating the sample with monoenergetic X-rays. The X-ray energy (*hv*) interacts with core electrons in the atom and causes the excitation of electrons to

overcome the binding energy (E_B) within their atomic orbital.[198] The excited electron is ejected from the orbital as a photoelectron with kinetic energy (E_K) as shown in **figure 2.6**.
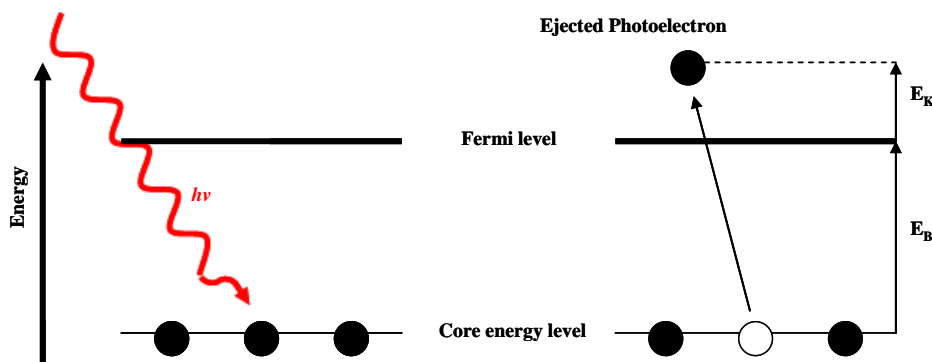
Figure 2.6 A cartoon representation of a photoelectron emitted from the core energy level.

By measuring the kinetic energy of the ejected photoelectron (**E_K**) using an electron spectrometer, the binding energy (**E_B**) of the surface element can be calculated using **equation 1**.

$$\mathbf{E_K} + \emptyset = \boldsymbol{hv}\textbf{-}\mathbf{E_B} \quad \text{(equation 1)}$$

Equation 1 describes the relationship between the X-ray (hv), binding energy (E_B), kinetic energy (E_K) and the work function ($\emptyset$) of the spectrometer.[40, 212]

The binding energy provides an atomic identification of the surface. Furthermore, the number of ejected electrons is proportional to the number of atoms on the surface, thus, a quantitative elemental composition of the surface can be derived. These data can be used to calculate the surface ratio between different elements, and thus determine the ratios of different surfactants on the surface.[212]

Angle resolved XPS (ARXPS) is a very powerful tool which is used in the study of the signal intensity of surface elements such as nitrogen (N), sulphur (S) and gold (Au), where the N and S signal is relatively weaker than gold.[213] By setting the incident angle of 15°, the X-ray mainly excites the surfactant's electrons rather than probing the substrate. Therefore, the surfactant's signal intensity of N and S are stronger and the surface ratio between the two elements can be determined.[214]

Chemical bonds formed on the surface between different elements causes a shift in binding energy. Using ARXPS, energy shifts of different bonds can be clearly attained (reduction in background noise signals), therefore specific chemical bonds (C-O, C-C=O, C-O-C=O, N-C-O) present on the surface can be identified.[214]

2.4 Ellipsometry

Ellipsometry uses elliptically polarized monochromatic light to determine the thickness of a SAM on a surface (**figure 2.7**).[40] When polarized light interacts with the surface at an angle, it resolves into its parallel (s-polarized) and perpendicular (p-polarized) component due to the refraction of light by surface appended molecules. When the s- and p-polarized reflected light beams are combined, the result is the elliptically polarized light. These s- and p-polarized components are reflected off the surface differently due to the refraction through the thin film and hence the amplitude and phases of both components are changed (**figure 2.7**).[215]

The self-assembled monolayers (SAMs) thickness value is based on the model of Air/SAM/Solid in which SAMs are assume to be defect free (homogenous) and with a refractive index of 1.51.[216] The model is calculated using the Cauchy transparent layer, where

the thickness is obtained using multi guess iterations and provides a thickness result with the lowest χ^2(chi-square distribution). Ellipsometry uses this data to estimate the thickness of the SAMs, which is a non-destructive technique generally performed under ambient environmental conditions, although it can also be performed under vacuum conditions.
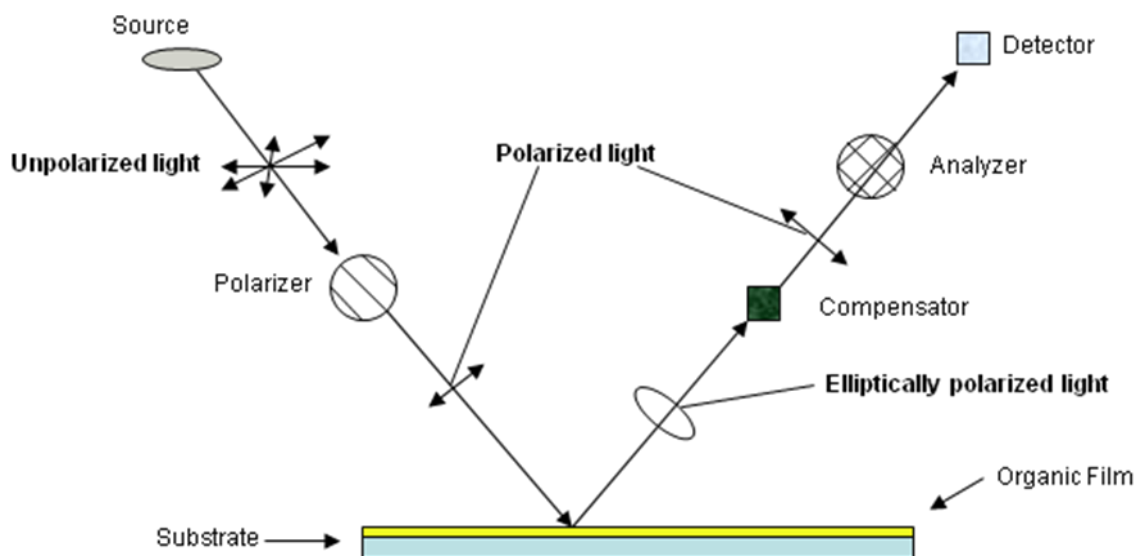
Figure 2.7 A cartoon representation of an ellipsometer.

2.5 Contact angle goniometry

A contact angle goniometer measures the static and dynamic contact angle of a surface. The general set up of a contact angle goniometer consists of a syringe filled a solvent, a fibre optic capable for illuminating the surface and a CCD camera connected to a computer for analysis. The solvent is added as a droplet onto the surface for contact angle measurements.

The contact angle (θ) is formed at a point of contact between the solid, liquid and vapour phases. The angle is the tangent measured at the three phase contact point, as shown in **figure 2.8**.
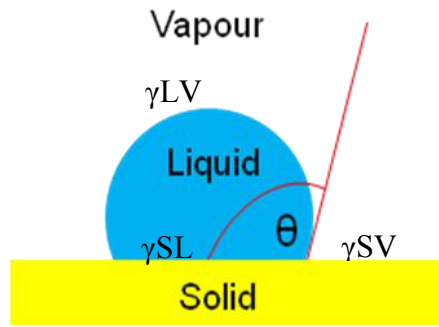
Figure 2.8 A liquid drop on a solid surface forming a contact angle.

The contact angle is governed by Young's Equation (**equation 2**)[40, 217] where γ_{SL} is the free energy of solid surface in contact with liquid, γ_{LV} is the free energy of the liquid-vapour interface and γ_{SV} is the free energy between the solid and the vapour.

$$\gamma_{SL} + \gamma_{LV}\cos\theta = \gamma_{SV} \quad \text{(equation 2)}$$

When a water droplet is in contact with a hydrophilic surface, the water spreads onto the surface to minimise free surface energy leading to a low contact angle ($<30^\circ$). In contrast, hydrophobic surfaces tend to have lower free surface energy and the water droplet does not spread onto the surface, therefore, producing a high contact angle ($>100^\circ$)[218] as shown in **figure 2.9**.

a)   b)

Low contact angle θ   **High contact angle θ**
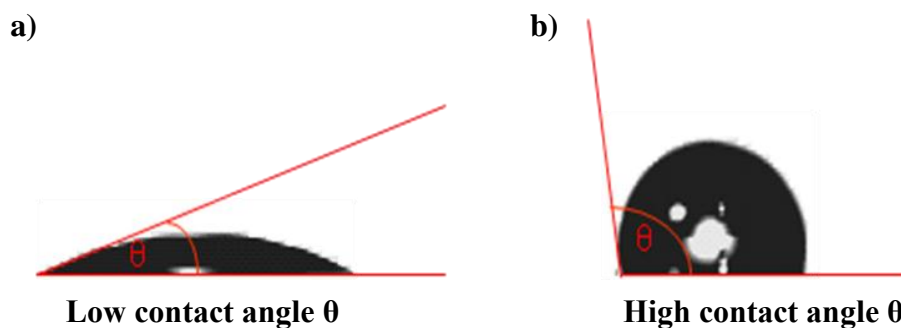
Figure 2.9 Picture of **a)** a low contact angle (hydrophilic surface) and **b)** high contact angle (hydrophobic surface).

Contact angle is measured by a free standing drop of a liquid on the surface, known as static contact angle (no syringe) or measured by a captive drop of liquid known as dynamic contact angle (with syringe) (**figure 2.10**). The dynamic contact angle is measured by adding and withdrawing water through the needle, where the addition of water produces the advancing contact angle (θ_a) and the withdrawal of water produces the receding contact angle (θ_r).
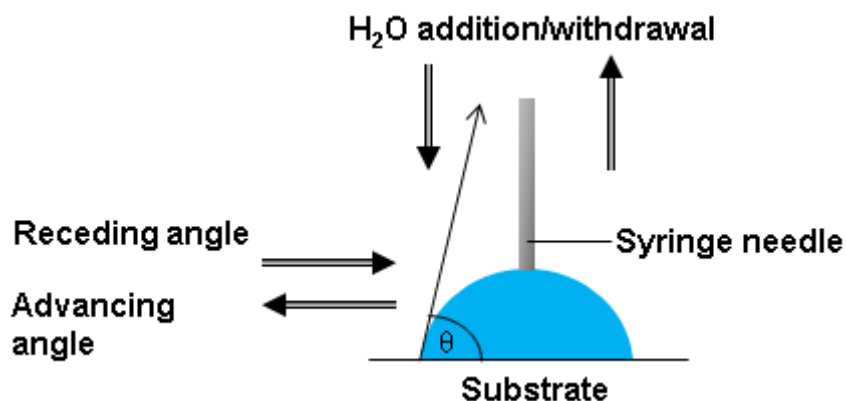
Figure 2.10 A cartoon representation of advancing and receding contact angles when water is added to or withdrawal from the surface.

The difference between the advancing and receding contact angles is known as the contact angle hysteresis ($\Delta\theta = \theta_a - \theta_r$). A small hysteresis ($< 5°$) indicates a homogenous, well ordered and crystalline SAM, whereas a large hysteresis suggests the surface is contaminated, non-homogenous and/or relatively rough.[219]

2.6 Electrochemistry

Cyclic voltammetry (CV) is developed from linear-sweep voltammetry,[199] which was the first technique employed in electrochemical investigations which provided redox information of chemical systems.

2.6.1 Linear sweep voltammetry

Linear-sweep voltammetry is conducted in a stationary solution which relies on materials being transported by diffusion to the electrode surface. The potential of the working electrode sweeps from a potential of E_1 where materials cannot be reduced or oxidised to a potential of E_2 in which electron transfer is driven rapidly (**figure 2.11**).
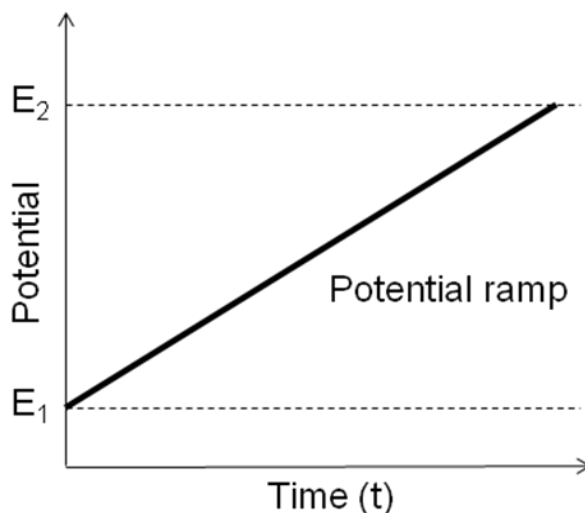
Figure 2.11 Linear sweep voltammetry: The potential ramp from E_1 to E_2.

The applied potential E is a function of the speed at which the potential is swept (v_s) and the time of the sweep (t) as shown in **equation 3.**[199]

$$E(t) = E_1 - v_s t \quad \text{(equation 3)}$$

The voltage behaviour is based on the assumption that the A/A^- active redox couple are irreversible (**equation 4**).

$$A + e^- \rightarrow A^- \text{ or } A^- \rightarrow A + e^- \quad \text{(equation 4)}$$
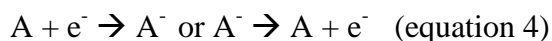
Initially, no current is passed through the system when the applied potential does not induce electron transfer. In the case when A reduces to A⁻ (**figure 2.12a**), as the applied potential is swept to a more negative value (**figure 2.12b**), electron transfer occurs on the electrode surface and current starts to pass through the system and produces a current response. As the applied potential (**E**) becomes more negative, the current increases exponentially until a maximum is reached at the redox peak potential (**E_p**), after which the current falls off.
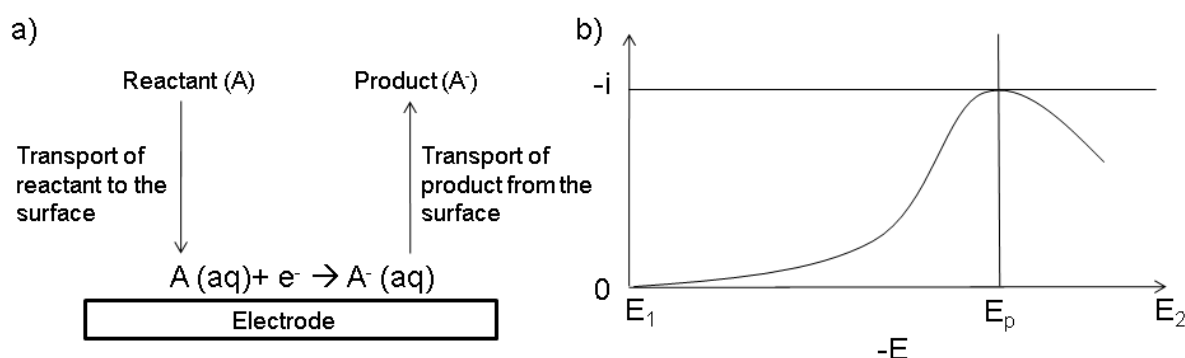
Figure 2.12 Schematic of **a)** reduction processes that happens on the surface

b) Corresponding current responses for an irreversible electron transfer reaction and the current peaks at the redox peak potential (E_p).

The rate at which the current increases is simply controlled by the reductive rate constant and the rate at which the electrode surface (A) is reduced. Once the maximum current has been reached, the current flowing is controlled by the diffusion rate of the reactant (A) from the solution to the electrode surface. The drop in the current is due to the depletion of A at the electrode surface. The limitation of linear sweep voltammetry in this technique can measure only the reduction or the oxidation process of a system.

2.6.2 Cyclic Voltammetry

Linear sweep voltammetry has been improved so that a potential swept reversibly between E_1 and E_2, resulting in a triangular potential cycle as shown in **figure 2.13**. This improvement allows the measurements of reduction and oxidation of the system sequentially, this technique is termed cyclic voltammetry.[199]
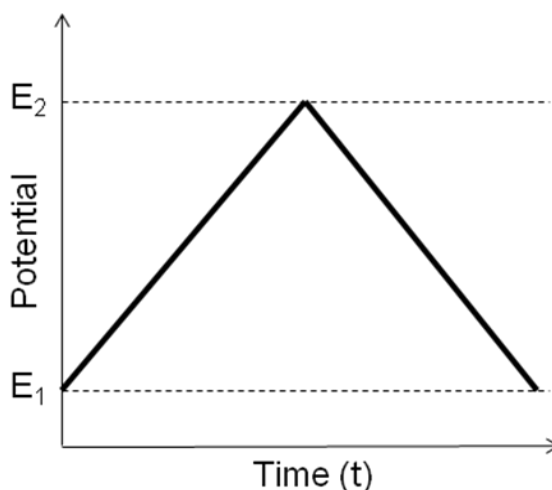
Figure 2.13 Cyclic sweep voltammetry: The reversible sweep of an applied potential as a function of time.

The shape of the forward sweep from E_1 to E_2 is identical to the linear sweep voltammetry as shown in **figure 2.13** where A is reduced to A⁻. The reverse sweep from E_2 back to E_1 indicates the oxidation of species A⁻ back to A as shown in **equation 5**.

$$A\,(aq) + e^- \underset{k_{ox}}{\overset{k_{red}}{\rightleftarrows}} A^-(aq)$$

(equation 5)
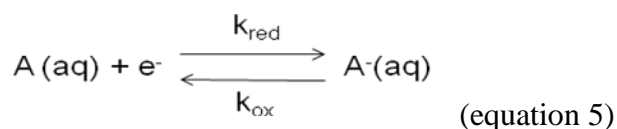
Figure 2.14 has shown the cyclic voltammogram for a reversible electron transfer reaction. As potential swept from positive to negative (forward scan), A is reduced to A⁻. Initially, the

current increases exponentially since there is a high concentration of A on the surface until the current reach maxima (i_p^{red}) at the potential of reduction redox peak potential (Ep^{red}), where A is reduced to A⁻. Post to the Ep^{red}, the current starts to drop due to the complete reduction of A to A⁻.

A current in the opposite sense to the forward scan (reverse scan) is observed due to the oxidation of A⁻ to A (**figure 2.14**). As the potential scans from negative to positive, the conversion of A⁻ to A is favourable. The current increases exponentially since there is a high concentration of A⁻ on the surface until the current reach maxima (i_p^{ox}) at the potential of oxidation redox peak potential (E_p^{ox}). Gradually, all of A⁻ on the surface is converted back to A and the current decreases as shown in the voltage-current curve in **figure 2.14**.
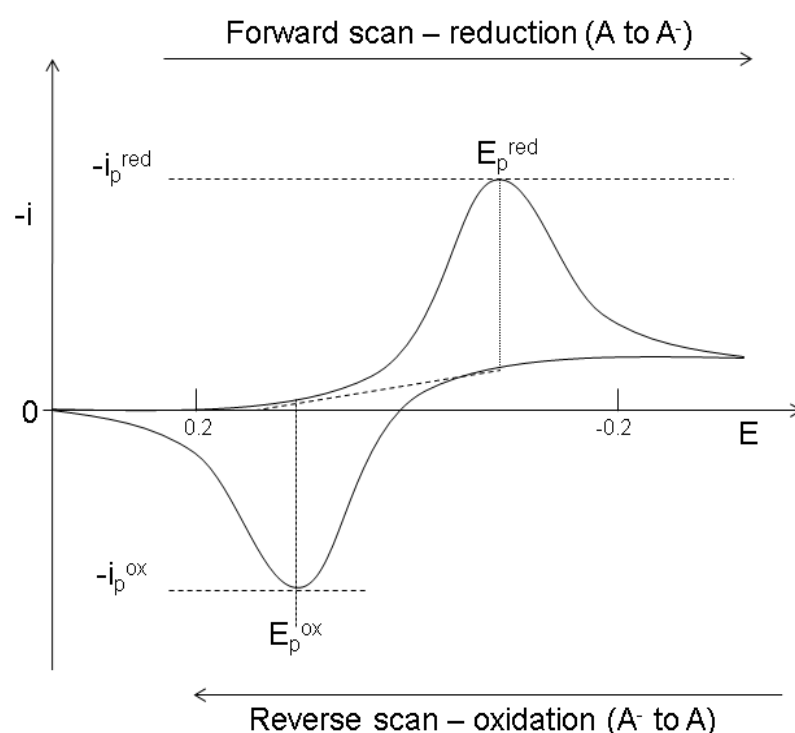
Figure 2.14 Voltage-current curve (cyclic voltammogram) for a reversible electron transfer reaction. E_p^{red}- reduction redox peak potential, E_p^{ox}- oxidation redox peak potential, i_p^{red}- current at reduction redox peak potential and i_p^{ox}- current at oxidation redox peak potential.

Cyclic voltammetry with an active redox couple can be employed to study the surface coverage and look for monolayer defects. Charge transfer on densely packed monolayers can not take place because ions in the electrolyte can not reach the surface. However, for a low density monolayer or a defective monolayer, there are regions where ions from electrolyte come into contact with the surface and charge transfer occurs which can be observed from the voltage-current curve.

We have so far discussed an electrochemical system that has an active redox couple (**equation 5** and **figure 2.14**). Current at the surface is generated by the transfer of electrons from the electrode to the redox species while current in solution is carried out by the migration of ions. However, a current can also be produced in the absence of a redox couple on the surface because the electrode acts as a capacitor in which two layers of charged electrodes are separated by a fixed distance (**d**). The potential drop between these two charged layers is linear (**figure 2.15**).
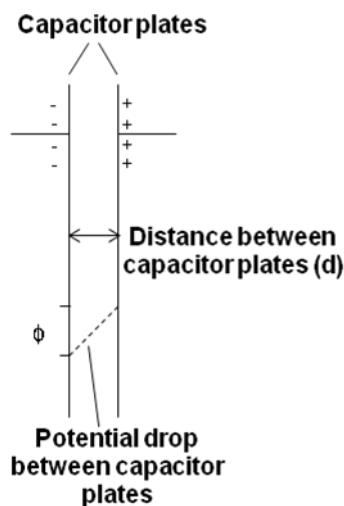
Figure 2.15 An electrical capacitor and the potential drop between the plates.

Based on the Helmholtz[220] model, a metal electrode possesses a charge density (q^m) which arises due to the absence (q^m positive) or excess of electrons (q^m negative) on the surface. In order for the electrode/electrolyte interface to maintain electrical neutrality, the charge on the electrode must be matched in solution by an equal but opposite charge (q^s) as shown in **equation 6**.

$$\mathbf{q^m = -q^s} \text{ (equation 6)}$$

The opposite charge ions (relative to the electrode surface) are attracted to the electrode surface to a distance limited by the solvation shell of the ion. The plane drawn through the centre of these solvated ions at a minimum distance from the metal surface is known as the Outer Helmholtz Plane (**OHP**) (**figure 2.16a**). The Helmholtz model states that the excess charge on the surface is completely balanced by the solution ions at the OHP and the surface/ions interface. A potential drop is observed between the electrode surface and the OHP. Helmholtz called this interface the "electrical double layer". This double layer has all the aspects of a typical capacitor in which two charged layers are separated by a distance (**d**) and potential drop across the surface is linear. (**figure 2.16b**)
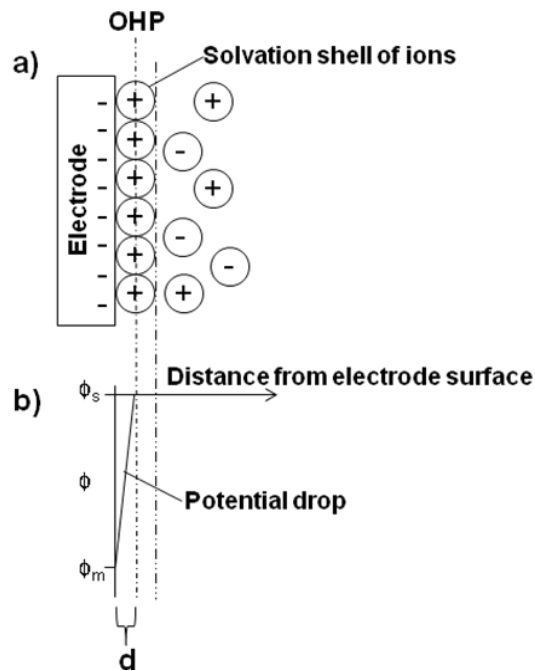
Figure 2.16 Schematic representations of **a)** the Helmholtz electrical double layer model and the **OHP** plane **b)** the potential drop across the interface between the two charged layers (electrode and OHP) at a distance (**d**).

The Helmholtz model was further improved by Gouy[221] and Chapman[222] where they concluded that excess charge density is not exclusively situated at the OHP. They suggested the attractive and repulsive forces of ions from the electrode surface are counteracted by Brownian motion in solution which tends to disperse excess ions on surface. Therefore, a single "diffusion layer" on the electrode surface is present instead of the OHP. Within the diffusion layer, the counteracting charge ion density (represented as point charges) (**figure 2.17a**) decreases as the distance from the electrode surface increases causing an inversely exponential potential drop across the diffusion layer as shown in **figure 2.17b**.
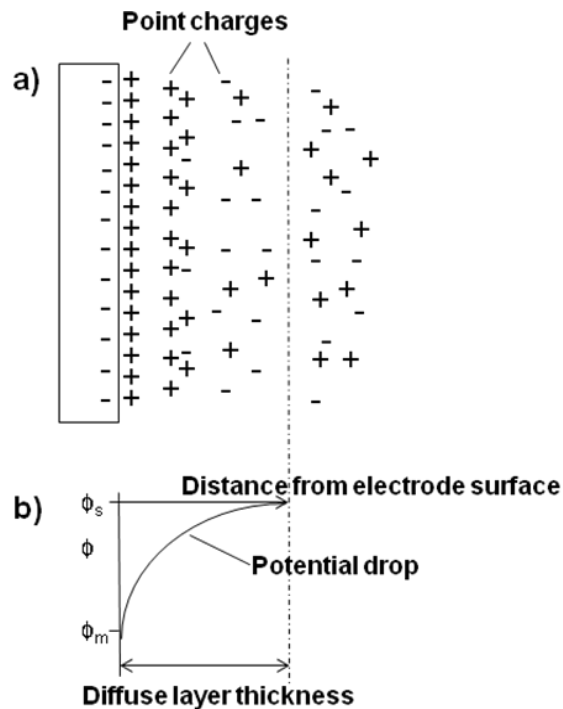
Figure 2.17 Schematic representation of **a)** the Guoy-Chapman model of electrical "double layer" and **b)** the potential drop across the diffusion layer.

In 1924 and 1947, Stern[223] and Grahame[224] further developed these two models respectively. Stern suggested that ions have a minimum distance of approach (OHP), as well as accepting the diffusion layer. He suggested the potential drops rapidly across the OHP and as the distance of ions from the electrode increases, the potential gradually falls. In 1947, Grahame further developed the model by suggesting that some ionic or uncharged species can penetrate into the OHP and the diffusion layer even though the surface is occupied by counteracting ions. This penetration occurs when an ion possesses no solvation shell and absorbs onto the electrode surface, even though the ions have the same charge as the surface (**figure 2.18a**). This model for the electrode/electrolyte interface was modified and a new plane of minimum approach was identified, the Inner Helmholtz Plane (**IHP**). The IHP is defined as the axis

through the centre of the specifically adsorb species and has an effect of reducing the charge density required to compensate the charge on the electrode (**figure 2.18b**).
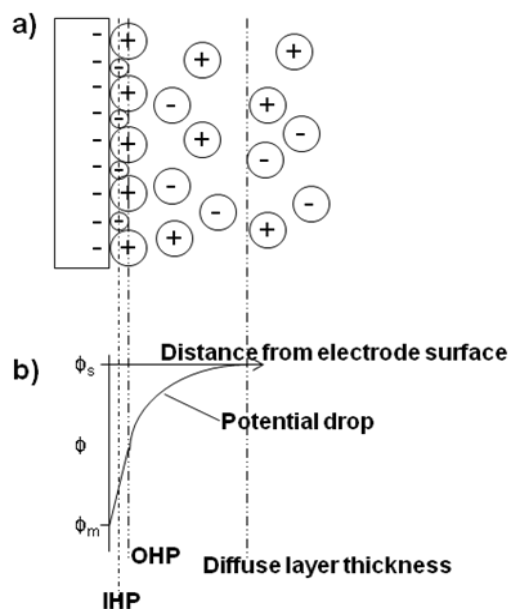
Figure 2.18 Schematic representation of **a)** Grahame model of electrical "double layer" and **b)** the potential drop across the **IHP**, **OHP** and the **diffusion layer**.

2.7 Surface Plasmon Resonance Spectroscopy (SPR)

Since the first observation by Woods in 1902,[225, 226] applications based on the surface plasmon resonance (**SPR**) spectroscopy are becoming more popular as a surface sensitive detection down to sub-monolayer coverage.

When Wood first irradiated polarized light on a mirror, he observed a pattern of dark and light bands in the reflected light. However, this phenomenon was not explained until 1968 when Otto,[227] Kretschmann[228] and Raether[229] reported the excitation of surface plasmons.

When polarized light is passed through a prism onto the back of a sensor chip with a thin metal film (normally 50 nm of gold), the light is reflected at an angle (θ_r) (**figure 2.19a**). The intensity of the reflected light passes through a minimum at a specific incidence angle (θ_i) at which light excites and induces surface plasmons. The photons of p-polarized light interact with the free electrons of the metal layer, inducing a wave-like oscillation of the free electrons and, therefore, reducing the reflected light intensity as illustrated by the drop of the intensity in **figure 2.19b**. A change of refractive index on the gold films causes an angle shift (θ_A to θ_B) of the intensity minimum of the reflected light.
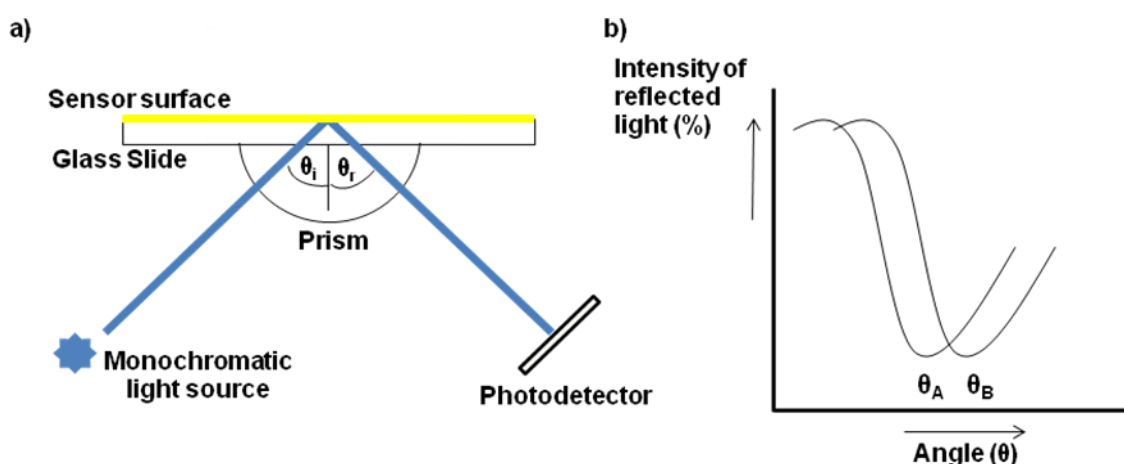
Figure 2.19 Schematic representation of **a)** polarized light shines from the light source onto the back of the sensor chip and reflected light intensity is measured in the photodetector. **b)** At certain angle of incidence (θ_i), excitation of surface plasmon occurs inducing a reduction of the intensity of the reflected light. A change of refractive index at the gold surface causes an angle shift (θ_A to θ_B) of the intensity minimum of the reflected light.

A change in refractive index (**Figure 2.20**) can occur by the adsorption of materials to the gold surface. Thus, a surface immersed in a solution to which a surface active molecule is injected can be monitored to reveal the kinetics of adsorption. At the end of the experiment,

the surface is washed with solution in the absence of active molecules, hence a reduction of angle.
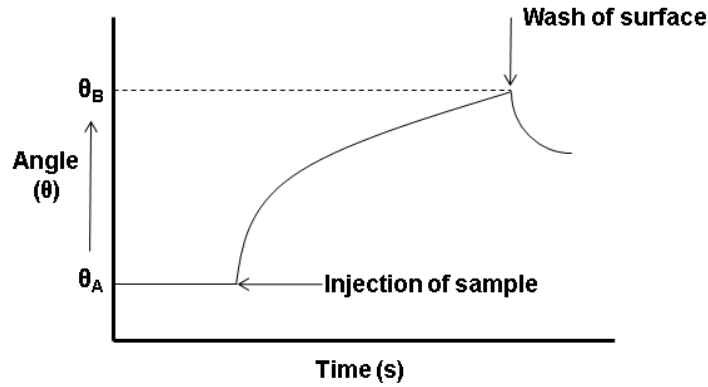
Figure 2.20 SPR sensorgram: The angle at which the intensity minimum is observed over time.

Initially, no change occurs at the sensor and a baseline is measured at the SPR angle (θ_A). After injection of the surface active materials, they adsorb to the surface inducing a change in the refractive index and cause a shift of the SPR angle to position θ_B. The change of SPR angle will result in a change of responsive unit (RU) which in turn translates into the mass of adsorbed materials onto the surface ($1\mu RU = 1$ ng.cm^{-2}).

SPR instrumentation can utilise 3 different optical systems to generate surface plasmons: surface with prisms, grating and optical waveguides.[230] Most SPR instruments use the surface with the prisms system. This system can be further divided into three sub-groups: fan-shaped beam, fixed angle and angle scanning SPR instruments. Results described in this thesis are obtained using the fan-shaped beam system. Therefore this system is described in greater detail.

In a fan-shaped beam instrument, a converging or diverging beam of p-polarised light is coupled to the higher refractive index medium (sensor chip) using a cylindrical or triangular prism. In a converging beam fan-shaped instrument, the beam focuses on a very narrow line on the sensor chip, whereas the diverging fan-shaped beam focuses on a large area on the sensor chip. A photodiode array detector is used to detect the reflected diverging beam with the SPR dip (dark area of the reflected beam) as shown in **figure 2.21**.
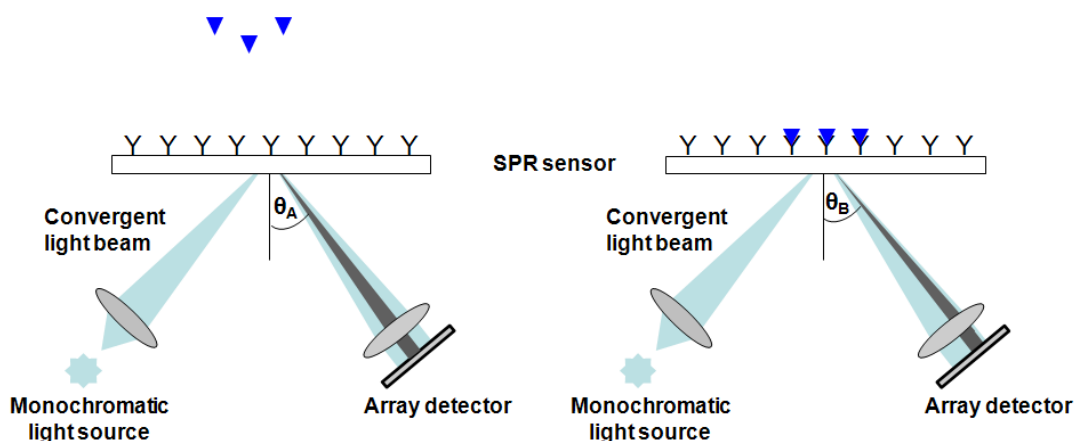
Figure 2.21 Schematic representations of the fan-shaped beam instrument and the angle shift (θ_A to θ_B) of SPR dip followed in real time as biomolecules adsorb onto the surface.

SPR sensors can only investigate a distance of 10-200 nanometers[231] above the metal surface. The penetration depth of the electromagnetic field (evanescent field) at which a signal is observed is between 10-200 nanometers,[231] and decays exponentially as the distance increases from the metal surface. SPR sensors lack intrinsic selectivity, meaning that any changes to the refractive index in the evanescent field can be observed by the change in reflected signal. These changes can be due to the refractive index difference in the medium (buffer composition and concentration) or changes in the surface environment. In order to permit selective detection of the SPR sensor, the metal surface is modified with specific ligands designed for capturing target compounds in the analyte that provide a measurable signal. This

is known as "direct detection". The ligand must also prevent any "non-specific binding" of undesired compounds onto the surface.

An SPR experiment is illustrated by a step-by-step analysis cycle (**figure 2.22**). Each measurement starts with conditioning the sensor surface with a suitable buffer solution (**step 1**). It is vital that the initial baseline is stable before injection of the surface active agent occurs. On injecting the solution containing the analyte, desired molecules are captured on the surface via the active ligands (**step 2**). Other components of the sample might adhere on the surface non-specifically due to the lack of suitable ligands on the surface; however, they are weakly bounded and easily washed off. Next, buffer solution is injected on the surface, the flow concentration of the analyte suddenly drops to zero, the analyte-ligand complex will start to dissociate via the displacement of surface bound analyte until equilibrium is reached (**step 3**). As shown in **figure 2.22**, the accumulated mass on the surface can be deduced by the change (**Δ**) of SPR response (**ΔR**). The dissociation step provides information that enables the dissociation kinetics to be studied. Finally, a regeneration solution is injected which breaks the binding between the analyte and the surface ligands (**step 4**).
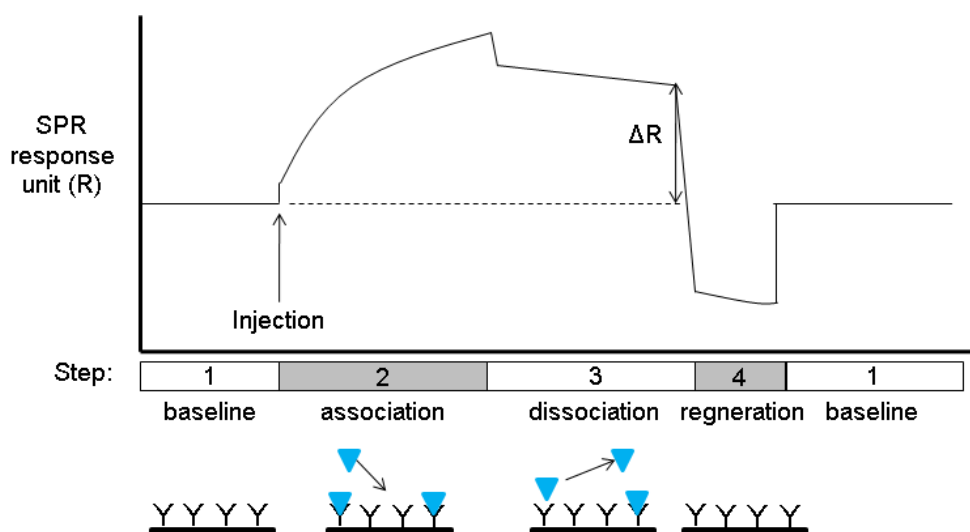
Figure 2.22 SPR sensorgram showing the steps of an analysis cycle.

Chapter 3

Study of Arp2/3 complex activity in filopodia of spreading cells using patterned biological surfaces

Chapter 3 is based upon an article entitled:

Abstract: *Cells use filopodia to explore their environment and to form new adhesion contacts for motility and spreading. The Arp2/3 complex has been implicated in lamellipodial actin assembly as a major nucleator of new actin filaments in branched networks. This chapter describes the fabrication and characterisation of patterned biological surfaces using patterning technology and several surface analytical techniques. This study explores the role of filopodia in the spreading of Mouse Embryonic fibroblast (MEF) cells and the function of Arp2/3 complex in this process. The results demonstrate that filopodia, produced by MEF cells interacted with the patterned fibronectin surface and guided lamellipodia protrusion. Arp2/3 complex, which is absent on the filopodia adhesion site, does not facilitate in the adhesion of filopodia on the fibronectin surface.*

3.0 Background

In a migrating cell, the leading edge (where protrusion occurs) contains 2 types of actin structure: (i) the branched network of actin filaments (lamellipodia), and (ii) the parallel bundles of actin filaments (filopodia).[232] Cells regulate the growth of actin filaments via a capping protein, gelosin,[233] on the barbed end (growing end) of the actin filament to prevent elongation and growth. The capping protein can be removed when signals trigger actin assembly leading to the growth of actin filaments. The growth of actin assembly is facilitated by a nucleation protein, namely Arp 2/3 complex (**figure 3.1 and figure 3.2**). The Arp2/3 complex is a seven subunits complex, containing 2 <u>A</u>ctin <u>r</u>elated <u>p</u>roteins (Arp) namely, Arp2 and Arp3, and 5 other subunits namely <u>Arp</u> 2/3 <u>C</u>omplex (ARPC 1-5).[233] The activation of Arp2/3 complex by the Wiskott - Aldrich syndrome (WASP) family proteins increases the binding to the side/barbed end of actin filaments and induces the formation of actin branching.[234, 235] There are two proposed actin branching models caused by the Arp 2/3 complex, the dendritic nucleation model (**figure 3.1**) and the barbed end branching model (**figure 3.3**).
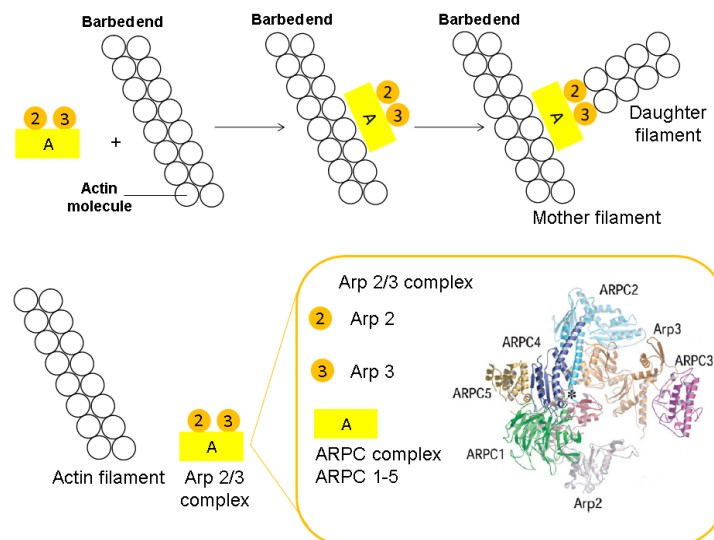
Figure 3.1 A cartoon representation of the dendritic nucleation model of Arp 2/3 complex on actin filament.[233]
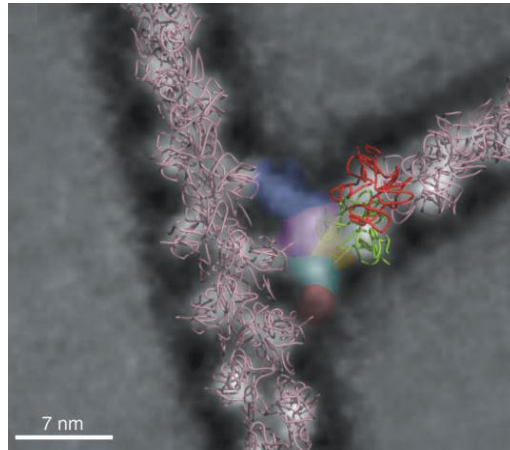
Figure 3.2 Electron micrograph of the dendritic nucleation model of the actin-bound Arp2/3 complex at the branch junction combined with the 2D reconstruction of actin filament (shown in pink). The Arp 2/3 complex facilitates the branching of actin filaments. The 2D reconstruction shows that Arp2 (red) and Arp3 (green) are the first two subunits of the daughter filaments. The other five subunits of the complex, namely ARPC 1-5 (shown in pale blue, purple, yellow, green and red) are anchors across 3 actin molecules on the mother filament.[236]

The dendritic nucleation model of actin polymerisation shows that the Arp2/3 complex accelerates the nucleation activity of the actin monomer, likely by serving as a template for the growth of new branching filaments by binding onto the side of pre-existing (mother) filaments.[237] Other structural analysis[236] by using cryo-electron micrographs shows that the Arp2/3 complex forms contact with three actin subunits on the mother filament. Arp2 and Arp3 form the first subunits on the newly branched (daughter) filaments as shown in **figure 3.1**.[236]

An alternative actin branching model to the dendritic nucleation model is the barbed end branching model (**figure 3.3**), where the activated Arp2/3 complex binds to the barbed end of

the actin filament rather than on the side as shown in **figure 3.1**. The Arp 2/3 complex is to initiate new branch formation while allowing the growth of the old branch. The Arp 2/3 complex competes with the capping protein in order to maintain actin assembly (**figure 3.3**).[238]
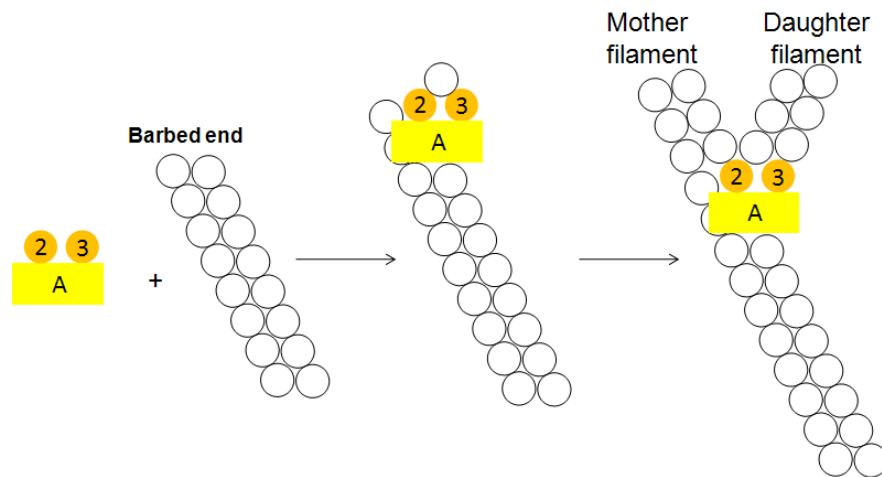
Figure 3.3 A cartoon representation of the barbed end branching model of Arp 2/3 complex on actin filament.[233]

The assembly of branch networks of actin filaments (**figure 3.4**) form specialised structures on the leading edge of the cell which pushes against the plasma membrane causing lamellipodia protrusions and cell motility.
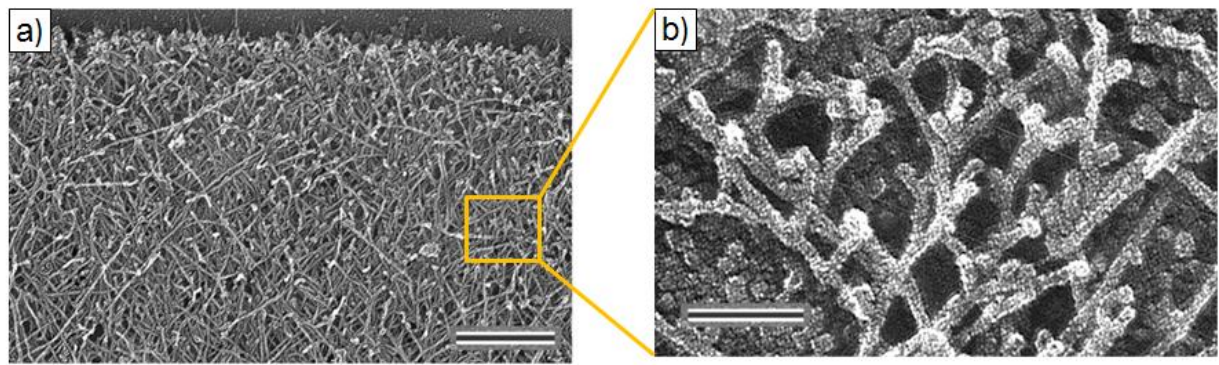
Figure 3.4 a) The actin cytoskeleton within the lamellipodia of a Xenopus keratinocyte. The scale bar represents 500 nm. **b)** Lamellipodial actin cytoskeleton at greater magnification showing the branching of actin filaments. The scale bar represents 100 nm.[239]

Some studies have proposed[240, 241] that filopodia are generated by the reorganisation of the Arp2/3 complex within the actin filament network in lamellipodia. Lamellipodial network is formed by Arp2/3-mediated dendritic nucleation. Elongation of some barbed ends in the network is terminated by capping protein, but other barbed ends bind to a complex of molecules known as the tip complex, that allows them to elongate continuously (**process 1, figure 3.5**). As the barbed end of the actin filament grows and elongates, it collides with other actin filaments and the tip complex mediates the clustering of the barbed end (**process 2, figure 3.5**). Convergence of actin filaments continue to grow together, while other barbed end actin filaments collides with the initial tip complexes, leading to the clustering of the barbed end, resulting in the convergence of more actin filaments (**process 3, figure 3.5**). The tip complexes initiates filament cross-linking by activating fascin, an actin cross-linking protein, which allows bundling of actin filaments, while the filaments elongate to ensure efficient pushing and forms a filopodium (**process 4, figure 3.5**). In the filopodium, the tip complex maintains its functions of promoting filament elongation and bundling, as well as fusion with other filopodia (**process 5, figure 3.5**).
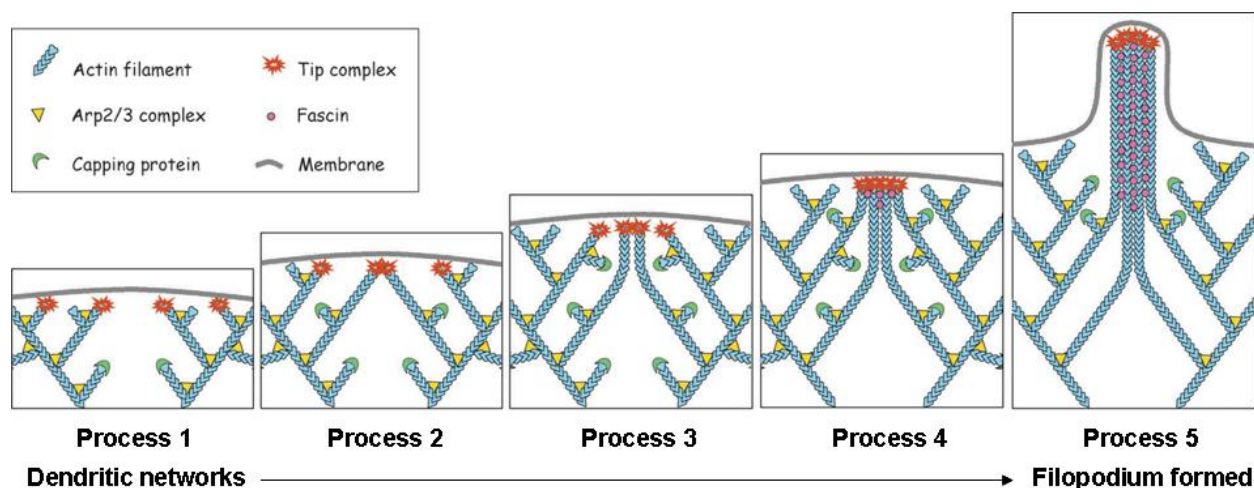
Figure 3.5 Convergent elongation model of filopodia initiation.[241]

3.1 Aim

Cells use filopodia to explore their environment and form new adhesion contacts for motility and spreading[154]. The Arp2/3 complex has been implicated in lamellipodial actin assembly as a major nucleator of new actin filaments in branched networks.[229] The interplay between filopodial and lamellipodial protrusions is an area of much interest as it is thought to be a key determinant of how cells make motility choices. Herein, the aim of this chapter is to determine whether the Arp2/3 is involved in the adhesion of filopodia to the surface, and to investigate whether filopodia in spreading cells may contain regions of lamellipodial activity, which could offer the cell flexibility in its motility choices.

3.2 Objectives

The objectives of chapter 3 are to use surface chemistry and patterning technologies to fabricate micropatterned surfaces of proteins on glass substrates for studies of cell behaviour. The objectives of this chapter can be broken down into 3 parts.

1) Hydrophobic surface formation using octadecyltrimethoxysilane (ODTMS) SAMs.

2) Bio-patterning of hydrophobic surfaces using fibronectin coated polydimethylsiloxane (PDMS) stamp.

3) Cell attachment on patterned fibronectin surfaces.

Objective 1: Hydrophobic surface formation

Hydrophobic surfaces provide an excellent platform for the adsorption of proteins on surfaces.[242] Whitesides *et al*.[242] demonstrated that the amount of protein adsorbed on a surface can be regulated by controlling the surface wettability. Hydrophobic surfaces, such as methyl-terminated SAMs, facilitate the protein adsorption, whereas hydrophilic surfaces e.g. ethylene glycol SAMs have been shown to be an inert surface for protein adsorption.[242]

Hydrophobic surfaces can be fabricated by forming ODTMS SAMs on glass. The formation of ODTMS SAMs on glass (**process 1**, **figure 3.6**) is to be carried out by immersing the glass substrate in ODTMS solution (anhydrous dichloromethane (DCM)). The formation of silane SAMs has been described in **section 1.1.2.2**. The SAM formation was determined by contact angle measurements, ellipsometry and atomic force microscopy. Alternatively, poly(dimethylsiloxane) (PDMS) coated glass substrate has been employed as a hydrophobic surface for protein adsorption.
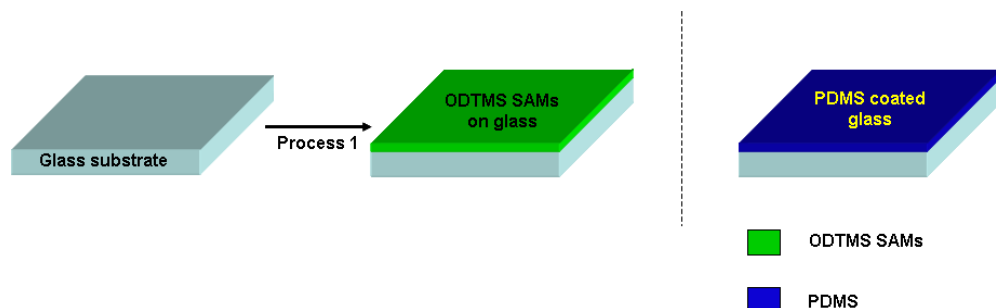
Figure 3.6 A cartoon representation of hydrophobic surfaces.

Objective 2: Bio-patterning of hydrophobic surfaces with fibronectin

Microcontact printing was employed to fabricate micropatterned features of fibronectin (**figure 3.7**) on ODTMS SAMs and PDMS coated glass substrate. Fibronectin was "inked"[91] onto the patterned PDMS stamp (**process 2**, **figure 3.7**), and subsequently "printed" onto the ODTMS SAMs (**process 3**, **figure 3.7**) and PDMS coated glass substrate (**process 4**, **figure 3.7**). The transfer of fibronectin by the removal of PDMS stamp (**process 5**, **figure 3.7**) on ODTMS SAMs and PDMS coated glass substrate forms ODTMS fibronectin (**OF**) substrate (**process 6**, **figure 3.7**) and PDMS fibronectin (**PF**) substrate (**process 7**, **figure 3.7**).
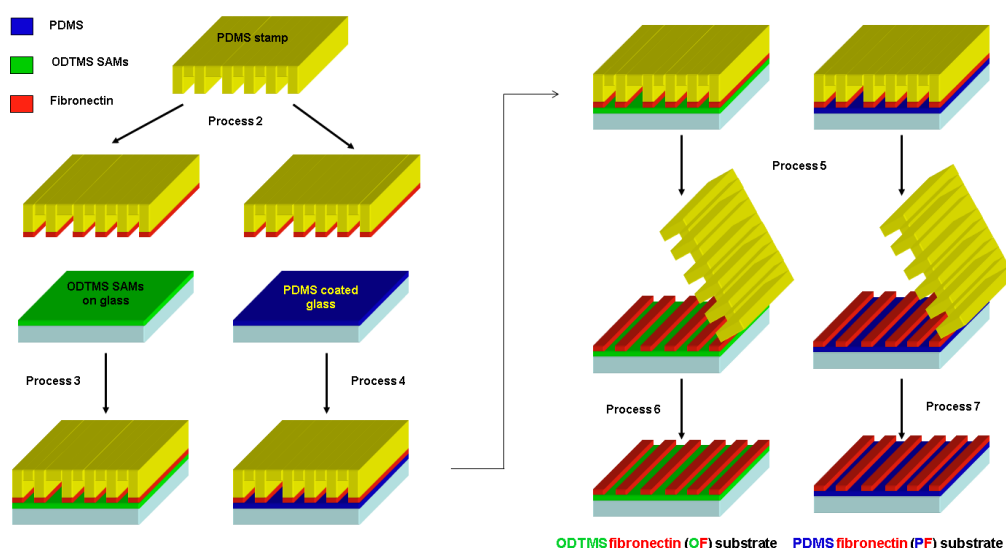
Figure 3.7 Schematic representations for the formation of the ODTMS fibronectin (OF) substrate and the PDMS fibronectin (PF) substrate.

Objective 3: Cell attachment

The PDMS fibronectin (**PF**) substrates were immersed in bovine serum albumin (BSA) solution to backfill the gaps between the fibronectin lines (**process 8**, **figure 3.8**). BSA ensures MEF cells only attach onto the fibronectin patterns, and prevent any attachments onto the PDMS surfaces.[243] MEF cells in PBS solution were drop casted onto the PF with BSA surfaces (**process 9**, **figure 3.8**) for the study of cell protrusion caused by filopodia and lamellipodia (**process 10**, **figure 3.8**) — actin filament bundles that guide cell migration. More specifically, fluorescence microscopy was employed to study the vinculin interaction with the fibronectin surfaces and the nucleation of Arp 2/3 complex on the filopodia. This part of the experiment was carried out in collaboration with Simon Johnston from the School of Biosciences.
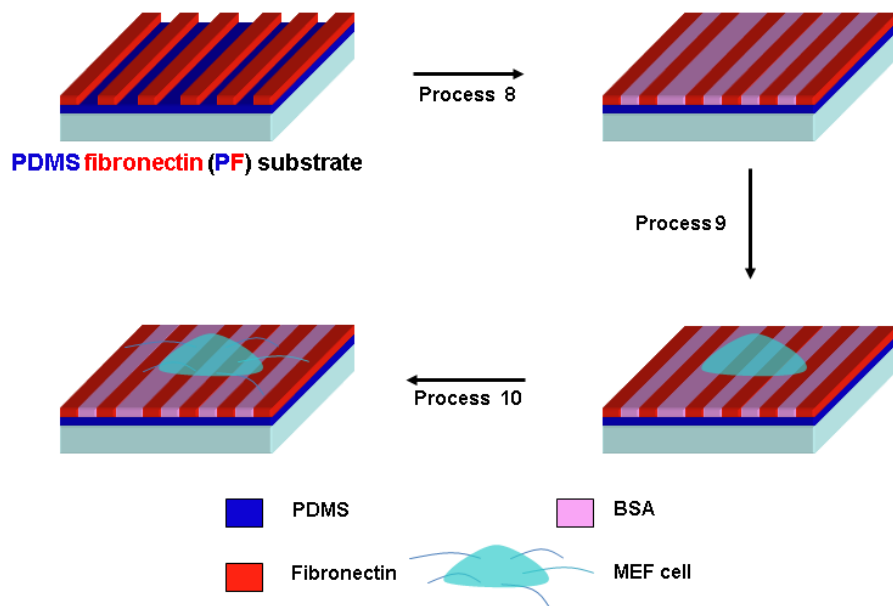
Figure 3.8 Schematic representation showing the fabrication of fibronectin/BSA patterned surfaces (**process 8**), followed by the introduction of MEF cells on the surface (**process 9**) and occurrence of cell protrusion (**process 10**).

3.3 Results and discussion

3.3.1 N-octadecyltrimethoxysilane (ODTMS) SAMs Formation

Glass substrates were cleaned by hot piranha solution to remove organic contamination on the substrate surface (**process 1, figure 3.9**). The cleaned glass substrates were rinsed with UHQ water and immersed into RCA solution under sonication to hydrolyze the silicon oxide groups on the surface (**process 2, figure 3.9**). The substrate was rinsed again with UHQ water to remove RCA solution. Solvent exchange of glass substrate was carried out by immersing the glass substrate in the solution of dichloromethane (DCM) and water at a ratio of 1:3 (**process 3, figure 3.9**), 2:2 (**process 4, figure 3.9**), 3:1 (**process 5, figure 3.9**), non-anhydrous DCM (**process 6, figure 3.9**) and anhydrous DCM (under (Ar) atmosphere) (**process 7, figure 3.9**) for 2 minutes at each process to remove excess water from the glass surface. Substrates were then immersed, under an argon (Ar) atmosphere, into a solution of octadecyltrimethoxysilane (ODTMS) (2.5 mM) in anhydrous DCM (5ml) and sonicated at room temperature for 1 hour (**process 8, figure 3.9**) to form the ODTMS SAMs (**process 9, figure 3.9**).
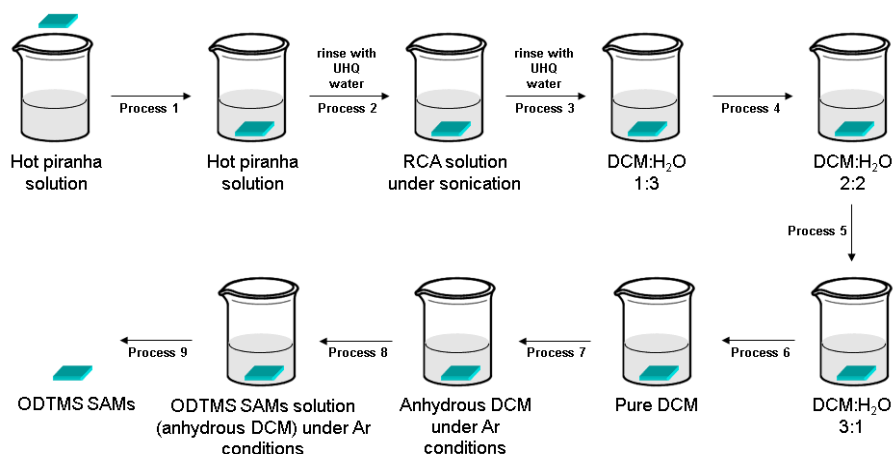
Figure 3.9 Schematic representations showing the experimental procedures of the ODTMS SAMs formation including the cleaning (**process 1**) and surface activation (**process 2**) of glass substrate. Solvent exchange was illustrated in **process 3 – 7**, and ODTMS SAMs formation in **process 8** and **process 9**.

Sonication, Ar atmosphere and anhydrous solvents were required to reduce polymerization of silane molecules in solution. The SAMs were then cured in an oven at 120 ^{o}C for 30 minutes at a reduced pressure to enhance the cross-linking of ODTMS SAMs. Contact angle, AFM and ellipsometry characterisation techniques were used to determine whether the SAM formation process had occurred.

3.3.1.1 Dynamic contact angle (θ) analysis of ODTMS SAMs on glass substrate

The advancing contact angle **(θ$_a$)** of the non clean glass substrate was $64^o \pm 4^o$. The substrate was then cleaned with hot piranha solution (90^oC) for 60 minutes, rinsed with UHQ water, followed by treatment with RCA solution, and rinsed with water, resulting in an advancing contact angle of $5^o \pm 2^o$. The reduction in advancing contact angle **θ$_a$** is a result of the high density of hydroxyl groups on the activated glass surface.[244]

The advancing contact angle **(θ$_a$)** of ODTMS SAMs was $68^o \pm 2^o$ (**table 3.1**), which is significantly greater than the advancing contact angle **(θ$_a$)** of glass after being treated with RCA solution and rinsed with UHQ water ($5^o \pm 2^o$). The change of contact angle indicates a change of surface wettability which suggests that ODTMS SAMs have been formed on the glass surface. However, the advancing contact angle **(θ$_a$)** of ODTMS is about 30 % lower than the value stated by Wu *et al*. (105°) [245] and Sugimura *et al*. (102°).[246] The difference in surface wettability might indicate the SAMs have not fully formed and contains defects on the surface, resulting in the reduction of contact angle.

Table 3.1 Summary of contact angle of ODTMS SAMs on glass compared with the contact angle of glass substrate and glass substrate after cleaning and activation.

Contact angle	Advancing	Receding
Glass substrate	64° ± 4°	27° ± 4°
Glass substrate after cleaning and activation	5° ± 2°	4° ± 2°
ODTMS SAMs	68° ± 2°	38° ± 5°

3.3.1.2 AFM topography

AFM topography imaging was used to examine the topography of the ODTMS SAMs. **Figure 3.10a** shows the AFM topography image of a clean glass surface and **figure 3.10b** shows a glass surface after immersion in an ODTMS solution. The root mean square (RMS) roughness of the clean glass surface is 0.52 nm. The RMS roughness of ODTMS SAMs on glass is 0.56 nm. The AFM images showed that ODTMS SAMs are homogenous, smooth and do not show any noticeable aggregate of polymerise ODTMS.[247]
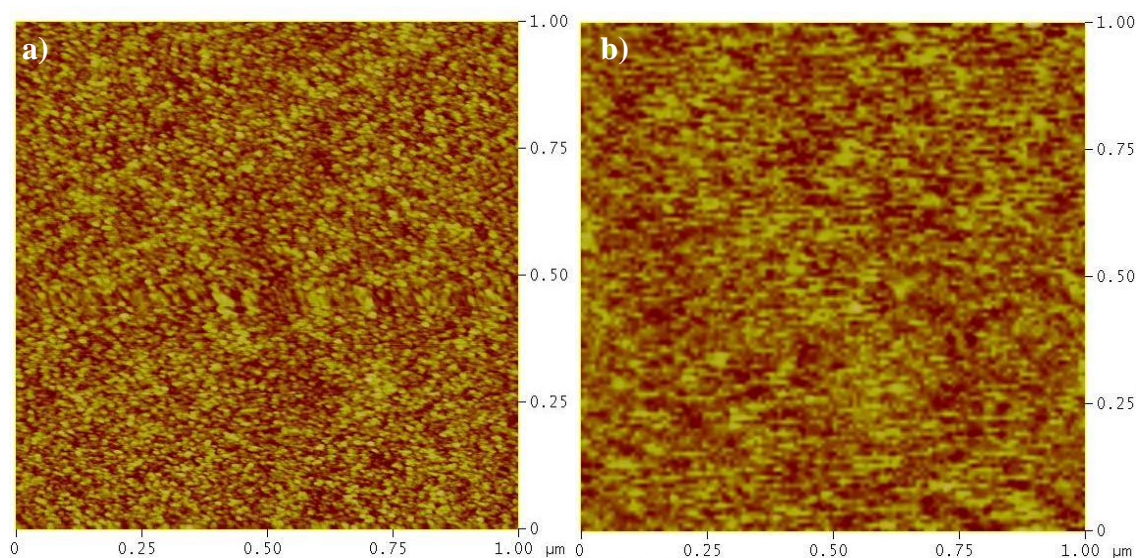
Figure 3.10 AFM images of **a)** clean glass substrate form after **process 2, figure 3.9** and **b)** ODTMS modified glass surface. (**process 9, figure 3.9**)

3.3.1.3 ODTMS SAM thickness by ellipsometry

Ellipsometry is designed to measure surface thickness on a reflective surface. However, glass is transparent and does not reflect, hence, a silicon substrate was used as the surface SiO_2 layer has similar SiO_2 surface chemistry to glass, but the underlying silicon affords reflection. In order to determine the thickness of ODTMS SAMs, SAMs were formed onto SiO_2 surface using the same SAM formation protocol as for glass (**figure 3.9**). The thickness of ODTMS SAM was determined to be 1.68 ± 0.16 nm (**Table 3.2**) which is in good agreement with the value (1.8 nm) reported by Sugimura et al.[246]

Table 3.2 Surface thickness of ODTMS SAMs.

Area	Thickness (nm)
1	1.85
2	1.61
3	1.56
4	1.54
5	1.84
average	1.68
error	0.16

The observed surface thickness was about 35 % lower than the calculated molecular length of ODTMS (2.59 nm) (Chem3D Ultra version 8.0 software and minimized energy through MM2). Given that the maximum titling angle for a silane molecule is 5°,[248] that means the minimum surface thickness due to titling effect should be 2.58 nm. However, we are observing a 35% surface thickness reduction; therefore, we can assume the tilting effect has minimal effect on the surface thickness.

By comparing the surface thickness and contact angle recorded with values reported by Wu *et al*.[245] and Sugimura *et al*.[246], we can conclude that ODTMS SAMs has partially formed with some defects on the SiO_2 surface.

3.3.2 Patterning of fibronectin on ODTMS SAMs on glass

Patterning of fibronectin on glass substrates was performed on glass cover slips as previously used by Calma *et al*.[249] Glass substrates of this type were used for their compatibility with the fluorescence microscope.

The purpose of using ODTMS SAMs is that proteins have been shown to adsorb strongly onto hydrophobic surfaces as described by Mrksich *et al*.[23, 250] Once ODTMS SAMs were formed on the substrate surface, fibronectin was transferred onto the ODTMS SAMs as lines i) 10 μm thick lines by 10 μm gap, ii) 5 μm thick lines by 5 μm gap and iii) 2.5 μm thick lines by 0.5 μm gap (**figure 3.11**) by microcontact printing (μCP) (**figure 3.7**) to form the OF surface. These OF surfaces were employed for the study of cell motility as described in **section 1.4**.

3.3.2.1 Silicon master and patterned PDMS stamp preparation

The lithographically silicon produced masters were prepared in collaboration with the research group of Prof. Steve Evans from Leeds University. The following masters were fabricated: i) the first master had lines of 10 μm in width separated by 10 μm gaps produced by optical lithography (**figure 3.11a**), ii) the second master (in house) was employed and had lines of 5 μm in width separated by 5 μm gaps, as shown by the optical image of the PDMS stamp fabricated from the 5 μm by 5 μm masters (**figure 3.11b**), and iii) the third master had

lines of 2.5 μm in width separated by 500 nm width gaps produced by e-beam lithography (**figure 3.11c**)
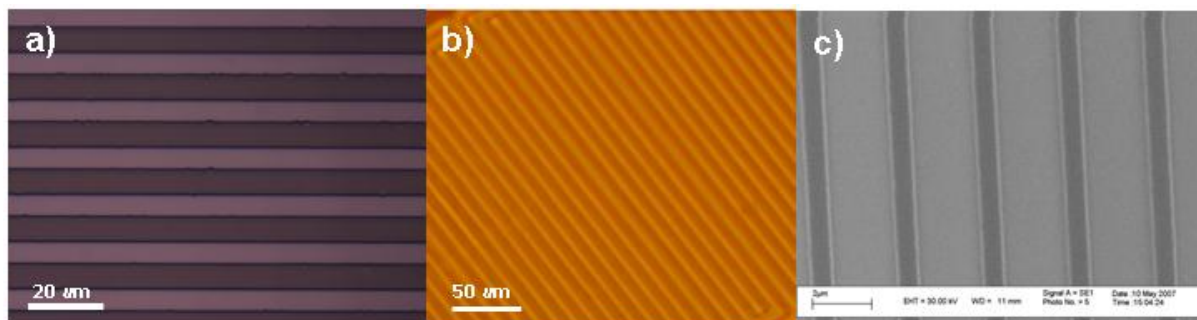
Figure 3.11 a) Optical image of the micropatterned (10 μm thick line x 10 μm gap) silicon master.

b) Optical image of the micropatterned (5 μm thick line x 5 μm gaps) PDMS stamp.

c) Scanning electron microscopy image of the micropatterned (2.5 μm thick line x 0.5 μm gaps) silicon master.

The PDMS stamp was prepared as described in **section 6.4.3.2**. After casting of the PDMS monomeric precursor on the master, the mixture was allowed to "de-gas" (removal of air from within the mixture) for 2 hours to avoid any stamp defects caused by air bubbles. The de-gassed PDMS mixture was cured in an oven to promote the cross-linking of the PDMS. The cured PDMS stamps were then carefully peeled from the masters. (**step b, figure 1.18**)

3.3.2.2 Microcontact printing of fibronectin

In order to visualise the printed micropatterns, fluorophore (Cy3) labelled fibronectin was patterned onto the glass substrate and examined by the fluorescence microscope. Fibronectin mixture (5 μg ml^{-1}) containing unlabelled fibronectin and Cy3 fibronectin in a 4:1 ratio was provided by Simon Johnston from the School of Biosciences. Stamps were inked for 30

seconds (using a cotton bud) or 40 minutes (drop-casting) (**process 2**, **figure 3.7**) using the fibronectin mixtures followed by rinsing the inked stamp with PBS for 1 minute to remove excess fibronectin. The inked stamps were placed into contact with ODTMS SAMs (**process 3**, **figure 3.7**) substrates. In order to ensure that the fibronectin did adsorb onto the ODTMS SAM surface, an initial experiment was conducted by using a non-patterned fibronectin coated PDMS stamp (30 seconds inking with cotton bud) and printing onto ODTMS SAMs surfaces. These fibronectin modified surfaces were characterised by ellipsometry and AFM as discussed below in **section 3.3.2.2.1** and **section 3.3.2.2.2**.

3.3.2.2.1 Fibronectin thickness on ODTMS SAMs by ellipsometry

The ellipsometric thickness of the non-patterned microcontact printed fibronectin was measured using SAMs of ODTMS on Si/SiO$_2$ substrates. The ellipsometric thickness after fibronectin absorption is shown in **table 3.3**. The average thickness shows a ~ 2 nm increase in thickness, but with a large variance over the surface. Thus, the fibronectin adsorption seems to be non-uniform and therefore, the surface was interrogated further with AFM.

Table 3.3 Surface thickness of fibronectin on ODMTS SAMs.

Area	Thickness (nm)
1	3.96
2	2.12
3	2.03
4	0.99
5	1.18

3.3.2.2.2 AFM topography

AFM images were taken on 2 different samples in order to deduce the adsorption of fibronectin on ODTMS SAMs on glass substrates. The RMS roughnesses of non-patterned

microcontact printed fibronectin on ODTMS SAMs are 7.99 nm and 17.9 nm, which are much higher than the RMS value for ODTMS SAMs on glass (0.56 nm). However, the adsorption of fibronectin was seen to be non-uniform (**figure 3.12a and 3.12b**) and features as high as 112 nm could be seen on the surface. The possible reason for such variable results may be due to performing AFM measurements in dry/air conditions, which induced aggregation of fibronectin on the surface. Ellipsometry was also carried out in dry/air conditions and it could justify the higher variation thickness observed in **table 3.3**. Thus, these results are inconclusive to determine fibronectin absorption on ODTMS SAMs surfaces, hence patterned fibronectin on ODTMS SAMs surfaces were imaged with the fluorescent microscope to examine the quality of adsorption.
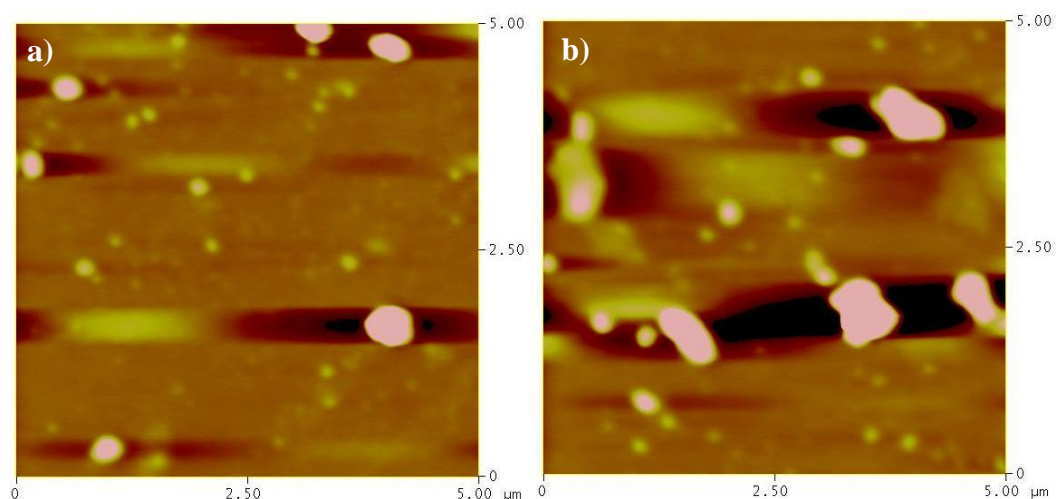
Figure 3.12 AFM images of non patterned microcontact printed fibronectin on ODTMS SAMs on glass. **a)** RMS value of 7.99 nm, **b)** RMS value of 17.9 nm.

3.3.2.2.3 Fluorescence imaging

Initial printing studies on ODTMS SAMs on glass were performed by depositing the fibronectin mixture on the patterned PDMS stamps using a cotton bud for 30 seconds. Moreover, the PDMS stamps were reused after sonication in ethanol. These conditions were

found to induce defects on the patterned surface as shown in **figure 3.13a**. Therefore, different conditions for printing were systematically investigated using a patterned PDMS stamp (**figure 3.7**) and better results (**figure 3.13b**) were obtained by 1) drop-casting the fibronectin solution on the PDMS stamp for 40 minutes and 2) employing a fresh PDMS stamp for each stamping. These conditions allowed better deposition to form a patterned fibronectin layer.
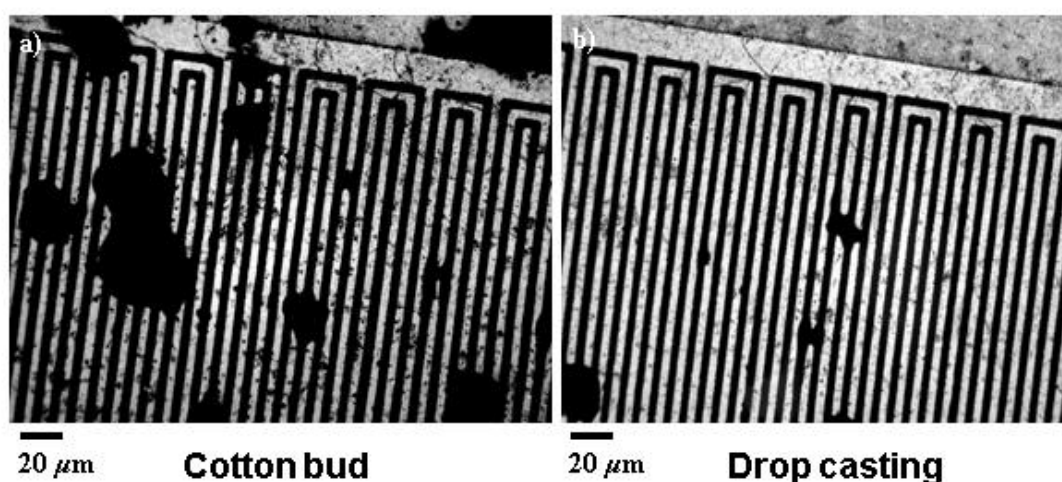
Figure 3.13 Fibronectin was printed onto ODTMS SAMs on glass to fabricate bio-structures of 5 μm thick lines by 5 μm gap using a patterned PDMS stamp with **a)** 30 seconds inking with cotton bud and **b)** 40 minutes inking by drop casting.

However, the patterned surfaces shown in **figure 3.13b** still contained some defects, meaning that the quality of the micropatterns was not adequate for the study of cell migration. Therefore, alternative surfaces were required in order to enhance the printing quality.

By utilising PDMS coated glass substrates with contact angle of $61^{o} \pm 2^{o}$ from the manufacturer as shown in **figure 3.7**, well defined fibronectin patterns on PDMS coated glass substrate (PF) were observed by fluorescence microscopy (**figure 3.14a and 3.14b**). It is

believed that the PDMS layer on glass promotes better fibronectin adsorption.[23, 250] After the formation of fibronectin patterns, the patterned substrates were incubated in bovine serum albumin (**BSA**) solution (Dulbecco's Modified Eagle's Essential Medium) (DMEM) for 60 minutes at 37 $^{\circ}$C, 5 % CO_2, 95 % air) to backfill the gaps between the fibronectin regions preventing non-specific attachment of cells onto the glass surface (**process 7**, **figure 3.8**). These PF surfaces were employed for the studies of cell spreading.
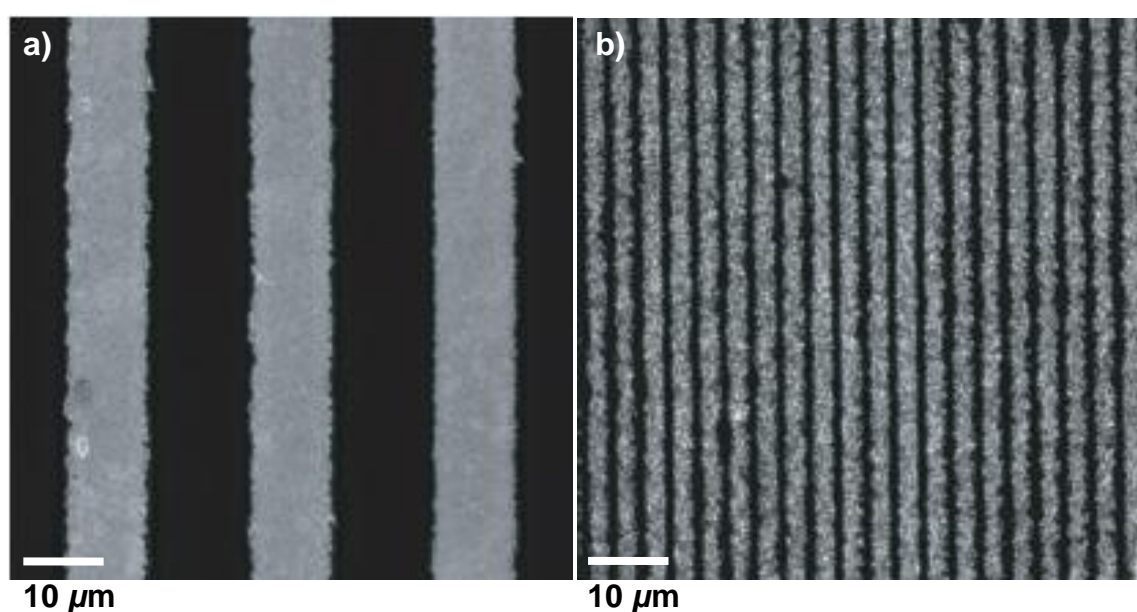
Figure 3.14 a) Fluorescence micrograph of 10 μm wide strips of fibronectin (bright line) separated by 10 μm of BSA (dark line) printed on PDMS coated glass substrate. **b)** Fluorescent micrograph of 2.5 μm wide strips of fibronectin separated by 0.5 μm of BSA printed on PDMS coated glass substrate.

3.3.3 Cell attachment on non-patterned and patterned fibronectin surfaces

3.3.3.1 Attachment of MEF cells on non-patterned fibronectin surfaces

This part of the project was done in collaboration with Simon Johnston, a PhD student in Professor Laura Machesky's group (School of Biosciences, University of Birmingham). Cell

spreading on specific well-defined surfaces is a methodology to study the cell biology of lamellipodia and filopodia. By observing spreading on a PF substrate there is a much greater chance of unravelling signalling processes during cell spreading. The cell motility studies were conducted by culturing MEF cells on non patterned fibronectin surfaces and cells were fixed with formaldehyde at 5, 15 and 60 minutes. Initial experiments demonstrated that after attachment to the fibronectin substrate, MEF cells produced filopodia within 5 minutes. Filopodia production was followed by extension of lamellipodia (**figure 3.15**) and cell spreading continued with these repeated cycles of filopodia and lamellipodia assembly as shown in **figure 3.15**. From these studies, it can be concluded that cells were able to spread on these fibronectin deposited layers, forming filopodia and lamellipodia.
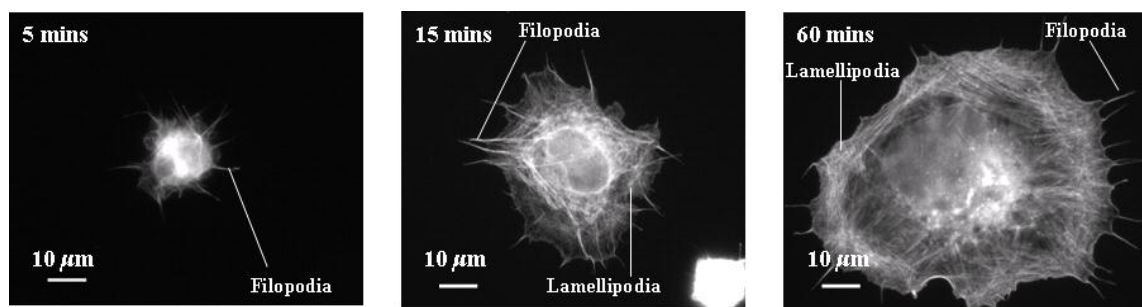
Figure 3.15 MEF cell spreading on fibronectin coated glass and fixed at 5, 15 and 60 minutes. Lamellipodia protrusions were guided by filopodia attachments as seen from images taken at 5, 15 and 60 minutes.

3.3.3.2 Attachment of MEF cells on PF surfaces

Cell attachment[153] depends on a delicate interplay between the cell and the extracellular matrix (ECM). The interaction between the cell and ECM are primarily mediated by integrins. Integrins are attached to the ECM through a complex linkage consist of talin, vinculin and α-actinin as previously discussed in **section 1.4.3**. By attaching fluorophores on the vinculin, (a

linkage between α-actinin and talin (**figure 1.36**)), the adhesion site of a cell to its surrounding matrix can be determined.

MEF cells were able to attach and form focal adhesion sites on 10 μm strips of fibronectin (**process 9**, **figure 3.8**). Cells were visualised by the fluorescently labelled actin and vinculin as shown in **figure 3.16a and figure 3.16b**. Brighter areas on the fibronectin strip suggest that a higher concentration of vinculin is present at the site of attachment, suggesting the formation of focal adhesion sites. Areas with a high vinculin presence (brighter colour) (**figure 3.16b**) are very similar to the focal adhesion points of filopodia on fibronectin strips (**figure 3.16a**). The fluorescence signal of the labelled vinculin on the BSA gaps was much weaker than seen on the fibronectin strips. Therefore, it can be concluded that the MEF cells do not attach to BSA gaps as shown in **figure 3.16a and 3.16b**.
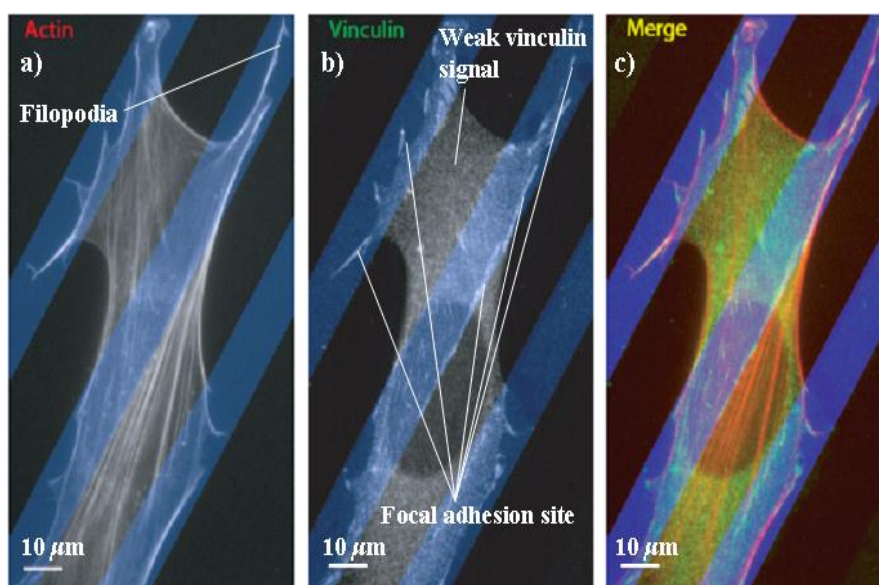
Figure 3.16 Fluorescent micrograph showing the response of MEF cells spread on 10 μm strips of fibronectin (blue colour) and 10 μm gaps of BSA (black colour). **a)** Micrograph of fluorescently labelled actin filament of MEF cell on fibronectin strips. **b)** Micrograph of fluorescently labelled vinculin of MEF cell on fibronectin strip. The brighter area on the

fibronectin strip has a high concentration of vinculin, where focal adhesion occurs. **c)** A

merge micrograph of fluorescently labelled actin filament and vinculin.

3.3.3.3 Spreading of MEF cells on PF surfaces

MEF cells were able to attach and spread onto the 10 μm strips of fibronectin (**process 10**,

figure 3.8). The velocity of the cell spreading (**process 10**, **figure 3.8**) on a patterned (10 μm

by 10 μm) surface was approximately half of that observed with cell spreading on non-

patterned fibronectin substrates. The reduction of the spreading rate is possibly due to the

reduced number of adhesion sites on the substrate. Cells were observed to only spread in the

direction and orientation of the fibronectin stripes that they initially make contact with. Cells

can be seen to produce filopodia that make contact with BSA surface within the gaps of the

pattern (**solid arrows**, **figure 3.17**) but did not produce persistent protrusions, like those seen

on the fibronectin strips (**hollow arrows**, **figure 3.17**).
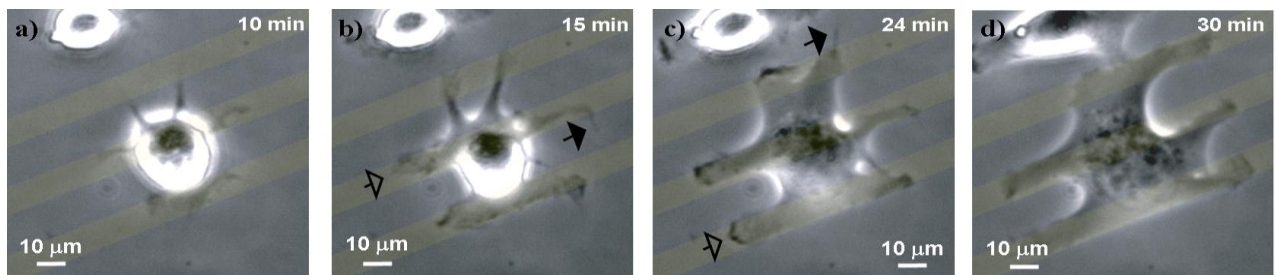
Figure 3.17 Images are single frames from a time-lapse of a MEF cell spreading on 10 μm

fibronectin strips. The position of the strips is shown by the yellow overlay that was added in

Adobe Photoshop. **a)** A MEF cell was attached on a patterned fibronectin surface for 10

minutes. **b)** Filopodia makes contact with BSA surface within the gaps of the pattern (**solid

arrows**) but did not produce persistent protrusions, like those seen on the fibronectin strips

(**hollow arrows**) after 15 minutes. **c)** and **d)** Filopodia continues to make contact with BSA

(**solid arrows**) but did not produce protrusions. However, protrusion continues on fibronectin strips (**hollow arrows**) after 24 minutes and 30 minutes.

MEF cells spreading behaviour on the smaller patterned surface (2.5 μm wide fibronectin strips and 0.5 μm wide BSA gap) is identical to the spreading behaviour on a non-patterned fibronectin surface as shown in **figure 3.15**. The lack of selectivity of the MEF cells on the smaller patterned surfaces is possibly due to the reduced BSA gap size, therefore, MEF cells can effortlessly locate an adhesion point on the fibronectin regions of the surface.

3.3.3.4 The role of Arp2/3 complex

To explore the role of Arp2/3 complex in the adhesion of filopodia to the surface, a micropatterned surface containing both adhesive (fibronectin) and non-adhesive (BSA) areas as shown previously in **sections 3.3.3.1 and section 3.3.3.2** was fabricated. This micropatterned surface had the advantage of activating outside-in signalling pathways while enabling study of the cell interaction with non-adhesive areas. MEF cells were able to spread on 10 μm strip as shown in **section 3.3.3.2**.

Cells spreading on these patterned surfaces frequently protrude filopodia into the non-adhesive areas as shown in **figure 3.17**. Vinculin was absent from areas of filopodia that were extended over non-adhesive areas, whereas Arp2/3 complex was often present (**figure 3.18**). Therefore, we can conclude that the localisation of Arp2/3 complex on filopodia is independent of local adhesion to a fibronectin surface.

Figure 3.18 Arp2/3 complex localisation to filopodia is independent of adhesion.

a) filopodia (actin filament shown in red) of MEF cell spread on 5 μm fibronectin stripes for 60 minutes. Arp2/3 complex (green dot) is present on BSA stripes (black area) as well as on the Cy3 fibronectin (blue strip). Left and middle panel scale bar is 10 μm, right panel is 5 μm. **b)** MEF cell spread on 10 μm fibronectin strip for 60 minutes. Scale bar is 10 μm. **c)** Enlargement and deconvolution of boxed area in B. Scale bar is 10 μm. Filopodia forms an adhesion point to the neighbouring fibronectin strip; there is a bright response for vinculin (red circle). However, the Arp2/3 complexes do not show localise response signal on where the adhesion occurs (green circle).

3.4 Conclusion

Fibronectin patterned substrates have been used in the study of cell migration. Using microcontact printing, fibronectin was initially patterned onto the octadecyltrimethoxysilane self-assembled monolayers on glass substrates. However, it was found that these surfaces were inadequate for the formation of high quality patterns. Therefore, new surfaces were investigated using poly(dimethoxysilane) coated glass substrates. The patterns on these substrates were shown to be densely packed, with well defined edges. BSA was used to backfill the fibronectin gaps in order to prevent the non-specific binding of MEF cells to the surface. Filopodia produced by MEF cells interacted with the fibronectin strips in order to guide the lamellipodia protrusions. However, filopodia that made contact with the BSA surface showed no adhesion. The results have also established that vinculin is involved in the adhesion of filopodia on patterned fibronectin surfaces, whereas, the localisation of Arp2/3 complexes is absent at the adhesion site on the fibronectin surface Hence, this result suggests that the localisation of Arp2/3 complex in filopodia is independent to the adhesion of filopodia to a fibronectin surface.

Chapter 4

Tuning specific biomolecular interactions using switchable biological surfaces

Chapter 4 is based upon an article entitled:

Abstract: *The ability to regulate biomolecular interactions on surfaces driven by external stimuli has great practical impact in the biomedical and biotechnology fields. This chapter describes the fabrication of responsive surfaces that rely on electro-switchable peptides to control biomolecular interactions on gold surfaces. This system is based upon the conformational switching of positively charged oligolysine peptides that are tethered to a gold surface, such that bioactive molecular moieties (biotin) incorporated on the oligolysines can be reversibly exposed (bio-active state) or concealed (bio-inactive state) on demand, as a function of surface potential. It is shown that the surface can be switched with over 90% efficiency by applying a negative potential on the surface. The surface has also shown reversible switching properties when a combination of negative and open circuit conditions are applied.*

4.0 Background

Biological surfaces in which the biomolecules "statically" interact with the external environment have been explored over the past few years[3] and have provided, for instance, important new insights into how cells probe their surroundings.[4, 14, 15] Whereas important progress on static biological surfaces has been made in the past, much research is now focusing on the development of dynamic or switchable biological surfaces.[23, 251] Such dynamic surfaces can be tremendously useful in diverse biological and medical applications, including biofouling,[252] chromatography,[162] drug delivery,[253] cell culture[254] and tissue engineering.[155] This field is in its infancy and early examples of switchable biological surfaces include surfaces that switch between bio-inert and bio-active states, under an external thermal-,[255] photo-,[149] chemical/biochemical-[256] or electrical-[179] induced stimulus, to trigger capture or release of biological entities such as DNA,[257] proteins,[8] antibodies,[17] enzymes,[34] and cells.[35] However, existing switchable surfaces rely mostly on non-specific interactions (*i.e.*, hydrophobic/hydrophilic and electrostatic) of the biomolecules with the active surface,[179] thus, lacking bio-specificity and selectivity, and substantially limiting the potential applications of such surface systems. There are relatively few reported examples in which specific biomolecular interactions have been dynamically controlled in response to applied stimuli.[149, 255, 256, 258, 259] RGD-functionalized surfaces have been successfully used to control cell adhesion properties upon application of a biochemical,[256] thermal,[255] and optical[149, 258] stimuli. In another example, a thermo-responsive oligo(ethylene glycol) derivative has been exploited to control the affinity between surface-tethered biotin groups and streptavidin.[259]

4.0.1 The Binding of neutravidin to biotin

The high affinity of avidin for biotin was first exploited in histochemical applications in the 1970's.[260, 261] This egg-white protein (avidin) and its bacterial counterpart, streptavidin, have since become standard reagents for diverse detection schemes.[65]

Avidin (pI of 10.5) is a glycosylated tetrameric protein of 4 x 126 amino acid residues.[262] Avidin can non-covalently bind up to four molecules of biotin. The avidin-biotin interaction with a dissociation constant (K_d) of 10^{-15} M is the strongest known biochemical non-covalent bond.[263] For model recognition systems, streptavidin is more often used than avidin. Streptavidin with an isoelectric point (pI) of 5, is a tetrameric protein, obtained from *Streptomyces avidinii*, and consists of four identical chains of 159 amino acid residues.[264] In streptavidin, most of the amino acids are neutral or acidic. The binding properties of streptavidin are comparable with avidin in which 4 biotin binding sites are also available. Two binding sites are on each of the two opposing faces of the molecule, and also have a high binding constant of 10^{-13} M. Neutravidin (pI of 6.3) is a deglycosylated version of avidin. This version of avidin reduces the non-specific protein adsorption on the surface, simultaneously, retaining its biotin binding properties ($K_d \sim 10^{-15}$ M).

The high binding affinity and the four biotin binding sites serve as an aid in amplifying the sensitivity of immunoassays, which have become a useful tool in the field of biology. When biotin is bound to avidin, it is buried inside a *β*-barrel central pocket. The deepest end of the pocket contains hydrogen bond donor/acceptor residues (Asn 12, Ser 16, Tyr 33, Thr 35, Asn 118), which recognize the polar head of the biotin ureido ring. In the deep end of the binding pocket, the ureido ring is hydrogen bonded (Asn 12 nD2, Ser 16 OG, Tyr 33 OH, Thr 35 OG1

and Asn 118 OD1) *via* the ureido carbonyl O and N atoms as shown in **figure 4.1**.[265] In the absence of biotin, the binding pockets appear to contain molecules of water. Overall, the binding of biotin to tetrameric avidin seems to be mediated by the extensive network of hydrogen bonds and Van der Waals forces in the binding pocket, leading to an association process which is practically irreversible.
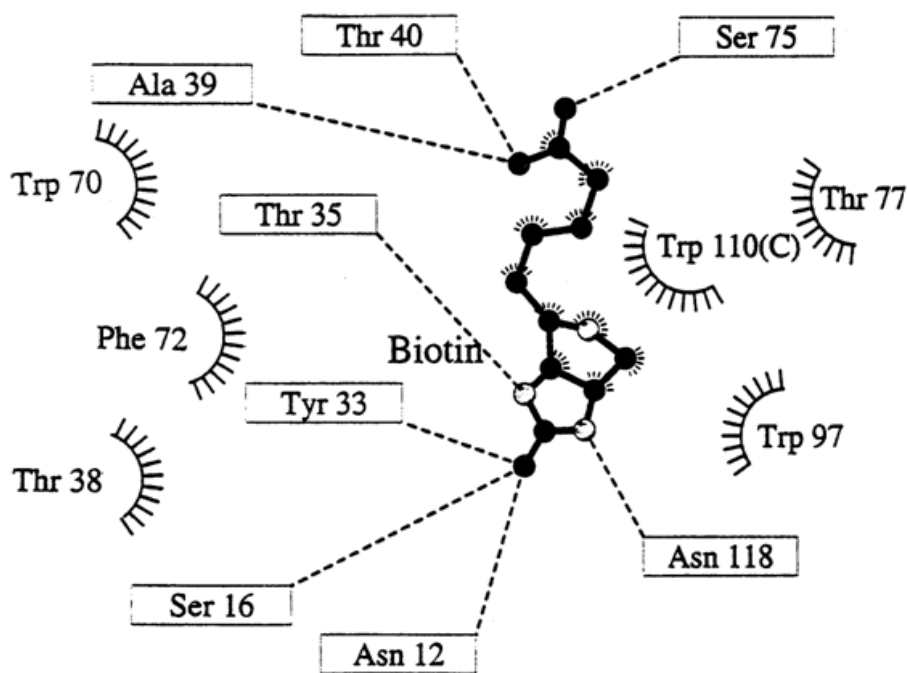
Figure 4.1 A schematic view of biotin recognition residue in the *β*-barrel central pocket of avidin.[265]

4.1 Aim

One of the major challenges in the field of switchable biological surfaces today is the design of new versatile surfaces with tunable biospecific interactions and this chapter reports significant advances towards such surfaces. The aim of this chapter is to develop a new class of responsive surfaces that rely on electro-switchable peptides to control biomolecular interactions on gold surfaces. This system is based upon the conformational switching of positively charged oligolysine peptides biotin-Lys-Lys-Lys-Lys-Cys (**biotin-KKKKC**) that

are tethered to a gold surface together with a bioinert spacer group, triethylene glycol thiol (**TEGT**), to create low density peptides mixed SAMs (**process 1**, **figure 4.2**). The bioactive moiety (biotin) incorporated on the oligolysines can be concealed (**bio-inactive state**) by applying a negative potential to the surface (**process 2**, **figure 4.2**), or exposed (**bio-active state**) by applying a positive potential (**process 3**, **figure 4.2**). The dynamic of switching the biological properties is studied by observing the binding events between the biotin and fluorescently labelled **neutravidin** (**process 2 and 3**, **figure 4.2**) using fluorescence microscopy and surface plasmon resonance.
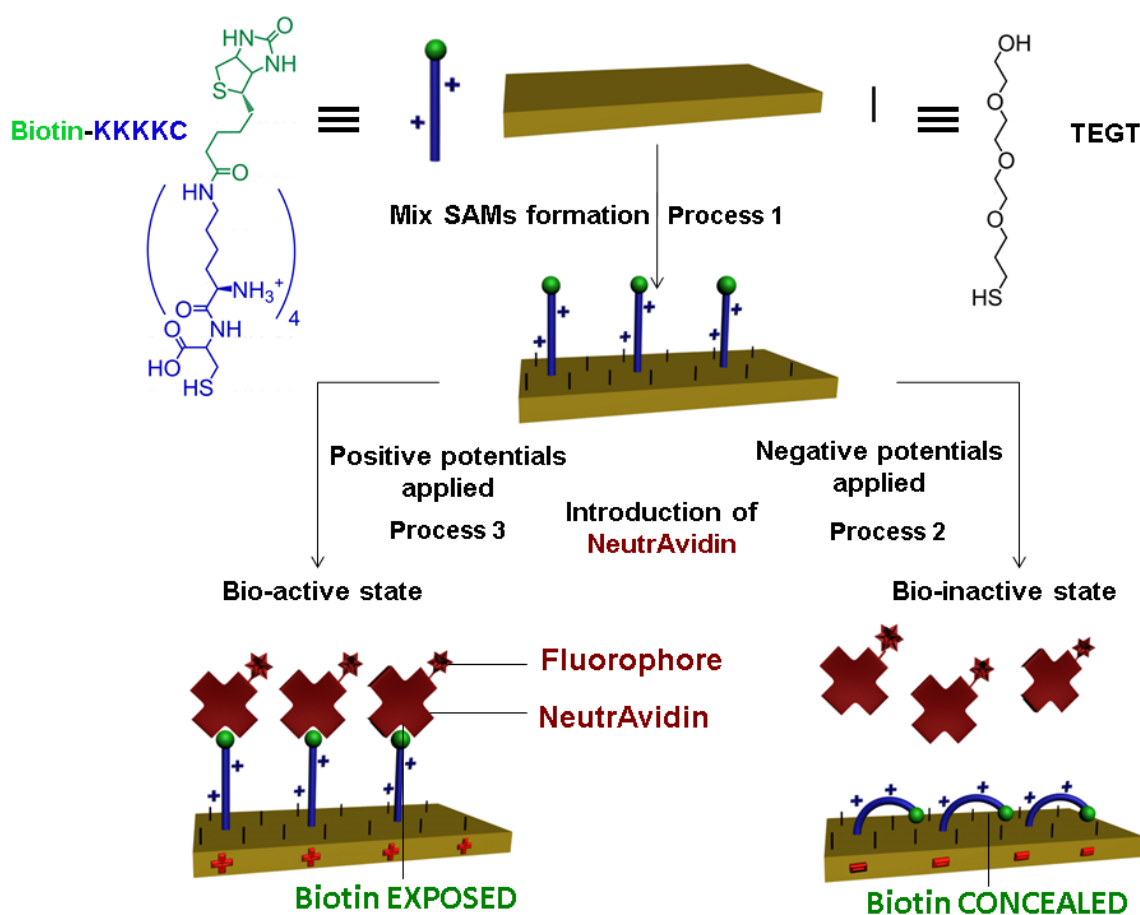
Figure 4.2 Schematic representation of the attachment of neutravidin on electro-switchable oligopeptide surfaces, characterised by fluorescence microscopy and surface plasmon resonance.

4.2 Objectives

1) Fabrication of low density peptides mixed self-assembled monolayers formed from biotin-KKKKC and TEGT to ensure sufficient spacing around biotin-KKKKC to enable neutravidin binding and switching capability.

2) Examine the stability of the mixed self-assembled monolayers surfaces when electrical potentials from - 0.6 V to + 0.9 V are applied on the surfaces.

3) Examine the switching properties of the mixed self-assembled monolayers surfaces by monitoring the interaction between the biotinylated surface and fluorescently labelled neutravidin when electrical potentials are applied.

4) Determine whether the mixed self-assembled monolayers can be reversibly switched, by modulation of the surface potential.

Objective 1: Mixed SAMs formation

The fabrication of switchable surfaces requires generating mixed SAMs of oligopeptide (**Biotin-KKKKC**) and the spacer group, tri(ethylene glycol) thiols (**TEGT**) on the gold surface (**Figure 4.3**). **TEGT** provides the spacing required to ensure that the oligolysine peptide can undergo conformational changes upon the application of electrical potentials.
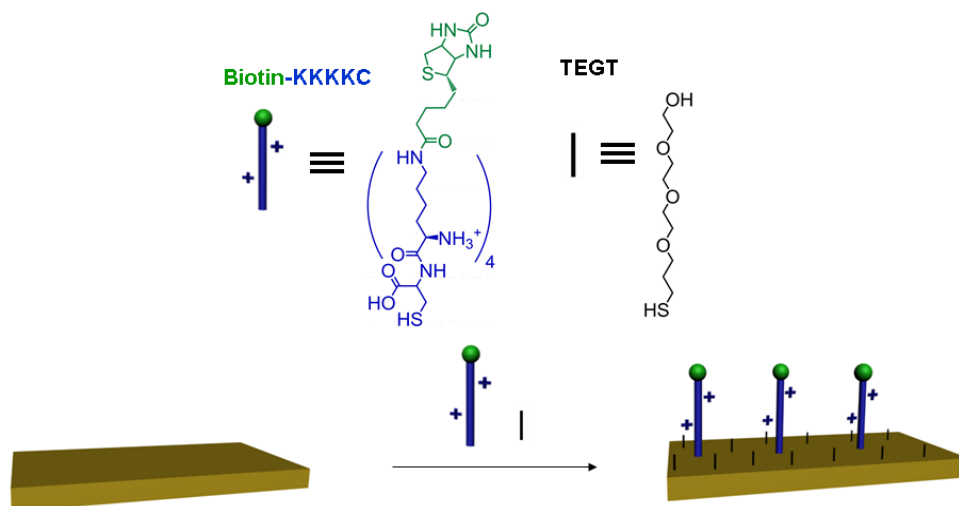
Figure 4.3 Schematic representation of mixed **Biotin**-**KKKKC**:**TEGT** SAMs formation.

Objective 2: Stability studies of the mixed SAMs

Prior to the switching studies, the stability of the mixed SAMs to surface electrical potentials needs to be assessed in order to obtain a working potential range to carry out the switching studies. **Figure 4.4** shows schematically the experimental set up to achieve this objective.
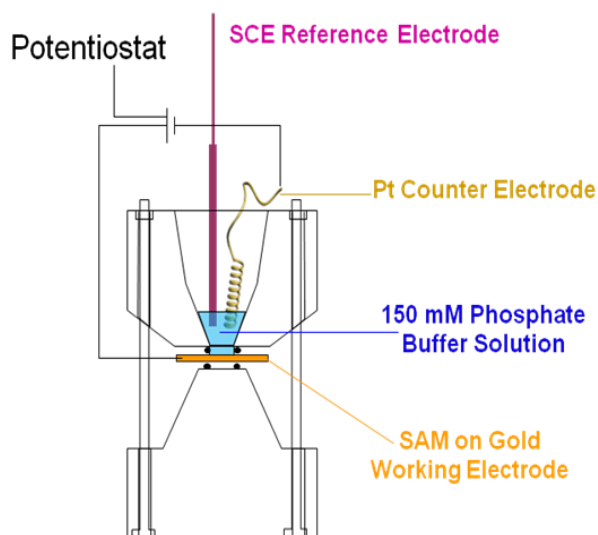
Figure 4.4 A schematic representation of the stability experimental set-up using a custom design Teflon cell.

Objective 3: Switching studies of mixed SAMs using fluorescence microscopy and surface plasmon resonance (SPR)

The switching studies adopt the same experimental set up as shown in **figure 4.4**. Upon the application of a positive potential on the mixed **biotin-KKKKC** and **TEGT** surface, the **biotin** group is exposed on the surface, resulting in the binding of fluorescently labelled **neutravidin**, (bio-active state). On the other hand, for the bio-inactive state, the application of a negative potential conceals the **biotin** group, reducing the binding moieties available on the surface.

Objective 4: Reversible switching studies of the mixed SAMs using SPR

The bio-activity of the mixed SAMs can, in principle, be reversibly controlled by switching the applied potentials on the surface from negative to open circuit conditions. This process can be observed by monitoring the binding activity of **neutravidin** onto the biotinylated surface using SPR (**figure 4.5**).

The mixed SAMs surface was first exposed to an external potential of - 0.4 V, resulting in the biotin moieties being concealed from the neutravidin solution. This lack of available binding group (**biotin**) will lead to the minimal binding of neutravidin on the surface. Upon the release of the negative potential (from - 0.4 V to open circuit), it is predicted that the biotin moieties will expose to the neutravidin solution, therefore, increasing the amount of neutravidin that binds onto the mixed SAMs surface.
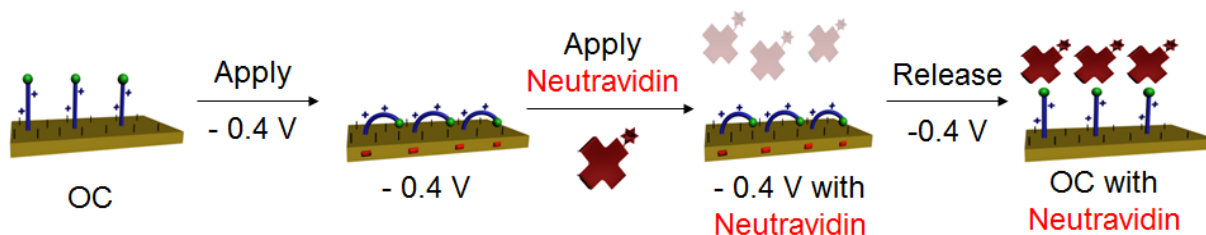
Figure 4.5 A cartoon representation showing the reversibility of biotin-KKKKC:TEGT mixed SAMs surface under OC conditions and applied potential of - 0.4 V.

4.3 Results and discussion

4.3.1 Mixed biotin-KKKKC:TEGT SAMs formation

Gold surfaces were functionalized with a two-component, mixed SAM of the biotin-KKKKC peptide and TEGT as shown in **figure 4.3**. Apart from ensuring sufficient spatial freedom for molecular orientation of the surface bound biotinylated peptide, the short oligo(ethylene glycol) groups prevent nonspecific interaction from the proteins.[266] In order to obtain a theoretical estimate of the surface ratio of biotin-KKKKC peptide and TEGT that would provide sufficient conformational mobility (**figure 4.2**) of the peptide on the surface, some assumptions and calculations were made. If we assume that the peptide first adopts and then bends in a fully extended conformation on the surface as shown in **figure 4.6**, the maximum possible molecular area that each peptide can occupy in the bent state is approximately 1.5 nm^2 (**figure 4.6**). The calculated area is based on the exposed section of the peptide with the exposed length of 3.1 nm and width of 0.5 nm (measurements obtained with Chem Draw 3D software). The area 1.5 nm^2 is the minimum and ideal area required for each peptide in the bent state. However, all calculated areas are estimated and the orientation of the peptide has not been considered. Hence, the area required for the peptide at the bent state has been doubled to 3 nm^2 to ensure sufficient spacing between peptides for conformational changes.

Assuming that each TEGT thiol molecule has a foot print area of 0.214 nm^{2},[267] a ratio of about 1 biotin-KKKKC peptide per 14 TEGT molecules needs to be achieved on the surface to provide sufficient conformational freedom for the bending. As reported in the literature,[59] the ratio of two components in solution are rarely identical from that in the SAM, due to the preferential adsorption of one of the components. Hence, surface characterisation techniques such as X-ray photoelectron spectroscopy (XPS), ellipsometry and contact angle goniometry were employed to determine the surface coverage of the mixed self-assembled monolayers.
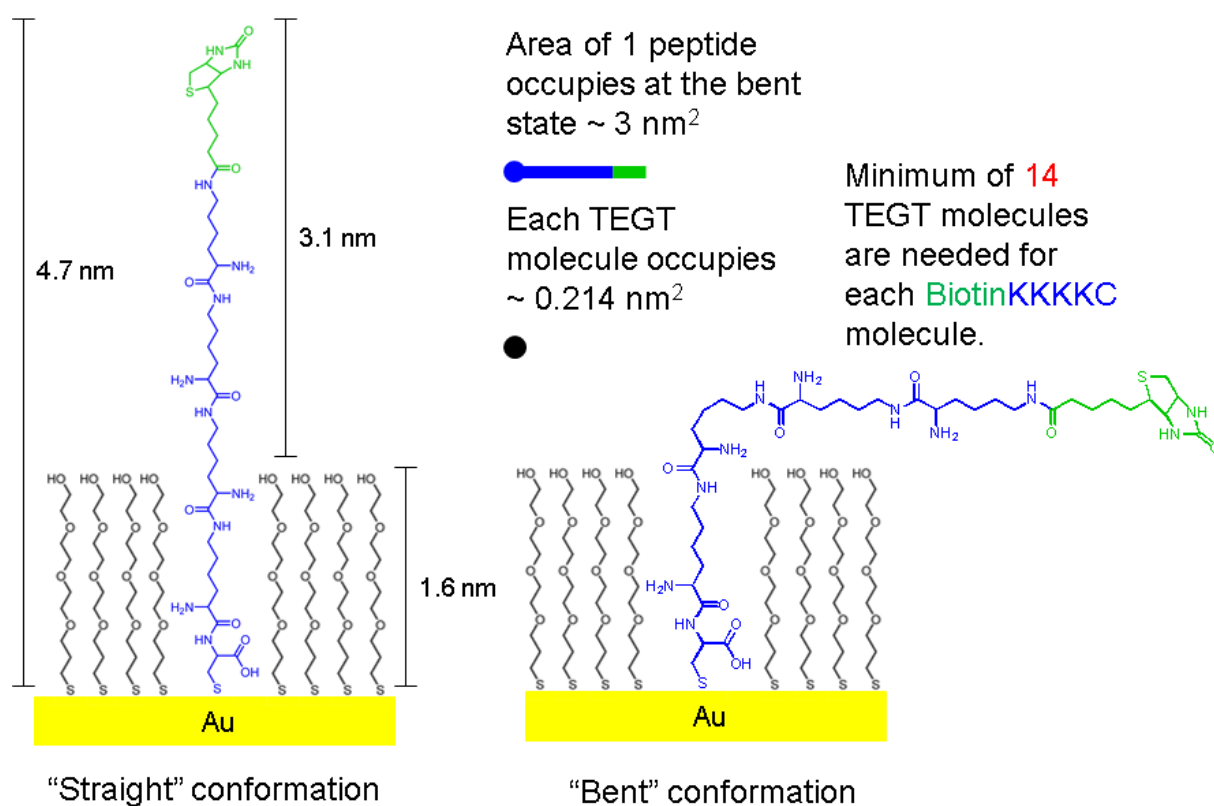
Figure 4.6 Schematic representation of the area occupied by a peptide in the bent state. The maximum molecular area was calculated based on the length of the exposed part of the peptide on the mixed SAM. The calculated fully extended molecular length of the peptide and TEGT are 4.7 nm and 1.6 nm, respectively, obtained with Chem Draw 3D.

4.3.1.1 XPS data analysis of mixed SAMs on gold substrates

In order to understand how the ratios in solution diverge from the ratios in the SAM, a systematic study was carried out using different solution concentration ratios of biotin-KKKKC and TEGT.

The mixed SAMs were formed by the immersion of the piranha cleaned gold substrates into in a mixed solution of the **biotin-KKKKC** (0.1 mM) and **TEGT** (0.1 mM) (HPLC EtOH containing 3% $N(CH_2CH_3)_3$) at separate volume ratios of 1:1, 1:5, 1:10, 1:20, 1:40, 1:50, 1:100, 1:500 for 12 hrs to ensure full SAM formation. The presence of $N(CH_2CH_3)_3$ prevents the formation of hydrogen bonds between the NH_2 functional groups of the bound thiolate peptide on the surface and the free thiol peptide in the bulk solution.[268] The mixed SAMs were subsequently rinsed by ethanolic solution containing ethanoic acid to rinse away any $N(CH_2CH_3)_3$ on the surface. The substrates were further rinsed with HPLC grade ethanol and dried under a constant stream of argon gas (full experimental procedures can be found in **section 5.4.2.2**). The prepared substrates were then characterised and analysed by XPS.

XPS confirmed the formation of pure and mixed SAMs, showing the signals from C(1s), O(1s), N (1s) and S(2p). High-resolution scans of the N (1s) region (**figure 4.7)** revealed nitrogen on the pure biotin-KKKKC SAMs and biotin-KKKKC:TEGT mixed SAMs, whereas, no N (1s) peak was observed in the pure TEGT SAM as expected. Deconvolution of the N (1s) XPS spectra of the pure biotin-KKKKC SAMs and biotin-KKKKC:TEGT mixed SAMs revealed two peaks, which support the presence of the peptide on the gold surface. The first peak, centered at 400.2 eV, is characteristic of amino (NH_2) and amide (CONH) moieties, whilst the second peak, centered at 402.0 eV, is attributed to the ammonium groups[269] of the

lysine (isoelectric point $= 9.7^{270}$). As the solution ratio of biotin-KKKKC:TEGT decreases, the N (1s) signal decrease, indicative of lower amount of surface bound peptide (**figure 4.7**).
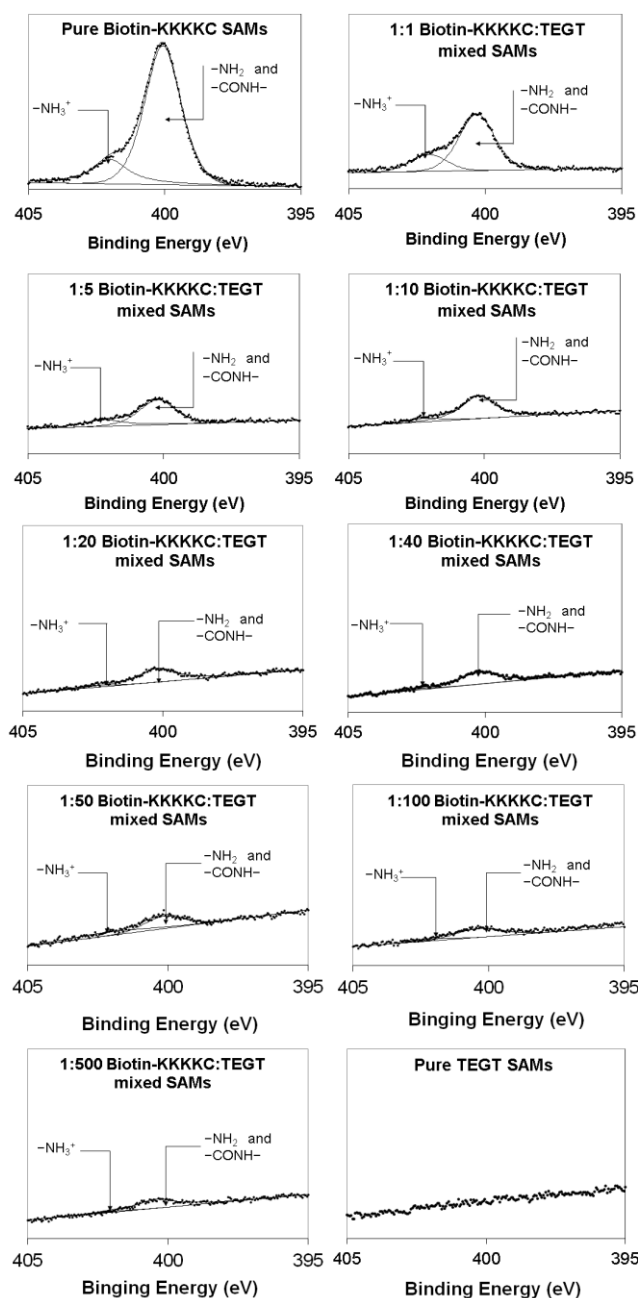
Figure 4.7 XPS spectra of the N (1s) peak regions of pure biotin-KKKKC SAMs, pure TEGT SAMs and mixed SAMs of different solution volume ratios of biotin-KKKKC and TEGT - 1:1, 1:5, 1:10, 1:20, 1:40, 1:50, 1:100 and 1:500. All graphs are displayed with the same y-scale for comparison purposes.

By integrating the area of the S (2p) and N (1s) peaks for the mixed monolayers (obtained by XPS), we were able to calculate the ratio of biotin-KKKKC to TEGT on the surface. The ratio calculation is based on the number of N and S atoms on each of the surfactants (biotin-KKKKC peptide consists of 11N and 2S, whilst TEGT has no N and 1S (**figure 4.6**)). If the N:S area ratio on the surface is 1:1, that means there are 11N and 11S present on the surface. Given that each peptide consists of 11N and 2S, which means the extra S present on the surface must be derived from TEGT. Using the number of N and S atoms for a 1:1 biotin-KKKKC:TEGT surface (N:S ratio of 11:3), we can construct a formula to determine the number of TEGT molecules per peptide on the surface (**formula 4.1**).

$$\text{Number of TEGT} = (11 \times \text{S area/N area})-2) \qquad \textbf{formula 4.1}$$

In order to validate that **formula 4.1** is accurate, we use the N:S area ratio of 11:3 and have determined the number of TEGT molecule per biotin-KKKKC peptide on the surface to be 1. To further verify this formula, more N:S ratios were tested. By substituting the N:S ratio of 1:1, 1:2, and 1:5 into **formula 4.1**, we deduce there are 9, 20 and 53 TEGT molecules per biotin-KKKKC peptide on the surface respectively. The integrated area of N, S and Au signal for each solution ratio of the mixed SAMs and the conversion of N:S area ratio to surface ratio are summarised in **table 6.1 and 6.2**. (**Appendix 1**).

Using surface ratios from appendix 1, we were able to establish the ratio of biotin-KKKKC to TEGT on the surface as a function of solution ratio and plotted it in **Figure 4.8**. For each solution volume ratio of biotin-KKKKC and TEGT, three independent samples were analyzed by XPS. Mixed SAMs prepared from solution ratios of 1:500, 1:100, 1:50, 1:40, 1:20, 1:10,

1:5, 1:1 of biotin-KKKKC:TEGT yielded an average N:S XPS ratio of 0.28, 0.41, 0.85, 0.71, 0.97, 1.38, 1.95, 2.56, respectively, which leads to surface ratios of biotin-KKKKC:TEGT SAMs of 1:38 ± 6, 1:22 ± 8, 1:11 ± 3, 1:16 ± 3, 1:13 ± 4, 1:5 ± 2, 1:6 ± 2, and 1:3 ± 2 respectively as shown in **figure 4.8** (full set of XPS data of different solution ratios is attached in **appendix 1**). As observed from **figure 4.8**, there is an inverse exponential relationship between the number of TEGT on the surface and the solution ratio. As the solution ratio of biotin-KKKKC:TEGT changes from 1:500 to 1:1, the number of TEGT molecules present on the surface decreases.
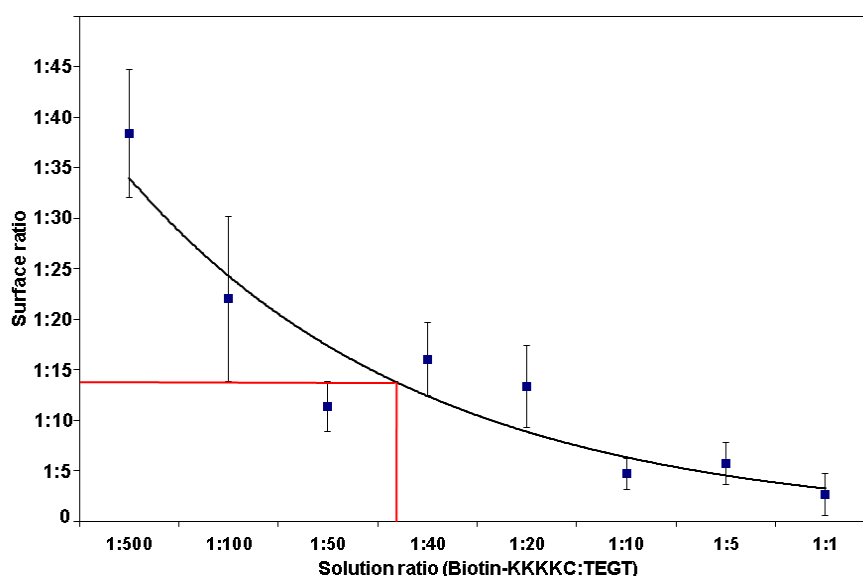
Figure 4.8 A graph to show the number of TEGT molecules per biotin-KKKKC peptide on surface at different solution ratios based on the XPS N:S area ratio.

The XPS data show that a mixed SAM solution ratio of ~1:40 is needed to achieve a minimum surface ratio of 1:14 as shown by the red line in **figure 4.8**. XPS data confirms that mixed SAMs solution ratio of 1:40 provides a surface ratio of 1 peptide to 16 TEGT molecules. Therefore, this solution ratio of 1:40 is employed as the optimum solution ratio for mixed SAMs formation.

4.3.1.2 Mixed SAMs thickness by ellipsometry

Ellipsometric thickness measurements of pure TEGT SAMs (1.09 nm ± 0.28 nm), pure biotin-KKKKC SAMs (2.55 nm ± 0.25 nm) and mixed biotin-KKKKC:TEGT SAMs at solution ratio of 1:500, 1:100, 1:50, 1:40, 1:20, 1:10, 1:5, 1:1 are plotted in **figure 4.9**. The observed thicknesses of pure TEGT SAMs and pure biotin-KKKKC SAMs are lowered than the theoretical thickness of 1.6 nm and 4.7 nm. The thicknesses of all mixed SAMs within experimental error are ~ 1.1 nm.

One might have expected the thickness to have increased as the amount of biotin-KKKKC increased; however, our results have demonstrated that the amount of biotin-KKKKC on the surface has no significant effect on the thickness measured. The reason for this lack of SAM thickness with increasing biotin-KKKKC content is possibly due to the significant amount of "bent" peptide on the surface, even at 1:1 solution ratios which translate to a ~ 1:3 surface ratio. This bending will mean the peptide is not at its fully stretched conformation until it is in a solution conditions. Hence, we would not expect the pure TEGT and pure biotin-KKKKC SAMs thickness be the same as the theoretical thickness in dry/air conditions of the ellipsometry.
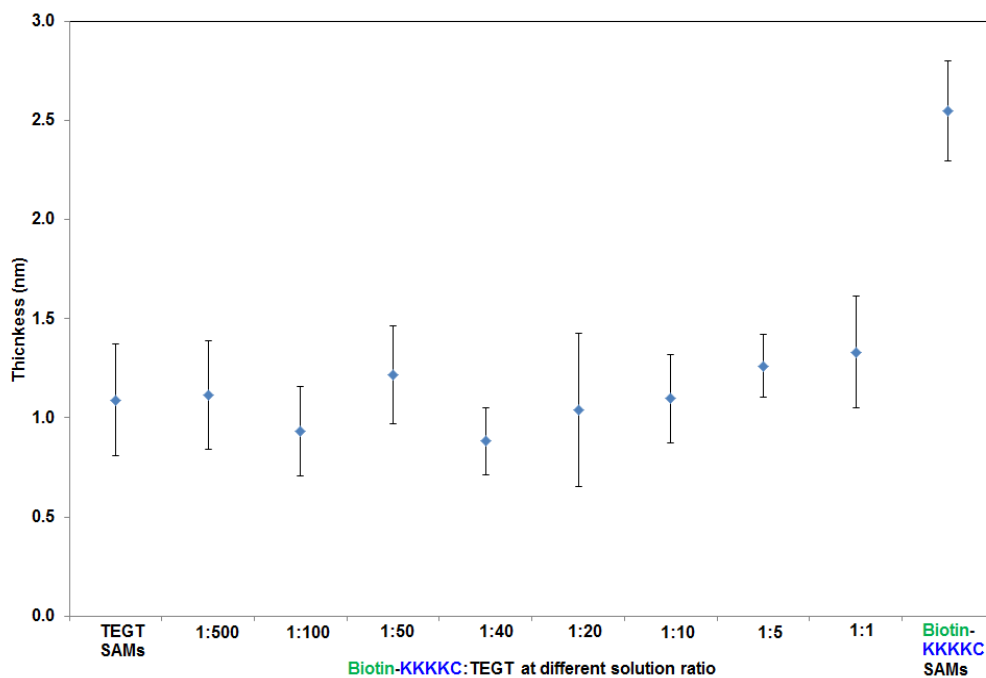
Figure 4.9 A graph to show the thickness of pure TEGT SAMs and the thickness of the mixed biotin-KKKKC:TEGT monolayers at different solution ratios.

4.3.1.2.1 Evidence for the 1:40 ratio being optimised

To probe the relationship between biotin-KKKKC:TEGT ratio and the degree of binding of streptavidin to the surface, various mixed SAMS were immersed in streptavidin solution (37 µg ml^{-1}) for 30 minutes, rinsed with PBS solution and dried under argon gas and analysed by ellipsometry. **Figure 4.10** compares the thickness measurements of the mixed SAMs surface as shown in **figure 4.9** and the thickness of the mixed SAMs surface after incubation with streptavidin.

A positive correlation exist between the surface thickness and the solution ratio of biotin-KKKKC:TEGT on the streptavidin treated surfaces. Whereas, the surface thickness of the mixed biotin-KKKKC:TEGT SAMs at different solution ratio are very similar. As the solution ratio increases from 1:500 to 1:10, there is an increase in the surface thickness when

the SAMs have been incubated with the streptavidin. The thickness data plateau at a solution ratio of ~1:40 with the surface thickness of 7.4 nm ± 1.4 nm. This result suggests a full saturation of streptavidin binding occurred at the solution ratio of 1:40, which was calculated to give the optimum surface ratio of 1:16.

Given that the diameter of streptavidin is approximately 4 nm,[271] and the chain length of each biotin-KKKKC peptide is 4.7 nm. The surface thickness of streptavidin adhered onto the mixed SAMs at solution ratio of 1:40 is 7.4 nm ± 1.4 nm, which agrees with the calculated thickness of streptavidin attached to the peptide. Thus, ellipsometry results may suggest that the solution ratio of 1:40 is the optimum ratio for an efficient binding of streptavidin.

However, the large error that was observed at the solution ratio of 1:50 might indicate agglomeration of streptavidin on some mixed SAMs surface as discussed in **chapter 3**, hence, a large variation of surface thickness was measured. Due to the possibility of agglomeration on the surface, data observed in **figure 4.10** should only be employed as indicative data to determine the surface biotin-KKKKC coverage.
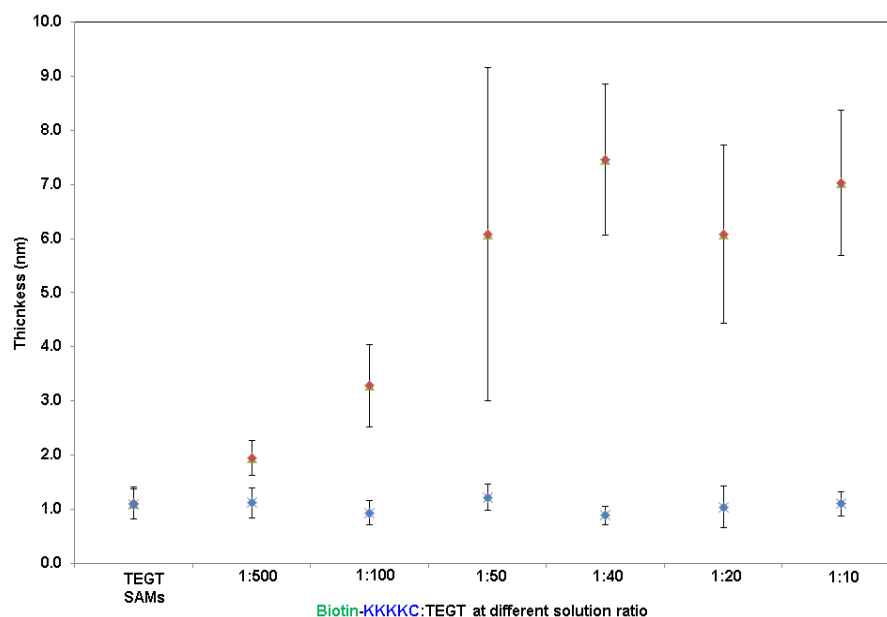
Figure 4.10 A graph to show the thickness of the mixed biotin-KKKKC:TEGT monolayers at different solution ratios after the incubation with streptavidin (brown data points) compared with the thickness of pure TEGT and mixed biotin-KKKKC:TEGT monolayers at different solution ratios (blue data points). Ellipsometry measurements were conducted by Ian Williams and Alice Pranzetti (project students) under my supervision.

4.3.1.3 Dynamic contact angle (θ) analysis of the 1:40 mixed SAMs on gold substrates

The mixed SAMs are formed by the immersion of the piranha cleaned gold substrates into biotin-KKKKC and TEGT solution (various concentration ratios) for 12 hours. Substrates were then characterised by contact angle goniometry.

The contact angle measurements of the biotin-KKKKC:TEGT mixed SAMs at different solution ratios are plotted in **figure 4.11**. The advancing contact angle of 1:500 mixed SAMs surface is $38^{o} \pm 3^{o}$, which is higher than the advancing contact angle of TEGT ($33^{o} \pm 1^{o}$). The

slight increase in contact angle indicated the presence of biotin-KKKKC on the surface. As the solution ratio and the number of the biotin-KKKKC present on the surface increases, the advancing contact angle of different mixed SAMs ratios remained very similar as shown by the overlaps of the contact angle on various substrates. Therefore, the contact angle data has concluded that the wettability remains constant even though the solution ratio increases from 1:500 to 1:1. Mixed SAMs formed from a solution ratio of 1:40 were further investigated as XPS and ellipsometry data suggested this is the optimum ratio for mixed SAMs formation.

Upon the mixed biotin-KKKKC:TEGT (1:40) SAMs formation, the substrate's advancing contact angles increased from $25^o \pm 6^o$ to $37^o \pm 4^o$ (**figure 4.11**). The water contact angle for a full biotinylated surface is $42^o \pm 2^o$, which agrees with a previous report of 42°.[272] The water contact angle for a full TEGT SAMs surface is $33^o \pm 1^o$, which agrees with a previous report of 32°.[273] The contact angle of our biotin-KKKKC:TEGT mixed SAMs at the solution ratio of 1:40 has not been previously reported and the angle that we obtained is in between the contact angle range of a biotinylated surface (42°) and the TEGT surface (32°). Given that we have observed a change of contact angles on the surface, we can assume that our surface contains both the biotin-KKKKC oligopeptide and TEGT, in agreement with XPS data (**section 4.3.1.1**) and ellipsometry measurements (**section 4.3.1.2**).
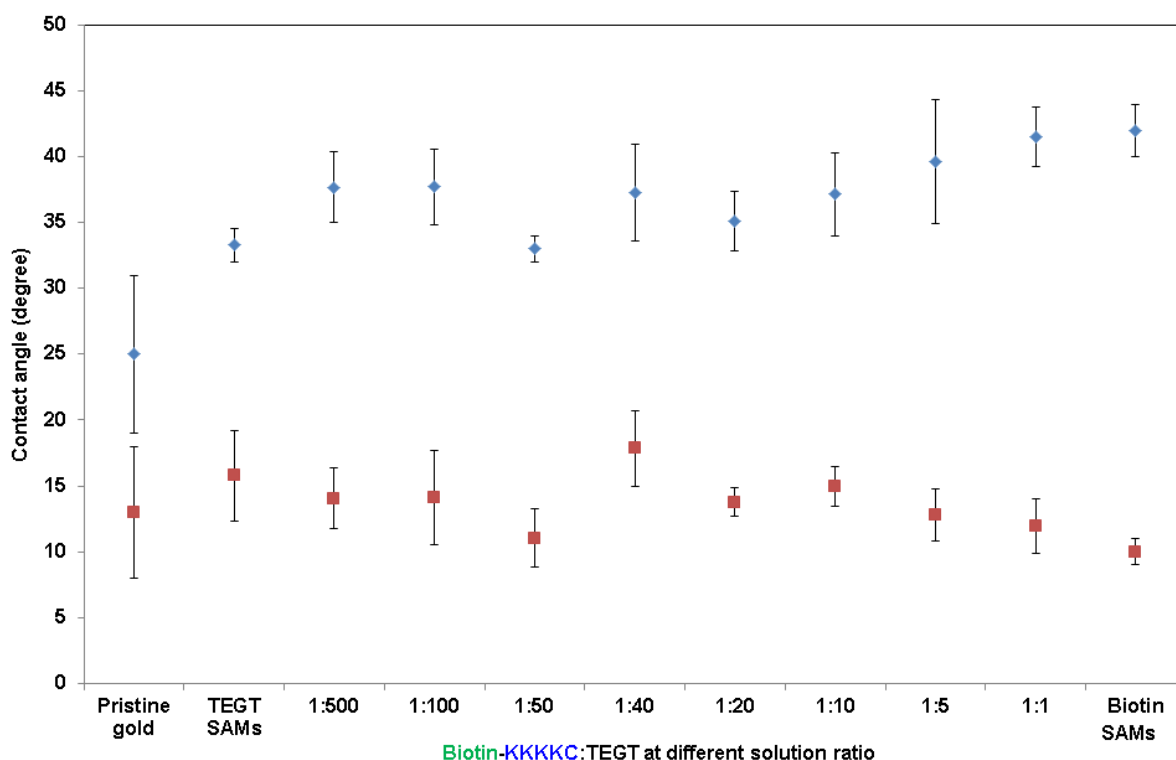
Figure 4.11 A graph to show the advancing contact angle (**blue** data point) and receding contact angle (**red** data point) of pure TEGT SAMs, pure biotin-KKKKC SAMs and the mixed biotin-KKKKC:TEGT monolayers at different solution ratios.

4.3.1.4 Summing up of SAM characterisation

The surface characterisation (XPS, ellipsometry and contact angle) results have proved that the solution ratio of 1:40 is the optimum solution ratio to provide sufficient spacing between each oligopeptide (biotin-KKKKC) in order to perform conformational changes (switching) on the surface. This solution ratio of 1:40 provides the surface ratio of 1:16, which is the minimum surface ratio required for the switching to occur. We next need to address is the stability of the mixed biotin-KKKKC:TEGT (solution ratio of 1:40) SAMs surfaces under various electrical potentials.

4.3.2 Stability of biotin-KKKKC:TEGT mixed SAMs (solution ratio of 1:40) under electrical potentials (-0.6 V to 0.9 V)

Information regarding the prospective range of surface potentials for switching was obtained by carrying out potential and time-dependent electrochemical stability experiments. The stability experiments use a potentiostat with a custom designed Teflon cell, equipped with the mixed SAMs gold substrates as the working electrode. A platinum wire was used as the counter electrode, a SCE as the reference electrode and PBS as the electrolyte (**figure 4.4**). Electrical potentials of − 0.6 V, - 0.3 V, - 0.1 V, open circuit (OC) (no potential applied), + 0.1 V, + 0.3 V, + 0.6 V, + 0.8 V and + 0.9 V were applied on the mixed biotin-KKKKC:TEGT (1:40) SAMs in PBS solution for 30 minutes prior to surface analysis by XPS and CV.

4.3.2.1 XPS analysis of the surfaces subjected to electrical potentials

The chemical state of the sulfur atom was probed using the XPS spectra of the S 2p emission (binding energy range of 160 eV to 170 eV) (**figure 4.12**). The XPS S area ($2p_{3/2}$ and S $2p_{1/2}$ doublets) were fitted with a fixed binding energy difference of 1.18 eV and an intensity ratio of 2:1, which reflected the multiplicity of these energy levels ($2p_{3/2}$ and S $2p_{1/2}$). The S $2p_{3/2}$ binding energy of sulfur is 163.9 eV, and the S $2p_{3/2}$ binding energy for sulfoxide species formed by oxidation of sulfur in air is about 167.7 eV.[274] No signals from oxidized sulphur species could be observed in all spectra as shown in **Figure 4.12** suggesting that the biotin-KKKKC:TEGT mixed SAMs are well formed on the surface.
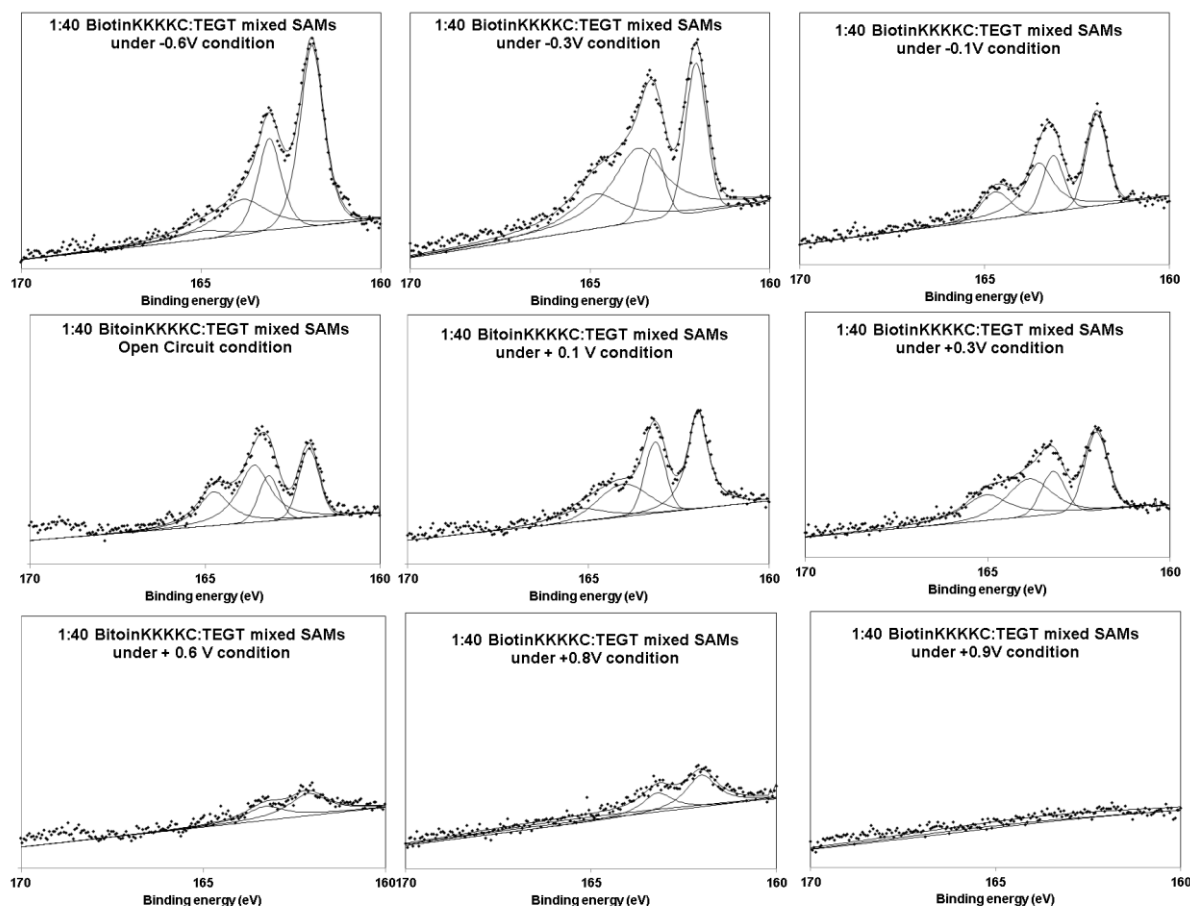
Figure 4.12 XPS spectra of the S (2p) peak regions of 1:40 biotin-KKKKC:TEGT SAMs at various electrical potentials of - 0.6 V, - 0.3 V, - 0.1 V, OC, + 0.1 V, + 0.3 V, + 0.6 V, + 0.8 V and + 0.9 V. All graphs are displayed with the same y-scale for comparison purposes.

Deconvolution of the S (2p) XPS spectra of the biotin-KKKKC:TEGT mixed SAMs revealed the area of S element peak under various electrical potentials (**figure 4.13**). The area at - 0.6 V and - 0.3 V has a sulphur/gold (S/Au) ratio of ~ 0.04 (red dash line, **figure 4.13**). The area at - 0.1 V, OC, + 0.1 V, and + 0.3 V has observed the S/Au ratio ranges between 0.02 and 0.03 (blue dash line, **figure 4.13**). Whereas, the application of + 0.6 V, + 0.8 V and + 0.9 V, the (S/Au) ratios has reduced to 0.01, 0.01 and 0 respectively (black dash line, **figure 4.13**). These S (2p) ratios under various electrical potentials indicate that the monolayer is stable

from - 0.6 V to + 0.3 V. The loss of S/Au ratios at potential greater than + 0.3 V suggests thiol based SAMs start to desorb and the monolayer has completely desorbs at + 0.9 V when the S/Au ratio drops to 0 (**figure 4.13**). These stability results under similar surface potentials agree with finding suggested by Reinhoudt *et al.*[275] and Lahann *et al.*[179]
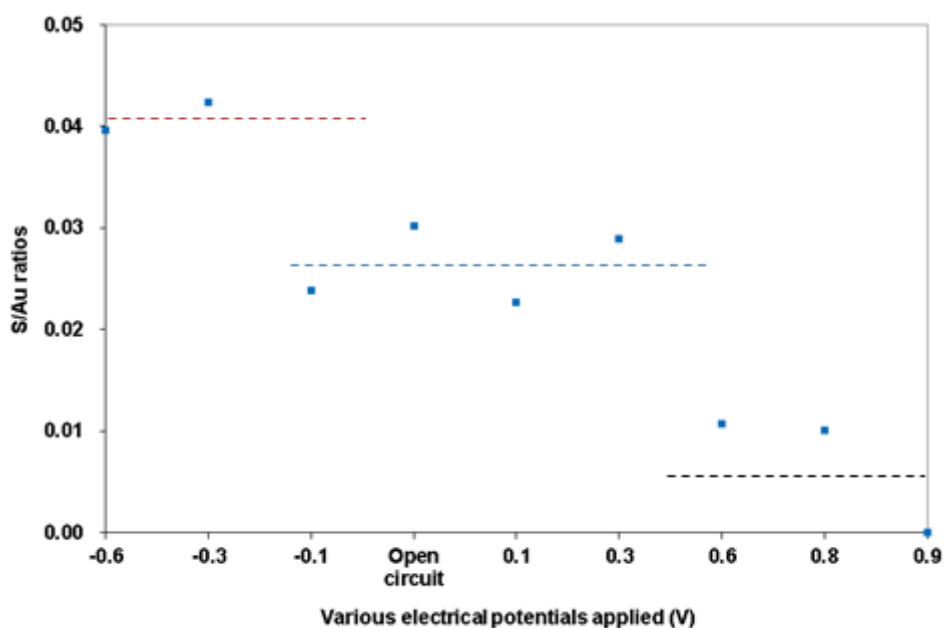
Figure 4.13 A graph to show the S/Au ratios of the biotin-KKKKC:TEGT (1:40) mixed SAMs under various electrical potentials. Due to the limitation of XPS availability, only 1 set of data was obtained for each electrical potential examined.

Figure 4.13 has demonstrated that biotin-KKKKC:TEGT (1:40) mixed SAMs on gold substrate (purchased from George Albert PVD) are stable from the range of − 0.6 V to + 0.3 V. However, when − 0.5 V was applied on the gold surface employed in the surface plasmon resonance (SPR gold) (purchased from Reichert technologies), we observed gold desorption from the glass substrate. A possible reason for such desorption occurring on the SPR gold layer is due to the thinner of chromium (Cr) adhesion layer underneath the gold (1 nm), in comparison with the gold surface employed in XPS (i.e. Cr layer of 5 nm). The decrease of

the Cr adhesive layer reduces the stability of gold layer leading to desorption on surface when – 0.5 V applies. Therefore, the negative surface potential employed to study the mixed SAMs stability was reduced from – 0.5 V to - 0.4 V where the gold layer did not desorb from the SPR gold.

4.3.2.2 Stability studies using cyclic voltammetry (CV)

Figure 4.14 shows the CV results for the pristine mixed SAMs (surfaces under OC conditions) and mixed SAMs after being conditioned in PBS at +0.3 V and - 0.4 V for 30 min. Pristine mixed SAMs exhibit three cathodic peaks at - 0.92 V, - 1.10 V, and - 1.21 V, which are associated with the reductive desorption of a thiol SAM from a polycrystalline gold surface.[276] The integration of the reductive desorption peaks has previously been used to quantify the surface coverage of SAMs, and reported as an evaluation tool for their potential and time dependent stability.[277] In other words, instability of SAMs for a given potential and time can be detected by a loss of the surface confined molecules, and thus a decrease in the reductive desorption peaks upon CV characterization. Consequently, in our studies the stability of the mixed SAMs can be monitored by comparing the intensity of the reductive desorption peaks of the mixed SAMs after being conditioned in PBS, at + 0.3 V and - 0.4 V for 30 min, to that of pristine mixed SAMs. The integration of the reductive desorption current of the pristine mixed SAMs gave a charge density of 230 ± 82 μCcm^{-2}. Similar reductive charges (within the error) were found for the reductive desorption of mixed SAMs after being conditioned in PBS at + 0.3 V (259 ± 76 μCcm^{-2}) and - 0.4 V (300 ± 92 μCcm^{-2}) for 30 min.
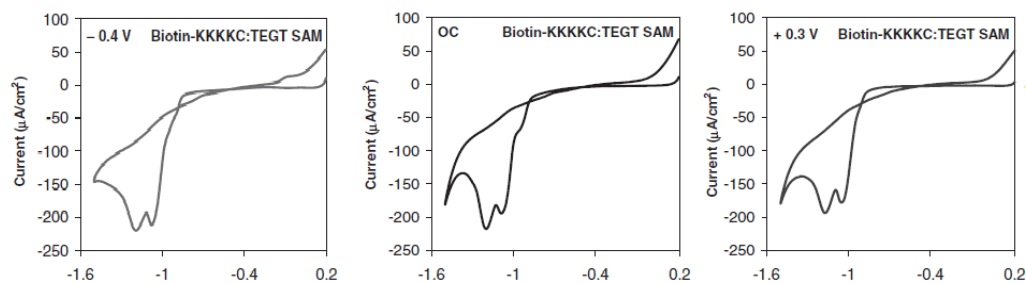
Figure 4.14 Cyclic voltammograms of pristine biotin-KKKKC:TEGT mixed SAMs at solution ratio of 1:40, biotin-KKKKC:TEGT mixed SAMs at a solution ratio of 1:40 after being conditioned in PBS at + 0.3 V and − 0.4 V for 30 min.

The CV and XPS results indicate that the surface confined molecules on the mixed SAMs have remained intact after being conditioned in PBS at + 0.3 V and - 0.4 V, and thus these surface potential were used as limiting conditions in the switching experiments.

4.3.3 The binding of neutravidin on switchable biotinylated surfaces

The dynamic of switching biological properties was first studied by observing the binding events between biotin and fluorescently labelled (alexa fluoro 488) streptavidin. The fluorescence images collected for pristine gold substrate and the streptavidin coated biotinylated surface showed very little contrast in terms of emitted wavelength. Both surfaces provide green images as shown in **figure 4.15**. The aggregation of streptavidin on the biotinylated surface is shown by the brighter green regions. The stronger fluorescence signal is due to the presence of higher fluorophore concentration. The aggregation of streptavidin on the surface may be caused by inter- and intra- molecular conformation rearrangement on the surface as suggested by Sethuraman *et al.*[278] Moreover, streptavidin has a pI of 5, which means at a physiological pH of 7.2, the streptavidin is negatively charged. Since the switching

study requires the application of an electrical potential on the surface, the charged streptavidin does not provide a suitable analyte for the switching studies proposed.
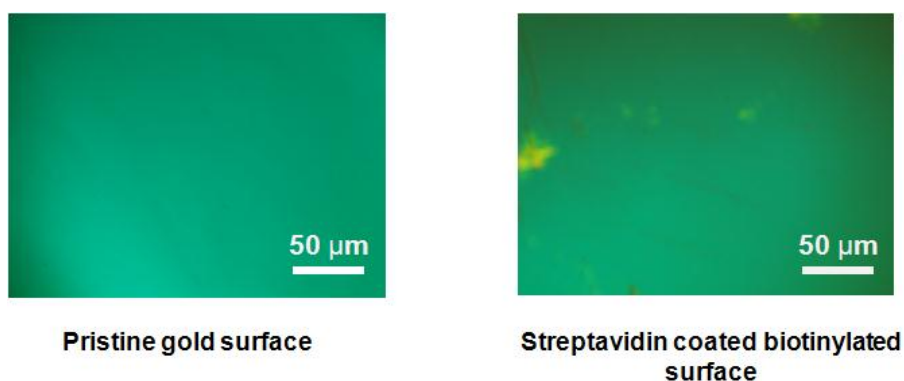
Figure 4.15 Fluorescence images of pristine gold surface and streptavidin coated biotinylated surface.

Therefore, we selected another fluorescently labelled (Alexa fluor 568) neutravidin, which has a pI of 6.3, and thus at a physiological pH of 7.2, the protein is almost neutral. The fluorophore (Alexa fluor 568) is red fluorophore and emits at a wavelength of 603 nm.

4.3.3.1 Switching studies of biotin-KKKKC:TEGT mixed SAMs (solution ratio of 1:40) surfaces, characterized using fluorescence microscopy

The binding of neutravidin to the biotin-KKKKC:TEGT mixed SAMs (solution ratio of 1:40) was performed in PBS at positive potential of + 0.3 V, negative potential of - 0.4 V and OC conditions (**figure 4.16**). The experiment employs the same set-up as shown in **figure 4.4**, where the mixed SAMs were exposed to the surface potential for 10 minutes prior to the introduction of fluorescently labelled neutravidin. Upon the introduction of neutravidin, surface potentials are maintained for a further 30 minutes to enable binding of neutravidin to the surface. The surfaces were rinsed with PBS solution for 10 minutes to remove any non-

specific binding of neutravidin on the surfaces. Neutravidin binding activity, as a result of the switching induced by potential stimulus, was monitored by fluorescence microscopy.

High fluorescence intensities were observed for an applied positive potential (+ 0.3 V) with the mean pixel intensity (MPI) of 81 (**figure 4.16a**) and at OC conditions with a MPI of 56 (**figure 4.16b**). Upon the application of negative potential (- 0.4 V), the MPI dropped to 27 (**figure 4.16c**). The MPI intensity difference from - 0.4 V to + 0.3 V demonstrate that biomolecular interactions on surfaces can potentially be controlled by electro-switchable oligopeptide SAMs.
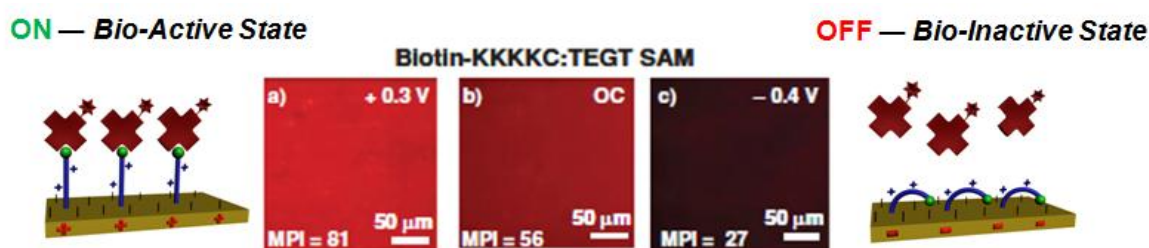
Figure 4.16 Fluorescence images of biotin-KKKKC:TEGT mixed SAMs treated with Alexa Fluor 568 neutravidin while applying **a)** + 0.3 V **b)** OC conditions and **c)** - 0.4 V.

However, the surface potential may be directing the assembly of the neutravidin on the surface. Thus, a control experiment was performed in which the biotin moiety was deleted. This control experiment involved forming a two-component SAM from TEGT and a peptide without the biotin moiety – KKKKC (**figure 4.17**) in a solution ratio of 1:40. Thus, no binding of neutravidin is expected at + 0.3 V, OC condition or - 0.4 V if the biotin and not the surface potential is responsible for the surface binding. An XPS spectrum for the control sample (KKKKC:TEGT SAMs) under open circuit conditions is attached in **appendix 2**, showing the control sample has similar S (2p) surface environment as the biotin-KKKKC:TEGT mixed SAMs surface. The two different sulfur environments deduced from

the XPS data suggested there are some unbound thiols present on the mixed biotin-KKKKC:TEGT SAMs and KKKKC:TEGT SAMs surface.

Figure 4.17 Schematic and cartoon representation of control mixed SAMs consisting of

KKKKC and TEGT

Control samples with a KKKKC:TEGT mixed SAM at a solution ratio of 1:40 exhibited reduced and similar fluorescence values for + 0.3 V (MPI of 15) (**figure 4.18a**), OC conditions (MPI of 21) (**figure 4.18b**) and - 0.4 V (MPI of 22) (**figure 4.18c**). These fluorescence results indicate that the binding which occurred on the biotin-KKKKC:TEGT SAMs was a result of the biotin non-covalently binding with the neutravidin, rather than non-specific binding on the mixed SAMs surface, medicated through surface potential.

Figure 4.18 Fluorescence images of KKKKC:TEGT mixed SAMs treated with Alexa Fluor 568 neutravidin while applying **a)** + 0.3 V **b)** OC conditions and **c)** - 0.4 V.

4.3.3.2 Switching studies of biotin-KKKKC:TEGT mixed SAMs surfaces using electrochemical SPR

SPR results provided further evidence that neutravidin binding to the surface was controlled by the applied potential. The SPR experiment employs a similar set-up as shown in **figure 4.4**. All electrodes employed in SPR experiment including the reference electrode, counter electrode and working electrodes are specifically designed to be used in conjunction with the SPR electrochemical cell.

A mixed biotin-KKKKC:TEGT SAM at a solution ratio of 1:40 was formed on a Reichert gold substrate. The treated gold substrate was employed as the working electrode to examine the switching properties. The surface was first conditioned for 10 mins in degassed PBS solution at + 0.3 V, - 0.4 V and OC conditions. Using degassed PBS as the electrolyte, neutravidin was introduced into the cell while applying electrical potentials of + 0.3 V, - 0.4 V and OC conditions. Neutravidin was introduced to the electrochemical cell, allowing incubation for 30 minutes as labelled on the graph (neutravidin, **figure 4.19**). Following the incubation, the surface was washed with degassed PBS solution for 20 minutes to remove any non-specifically adsorbed neutravidin as labelled on the graph (PBS Wash, **figure 4.19**).

An SPR response of 2180 response units (**black solid line**, **figure 4.19**) (*i.e.* ~ 2.18 ng mm^{-2})[279, 280] was observed under OC conditions, showing that the mixed SAMs have a good binding affinity to neutravidin. However, the binding affinity was found to be tunable by changing the applied voltage as shown in **figure 4.19**. A positive potential of + 0.3 V caused the SPR response to increase to 3520 response units (**blue solid line**, **figure 4.19**) (*i.e.* ~ 3.5 ng mm^{-2}), whereas a negative potential of - 0.4 V induced a large reduction in binding affinity, with the SPR response decreasing to 290 response units (**red solid line**, **figure 4.19**) (*i.e.* ~ 0.3 ng mm^{-2}). Thus, depending on the electrical potential applied to the mixed SAMs, bioactive molecules incorporated onto the SAM can be exposed for binding (+ 0.3 V, bio-active state) or concealed (- 0.4 V, bio-inactive state) to the extent that the binding affinity can be reduced to over 90% of its bio-active state from + 0.3 V condition.

To verify that the changes in binding upon application of a positive or negative surface potential occurs due to changes in the conformational orientation of the biotin instead of protein adsorption due to electrostatic interactions via the surface potential, **control** samples with a KKKKC:TEGT mixed SAM at a solution ratio of 1:40 (**dash lines, figure 4.19**) and a pure TEGT SAM (**appendix 3**) were analyzed by SPR.

Figure 4.19 demonstrates that the amount of neutravidin that adsorbed non-specifically onto the KKKKC:TEGT mixed SAM surface under + 0.3 V (blue dash line), OC conditions (black dash line) and − 0.4 V (red dash line) were negligible. These SPR results prove that the binding occurred on the biotin-KKKKC:TEGT mixed SAMs was a result of biotin non-covalently bonded with the neutravidin under various electrical potentials, rather than non-specific binding on the mixed SAMs surface.

Control SPR experiments were performed using pure TEGT SAMs (**appendix 3**), revealing that TEGT SAMs adsorb insignificant amounts of proteins under + 0.3 V (blue dash line), OC conditions (black dash line) and - 0.4 V (red dash line). These results are in agreement with previous SPR studies on SAMs terminated with tri(ethylene glycol) groups.[64] The proposed switching mechanism is thus supported by systematic control experiments.
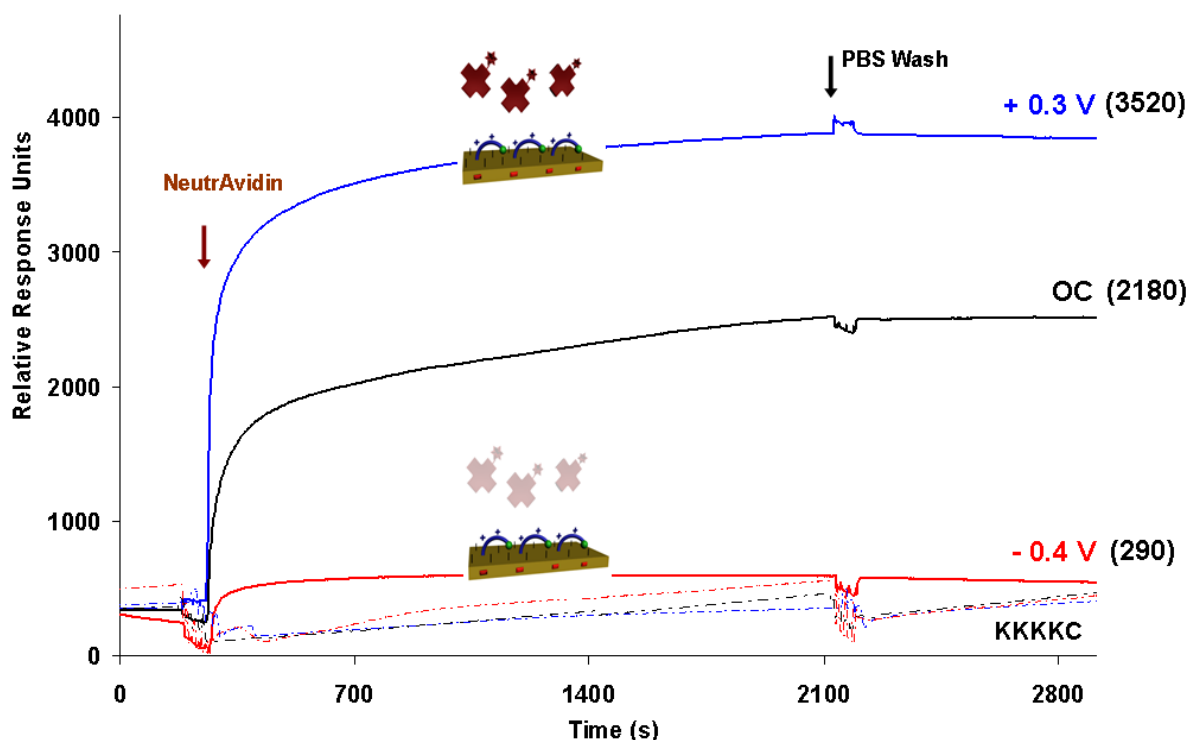
Figure 4.19 SPR sensorgram traces showing the binding of neutravidin (37 µgml^{-1}) to the biotinKKKKC:TEGT mixed SAMs at a solution ratio of 1:40 (solid line) and KKKKC:TEGT mixed SAMs at a solution ratio of 1:40 (dash line) under + 0.3 V (**blue** line), OC conditions (**black** line) and an -0.4 V (**red** line). After neutravidin binding for 30 mins, the surfaces were washed with PBS for 20 mins to remove any non-specifically adsorbed neutravidin.

A further experiment has been conducted to study the switching properties of the biotinKKKKC:TEGT mixed SAMs (solution ratio of 1:40) under a potential of - 0.3 V and -

0.4 V as illustrated in **figure 4.20**. A negative potential of - 0.3 V caused the SPR response to decrease to 1506 response units (*i.e.* ~ 1.5 ng mm^{-2}) comparing with the response unit at OC condition of 2180 (*i.e.* ~ 2.18 ng mm^{-2}), a decrease of 31 % response unit. Whereas, the application of - 0.4 V has further decreased the response unit to 290 (*i.e.* ~ 0.3 ng mm^{-2}), a decrease of 86 %. **Figure 4.20** has demonstrated that the switching ability of the biotinKKKKC:TEGT mixed SAMs is different at different electrical potentials. Hence, this may suggest the switching ability of the mixed SAMs can be regulated by varying the potential applied on the surface.
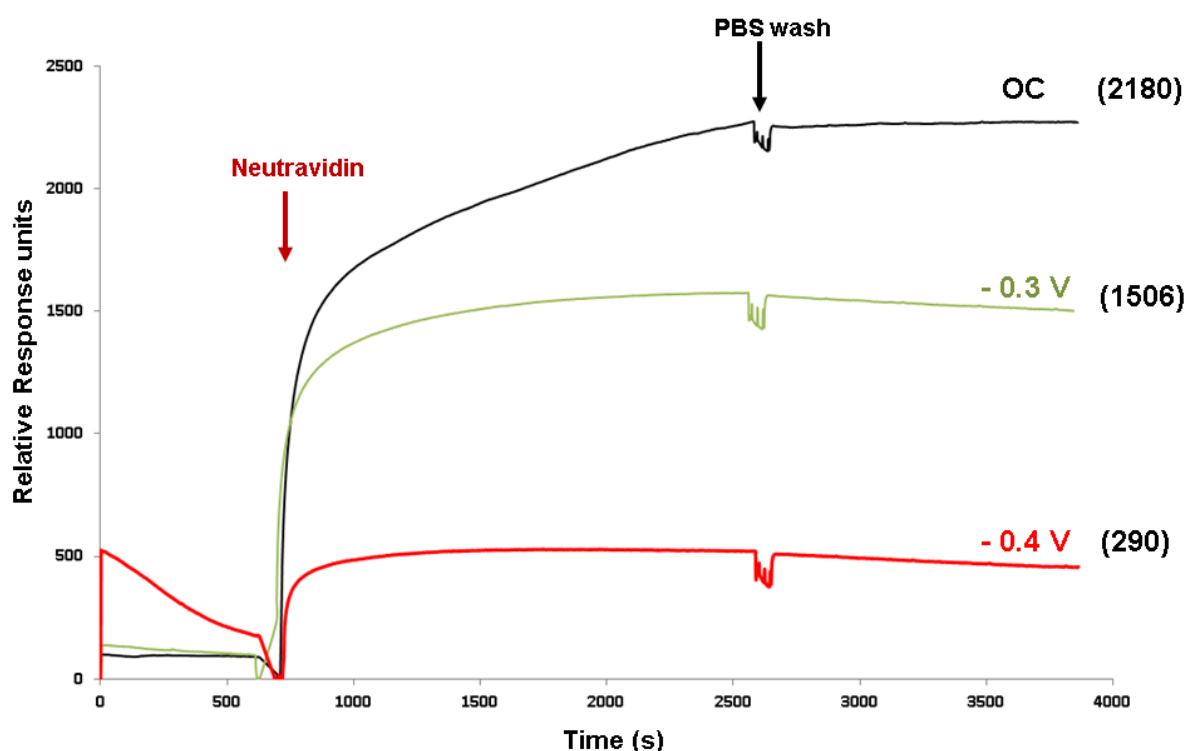
Figure 4.20 SPR sensorgram traces showing the binding of neutravidin (37 µgml^{-1}) to the biotinKKKKC:TEGT mixed SAMs at a solution ratio of 1:40 under OC conditions (**black** line), - 0.3 V (**green** line), and an - 0.4 V (**red** line). After neutravidin binding for 30 mins, the surfaces were washed with PBS for 20 mins to remove any non-specifically adsorbed neutravidin.

4.3.3.3 Reversible switching studies of biotin-KKKKC:TEGT mixed SAMs surfaces using electrochemical SPR

The question of whether the switchable surfaces undergo reversible dynamic conformational changes induced by a surface potential, such that the bioactive biotin moieties incorporated on the oligolysines can be reversibly exposed (bio-active state) or concealed (bio-inactive state) on demand, as shown in **figure 4.5**, was addressed.

A switching cycle between a bio-active state and bio-inactive state was monitored by SPR (**figure 4.21**), by first flowing PBS over the biotin-KKKKC:TEGT mixed SAMs under OC conditions, then exposing the biotin-KKKKC:TEGT mixed SAMs to - 0.4 V and to a neutravidin solution. The process was followed by a release of the electrical potential and then a return to OC conditions while the neutravidin solution was still passing through the system. As expected, when the surface is switched from being under OC conditions to being under a negative potential of -0.4 V (bio-inactive state) in neutravidin solution, minimal protein binding of ~ 300 response units (*i.e.* ~ 0.3 ng mm^{-2}) was observed. Returning the surface to a bio-active state (OC conditions) induces an immediate and large increase in neutravidin binding up to ~ 2500 response units (*i.e.* ~ 2.5 ng mm^{-2}). A control experiment involved employing KKKKC:TEGT mixed SAMs (solution ratio 1:40) to undergo the reversible switching study is shown as the red dash line (**figure 4.21**). In the absence of a biotin moiety on the surface, there is a very minimum amount of neutravidin non-specifically adsorbed on the surface. These results agree with previous data observed in **section 4.3.3.2** and have shown that the developed switchable surface allows reversible control of biomolecular interactions.
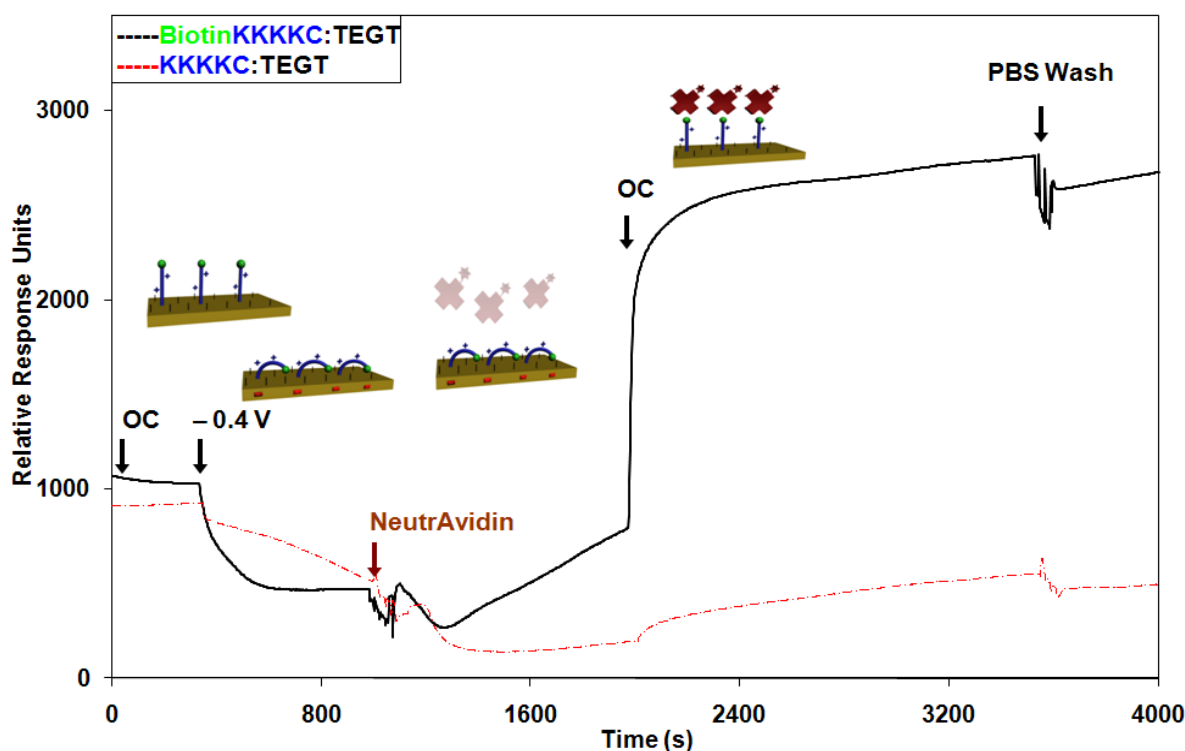
Figure 4.21 SPR sensorgram traces showing the response of a biotin-KKKKC:TEGT mixed SAM at a solution ratio 1:40 and KKKKC:TEGT mixed SAM at a solution ratio of 1:40 to successive OC conditions, -0.4 V for 10 min, neutravidin (37 μg ml^{-1}) for 15 min while still applying -0.4 V, OC for 25 min while the neutravidin solution was still passing through the system and PBS wash.

4.4 Conclusion

The optimum biotin-KKKKC:TEGT mixed SAM surface for creating a switchable biological surface has been determined using data from XPS, CV, ellipsometry, fluorescence microscopy and SPR.

XPS and ellipsometry data has identified that the solution ratio of 1:40 provides the optimum surface ratio of 1:16. This optimum surface ratio fulfilled the minimum surface ratio required

to provide enough spacing for an oligopeptide to induce conformational change upon the application of negative potentials.

The stability of the mixed SAMs surface, when electrical potentials were applied, was determined by XPS and CV studies. The XPS data has shown that a mixed SAMs surface is stable from - 0.6 V to + 0.3 V and CV data provided further stability data at the desired potentials of - 0.4 V and + 0.3 V.

The binding of biomolecules (neutravidin) on mixed SAMs surfaces under + 0.3 V, OC conditions and – 0.4 V were deduced by fluorescence microscopy and quantified by SPR. The fluorescence intensities changes from 81 to 27 when electrical potentials of + 0.3 V and - 0.4 V are applied on the surface. Similarly, the SPR response units have been reduced from 3520 to 290. These results demonstrated that biomolecular interactions on surfaces can be efficiently controlled by electro-switchable oligopeptide SAMs. Thus, depending on the electrical potential applied to the mixed SAMs, bioactive molecules (biotin) incorporated onto the SAM can be fully exposed for binding (+ 0.3 V, bio-active state) or concealed (- 0.4 V, bio-inactive state) to the extent that the binding affinity can be reduced to over 90% of its bio-active state. The SPR response unit (290 response units) observed when -0.4 V was applied on the surface may suggest some biotin moieties were still available for binding when negative potentials were applied as shown in **figure 4.22**. Further SPR experiments (**figure 4.20**) have shown the amount of switching on the biotin-KKKKC:TEGT mixed SAM can be controlled by varying the potential applied on the surface as seen by the response unit between -0.3 V (1506 response units) and -0.4 V (290 response units).

SPR has been employed to study the reversibility of the biotin-KKKKC:TEGT mixed SAM surface. The SPR sensorgram has proved that this mixed SAMs surface has the capability to reverse its bio-functionality when electrical potentials switch from a negative potential to OC conditions.

In summary, we have developed a novel switchable and reversible system for presenting biomolecules from a surface by applying an electrical potential. This technology takes advantage of the unique dynamic properties of surface-confined charged peptide linkers to induce On-Off switching of specific biomolecular interactions, setting the stage for advances in biological research, medicine, biotechnology, and bioengineering.[251]
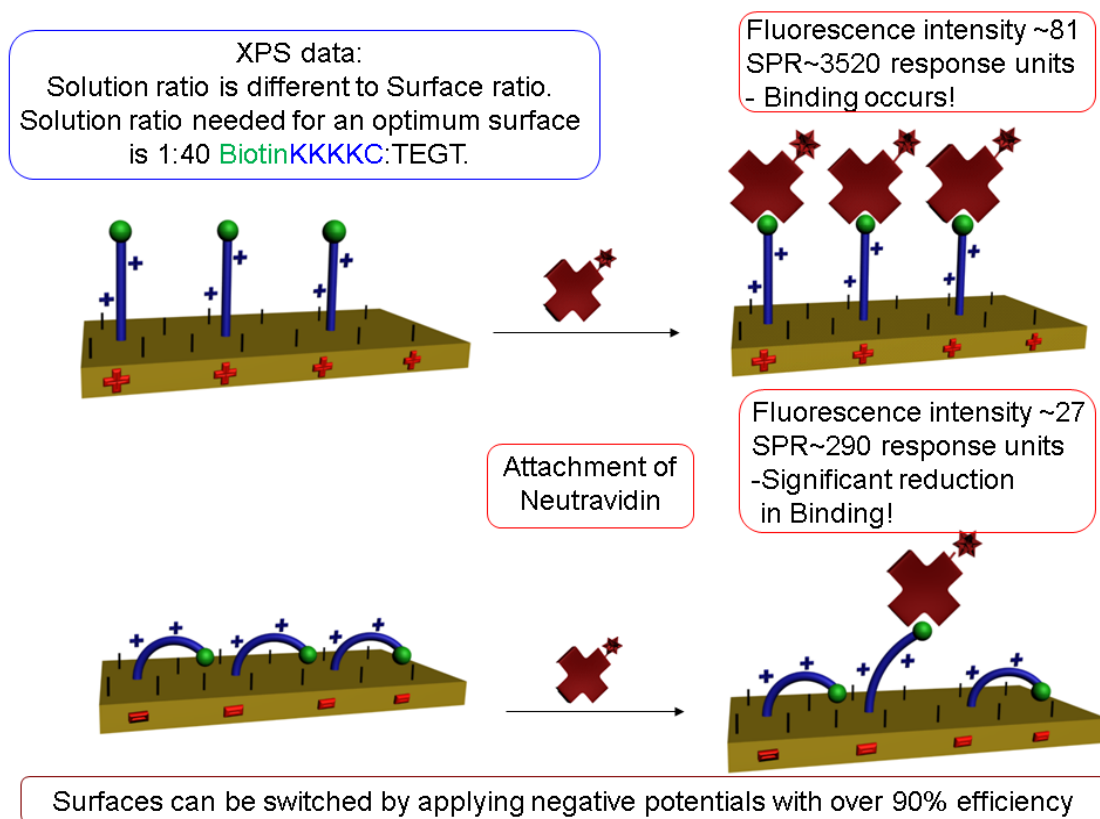
Figure 4.22 Cartoon representation of the overview of the switchable biological surfaces.

Chapter 5

Experimental procedures, protocols and synthesis

Abstract: *This chapter describes the experimental techniques used during the investigations performed throughout the work described in this thesis. Experimental protocols and data analysis by various equipments have been described.*

5.0 Experimental

5.1 Materials

Silicon wafer

Silicon wafers (Si/SiO$_2$) were purchased from Virginia Semiconductors Inc. and were of the type:

- <111> orientation

- Resistance of 1-10 Ω cm^{-1}

- 100 nm (+5%) thick oxide layer on both sides

- Polished on one side

Glass substrate

Glass cover slips were purchased from VWR international. www.uk.vwr.com and were the type:

- Borosilicate glass

- 22 x 32 mm

- Thickness: No.1

Gold substrates

Polycrystalline gold substrates were purchased from George Albert PVD, Germany and consisted of a 50 nm gold layer deposited onto glass covered with a thin layer (5 nm) of chromium as the adhesion layer. Polycrystalline gold substrates employed in SPR were purchased from Reichert Technologies, USA, consisted of 49 nm gold with 1 nm chromium.

Chemicals

Commercially available chemicals and solvents were purchased from Aldrich Chemicals and Fisher Chemicals and were used as received. UHQ (ultra high quality) H_2O (resistivity >18 Ω cm^{-1}, TOC reading of < 3 ppb) was purified by using a Millipore-Q Integral 5 water purification system Oligopeptides (Biotin-KKKKC and KKKKC) were synthesised by Peptide Protein Research Ltd. (Wickham, UK) to > 95 % purity and verified by HPLC and mass spectrometry. Neutravidin and Alexa Fluor 568 Protein Labelling Kit were purchased from Invitrogen. Phosphate buffered saline (PBS) solution was prepared from a 10× concentrate PBS solution (1.37 M sodium chloride, 0.027 M potassium chloride, and 0.119 M phosphate buffer) from Fisher BioReagents. Poly(dimethoxysiloxane) prepolymer and curing agent were purchased from Dow Corning. (Sylgard® 184 silicone elastomer kit).

Fluorescently labelled fibronectin was provided by Simon Johnston, School of Biosciences, University of Birmingham.[4]

Fluorescently labelled neutravidin was provided by Marzena Allen, School of Chemical Engineering, University of Birmingham as described in **section 5.5**.

TEGT was synthesised by Dr. Parvez Iqbal, School of Chemistry, University of Birmingham, through a multistep route (**figure 5.1**). The commercially available triethylene glycol was alkylated with allyl bromide at reflux in basic conditions to obtain **1 (figure 5.1)**. **1** was converted to **2 (Figure 5.1)** in the presence of thioacetic acid and AIBN heated at reflux for 1 hour(hr). Deprotection of **2** was performed in mild acidic conditions at reflux for 4 hrs to obtain **TEGT**.
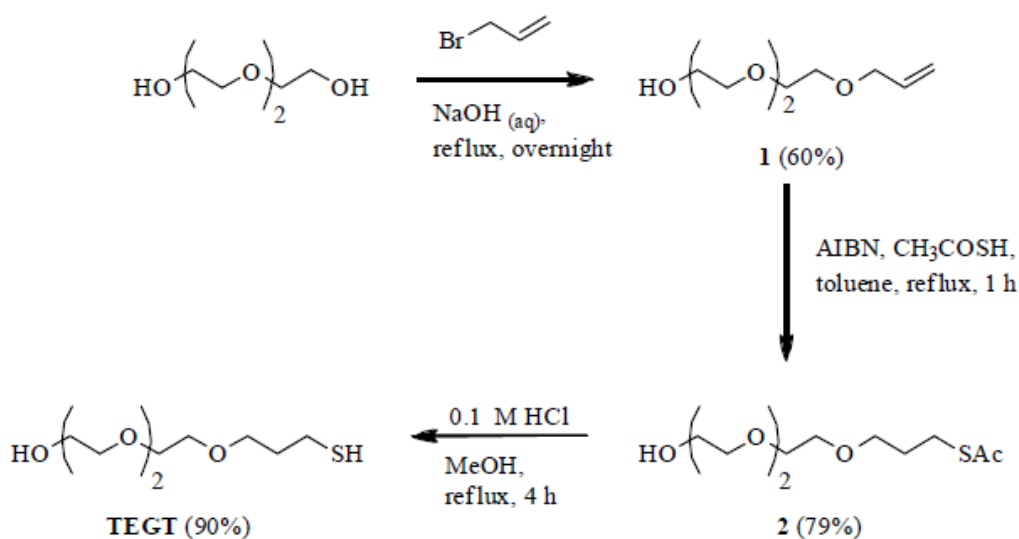
Figure 5.1 Synthesis of TEGT

NMR. [1]H Nuclear Magnetic Resonance (NMR) spectra were recorded on a Bruker AC 300 (300.13 MHz) spectrometer. ^{13}C NMR spectra were recorded on a Bruker AV 300 (75.5 MHz) using Pendent pulse sequences. All chemical shifts are quoted in ppm to higher frequency from Me4Si using either deuterated chloroform ($CDCl_3$) or deuterated methanol (CD_3OD) as the lock, and the residual solvent as the internal standard. The coupling constants are expressed in Hertz (Hz) with multiplicities abbreviated as follows; s = singlet, d = doublet, dd = double doublet, t = triplet, q = quartet and m = multiplet.

Mass Spectrometry (MS). Low and high resolution Electrospray Mass Spectrometry was performed on a micromass Time of Flight (TOF) instrument using methanol as the mobile phase.

Infrared Spectroscopy (IR). The IR spectra were recorded as thin solid films on NaCl discs using a Perkin Elmer 1600 FT-IR.

Elemental Analysis. Elemental analysis was carried out on a Carlo Erba EA 1110 (C H N) instrument.

Synthesis of TEGT

2-(2-(2-allyloxy)ethoxy)ethoxy) ethanol (1). A mixture of triethylene glycol (24.17 g, 16.11 mmol) and 50 % aqueous NaOH (0.64 g, 16.00 mmol) was heated under reflux under an N_2 atmosphere for 30 minutes. Followed by the addition of 11-bromoundec-1-ene (1.95 g, 16.11 mmol), the reaction mixture was heated for a further 20 h under N_2 atmosphere. The organic layer was extracted with Et_2O (3 x 50 ml) and dried (MgSO$_4$), filtered and concentrated *in vacuo*. The crude product was purified by column chromatography on silica gel (eluent: EtOAc) and solvent removed *in vacuo* to give a pale yellow oil (2.06 g, 60 %). vmax/cm^{-1} (film): 3436 m, 2874 m, 1737 s; ^{1}H NMR (300 MHz; CDCl$_3$; Me$_4$Si) δH 6.01-5.84 (m, 1H, -CH$_2$*CH*CH$_2$), 5.33-5.15 (m, 2H, -CH$_2$CH*CH$_2$), 4.02 (d, *J* = 5.67 Hz, 2H, -*CH$_2$*CHCH$_2$), 3.76-3.58 (m, 12H, -O*CH$_2$CH$_2$*O-), 2.56 (s, 1H, *OH*); ^{13}C NMR (75 MHz; CDCl$_3$; Me$_4$Si) δC 134.7, 117.2, 722.5, 72.3, 70.6, 70.4, 69.4, 61.8; (ESMS): 213 ([M + Na]+, 100%); HRMS: found 213.1098. Calc. mass for C$_9$H$_{18}$O$_4$Na: 213.1103.

S-3-(2-(2-hydroxyethoxy)ethoxy)propyl ethanoate (2). To a solution of **1** (1.35 g, 7.71 mmol) in toluene (25 ml), thioacetic acid (1.17 g, 15.43 mmol) and AIBN (catalytic amount) were added. The solution was heated under reflux for 1 h. The reaction mixture was quenched by addition of 1M $NaHCO_3$ (50 ml) and the organic layer extracted with EtOAc (3 x 25 ml). The combined organic layers were washed with 1 M $NaHCO_3$ (3 x 25 ml) and brine (25 ml). The organic layer was dried ($MgSO_4$), filtered and solvent removed *in vacuo* to yield a pale yellow oil (1.45 g, 79 %). vmax/cm-1 (film): 3460m, 2871m, 1693m; ^{1}H NMR (300 MHz; $CDCl_3$; Me4Si) δH 3.74-3.55 (m, 12H, -OCH_2CH_2O-), 3.50 (t, J = 6.20 Hz, 2H, -CH_2(CH_2)$_2$SAc), 2.94 (t, J = 7.20 Hz, 2H, -O(CH_2)$_2$$CH_2$SAc), 2.31 (s, 3H, -*SAc*), 1.89- 1.80 (m, 2H, -OCH$_2$$CH_2CH_2$SAc); ^{13}C NMR (75 MHz; $CDCl_3$; Me_4Si) δC 196.0, 72.2, 70.3, 70.2, 70.0, 69.8, 69.2, 68.8, 61.3, 30.2, 29.2, 25.6; (ESMS): 289 ([M + Na]+, 100 %); HRMS: found 89.1082. Calc. mass for $C_{11}H_{22}O_5SNa$: 289.1086.

2-(2-(2-(3-mercaptopropoxy)ethoxy)ethoxy)ethanol (TEGT). A solution of **2** (1.35 g, 5.40 mmol) in 0.1 M HCl (1.00 ml) made up in MeOH (100 ml) was heated under reflux under N_2 atmosphere for 4 h. The reaction was concentrated *in vacuo*. The crude product was purified by column chromatography on silica gel (eluent: EtOAc) to yield a pale yellow oil (1.03 g, 90 %). Elemental analysis found: C, 47.89 %; H, 9.23%. Calc. for $C_9H_{20}O_4S$: C, 48.18%; H, 8.99%; vmax/cm^{-1} (film): 3454brm, 2871m; ^{1}H NMR (300 MHz; $CDCl_3$; Me_4Si) δH 3.80-3.56 (m, 14H, -OCH_2CH_2O-, -OCH_2(CH_2)$_2$SH), 2.65 (q, J = 7.51 Hz, 2H, -O(CH_2)$_2$$CH_2$SH), 1.92-1.82 (m, 2H, -OCH$_2$$CH_2CH_2$SH), 1.42 (t, J = 7.51, 1H, -*SH*); ^{13}C NMR (75 MHz; $CDCl_3$; Me_4Si) δC 72.4, 70.5, 70.4, 70.2, 70.01, 69.0, 61.6, 33.5, 21.2; (EIMS): 247 ([M + Na]+, 100 %); HRMS: found 247.0977. Calc. mass for $C_9H_{20}O_4SNa$: 247.0980.

5.2 Cleaning of glassware

All organic contaminants are removed from glassware prior to use via a set cleaning procedure.[75] Glassware was immersed in piranha solution (70% H_2SO_4, 30% H_2O_2) for 30 minutes, rinsed and then sonicated in UHQ H_2O (resistivity 18Ω cm^{-1}), followed by oven drying at 127 ^{o}C for 30 mins. Finally the glassware was rinsed, and then sonicated in ethanol (EtOH) for 30 mins before being dried in the oven for 24 hrs prior use. (*Caution*: *Piranha solution is a very strong oxidant and reacts violently with many organic compound. It should be handled with extreme care*.)

5.3 Cleaning plastic equipment

To clean plastic equipment (vials plastic lid and rubber suba seal), it was rinsed with UHQ H_2O, sonicated in UHQ H_2O for 30 mins followed by rinsing with EtOH and a final sonication in EtOH for 30 mins.

5.4 Surface formation

5.4.1 Substrate cleaning

Silicon wafers and glass substrates were cut to approximately 1 cm x 1 cm using a diamond tipped scriber. The substrates were then rinsed with ethanol to clear the surface of any dust that was produced from the cutting process. The cut silicon was then immersed into piranha solution at 90-100 ^{o}C for 60 mins. Once cooled, the piranha solution was rinsed off the substrate with UHQ water, and each one was sonicated in RCA solution (UHQ water; 30 % H_2O_2; NH_4OH in a ration 5:1:1) for 60 mins. Sonication in RCA at this stage functionalises the surface with hydroxyl groups to allow monolayer formation. Continuous rinsing of the substrate in UHQ water for 1 min finishes the cleaning procedure. The substrates are then

stored in UHQ water and used within 2 days to minimise loss of surface hydroxyl groups [75].

Glass substrates follow the exact same cleaning method as silicon wafer.

Gold on glass substrates were cleaned by immersion in piranha solution (7:3, H_2SO_4:30 % H_2O_2) at room temperature for 10 mins, rinsing with UHQ H_2O for 1 min and HPLC grade EtOH thoroughly for 1 min.[17]

5.4.2 SAM formation

5.4.2.1 Silane SAMs formation

The cleaned silica and glass substrates were transferred from UHQ H_2O into anhydrous dichloromethane (DCM) by stepwise exchange (DCM : H_2O)- 1:3, 2:2, 3:1, DCM and anhydrous DCM. The wafers were immersed, under an argon atmosphere, into a 2.5 mM solution of octadecyltrimethoxysilane in anhydrous DCM (5 ml) and sonicated at room temperature for 1 hr. Sonication provides ultrasonic agitation and hence prevents undesired physisorption of any polymeric siloxanes that may form in solution.[281] The substrates were then rinsed for 1 min each with DCM and chloroform. This was followed by sonication of the wafers twice in fresh DCM for 5 min and followed by a final sequential rinsing of 1 min with DCM and chloroform. Each sample was then dried under a steady stream of argon and cured at 120 ^{o}C for 30 mins under vacuum to promote cross-linking of the SAMs[75].

5.4.2.2 Thiol SAMs formation

Solutions of the Biotin-Lys-Lys-Lys-Lys-Cys oligopeptide (0.1 mM) and TEGT (0.1 mM) were prepared in HPLC EtOH containing 3 % (v/v) $N(CH_2CH_3)_3$, and mixed at the volume ratio of 1:1, 1:5, 1:10, 1:20, 1:40, 1:50, 1:100, and 1:500. Subsequently, the clean Au

substrates were immersed in the mixed solutions for 12 hrs to form the mixed SAMs on the Au surfaces. The substrates were rinsed with an ethanolic solution containing 10 % (v/v) CH_3COOH, and UHQ H_2O, follow by rinsing with HPLC EtOH and dried under argon gas. Note that the mixed SAMs were deposited in the presence of $N(CH_2CH_3)_3$ to prevent the formation of hydrogen bonds between the NH_2 functional groups of the bound thiolate peptide on Au surface and that of free thiol peptide in the bulk solution.[268]

5.4.3 Patterned surface formation

Three different poly(dimethylsiloxanes) (PDMS) stamp configurations were employed for the microcontact printing experiments. One stamp consisted of 10 μm wide strips separated by 10 μm gaps, one stamp consisted of 5 μm wide strips separated by 5 μm gaps and the other of 2.5 μm wide strips separated by 500 nm gaps.

5.4.3.1 Silicon master preparation

Silicon masters containing a negative relief of the PDMS stamp mould were manufactured by Jonathan Bramble, a PhD student from Professor Steve Evans group, University of Leeds. A silicon wafer was prepared by ultrasonic cleaning for 5 mins in Decon 90 detergent, UHQ water, acetone and UHQ water. The wafer was subsequently cleaned in piranha etch solution for 20 mins and rinsed thoroughly in UHQ water. The wafer was dried with nitrogen, dehydrated in an oven at 150 ^{o}C for 1 hr and left to cool slowly. The negative tone photoresist SU8 2000 (MicroChem Corp.) was used to fabricate the stamp masters. For the 10 μm wide strips separated by 10 μm gaps, SU8 2000 was spin coated onto the wafer to leave a 2 μm thick film which was determined using an Alpha-Step surface profiler (KLA-Tencor). The SU8 was patterned using standard UV lithography following the standard procedures

described by MicroChem. Firstly, the wafer was baked at 65°C for 1 min followed by a further bake at 95 ^{o}C for 2 mins. The wafer was allowed to cool slowly to room temperature. An exposure dose of 80 mJ/cm^2 (measured at 365 nm) was found to give the best results. A post-exposure bake at 55 ^{o}C for 1 hr was performed to crosslink the SU8 material. The wafer was allowed to cool slowly to room temperature, developed for 1 min using SU8 developer, rinsed with iso-propanol (IPA) and dried with nitrogen.

For 2.5 μm wide strips separated by 500 nm gaps, the SU8 was patterned using electron-beam lithography (EBL). SU8 2000 was spin coated onto a wafer to give a thickness of 500 nm. The same pre-exposure bake conditions were used as described above. A Raith 150 EBL system was used to directly write the required features into the SU8 film. The exposure parameters used were an accelerating voltage of 30 kV, a beam current of 40 pA and a dose of 3 μC/cm^2. The same post exposure bake and development was performed as described above. Following the formation of the master, it was necessary to silanise the surface to aid the removal of PDMS stamp. The wafer was silanised with perfluorodecyltriethoxylsilane (Fluorochem Ltd.) via vapour phase deposition.

5.4.3.2 PDMS stamp preparation

Patterned PDMS (Sylgard 184, Dow Corning) stamps were prepared from custom-designed topographic masters as described above. Silicone elastomer (base) was vigorously mixed with curing agent for 10 mins at a 10:1 ratio mixture. The elastomer mixture was poured onto the patterned masters and was allowed to de-gas (to remove air bubble trapped in the PDMS elastomer during vigorous mixing) for 1 hr approximately in an open air environment. Once all trapped air bubble has surfaced, the elastomer mixture was then placed in a 60 ^{o}C oven for

2 hrs to enhance the cross linkage (solidification) of the polymer. The solidified PDMS stamps were carefully peeled from the masters and they were ready to use for printing.

5.4.4 Non patterned and patterned protein adsorption on surfaces

Coverslips were coated with 10 μg/ml fibronectin from human plasma (F-2006 Sigma) in PBS for 1hr at room temperature. After coating, cover slips were washed three times in PBS and blocked with 10 mg/ml denatured BSA (fatty acid free A8806; Sigma) for 1 hr at room temperature. Cells are unable to spread or lay down ECM components on glass blocked with BSA in this way.[243]

5.4.4.1 Protein patterning on glass surfaces

In order to localise the micro-patterns, fibronectin was labelled with the fluorophore Cy3. Cy3 as a bisfunctional NHS-ester (Amersham, Buckingham, UK) was coupled to fibronectin in 0.1M sodium carbonate buffer (pH 9.3) for 30 mins at room temperature. Cy3 fibronectin was dialysed against 1L PBS for 24 hrs with two changes of buffer. To produce fluorescently labelled micro-patterns, fibronectin was doped with Cy3 fibronectin in a 4:1 ratio. Stamps were inked between 5 and 40 mins, washed and placed in contact with glass cover slip to produce a pattern. To block uncoated areas of the pattern, the surfaces were coated with heat denatured BSA for 1 hr.[243]

5.5 Dye labelling of neutravidin

Dye labelling of neutravidin was carried out by Marzena Allen following procedures set out by the manufacturer, Invitrogen. Labelling of neutravidin was carried out with Alexa Fluor 568 Protein Labelling Kit according to the manufacturer's instructions. In brief, a solution of

sodium bicarbonate (0.05 ml, 1M) was added to neutravidin (0.5 ml, 2 mg/ml) in PBS. The protein solution was transferred to the vial of reactive dye, stirred for 1 hour at room temperature and incubated at 4 ^{o}C overnight. The labelled protein was separated from the unreacted dye by fine size exclusion chromatography in a Bio-Rad BioGel P-30 resin column. The degree of labelling was determined by measuring the UV-vis absorbance at 280 nm and 577 nm and found to be ~2.44 moles of Alexa Fluor 568 dye per mole of neutravidin.

5.6 Surface characterisation

5.6.1 AFM

AFM images were acquired using a Dimension D3100 Nanoscope AFM from Veeco, USA. Images were acquired in tapping mode, using RTESP silicon tips. These AFM images of this size (5 μm by 5 μm), allow for the long range quality of the surfaces to be assessed and checked for the presence of impurities or structures on the surface.

5.6.2 Contact angle goniometry

Contact angles of substrates were determined using the sessile drop method, using a home built contact angle apparatus equipped with a charge coupled device (CCD) video camera linked to a computer for image capture. All data was collected at room temperature and pressure under ambient humidity conditions. A 1 μL gastight syringe was used for changing the volume of the droplet for all measurements, allowing volume adjustments of ~ 1 μL to be performed manually. The droplet was released onto the sample surface from a blunt-ended needle of ~ 1 mm diameter. The advancing and receding contact angles were taken as the volume of a water drop on the substrate surface was increased and decreased using the 1 μL syringe. Analysis was carried out using software from FTA. A minimum of six measurements were performed for

each sample. All errors presented are the standard error of the mean advancing or receding contact angle.

5.6.3 Ellipsometry

Ellipsometry measurements were taken using a Jobin-Yvon UVISEL ellipsometer with a He-Ne laser light source at an angle of incidence of 70 ℃ using a wavelength range of 280–800 nm. The ellipsometric parameters, Δ and ψ, were recorded for both the bare, clean substrates and for the substrates on which SAMs were formed. DeltaPsi software was used to determine the film thickness

The angle of incidence between the analyser and the polariser was set to 70° and was maintained for all subsequent measurements. All measurements were made under conditions of ambient temperature, pressure and humidity. SAM thicknesses are averages of a minimum of six measurements, each made at a different location on the substrate.

5.6.4 Fluorescence Microscopy

5.6.4.1 Fluorescence Microscopy of Fixed Cells and Image Processing

A Zeiss Axioskop 2 microscope with a 63x 1.4NA Plan Apochromat lens was used for fluorescent microscopy of fixed cells. Images were captured using a Qimaging 12-bit QICAM with a 0.63x camera lens and Openlab software (Improvision) and saved as 12-bit tif files. Images were processed in Adobe Photoshop (Adobe). The image histogram was adjusted to make full use of the available greys, without adjusting gamma, converted to 8-bit and where necessary merged with corresponding images, taken with different fluorescent filters, to make an 8-bit/channel RGB file. Regions of interest where selected from merged images and scale

bars were added. Where image size was adjusted for making figures this was done in Photoshop without resampling of the image.

5.6.4.2 Fluorescence Microscopy Switching Studies on Mixed SAMs

Fluorescence images were collected on a Zeiss SM-LUX fluorescent microscope, equipped with a Canon Powershot G5 monochrome camera using a mercury lamp as the light source. Pictures were acquired using software remote capture with identical exposure parameters and analyzed using Image J 1.40g (NIH). No post exposure image processing was performed.

Electrical potentials were applied to the mixed SAMs on Au using a Gamry PCI4/G300 with a custom designed Teflon cell, equipped with the functionalized Au substrate as the working electrode, a Pt wire as the counter electrode, and a SCE as the reference electrode. For the bioactive state (neutravidin-biotin binding), an electrical potential of + 0.3 V was applied for 10 mins on the gold substrate in a 500 μL PBS solution, followed by adding of a 500 μL PBS solution of the fluorescently-labelled neutravidin (74 μg mL^{-1}), whilst maintaining the + 0.3 V potential for a further 30 mins in the dark. The substrates were rinsed with PBS for 10 min and mounted for fluorescence microscopy. For the bio-inactive state (neutravidin-biotin non-binding), the same procedure was used but with - 0.4 V applied to the surface. Similar incubation conditions were used for open circuit conditions (no applied potential). Fluorescence intensity - mean pixel intensity (MPI) values were calculated using image J software.

5.6.5 Cyclic Voltammetry

5.6.5.1 Potential and Time-Dependent Stability Studies of the Mixed SAMs

Potential and time-dependent stability studies were performed using a Gamry PCI4/G300 with a custom-designed Teflon cell, equipped with the functionalized Au substrate as the working electrode, a Pt wire as the counter electrode, and a SCE as the reference electrode. The planar gold working electrode exposes a circular geometric area of 75.2 mm^2 to the electrolyte solution. Electrical potentials of + 0.3 V and - 0.4 V were applied for 30 mins to the mixed SAMs in PBS solution. Subsequently, the mixed SAMs were removed from the PBS solution, rinsed with UHQ water, and analyzed by CV in a 0.1 M KOH solution by sweeping the potential in the negative direction from + 0.3 V to - 1.5 V and then to + 0.3 V at a scan rate of 50 mV s^{-1} . The KOH solution was purged with Ar for ~20 mins prior to each measurement and kept under Ar during the course of the experiment. Similar CV measurements were performed on pristine mixed SAMs. The charge density reported is the average of five measurements.

5.6.6 X-Ray Photoelecton Spectroscopy (XPS)

XPS spectra were obtained on the Scienta ESCA300 instrument based at the Council for the Central Laboratory of the Research Councils (CCLRC) in The National Centre for Electron Spectroscopy and Surface Analysis (NCESS) facility at Daresbury, UK. XPS experiments were carried out using a monochromatic Al Kα X-ray source (1486.7 eV) and a take off angle of 15 °. High-resolution scans of N (1s) and S (2p) were recorded using a pass energy of 150 eV at a step size of 0.05 eV. The binding energy (BE) scale was calibrated by setting the Au 4f$_{7/2}$ core levels of pure metals to values of 84.0 eV. Fitting of XPS peaks was performed

using the *Avantage* V *2.2* processing software. Sensitivity factors used in this study were: N (1s), 1.73; S (2p), 2.08; Au (4f 7/2), 9.58; Au (4f 5/2), 7.54.

5.6.7 Surface Plasmon Resonance Spectroscopy (SPR)

SPR switching experiments were performed with a Reichert SR7000DC dual channel spectrometer (Buffalo, NY, USA) at 25 ° C using a three-electrode electrochemical cell and a Gamry PCI4/G300 potentiostat. The SAMs prepared on Reichert Au sensor chips served as the working electrode, the counter electrode was a Pt wire, and a SCE was used as the reference electrode. Prior to the neutravidin binding studies, the sensor chips were equilibrated with degassed PBS, followed by application of either + 0.3 V, - 0.4 V or open circuit conditions for 10 mins while passing degassed PBS through the electrochemical cell at a flow rate of 100 μL min^{-1}. While still applying a potential, Alexa Fluor 568 neutravidin (500 μL, 37 μg mL^{-1}), was injected over the sensor chip surface for 10 secs at 1500 μL min^{-1} and then 30 min at 8 μL min^{-1} (the decrease in flow rate from 1500 to 8 μL min^{-1} ensures that sufficient exposure time is provided for binding to occur between the biotin on the surface and neutravidin in solution). In order to remove any unbound neutravidin, the sensor chips were washed with degassed PBS for 10 secs at a flow rate of 1500 μL min^{-1}, followed by 20 mins at a flow rate of 100 μL min^{-1} while still applying a potential to the chips. The SPR signal was measured in response unit, where 996 response unit is equivalent to 1μg mm^{-2}.[279, 280]

Chapter 6

Conclusions and Future work

6.0 Conclusions

The work performed in this thesis has employed and integrated microstructure fabrication technology and switchable surfaces with biology.

The fabrication of patterned biological surfaces have provided a platform to explore how cells uses filopodia to probe their surrounding environment and form new adhesion contacts for cell motility and spreading. The study especially explored the role of filopodia in the spreading of Mouse Embryonic fibroblast (MEF) cells and the function of Arp2/3 complex in this process. The fabricated patterned biological surfaces have demonstrated that filopodia, produced by MEF cells, interacted with the fibronectin patterned regions and guided lamellipodia protrusion. The novel patterned biological surfaces also allowed us to learn more about the involvement of Arp2/3 complex in cell spreading, and in particular, that the localisation of Arp2/3 complex to filopodia is independent of adhesion.

A novel approach of fabricating responsive surfaces that rely on electro-switchable peptides (biotin-KKKKC) to control biomolecular interactions on gold surface have been developed. This system is based upon the conformational switching of positively charged oligolysine peptide that are tethered to a gold surface, such that bioactive molecular moieties (biotin) incorporated on the peptide can be reversibly exposed (bio-active state) or concealed (bio-inactive state) as a function of surface potential. The results have shown that the surface bio-functionality can be switched with over 90% efficiency by applying a negative potential on

the surface. The surface has also exhibited reversible switching properties when a combination of negative potential and open circuit conditions was applied. This novel switchable surface technology takes advantage of the unique dynamic properties of surface-confined charged peptide linkers to induce On-Off switching of specific biomolecular interactions, paving new advances in biological, medicinal research and biotechnology.

Chapter 3 examined the possibility of employing microstructured surfaces for the study of cell motility. The first objective of this chapter was the development of a hydrophobic surface for the adsorption of fibronectin onto the surface. Octadecytrimethoxylsilane (ODTMS) was first employed to create hydrophobic SAMs on a glass surface. However, fluorescence images have illustrated that the quality of the fibronectin patterns was not adequate for the cell motility studies due to defects present on the surface. Therefore, an alternative hydrophobic surface, poly(dimethylsiloxane) (PDMS) coated glass substrate was employed. Patterns produced on the PDMS coated glass surface have shown an improved pattern quality with very little defects observed.

The projecet was next moved onto the investigation of cell motility. The patterned fibronectin surface was backfilled with bovine serum albumin (BSA), to ensure cells only attached to the fibronectin surface and not to the glass substrate. MEF cells were incubated onto the patterned surfaces, and fluorescence results demonstrated that the filopodia that cells deployed to probe their surroundings only attached onto the fibronectin strips but not on the BSA regions. After the filopodia anchored onto the fibronectin surface, MEF cells start to protrude and spread along the fibronectin strips.

The final objective of this chapter was to determine the role of the Arp2/3 complex during cell protrusion, specifically looking at the presence of Arp 2/3 complex in filopodia. The results have suggested that where attachments occurred, a strong signal of vinculin was observed. However, the localisation of the Arp 2/3 complex was absent at the attachment site, suggesting Arp2/3 complex does not facilitate the adhesion of filopodia to a fibronectin surface.

Chapter 4 examines the switching properties of the mixed biotin-KKKKC:TEGT SAMs by applying various electrical potentials on the surface. By employing fluorescently labelled neutravidin as the biomolecule that attach to the biotinylated surface, we demonstrated that the mixed biotin-KKKKC:TEGT SAMs can undergo switching between a bio-inactive state and bio-active state under various electrical potentials.

We first conducted a systematic study to determine the solution ratio that provides an optimum mixed biotin-KKKKC:TEGT SAM surface for the switching studies. XPS, data have shown that a solution ratio of 1:40 provides a surface ratio of 1:16. This surface ratio is the minimum surface ratio required to ensure sufficient spacing between each oligopeptide in order to perform a successful conformational change when negative potentials are applied to the surface.

We next addressed the stability of the mixed SAMs under various electrical potentials. Using XPS and CV data, we determined that the mixed SAMs are stable from the range of -0.6 V to $+0.3$ V. Therefore, we can use potentials within this range to perform the switching experiments without concerns of thiols SAMs desorbing from the surface.

The switching experiments were conducted by employing fluorescently labelled neutravidin attaching onto the mixed biotin-KKKKC:TEGT SAMs surface under an electrical potential of – 0.4 V, where the biotin moieties were concealed (bio-inactive state), and at + 0.3 V, where the biotin moieties were exposed to neutravidin solution (bio-active state). Images captured from fluorescence microscopy have demonstrated a reduction of fluorescence intensity from 81 to 27 between + 0.3 V and -0.4 V. This data supports the hypothesis that the oligopeptide has undergone a conformation change under a negative electrical potential. SPR data which measures the amount of biomolecules attached onto the surface has further support this switching properties. Upon the application of + 0.3 V to the mixed biotin-KKKKC:TEGT SAMs surface in the neutravidin solution, we observed a response of 3520 response units, whereas mixed biotin-KKKKC:TEGT SAMs that were exposed to – 0.4 V in the neutravidin solution had a response of 290 units; a reduction of over 90%. Thus, depending on the applied potential on the mixed biotin-KKKKC:TEGT SAMs, the bio-functionality of the surface can be controlled.

The final objective of this chapter was to explore the reversible switching properties of the mixed biotin-KKKKC:TEGT SAMs. The mixed SAMs were first exposed to an electrical potential of - 0.4 V in a neutravidin solution, where minimum binding (compare to open circuit condition) of ~300 response units occurred. Upon the release of the negative potential, the mixed SAMs surface returned to the open circuit conditions, where a large increase in neutravidin binding (i.e. ~2500 response units) was observed. This data has shown that the developed switchable surfaces allow reversible control of biomolecular interactions.

This thesis shows how nanotechnology, more specifically self-assembled monolayers, can be integrated with biomolecules to fabricate new biological surfaces. The switchable biological surface concept has a vast amount of applications, and can be incorporated into future devices to enhance our knowledge in medicine and biology which was not possible prior to this development.

6.1 Future work

The next stage of this project is to investigate the switching properties of various lengths of oligolysine peptides, namely biotinKKC, biotinKKKC and biotinKKKKKKC. By employing these peptides, we will be able to learn how different number of lysine molecules on the oligolysine peptide can affect the switching capability on the surface, offering us new insights in the switching properties of these novel surface-confined peptide monolayers..

The next project based on the current research is to incorporate micro-contact printing (**chapter 3**) in combination with switchable biological surfaces (**chapter 4**) to create a quick, simple and reusable bio-assay tool. The objective is to create micro or nanostructure surfaces with switching properties that permit the new experimental approaches to study the regulation and dynamics of cell signalling.

Surfaces equipped with dynamic molecular cues, mimicking key aspects of structure and function of natural environment, will offer completely new opportunities for mechanistic studies for the pathway by which cell sense, integrate and respond to changes in their environments. For example, by replacing the biotin moieties on the biotinKKKKC with

progesterone, a new type of switchable biological surface which can determine human sperm cell quality can be fabricated.

By applying electrical potentials onto the surface, we will be able to control the bio-activity state on the surface. Upon the application of a negative potential, the progesterone oligolysine peptide will adopt a gauche conformation where the progesterone group will be concealed (bio-inactive state). When a positive potential applies onto the surface, the progesterone group will be exposed, hence bio-active state. This switching mechanism will allow the investigation of the stimulus activated $[Ca^{2+}]$ signal in human sperm cells; thus, we will be able to determine the sperm cells quality and possibly open up new opportunities in studying human infertility.

References

1. Preece, J. A., Stoddart, J. F., **Concept transfer from biology to materials**. *Nanobiology* **1994,** 3, 149.

2. Service, R. F., **Biology offers nanotechs a helping hand.** *Science* **2002,** 298, 2322.

3. Mendes, P. M., Yeung, C. L., Preece, J. A., **Bio-nanopatterning of surfaces**. *Nanoscale Res. Lett.* **2007,** 2, 273.

4. Johnston, S. A., Bramble, J. P., Yeung, C. L., Mendes, P. M., Machesky, L. M., **Arp2/3 complex activity in filopodia of spreading cells**. *BMC Cell Bio* **2008,** 9, 65.

5. Sun, A., Lahann, L., **Dynamically switchable biointerfaces**. *Soft Matter* **2009,** 5, 1555.

6. Wischerhoff, E., Badi, N., Lutz, J. F., Laschewsky, A., **Bioactive surfaces**. *Soft Matter* **2010,** 6, 705.

7. Niemeyer, C. M., Mirkin, C. L., *Nanobiotechnology*. Wiley-VCH Verlag GmbH & Co. KGaA, Weinheim: **2004**.

8. Mu, L., Liu, Y.,Cai, S., Kong, J., **A smart surface in a microfluidic chip for controlled protein separation**. *Chem. Eur. J.* **2007,** 13, 5113.

9. McBain, S., Yiu, H., Dobson, J., **Magnetic nanoparticles for gene and drug delivery**. *Int. J. Nanomed* **2008,** 3, 169.

10. Gao, J., Gu, H., Xu, B., **Multifunctional magnetic nanoparticles**. *Accounts Chem. Res.* **2009,** 42, 1097.

11. Salata, O. V., **Applications of nanoparticles in biology and medicine**. *J. Nanobiotechnology* **2004,** 2, 3.

12. Wu, L., Chu, H. S., Koh, W. S., Li, E. P., **Highly sensitive graphene biosensors based on surface plasmon resonance**. *Opt. express* **2010,** 18, 14395.

13. Misra, R., Acharya, S., Sahoo, K., **Cancer nanotechnology: application of nanotechnology in cancer therapy**. *Drug Discovery Today* **2010,** 15, 842.

14. Stevens, M. M., George, J. H., **Exploring and engineering the cell surface interface**. *Science* **2005,** 310, 1135.

15. Cavalcanti-Adam, E. A., Volberg, T., Micoulet, A., Kessler, H., Geiger, B., Spatz, J. P., **Cell spreading and focal adhesion dynamics are regulated by spacing of integrin ligands**. *Biophys. J.* **2007,** 92, 2964.

16. Mendes, P. M., Chen, Y., Palmer, R. E., Nikitin, K., Fitzmaurice, D., Preece, J. A., **Nanostructures from nanoparticles**. *J. Phys. Condens. Matter.* **2003,** 15, S3047.

17. Mendes, P. M., Christman, K. L., Parthasarathy, P., Schopf, E., Ouyang, J., Yang, Y., Preece, J. A., Maynard. H. D., Chen, Y., Stoddart, J. F., **Electrochemically controllable conjugation of proteins on surfaces**. *Bioconjugate Chem.* **2007,** 18, 1919.

18. Kambhampati, D., *Protein microarray technology*. Wiley-VCH Verlag GmbH & Co. KGaA, Weinheim: **2004**.

19. Patolsky, F., Timko, B. P., Yu, G., Gang, Y., Greytak, A. B., Zheng, G., Lieber, C. M., **Detection, stimulation, and inhibition of neuronal signals with high-density nanowire transistor arrays**. *Science* **2006,** 313, 1100.

20. Shekhawat, G., Tark, S. H., Dravid, V., **MOSFET-embedded microcantilevers for measuring deflection in biomolecular sensors**. *Science* **2006,** 311, 1592.

21. Christman, K. L., Enriquez-Rios, V. D., Maynard, H. D., **Nanopatterning proteins and peptides**. *Soft Matter* **2006,** 2, 928.

22. Dermidov, V. V., **Nanobiosensors and molecular dignostics: a promising partnership**. *Expert Rev. Mol. Diagn* **2004,** 4, 267.

23. Mrksich, M., **Dynamic substrates for cell biology**. *MRS Bulletin* **2005,** 30, 180.

24. Lin, C. X., Liu, Y., Yan, H., **Self-assembled combinatorial encoding nanoarrays for multiplexed biosensing**. *Nano Lett.* **2007,** 7, 507.

25. Cui, Y., Wei, Q. Q., Park, H., Lieber, C. M., **Nanowire nanosensors for highly sensitive and selective detection of biological and chemical species**. *Science* **2001,** 293, 1289.

26. Zhang, F., Skoda, M. W. A., Jacobs, R. M. J., Zorn, S., Martin, R. A., Martin, C. M., Clark, G. F. Goerigk, G., Schreiber, F., **Gold nanoparticles decorated with oligo(ethylene glycol) thiols: Protein resistance and colloidal stability**. *J. Phys. Chem. A* **2007,** 111, 12229.

27. Yeo, W. S., Yousaf, M. N., Mrksich, M., **Dynamic interfaces between cells and surfaces: Electroactive substrates that sequentially release and attach Cells**. *J. Am. Chem. Soc* **2003,** 125, 14994.

28. Ulman, A., **Formation and structure of self-assembled monolayers**. *Chem. Rev.* **1996,** 96, 1533.

29. Wilbur, J. L., Whitesides, G. M., *Nanotechnology*. Springer Verlag: New York, **1999**.

30. Ercolani, G., **Assessment of cooperativity in self-assembly**. *J. Am. Chem. Soc* **2003,** 125, 16097.

31. Schneider, J. P., Pochan, D. J., Ozbas, B., Rajagopal, K., Pakstis, L., Kretsinger, J., **Responsive hydrogels from the intramolecular folding and self-assembly of a designed peptide**. *J. Am. Chem. Soc* **2002,** 124, 15030.

32. van Esch, J. H., **More than the sum of its parts**. *Nature* **2010,** 446, 193.

33. Vericat, C., Vela, M. E., Benitez, G., Carro, P., Salvarezza, R. C., **Self-assembled monolayers of thiols and dithiols on gold: new challenges for a well-known system**. *Chem. Soc. Rev.* **2010,** 39, 1805.

34. Tatsuma, T., Saito, K., Oyama, N., **Enzyme-exchangeable enzyme electrodes employing a thermoshrinking redox gel**. *J. Chem. Soc., Chem Commun* **1994**, 1853.

35. Yamada, N., Okano, T., Sakai, H., Karikusa, F., Sawasaki, Y., Sakurai, Y., **Thermo-responsive polymeric surfaces; control of attachment and detachment of cultured cells**. *Makromol. Chem., Rapid Commun.* **1990,** 11, 571.

36. Schreiber, F., **Self-assembled monolayers: from "simple" model systems to biofunctionalized interfaces**. *J. Phys. Condens. Matter.* **2004,** 16, R881.

37. Onclin, S., Ravoo, B. J., Reinhoudt, D. N., **Engineering silicon oxide surfaces using self-assembled monolayers**. *Angew. Chem. Int. Ed. Engl.* **2005,** 44, 6282.

38. Love, J. C., Estroff, L. A., Kriebel, J. K., Nuzzo, R. G., Whitesides, G. M., **Self-assembled monolayers of thiolates on metals as a form of nanotechnology**. *Chem. Rev.* **2005,** 105, 1103.

39. Delamarche, E., Michel, B., Biebuyck, H. A., Gerber, C., **Golden interfaces: The surface of self- assembled monolayers**. *Adv. Mat.* **1996,** 8, 719.

40. Ulman, A., *An introduction to ultra-thin films. From langmuir-blodgett to self-assembly*. Academic Press: San Diego, **1991**.

41. Iqbal, P., Critchley, K., Bowen, J., Attwood, D., Tunnicliffe, D., Evans, S. D., Preece, J. A., **Fabrication of a nanoparticle gradient substrate by thermochemical manipulation of an ester functionalized SAM**. *J. Mater. Chem.* **2007,** 17, 5097.

42.   Hara, M., Tamada, K., Hahn, C., Nishida, N., Knoll, W., **Adsorption and desorption processes of self-assembled monolayers studied by surface-sensitive microscopy and spectroscopy** *Supramolecular Science* **1996,** 3, 103.

43.   Kankate, L., Turchanin, A., Golzhauser, A., **On the Release of Hydrogen from the S-H groups in the Formation of Self-Assembled Monolayers of Thiols**. *Langmuir* **2009,** 25, 10435.

44.   Hara, M., Sasabe, H., Knoll, W., **Ordered nucleation of a self-assembled monolayer on Au(111) studied by scanning tunneling Microscopy**. *Thin Solid Films* **1996,** 273, 66.

45.   Rodriguez, L. M., Gayone, J. E. M., Sanchez, E. A., Grizzi, O., Blum, B., Salvarezza, R. C., Xi, L., Lau, W. M., **Gas phase formation of dense alkanethiol layers on GaAs (110)**. *J. Am. Chem. Soc* **2007,** 129, 7807.

46.   Zuo, G., Liu, X., Yang, J., Li, X., Lu, X., **Study of the adsorption kinetics of thiol-derivatized porphyrin on the surface of gold electrode**. *J. Electronanl. Chem.* **2007,** 605, 81.

47.   Porter, M. D., Bright, T. B., Allara, D. L., Chidsey, C. E. D., **Spontaneously organized molecular assemblies. 4. Structural characterization of n-Alkyl thiol monolayers on gold by optical ellipsometry, infrared spectroscopy, and electrochemistry**. *J. Am. Chem. Soc* **1987,** 109, 3559.

48.   Bowen, J., Pettitt, M. E., Kendall, K., Leggett, G., Preece, J. A., Callow, M. E., Callow, J. A., **The influence of surface lubricity on the adhesion of *Navicula perminuta* and *Ulva linza* to alkanethiol self-assembled monolyers**. *J. R. Soc. Interface* **2007,** 4, 473-.

49. Nuzzo, R. G., Zegarskii. B. R., Dubois, H., **Fundamental studies of the chemisorption of organosulfur compounds on Au(111). Implications for molecular self-assembly on gold surfaces**. *J. Am. Chem. Soc* **1987,** 109, 733.

50. Major, R. C., Zhu, X. Y., **Two-step approach to the formation of organic monolayers on the silicon oxide surface**. *Langmuir* **2001,** 17, 5576.

51. Doering, R., Nishi, Y., *Handbook of semiconductor manufacturing technology*. 2nd ed.; CRC Press: Dallas, USA, **2007**.

52. Balgar, T., Bautista, R., Hartmann, N., Hasselbrink, E., **An AFM study of the growth kinetics of the self-assembled octadecylsiloxane monolayer on oxidized silicon**. *Surf. Sci.* **2003,** 532-535, 963.

53. Tripp, C. P., Hair, M. L., **An infrared study of the reaction of octadecyltrichlorosilane with silica**. *Langmuir* **1992,** 8, 1120.

54. Resch, R., Grasserbauer, M., Friedbacher, G., Vallant, Th. Brunner, H., Mayer, U., Hoffmann, H., **In situ and ex situ AFM investigation of the formation of octadecylsiloxane monolayers**. *Appl. Surf. Sci* **1999,** 140, 168.

55. Jans, K., Bonroy, K., de Palma, R., Reekmans, G., Jans, H., Laureyan, W. Smet, M., Borghs, G., maes, G., **Stability of mixed PEO-thiol SAMs for biosensing applications**. *Langmuir* **2008,** 24, 3949.

56. Bain, C. D., Whitesides, G. M., **Modeling organic surfaces with self-assembled monolayers**. *Angew. Chem. Int. Ed. Engl.* **1989,** 28, 506.

57. Luderer, F., Walschus, U., **Immobilization of oligonucleotides for biochemical sensing by self-assembled monolayers: Thiol organic bonding on gold and silanization on silica surfaces**. *Top. Curr. Chem.* **2005,** 260, 37.

58. Bain, C. D., Whitesides, G. M., **Formation of monolayers by the coadsorption of thiols on gold: Variation in the length of the alkyl chain**. *J. Am. Chem. Soc* **1989,** 111, 7164.

59. Laibinis, P. E., Fox, M. A., Folkers, J. P., Whitesides, G. M., **Comparisons of self-assembled monolayers on silver and gold: Mixed monolayers derived from HS(CH2)21X and HS(CH2)ioY (X, Y = CH3, CH20H) have similar properties**. *Langmuir* **1991,** 7, 3167-.

60. Rissner, F., Rangger, G. M., Hofmann, O. T., Track, A. M., Heimel, G., Zojer, E., **Understanding the electronic structure of metal/SAM/organic-semiconductor heterojunctions**. *ACS Nano* **2009,** 3, 3513.

61. Chelmowski, R., Prekelt, A., Grunwald, C., Woll, C., **A case study on biological activity in a surface-bound multicomponent system: The biotin-streptavidin-peroxidase system**. *J. Phys. Chem. A* **2007,** 111, 12295.

62. Zacher, D., Shekhah, O., Woll, C., Fischer, R. A., **Thin films of metal-organic frameworks**. *Chem. Soc. Rev.* **2009,** 38, 1418.

63. Chelmowski, R., Koster, S. D., Kerstan, A., Prekelt, A., Grunwald, C., Winkler, T., Meltzler-nolte, N., Terfort, A., Woll, C., **Peptide-based SAMs that resist the adsorption of proteins**. *J. Am. Chem. Soc* **2008,** 130, 14952.

64. Kankate, L., Werner, U., Turchanin, A., Golzhauser, A., **Protein resistant oligo(ethylene glycol) terminated self-assembled monolayers of thiols on gold by vapor deposition in vacuum**. *Biointerphases* **2010,** 5, 30.

65. Gonzalez, M., Bagatolli, L. A., Echabe, I., Arrondo, J. L. R., Argarana, C. E., Cantor, C. R., Fiedelio, G. D., **Interaction of biotin with streptavidin**. *J. Biol. Chem* **1997,** 272, (17), 11288.

66. Gonzalez, M., Bagatolli, L. A., Echabe, I., Arrondo, J. L. R., Argarana, C. E., Cantor, C. R., Fiedelio, G. D., **Interaction of biotin with streptavidin**. *J. Biol. Chem* **1997,** 272, 11288.

67. Grunwald, C., Eck, W., Optiz, N., Kuhlmann, J., Woll, C., **Fabrication of 2D-protein arrays using biotinylated thiols: Results from fluorescence microscopy and atomic force microscopy**. *Phys. Chem. Chem. Phys* **2004,** 6, 4358.

68. Chambers, R. C., Inman, C. E., Hutchison, J. E., **Electrochemical detection of nanoscale phase separation in binary self-assembled monolayers**. *Langmuir* **2005,** 21, 4615.

69. Vericat, C., Vela, M. E., Salvarezza, R. C., **Self-assembled monolayers of alkanethiols on Au(111): Surface structures, defects and dynamics**. *Phys. Chem. Chem. Phys* **2005,** 7, 3258.

70. Lee, L. Y. S., Lennox, R. B., **Ferrocenylalkylthiolate labeling of defects in alkylthiol self-assembled monolayers on gold**. *Phys. Chem. Chem. Phys* **2007,** 9, 1013.

71. Creager, S. E., Hockett, L. A., Rowe, G. K., **Consequences of microscopic surface roughness for molecular self -assembly**. *Langmuir* **1992,** 8, 854.

72. Miller, C., Cuendet, P., Gratzel, M., **Adsorbed hydroxy thiol monolayers on goid electrodes: Evidence for electron tunneling to redox species in solution**. *J. Phys. Chem.* **1991,** 95, 877.

73. Tour, J. M., *Molecular electronics*. World Scientific: River Edge, N. J., **2003**.

74. Larcel, M. J., Whelan, C. S., Craighead, H. G., Seshadri, K., Allara, D. L., **High-resolution silicon patterning with self-assembled monolayer resists**. *J. Vac. Sci. Technol. B* **1996,** 14, 4085.

75. Mendes, P. M., Susanne, J., Critchley, K., Plaza, J., Chen. Y., Nikitin, K., Palmer, R. E., Preece, J. A., Evans, S. D., Fitzmaurice, D., **Gold nanoparticels patterning of silicon wafers using chemical E-beam lithography**. *Langmuir* **2004,** 20, 3766.

76. Tseng, A. A., Chen, K., Chen, C. D., Ma, K. J., **Electron beam lithography in nanoscale fabrication: Recent development**. *T. Electron. Pa. M.* **2003,** 26, 141.

77. Ito, T., Okazaki, S., **Pushing the limits of lithography**. *Nature* **2000,** 106, 1027.

78. Lee, C. S., Baker, S. E., Marcus, M. S. Yang, W., Eriksson, M. A., Hamers, R. J., **Electrically addressable biomolecular functionalization of carbon nanotube and carbon nanofiber electrodes**. *Nano Lett.* **2004,** 4, 1713.

79. Gu, J., Yam, C. M., Li, S., Cai, C., **Nanometric protein arrays on protein-resistant monolayers on silicon surfaces**. *J. Am. Chem. Soc* **2004,** 126, 8089.

80. Sun, S., Montague, M., Critchley, K., Chen, M. S., Dressick, W. J., Evans, S. D., Leggett, G. J., **Fabrication of biological nanostructures by scanning near-field photolithography of chloromethylphenylsiloxane monolayers**. *Nano Lett.* **2006,** 6, 29.

81. Liu, G. Y., Xu, S., Qian, Y., **Nanofabrication of self-assembled monolayers using scanning probe lithography**. *Acc. Chem. Res.* **2000,** 33, 457.

82. Liu, M., Amro, N. A., Chow, C. S., Liu, G. Y., **Production of nanostructures of DNA on surfaces**. *Nano Lett.* **2002,** 2, 863.

83. Piner, R. D., Xhu, J., Xu, F., Hong, S., Mirkin, C. A., **Dip-pen nanolithography**. *Science* **1999,** 283, 661.

84. Weimann, T., Geyer, W., Hinze, P., Stadler, V., Eck, W., Golzhauser, A., **Nanoscale patterning of self-assembled monolayers by E-beam lithography**. *Micro. Engn.* **2001,** 57-58, 903.

85. Falconnet, D., Pasqui, D., Park, S., Eckert, R., Schift, H., Gobrecht, J., BArbucci, R., Textor, M., **A novel approach to produce protein nanopatterns by combining nanoimprint lithography and molecular self-assembly**. *Nano Lett.* **2004,** 4, 1909.

86. Hoff, J. D., Cheng, L. J., Meyhofer, E., Guo, L. J., Hunt, A. J., **Nanoscale protein patterning by imprint lithography**. *Nano Lett.* **2004,** 4, 853.

87. Odom, T. W., Love, J. C., Wolfe, D. B., Paul, K. E., Whitesides, G. M., **Improved pattern transfer in soft lithography using composite stamps**. *Langmuir* **2002,** 18, 5314.

88. Kumar, A., Whitesides, G. M., **Features of gold having micrometer to centimeter dimensions can be formed through a combination of stamping with an elastomeric stamp and an alaknethiol "ink" follow by chemical etching**. *Appl. Phys. Lett.* **1993,** 63, 2002.

89. Goetting, L. B., Deng, T., Whitesides, G. M., **Microcontact printing of alkanephosphonic acids on aluminium : Pattern Transfer by Wet Chemical Etching**. *Langmuir* **1999,** 15, 1182.

90. Agarwai, G., Sowards, L. A., Naik, R. R., Stone, M. O., **Dip-pen nanolithography in tapping mode**. *J. Am. Chem. Soc* **2003,** 125, 580.

91. Li, H. W., Muir, B. V. O., Fichet, G., Huck, W. T. S., **Nanocontact printing: A route to sub-50-nm-scale chemical and biological patterning**. *Langmuir* **2003,** 19, 1963.

92. Bernard, A.; Delamarche, E.; Schmid, H.; Michel, B.; Bosshard, H. R.; Biebuyck, H., **Printing Patterns of Proteins**. *Langmuir* **1998,** 14, (9), 2225.

93. Bernard, A., Renault, J. P.; Michel, B., Bosshard, H. R., Delamarche, E., **Microcontact Printing of Proteins**. *Adv. Mat.* **2000,** 12, 1067.

94.   Rozkiewicz, D. I., Kraan, Y., Werten, M. W. T., Wolf, F. A. Subramaniam, V., Ravoo, B. J., Reinhoudt, D. N., **Covalent Microcontact Printing of Proteins for Cell Patterning**. *Chem. Eur. J* **2006,** 12, (24), 6290.

95.   Gerding, J. D., Willard, D. M., VanOrden, A., **Single-Feature Inking and Stamping: A Versatile Approach to Molecular Patterning**. *J. Am. Chem. Soc.* **2005,** 127, (4), 1106.

96.   Inerowicz, H. D., Howell, S., Regnier, F. E., Reifenberger, R., **Multiprotein Immunoassay Arrays Fabricated by Microcontact Printing**. *Langmuir* **2002,** 18, (13), 5263.

97.   Odom, T. W., Love, J. C., Wolfe, D. B., Paul, K. E., Whitesides, G. M., **Improved Pattern Transfer in Soft Lithography Using Composite Stamps**. *Langmuir* **2002,** 18, (13), 5314.

98.   Li, H. W., Muir, B. V. O., Fichet, G., Huck, W. T. S., **Nanocontact Printing: A Route to Sub-50-nm-Scale Chemical and Biological Patterning**. *Langmuir* **2003,** 19, (6), 1963.

99.   Renault, J. P., Bernard, A., Bietsch, A., Michel, B., Bosshard, H. R., Delamarche, E., Kreiter, M., Hecht, B., Wild, U. P., **Fabricating Arrays of Single Protein Molecules on Glass Using Microcontact Printing**. *J. Phys. Chem. B* **2003,** 107, (3), 703.

100.   Csucs, G., Kunzler, T., Feldman, K.., Robin, F., Spencer, N. D., **Microcontact printing of macromolecules with submicrometer resolution by means of polyolefin stamps**. *Langmuir* **2003,** 19, 6104.

101.   Wilson, D. L., Martin, R., Hong, S., Cronin-Golomb, M., Mirkin, C. A., Kaplan, D. L., **Surface organization and nanopatterning of collagen by dip-pen nanolithography**. *PNAS* **2001,** 98, 13660.

102. Piner, R. D., Mirkin, C. A., **Effect of water on lateral force microscopy in air**. *Langmuir* **1997,** 13, 6864.

103. Weeks, B., Vaughn, M. W., DeYoreo, J. J., **Direct imaging of meniscus formation in atomic force microscopy using environmental scanning electron microscopy**. *Langmuir* **2005,** 21, 8096.

104. Ginger, D. S., Zhang, H., Mirkin, C. A., **The evolution of dip-pen nanolithography**. *Angew. Chem. Int. Ed. Engl.* **2004,** 43, 30.

105. Hong, S., Zhu, J., Mirkin, C. A., **Multiple ink nanolithography: Toward a multiple-pen nano-plotter**. *Science* **1999,** 286, 523.

106. Lee, K. B., Lim, J. H., Mirkin, C. A., **Protein nanostructures formed via direct-write dip-pen nanolithography**. *J. Am. Chem. Soc* **2003,** 125, 5588.

107. Sheehan, P. E., Whitman, L. J., **Thiol diffusion and the role of humidity in "Dip Pen Nanolithography"**. *Phys. Rev. Lett.* **2002,** 88, 156104.

108. Manandhar, P., Jang, J., Schatz, G. C., Ratner, M. A. Hong, S., **Anomalous surface diffusion in nanoscale direct deposition processes**. *Phys. Rev. Lett.* **2003,** 90, 115505.

109. Weeks, B. L., Noy, A., Miller, A. E., De Yoreo, J. J., **Effect of dissolution kinetics on feature size in dip-pen nanolithography**. *Phys. Rev. Lett.* **2002,** 88, 255505.

110. Hampton, J. R., Dameron, A. A., Weiss, P. S., **Transport rates vary with deposition time in dip-pen nanolithography**. *J. Phys. Chem. B* **2005,** 109, 23118.

111. Vettiger, P., Despont, M., Drechsler, U., Durig, U., Haberle, W., Lutwyche, M. I., Rothuizen, H. E., Stutz, R., Widmer, R., Binnig, G. K., **The "Millipede"-More than one thousand tips for future AFM storage.** *IBM J. Res. Develop.* **2000,** 44, 323.

112. Salaita, K., Lee, S. W., Wang, X. Huang, L., Dellinger, T. M., Liu, C., Mirkin, C. A., **Sub-100 nm, centimeter-scale, parallel dip-pen nanolithography**. *Small* **2005,** 1, 940.

113. Zhang, M., Bullen, D., Chung, S. W., Hong, S., Ryu, K. S., Fan, Z., Mirkin, C. A., Liu, C., **A MEMS nanoplotter with high-density parallel dip-pen nanolithography probe arrays**. *Nanotechnology* **2002,** 13, 212.

114. Hong, S., Mirkin, C. A., **A nanoplotter with both parallel and serial writing capabilities**. *Science* **2000,** 288, 1808.

115. Mirkin, C. A., Hong, S., Demers, L., **Dip-pen nanolithography: Controlling surface architecture on the sub-100 nanometer length scale**. *Chem. Phys. Chem* **2001,** 2, 37.

116. Stellacci, F., **Towards industrial-scale molecular nanolithography**. *Adv. Funct. Mater* **2006,** 16, 15.

117. Kim, K. E., Ke. C. Moldovan, N., Espinosa, H. D., **Massively parallel multi-tip nanoscale writer with fluidic capabilities- Fountain pen nanolithography (FPN)**. In *4th International Symmposium on MEMS and Nanotechnology*, Charlotte, **2003**; pp 235.

118. Salaita, K., Wang, Y., Fragala, J., Vega, R. A., Liu, C., Mirkin, C. A., **Massively parallel dip–pen nanolithography with 55000-pen two-dimensional arrays**. *Angew. Chem.* **2006,** 118, 7378.

119. Lee, K. B., Park, S. J., Mirkin, C. A., Smith, J. C., Mrksich, M., **Protein nanoarrays generated by dip-pen nanolithography**. *Science* **2002,** 295, 1702.

120. Zhang, H., Lee, K. B., Li, Z., Mirkin, C. A., **Biofunctionalized nanoarrays of inorganic structures prepared by dip-pen nanolithography**. *Nanotechnology* **2003,** 14, 1113.

121. Lee, K. B., Kim, E. Y., Mirkin, C. A., Wolinsky, S. M., **The use of nanoarrays for highly sensitive and selective detection of human immunodeficiency virus type 1 in plasma**. *Nano Lett.* **2004,** 4, 1869.

122. Harriott, L. R., **Scattering with angular limitation projection electron beam lithography for suboptical lithography**. *J. Vac. Sci. Technol. B* **1997,** 15, 2130.

123. Sohda, Y., Ohta, H., Murai, F., Yamamoto, J., Kawano, H., Satoh, H., Itoh, H., **Recent progress in cell-projection electron-beam lithography**. *Microelectron. Engn.* **2003,** 67-68, 78.

124. van Bruggen, M. J., van Someran, B., Kruit, P., **Multibeam electron source for nanofabrication using electron beam induced deposition**. *Microelctron. Engn.* **2006,** 83, 771.

125. Chang, T. H. P., Mankos, M., Lee, K. Y., Muray, L. P., **Multiple electron-beam lithography**. *Microelctron. Engn.* **2001,** 57-58, 117.

126. Mendes, P. M., Preece, J. A., **Precision chemical engineering: integrating nanolithography and nanoassembly**. *Curr. Opin. Colloid Interface Sci* **2004,** 9, 236.

127. Harnett, C. K., Satyalakshmi, K. M., Craighead, H. G., **Bioactive templates fabricated by low-energy electron beam lithography of self-assembled monolayers** *Langmuir* **2001,** 17, 178.

128. Rundqvist, J., Hoh, J. H., Haviland, D. B., **Directed immobilization of protein-coated nanospheres to nanometer-scale patterns fabricated by electron beam lithography of poly(ethylene glycol) self-assembled monolayers**. *Langmuir* **2006,** 22, 5100.

129. Zhang, G. J., Tanii, T., Miyake, T., Funatsu, T., Ohdomari, I., **Attachment of DNA to microfabricated arrays with self-assembled monolayer**. *Thin Solid Films* **2004,** 464-465, 452.

130. Lussi, J. W., Tang, C., Kuenzi, P. A., Staufer, U., Csucs, G., Voros, J., Danuser, G., Hubbell, J. A., Textor, M., **Selective molecular assembly patterning at the nanoscale: a novel platform for producing protein patterns by electron-beam lithography on SiO2/indium tin oxide-coated glass substrates**. *Nanotechnology* **2005,** 16, 1781.

131. Kunzi, P. A., Lussi, J., Aeschimann, L., Danuser, G., Textor, M., de Rooji, N. F., Staufer, U., **Nanofabrication of protein-patterned substrates for future cell adhesion experiments**. *Microelectron. Engn.* **2005,** 78-79, 582.

132. Senarantne, W., Sengupta, P., Jakubek, V., Holowka, D., Ober, C. K., Baird, B., **Functionalized surface arrays for spatial targeting of immune cell signalling**. *J. Am. Chem. Soc* **2006,** 128, 5594.

133. Cherniavskaya, O., Chen, C. J., Heller, E., Sun, E., Provezano, J., Kam, L., Hone, J., Sheetz, M. P., Wind, S. J., **Fabrication and surface chemistry of nanoscale bioarrays designed for the study of cytoskeletal protein binding interactions and their effect on cell motility**. *J. Vac. Sci. Technol. B* **2005,** 23, 2972.

134. Powell, T., Yoon, J. Y., **Fluorescent biorecognition of gold nanoparticle-IgG conjugates self-assembled on E-beam patterns**. *Biotechnol. Prog.* **2006,** 22, 106.

135. Denis, F. A., Pallandre, A., Nysten, B., Jonas, A. M., Dupont-Gillain, C. C., **Alignment and assembly of adsorbed collagen molecules induced by anisotropic chemical nanopatterns**. *Small* **2005,** 10, 984.

136. Borini, S., D'Auria, S., Rossi, M., Rossi, A. M., **Writing 3D protein nanopatterns onto a silicon nanosponge**. *Lab Chip* **2005,** 5, 1048.

137. Sun, H., Wirsen, A., Albertsson, A. C., **Electron beam-induced graft polymerization of acrylic acid and immobilization of arginine-glycine-aspartic acid-containing peptide onto nanopatterned polycaprolactone**. *Biomacromolecules* **2004,** 5, 2275.

138. Hong, Y., Krsko, P., Libera, M., **Protein surface patterning using nanoscale PEG hydrogels**. *Langmuir* **2004,** 20, 11123.

139. Bhushan, B., **Nanotribology and nanomechanics of MEMS/NEMS and BioMEMS/BioNEMS materials and devices**. *Microelctron. Engn.* **2007,** 84, 387.

140. Liu, Y., Mu, L., Liu, B., Kong, J., **Controlled switchable surface**. *Chem. Eur. J.* **2005,** 11, 2622.

141. Li, C., Ren, B., Zhang, Y., Cheng, Z., Liu, X., Tong, Z., **A novel ferroceneylazobenzene self-assembled monolayer on an ITO electrode: Photochemical and electrochemical behaviors**. *Langmuir* **2008,** 24, 12911.

142. Riskin, M., Basnar, B., Chegel, V. I., Katz, E., Willner, I., Shi, F., Zhang, X., **Switchable surface properties through the electrochemical or biocatalytic generation of Ag0 nanoclusters on monolayer-functionalized electrodes**. *J. Am. Chem. Soc* **2006,** 128, 1253.

143. Hayashi, G., Hagihara, M., Dohno, C., Nakatani, K., **Photoregulation of a peptide-RNA interaction on a gold surface**. *J. Am. Chem. Soc* **2007,** 129, 8678.

144. TYeo, W. S., Mrksich, M., **Electroactive Self-Assembled Monolayers that Permit Orthogonal Control over the Adhesion of Cells to Patterned Substrates**. *Langmuir* **2006,** 22, 10816.

145. Chan, E. W. L., Yousaf, M. N., **Immobilization of ligands with precise control of density to electroactive surfaces**. *J. Am. Chem. Soc* **2006,** 128, 15542.

146. Liu, Y., Mu, L., Liu, B., Zhang, S., Yang, P., Kong, J., **Controlled protein assembly on a switchable surface**. *Chem. Commun.* **2004**, 11945.

147. Yeo, W. S., Mrksich, M., **Electroactive self-assembled monolayers that permit orthogonal control over the adhesion of cells to patterned substrates**. *Langmuir* **2006,** 22, 10816.

148. Ebara, M., Yamato, M., Aoyagi, T., Kikuchi, A., Sakai, K., Okano, T., **A novel approach to observing synergy fffects of PHSRN on integrin–RGD binding using intelligent surfces**. *Adv. Mater.* **2008,** 20, 3034.

149. Auernheimer, J., Dahmen, C., Hersel, U., Bausch, A., Kessler, H., **Photoswitched cell adhesion on surfaces with RGD peptides**. *J. Am. Chem. Soc* **2005,** 127, 16107.

150. Kleinman, H. K., Philp, D., Hoffman, M. P., **Role of the extracellular matrix in morphogenesis**. *Curr. Opin. Biotechnol.* **2003,** 14, 526.

151. Caldas, C., Coeiho, V., Kalil, J., Moro, A. M., Maranhao, A. O., Brigido, M. M., **Humanization of the anti-CD18 antibody 6.7: an unexpected effect of a framework residue in binding to antigen**. *Molecular Immunology* **2003,** 39, 941.

152. She, S., Xu, B., He, M., Lan, X., Wang, Q., **Rnesmearc2h3-H1 suppresses hepatocarcinoma cell adhesion and migration on fibronectin by modulating glycosylation of integrin beta1**. *J. Exp. Clin. Canc. Res.* **2010,** 29, 93.

153. Becker, W. M., Kleinsmith, L. J., Hardin, J., Bertoni, G. P., *The world of the cell*. Benjamin Cummings: San Francisco, **2008**.

154. Sheetz, M. P., Felsenfeld, D. P., Galbraith, C. G., **Cell migration: regulation of force on extracellular matrix-integrin complexes**. *Trends. Cell. Biol.* **1998,** 8, 51.

155. Lutolf, M. P., Hubbell, J. A., **Synthetic biomaterials as instructive extracellular microenvironments for morphogenesis in tissue engineering.** *Nat. Biotechnol.* **2005,** 23, 47.

156. Yoshida, K., Soldati, T., **Dissection of amoeboid movement into two mechanically distinct modes**. *J. Cell. Sci.* **2006,** 119, 3833.

157. Fan, C., Plaxco, K. W., Heeger, A. J., **Electrochemical interrogation of conformational changes as a reagentless method for the sequence-specific detection of DNA**. *PNAS* **2003,** 100, 9134.

158. Rant, U., Arinaga, K., Scherer, S., Pringsheim, E., Fujita, S., Yokoyama, N., Tornow, M., Abstreiter, G., **Switchable DNA interfaces for the highly sensitive detection of label-free DNA targets**. *PNAS* **2007,** 104, (44), 17361.

159. Mao, Y., Kuo, C., Ouyang, Q., **Studies of temperature-dependent electronic transduction on DNA hairpin loop sensor**. *Nucl. Acid. Res.* **2003,** 31, e108.

160. Ricci, F., Bonham, A. J., Mason, A. C., Reich, N. O., Plaxco, K. W., **Reagentless, electrochemical approach for the specific detection of double- and single-stranded DNA binding proteins**. *Anal. Chem* **2009,** 81, 1608.

161. Huber, D. L., Manginell, R. P., Samara, M. A., Kim, B., Bunker, B. C., **Programmed adsorption and release of proteins in a microfluidic device**. *Science* **2003,** 301, 352.

162. Yamanaka, H., Yoshizako, K., Akiyama, Y., Sota, H., Hasegawa, Y., Shinohara, Y., Kikuchi, A., Okano, T., **Affinity chromatography with collapsibly tethered ligands**. *Anal. Chem* **2003,** 75, 1658.

163. Yoshizako, K., Akiyama, Y., Yamanaka, H., Shinohara, Y., Hasegawa, Y., Carredano, E., Kikuchi A., Okano, T., **Regulation of protein binding toward a ligand on**

chromatographic matrixes by masking and forced-releasing effects using thermoresponsive polymer. *Anal. Chem.* **2002,** 74, 4160.

164. Nagase, K., Kobayashi, J., Kikuchi, A., Akiyama, Y., Kanazawa, H., Okano, T., **Interfacial property modulation of thermoresponsive polymer brush surfaces and their interaction with biomolecules**. *Langmuir* **2007,** 23, 9409.

165. Yousaf, M. N., Houseman, B. T., Mrksich, M., **Using electroactive substrates to pattern the attachment of two different cell populations**. *PNAS* **2001,** 98, 5992.

166. Yeo, W. S., Hodneland, C. D., Mrksich, M., **Electroactive monolayer substrates that selectively release adherent cells**. *ChemBioChem* **2001,** 7, 590.

167. Yousaf, M. N., Houseman, B. T., Mrksich, M., **Turning on cell migration with electroactive substrates**. *Angew. Chem. Int. Ed.* **2001,** 40, 1093.

168. Curreli, M., Li, C., Sun, Y., Lei, B., Gundersen M. A., Thompson, M. E., Zhou, C., **Selective functionalization of In2O3 nanowire mat devices for biosensing applications**. *J. Am. Chem. Soc* **2005,** 127, 6922.

169. Mali, P., Bhattacharjee, N., Searson, P. C., **Electrochemically programmed release of biomolecules and nanoparticles**. *Nano Lett.* **2006,** 6, 1250.

170. Yeo, W. S., Mrksich, M., **Electroactive substrates that reveal aldehyde groups for bio-immobilization**. *Adv. Mater.* **2004,** 16, 1352.

171. Steuerman, D. W., Tseng, H. R., Peters, A. J., Flood, A. H., Jeppesen, J. O., Nielsen K. A., Stoddart, J. F., Heath, J. R., **Molecular-mechanical switch-based solid-state electrochromic devices**. *Angew. Chem. Int. Ed.* **2004,** 43, 6486.

172. Katz, E., Sheeney-Haj-Ichia, L., Willner, I., **Electrical contacting of glucose oxidase in a redox-active rotaxane configuration**. *Angew. Chem.* **2004,** 116, 3354.

173. Tencer, M., Berini, P., **Toposelective electrochemical desorption of thiol SAMs from neighboring polycrystalline gold surfaces**. *Langmuir* **2008,** 24, 12097.

174. Inaba, R., Khademhosseini, A., Suzuki, H., Fukuda, J., **Electrochemical desorption of self-assembled monolayers for engineering cellular tissues**. *Biomaterials* **2009,** 30, 3573.

175. Hoover, D. K., Lee, E. J., Chan, E. W. L., Yousaf, M. N., **Electroactive nanoarrays for biospecific ligand mediated studies of cell adhesion**. *ChemBioChem* **2007,** 8, 1920.

176. Chan, E. W. L., Yousaf, M. N., **Site-selective immobilization of ligands with control of density on electroactive microelectrode arrays**. *Chem. Phys. Chem* **2007,** 8, 1469.

177. Lee, S., Shon, Y. S., Colorado, R., Guenard, R. L., Lee, R., Perry, S. S., **The influence of packing density and surfce order on the frictional properties of alkanethiols self-assembled monolayers (SAMs) on gold: A comparison of SAMs derived from normal and spiroalkanethiols**. *Langmuir* **2000,** 16, (5), 2220.

178. Shao, H. B., Yu, H. Z., Zhao, J. W., Zhang, H. L., Liu, Z. F., **The effect of packing density on the electron transfer kinetics of an azobenzenethiol monolayer on gold**. *Chem Lett* **1997,** 26, (8), 749.

179. Lahann, J., Mitragotri, S., Tran, T. N., Kaido, H., Sundaram, J., Choi, I. S., Hoffer, S., Somorjai, G. A., Langer, R., **A reversibly switching surface**. *Science* **2003,** 299, 371.

180. Yang, X., Wang, Q., Wang, K., Tan, W., Yao, J., Li, H., **Electrical switching of DNA monolayers investigated by surface plasmon resonance**. *Langmuir* **2006,** 22, 5654.

181. Rant, U., Arinaga, K., Fujita, S., Yokoyama, N., Abstreiter, G., Tornow, M., **Dynamic electrical switching of DNA layers on a metal surface**. *Nano Lett.* **2004,** 4, 2441.

182. Mao, Y., Luo, C., Deng, W., Jin, G., Yu, X., Zhang, Z., Ouyang, Q., Chen, R., Yu, D., **Reversibly switchable DNA nanocompartment on surfaces**. *Nucl. Acid. Res.* **2004,** 32, e144.

183. Rant, U., Arinaga, K., Scherer, S., Pringsheim, E., Fujita, S., Yokoyama, N., Tornow, M., Abstreiter, G., **Switchable DNA interfaces for the highly sensitive detection of label-free DNA targets**. *PNAS* **2007,** 104, 17364.

184. Mao, Y., Liu, D., Wang, S., Luo, S., Wang, W., Yang, Y., Ouyang, Q., Jiang, L., **Alternating-electric-field-enhanced reversible switching of DNA nanocontainers with pH**. *Nucl. Acid. Res.* **2007,** 35, e33.

185. Wang, S., Liu, H., Liu, D., Ma, X., Fang, X., Jiang, L., **Enthalpy-driven three-state switching of a superhydrophilic/superhydrophobic surface**. *Angew. Chem. Int. Ed.* **2007,** 46, 3915.

186. Rant, C., Arinaga, K., Fujita, S., Yokoyama, N., Abstreiter, G., Tornow, M., **Electrical manipulation of oligonucleotides grafted to charged surfaces**. *Org. Biomol. Chem.* **2006,** 4, 3448.

187. Bardecker, J. A., Afzali, A., Tulevski, G. S., Graham, T., Hannon, J. B., Jen, A. K. Y., **Directed assembly of single-walled carbon nanotubes via drop-casting onto a UV-patterned photosensitive monolayer**. *J. Am. Chem. Soc* **2008,** 130, 7226.

188. Campbell, D. J., Herr, B. R., Hulteen, J. C., Van Duyne, R. P., Mirkin, C. A., **Ion-gated electron transfer in self-assembled monolayer films.** *J. Am. Chem. Soc* **1996,** 118, 10211.

189. Namiki, K., Sakamoto, A., Murata, M., Kume, S., Nishihara, H., **Reversible photochromism of a ferrocenylazobenzene monolayer controllable by a single green light source**. *Chem. Commun.* **2007**, 4650.

190. Aleveque, O., Blanchard, P. Y., Gautier, C., Dias, M., Breton, T., Levillain, E., **Electroactive self-assembled monolayers: Laviron's interaction model extended to non-random distribution of redox centers**. *Electrochem. Commun.* **2010,** 12, 1462.

191. Hayashi, G., Hagihara, M., Nakatani, K., **RNA aptamers that reversibly bind photoresponsive azobenzene-containing peptides**. *Chem. Eur. J.* **2009,** 15, 424.

192. Immos, C. E., Lee, S. J., Ginstaff, M. W., **Conformationally gated electrochemical gene detection**. *ChemBioChem* **2004,** 5, 1100.

193. Immos, C. E., Lee, S. J., Ginstaff, M. W., **DNA-PEG-DNA triblock macromolecules for reagentless DNA detection**. *J. Am. Chem. Soc* **2004,** 126, 10814.

194. Xiao, Y., Lubin, A. A., Baker, B. R., Plaxco, K. W., Heeger, A. J., **Single-step electronic detection of femtomolar DNA by target-induced strand displacement in an electrode-bound duplex**. *PNAS* **2006,** 105, 16677.

195. Mejillano, M. R., Kojima, S. I., Applewhite, D. A., Gertler, F. B., Svitkina, T. M., Borisy, G. G., **Lamellipodial versus filopodial mode of the actin nanomachinery: Pivotal role of the filament barbed end**. *Cell* **2004,** 118, 363.

196. Binning, G., Quate, C. F., Gerber, C., **Atomic force microscopy with simultaneous a.c. conductive contrast for the analysis of carbon fibre surfaces**. *Phys. Rev. Lett.* **1986,** 56, 930.

197. Lakowicz, J. R., **Principles of fluorescence spectroscopy** [electronic resource]. In Lakowicz, J. R., Ed. Springer Science+Business Media, LLC: Boston, MA, 2006.

198. Briggs, D., Seah, M. P., *Practical surface analysis volume 1-auger and X-ray photoelectron spectroscopy*. John Wiley & Sons: Chichester (UK), **1996**.

199. Fisher, A. C., *Electrode dynamics* Oxford : Oxford University Press: Oxford **1996**.

200. Schasfoort, R. B. M., Richard, B. M., Tudos, A. J., *Handbook of surface plasmon resonance* Cambridge : Royal Society of Chemistry: Cambridge, **2008**.

201. Binnig, G., Rohrer, H., Gerber, C., Weibel, E., **Surface studies by scanning tunneling microscopy**. *Phys. Rev. Lett.* **1982,** 49, 57.

202. Ikai, A., **STM and AFM of bio/organic molecules and structures**. *Surf. Sci. Rep.* **1996,** 26, 261.

203. Digital Instruments Veeco Metrology Group (Santa Barbara, U., *Digital instruments veeco metrology group, multimode™ SPM instruction manual version 4.31ce*. Digital Instruments Veeco Metrology Group: Santa Barbara, USA, **1999**; p 1-5.

204. Servoli, E., Maniglio, D., Aguilar, M. R., Motta, A., Roman, J. S., Belfiore, L. A., Migliaresi, C. , **Quantitative analysis of protein adsorption via atomic force microscopy and surface plasmon resonance**. *Macromol. Biosci* **2008,** 8, 1126.

205. Attard, G., Barnes, C. In *Surfaces*, Oxford, **1998**; Oxford University Press Oxford, 1998; p 61.

206. Wouters, D., Schubert, U. S., **Nanolithography and nanochemistry: Probe-related patterning techniques and chemical modification for nanometer-sized devices**. *Angaw. Chem. Int. Ed* **2004,** 43, 2480.

207. Meyer, E., Heinzelmann, H., Grutter, P., Jung, T., Hidber, H-D., Rudin, H., Guntherodt, H. J., **Atomic force microscopy for the study of tribology and ahesion**. *Thin Solid Films* **1989,** 181, 527.

208. Gholamrezaie, F., Mathijssen, S. G. J., Smits, E. C. P., Genus, T. C. T., van Hal, P. A., Ponomarenko, S. A., Flesch, H. G., Resel, R., Cantatore, E., Blom, P. W. M., de Leeuw, D. M., **Ordered semiconducting self-assembled monolayers on polymeric surfaces utilized in organic integrated circuits**. *Nano Lett.* **2010,** 10, 1998.

209. Nnebe, I., Schneider, J. W., **Tapping-mode AFM – force measurement capabilities on compliant surfaces**. *Mat. Res. Soc. Symp. Proc.* **2004,** 790, 4.3.1.

210. Kueng, A., Kranz, C., Lugstein, A., Bertagnolli, E., Mizaikoff, B., **Integrated AFM–SECM in tapping mode: Simultaneous topographical and electrochemical imaging of enzyme activity**. *Angew. Chem. Int. Ed.* **2003,** 42, 3237.

211. Berlman, I. B., *Handbook of fluorescence spectra of aromatic molecules*. 2nd ed.; Academic Press: New York, **1971**.

212. Turner, N., Schreifels, J. A. , **Surface analysis: X-ray photoelectron spectroscopy and auger electron spectroscopy**. *Anal. Chem.* **1994,** 66, 163R.

213. Dietrich, P. M., Graf, N., Gross, T., Lippitz, A., Krakert, S., Schupbach, B., Terfort, A., Unger, W. E. S., **Amine species on self-assembled monolayers of w-aminothiolates on gold as identified by XPS and NEXAFS spectroscopy**. *Surf. Interface Anal.* **2010,** 42, 1184.

214. Perruchot C., W. J. F., Lowe C., White, R. G., Cumpson P. J., **Angle-resolved XPS characterization of urea formaldehyde–epoxy systems**. *Surf. Interface Anal.* **2002,** 33, 869.

215. Gonçalves D., I. E. A., **Fundamentals and applications of spectroscopic ellipsometry**. *Quim. Nova* **2002,** 25, (5), 794.

216. Kim S-H, O. K.-S., Im J-H,Kim J-H,Koh K-N,Kang S-W., **Photoinduced refractive index change of self-assembled spiroxazaine monolayer based on surface plasmon resonance**. *Dyes and Pigments* **2000,** 46, 55.

217. Chaudhury M K, **Interfacial interaction between low-energy surfaces**. *Materials Science and Engineering* **1996,** R16, 97.

218.	Bowen, J., Pettitt, M. E., Kendall, K., Leggett, G. J., Preece, J. A., Callow, M. E., Callow, J. A., **The influence of surface lubricity on the adhesion of Navicula perminuta and Ulva linza to alkanethiol self-assembled monolayers**. *J. R. Soc. Interface* **2007,** 4, 473.

219.	Chen W., F. A. Y., Hsieh M C.,Oner D.,; Youngblood J., M. T. J., **Ultrahydrophobic and Ultralyophobic Surfaces: Some Comments and Examples**. *Langmuir* **1999,** 15, 3395.

220.	von Helmholtz, H. L. F., **Some laws concerning the distribution of electrical currents in conductors**. *Ann. Physik* **1853,** 89, 211.

221.	de Levie, R., **Notes on guoy diffuse-layer theory**. *J. Electroanal. Chem* **1990,** 278, 17.

222.	Chapman, D. L., **A contribution to the theory of electrocapillarity** *Phil. Mag* **1913,** 25, 475.

223.	Stern, O., **The stern theory of electrochemical double layer**. *Electrochem.* **1924,** 30, 508.

224.	Grahame, D. C., **The electrical double layer and the theory of electrocapillarity**. *Chem. Rev.* **1947,** 41, 441.

225.	Wood, R. W., **On a remarkable case of uneven distribution of light in a diffraction grating spectrum**. *Philos. Mag* **1902,** 4, 396.

226.	Wood, R. W., **Diffraction gratings with controlled groove form and abnormal distribution of intensity**. *Philos. Mag* **1912,** 23, 310.

227.	Otto, A., **Excitation of nonradiative surface waves in silver by the method of frustrated total reflection**. *Z. Phys.* **1968,** 216, 398.

228. Kretschmann, E., **The determination of optical constants of metals by excitation of Oberflachenplasmaschwingugnen**. *Z. Phys* **1971,** 241, 313.

229. Kretschmann, E. R., H., **Radiative decay of nonradiative surface plasmon excited by light**. *Z. Naturforsch., Teil A.* **1968,** 23, 2135.

230. Homola, J., **Surface plasmon resonance based sensors**. In *Springer Series on Chemical Sensors and Biosensors.*, Wolfbeis, O. S. S., Berlin, Ed. 2006; Vol. 4.

231. Patskovsky, S., Jacquemart, R., Meunier, M., Crescenzo, G. D., Kabashin, A. V., **Phase-sensitive spatially-modulated surface plasmon resonance polarimetry for detection of biomolecular interactions**. *Sensors actuat. B-Chem.* **2008,** 133, 628.

232. Lodish, H., Berk, A., Kaiser, C. A., Krieger, M., *Molecular cell biology*. 6th ed.; W. H. Freeman & Co Ltd: New York, **2007**; p 1296.

233. Millard, T. H., Sharp, S. J., Machesky, L. M., **Signalling to actin assembly via the WASP (Wiskott–Aldrich syndrome protein)-family proteins and the Arp2/3 complex**. *Biochem. J.* **2004,** 280, 1.

234. Takenawa, T., Suetsugu, S., **The WASP–WAVE protein network: connecting the membrane to the cytoskeleton**. *Nat. Rev. Mol. Cell Bio.* **2007,** 8, 37.

235. Machesky, L. M., Mullins, R. D., Higgs, H. N., Kaiser, D. A., Blanchoin, L., May, R. C., Hall, M. E., Pollard, T. D., **Scar, a WASP-related protein, activates nucleation of actin filaments by the Arp2/3 complex**. *PNAS* **1999,** 96, 3739.

236. Volkmann, N., Amann, K. J., Stoilova-McPhie, S., Egile, C., Winter, D. C., Hazwlwood, L., Heuser, J. E., Li, R., Pollard, T. D., Hanei, D., **Structure of Arp2/3 complex in its activated state and in actin filament branch junctions**. *Science* **2001,** 293, 2456.

237. Mullins, R. D., Heuser J. A., Pollard, T. D., **The interaction of Arp2/3 complex with actin: Nucleation, high affinity pointed end capping, and formation of branching networks of filaments**. *PNAS* **1998,** 95, 6181.

238. Pantaloni, D., Boujemaa, R., Didry, D., Gounon, P., Carlier, M. F., **The Arp2/3 complex branches filament barbed ends: functional antagonism with capping proteins**. *Nat. Cell. Biol.* **2000,** 2, 358.

239. Svitkina, T. M., Borisy, G. G., **Arp2/3 complex and actin depolymerizing factor/cofilin in dendritic organization and treadmilling of actin filament array in lamellipodia**. *J. Cell. Bio.* **1999,** 145, 1009.

240. Biyasheva, A., Svitkina, T., Kunda, P., Baum, B., Borisy, G., **Casade pathway of filopodia formation downstream of SCAR**. *J. Cell. Sci.* **2004,** 117, 837.

241. Svitkina, T. M., Bulanova, E. A., Chaga, O. Y., vignjevic, D. M., Kojima, S., VAsiliev, J. M., Borisy, G. G., **Mechanism of filopodia initiation by reorganization of a dendritic network**. *J. Cell. Bio.* **2003,** 160, 409.

242. Prime, K. L., Whitesides, G. M., **Self-assembled organic monolayers: model systems for studying adsorption of proteins at surfaces**. *Science* **1991,** 252, 1164.

243. Pesen, D., Erlandsson, A., Ulfendahl, M., Haviland, D. B., **Image reversal for direct electron beam patterning of protein coated surfaces**. *Lab Chip* **2007,** 7, 1603.

244. Turan, E., Caykara, T., **Construction of hydroxyl-terminated poly(N-isopropylacrylamide) brushes on silicon wafer via surface-initiated atom transfer radical polymerization**. *J. Polym. Sci.Pol. Chem.* **2010,** 48, 3880.

245. Wu, Y., Kouno, M., Saito, N., Nae, F.A., Inoue, Y., Takai, O., **Patterned hydrophobic–hydrophilic templates made from microwave-plasma enhanced chemical vapor deposited thin films**. *Thin Solid Films* **2007,** 515, 4203.

246. Sugimura, H., Saito, N., Ishida, Y., Ikeda, I., Hayashi, K., **Photochemical reaction of organosilane self-assembled monolayer as studied by scanning probe microscopy**. *J. Vac. Sci. Technol. A* **2004,** 22, 1428.

247. Lee, M. H., Boettiger, D., Ducheyne, P., Composto, R. J., **Self-assembled monolayers of omega-functional silanes: A platform for understanding cellular adhesion at the molecular level**. *Silanes and Other Coupling Agents* **2007,** 4, 1.

248. Li, J. R., Garno, J. C., **Eluciating the role of surface hydrolysis on preparing organosilane nanostructures via particle lithography**. *Nano Lett.* **2008,** 8, (7), 1916.

249. Calma, M. C., Reinhoudt, D. N., **New materials for metal ion sensing by self-assembled monolayers on glass**. *Adv. Mater.* **2001,** 15, 1171.

250. Collier, J. H., Mrksich, M., **Engineering a biospecific communication pathway between cells and electrodes**. *PNAS* **2006,** 103, 2021.

251. Mendes, P. M., **Stimuli-responsive surfaces for bio-appliations**. *Chem. Soc. Rev.* **2008,** 37, 1.

252. Ista, L. K., Lopez, G. P., **Lower critical solubility temperature materials as biofouling release agents**. *J. Ind. Microbiol. Biotechnol.* **1998,** 20, 121.

253. Anikin, K., Rocker, C., Wittemann, A., Wiedenmann, J., Ballauff, M., Nienhaus, U., **Polyelectrolyte-mediated protein adsorption: fluorescent protein binding to individual polyelectrolyte nanospheres**. *J. Phys. Chem. B* **2005,** 109, 5418.

254. Yamato, M., Konno, C., Utsumi, M., Kikuchi, A., Okano, T., **Thermally responsive polymer-grafted surfaces facilitate patterned cell seeding and co-culture**. *Biomaterials* **2002,** 23, 561.

255. Ebara, M., Yamato, M., Aoyagi, T., Kikuchi, A., Sakai, K., Okano, T., **Temperature-responsive cell culture surfaces enables "On-Off" affinity control between cell integrins and RGDS ligands**. *Biomacromolecules* **2004,** 5, 505.

256. Ulijn, R. V., **Enzyme-responsive materials: a new class of smart biomaterials**. *J. Mater. Chem.* **2006,** 16, 2217.

257. Callari, F. L., Petralia, S., Conoci, S., Sortino, S., **Light-triggered DNA release by dynamic monolayer films**. *New J. Chem.* **2008,** 32, 1899.

258. Liu, B., Xie, Y. Y., Shao, H. W., Jiang, X. Y., **Using azobenzene-embedded slef-assembled monolayers to photochemically control cell adhesion reversibility**. *Angew. Chem.-Int. Edit.* **2009,** 48, 4406.

259. Zareie, H. M., Boyer, C., Bulmus, V., Nateghi, E., Davis, T. P., **Temperature-responsive self-assembled monolayers of oligo(ethylene glycol): control of biomolecular recognition**. *ACS Nano* **2008,** 2, 757.

260. Becker, J. M., Wilchek, M., **Inactivation by avidin of biotin-modified bacteriophage**. *Biochim. Bioohys. Acta* **1972,** 264, 165.

261. Heitzmann, H., Richards, F. M., **Use of avidin-biotin complex for specific staining of biological membranes in electron microscopy**. *PNAS* **1974,** 71, (9), 3537.

262. Hiller, Y., Gershoni, J. M., Bayer, E. A., Wilchek, M., **Biotin binding to avidin**. *Biocehm. J.* **1987,** 248, 167.

263. Green, N. M., **Avidin- the use of C14 biotin for kinetic studies and for assay**. *Biochem. J.* **1963,** 89, 585.

264. Tausig, F., Wolf, F.J., **Streptavidin-a substance with avidin-like properties produced by microorganisms**. *Biocehm Biophys Res Commun* **1964,** 14, 205.

265. Rosano, C., Arosio, P., Bolognesi, M., **The X-ray three-dimensional structure of avidin**. *Biomol. Eng.* **1999,** 16, 5.

266. Mrksich, M., **What can surface chemistry do for cell biology?** *Curr. Opin. Chem. Biol* **2002,** 6, 794.

267. Strong, L., Whitesides, G. M., **Structures of self-assembled monolayer films of organosulfur compounds adsorbed on gold single crystals: Electron diffraction studies**. *Langmuir* **1988,** 4, 546.

268. Wang, H., Chen, S., Li, L., Jiang, S., **Improved Method for the Preparation of Carboxylic Acid and Amine Terminated Self-Assembled Monolayers of Alkanethiolates**. *Langmuir* **2005,** 21, (7), 2633.

269. Hooper, A. E., Werho, D., Hopson, T., Palmer, O., **Evaluation of amine- and amide-terminated self-assembled monolayers as "Molecular glues" for Au and SiO2 substrates**. *Surf. Interface Anal.* **2001,** 31, 809.

270. Dewick, P. M., *Essentials of organic chemistry: for students of pharmacy, medicinal chemistry and biological chemistry*. John Wiley and Sons: 2006.

271. Li, H., Park, S. H., Reif, J. H., LaBean, T. H., Yan, H., **DNA-templated self-assembly of protein and nanoparticle linear arrays**. *J. Am. Chem. Soc* **2003,** 126, 418.

272. Perez-Luna, V. H., O'Brien, M. J., Opperman, K. A., Hampton, P. D., Lopez, G. P., Klumb, L. A., Stayton, P. S., **Molecular recognition between genetically engineered streptavidin and surface-bound biotin**. *J. Am. Chem. Soc* **1999,** 121, 6469.

273. Yoon, K. R., Chi, Y. S., Lee, K. B., Lee, J. K., Kim, D. J., Koh, Y. J., Joo, S. W., Yun, W. S., Choi, I .S., **Surface initiated, ring opening polymerization of p-dioxanone from gold and silicon oxide surfaces**. *J. Mater. Chem.* **2003,** 13, 2910.

274. Laiho, T., Leiro, J. A., Lukkari, J., **XPS study of irradiation damage and different metal-sulfur bonds in dodecanethiol monolayers on gold and platinum surfaces**. *Appl. Surf. Sci.* **2003,** 212-213, 525.

275. Beulen, M. W. J., Kastenberg, M. I., van Veggel, F. C. J. M., Reinhoudt, D. N., **Electrochemical stability of self-assembled monolayers on gold**. *Langmuir* **1998,** 14, 7463-.

276. Lemay, D. M., Shepherd, J. L., **Electrochemical fabrication of a heterogeneous binary SAM on polycrystalline Au**. *Electrochimica Acta* **2008,** 54, 388.

277. Everett, W. R., Fritsch-Faules, I., **Factors that influence the stability of self-assembled organothiols on gold under electrochemical conditions**. *Anal. Chim. Acta* **1995,** 307, 253.

278. Sethuraman A., G., B., **Protein structural perturbation and aggregation on homogeneous surfaces**. *J. Biophys.* **2005,** 88, 1322.

279. Lahiri, J., Isaacs, L., Tien, J., Whitesides, G. M., **A strategy for the generation of surfaces presenting ligands for studies of binding based on an active ester as a common reactive intermediate: A surface plasmon resonance study**. *Anal. Chim.* **1999,** 71, 777.

280. Stenberg, E., Persson, B., Roos, H., Urbaniczky, C., **Quantitative determination of surface concentration of protein with surface plasmon resonance using radiolabeled proteins**. *J. Colloid. Inter. Sci.* **1991,** 143, 513.

281. Sugimura, H., Saito, N., Ishida, Y., Ikeda, I., Hayashi, K., **Photochemical reaction of organosilane self-assembled monolayer as studied by scanning probe microscopy**. *J. Vac. Sci. Technol. A* **2004,** 22, (4), 1428.

Appendix 1

Set 1								
solution ratio (P1:TEGT)	N area	S area	Au area	N/Au	S/Au	N/S	surface ratio	No. of TEGT
1:1	0.1	0.06	1.04	0.10	0.06	1.67	1:5	5
1:5	0.18	0.09	1.8	0.10	0.05	2.00	1:4	4
1:10	0.08	0.06	2.04	0.04	0.03	1.33	1:6	6
1:20	0.07	0.07	2.12	0.03	0.03	1.00	1:9	9
1:40	0.04	0.06	2.19	0.02	0.03	0.67	1:15	15
1:50	0.05	0.07	1.58	0.03	0.04	0.71	1:14	14
1:100	0.04	0.06	1.64	0.02	0.04	0.67	1:15	15
1:500	0.01	0.04	1.47	0.01	0.03	0.25	1:42	42
Set 2								
solution ratio (P1:TEGT)	N area	S area	Au area	N/Au	S/Au	N/S	surface ratio	No. of TEGT
1:1	0.23	0.07	2.17	0.11	0.03	3.29	1:1	1
1:5	0.11	0.1	2.98	0.04	0.03	1.10	1:8	8
1:10	0.14	0.09	2.44	0.06	0.04	1.56	1:5	5
1:20	0.04	0.07	3.18	0.01	0.02	0.57	1:17	17
1:40	0.06	0.08	2.65	0.02	0.03	0.75	1:13	13
1:50	0.05	0.06	2.63	0.02	0.02	0.83	1:11	11
1:100	0.02	0.09	1.65	0.01	0.05	0.22	1:48	48
1:200	0.01	0.06	2.32	0.00	0.03	0.17	1:62	62
1:500	0.02	0.08	2.74	0.01	0.03	0.25	1:42	42
Set 3								
solution ratio (P1:TEGT)	N area	S area	Au area	N/Au	S/Au	N/S	surface ratio	No. of TEGT
1:1	0.19	0.07	0.95	0.20	0.07	2.71	1:2	2
1:5	0.11	0.04	1.10	0.10	0.04	2.75	1:2	2
1:10	0.10	0.08	1.42	0.07	0.06	1.25	1:7	7
1:20	0.08	0.06	1.69	0.05	0.04	1.33	1:6	6
1:40	0.05	0.07	1.75	0.03	0.04	0.71	1:13	13
1:50	0.06	0.06	1.83	0.03	0.03	1.00	1:9	9
1:100	0.02	0.06	1.98	0.01	0.03	0.33	1:31	31
1:200	0.03	0.06	2.32	0.01	0.03	0.50	1:20	20
1:500	0.02	0.06	2.16	0.01	0.03	0.33	1:31	31

Table 6.1 XPS data of biotin-KKKKC:TEGT SAMs at different solution ratio.

Average of set 1 - 3							
N/S ratio						No. of TEGT	
solution ratio (P1:TEGT)	1st	2nd	3rd	average	error	average	error
1:1	1.67	3.29	2.71	2.56	0.82	2.67	2.08
1:5	2.00	1.10	2.75	1.95	0.83	5.67	2.08
1:10	1.33	1.56	1.25	1.38	0.16	4.67	1.53
1:20	1.00	0.57	1.33	0.97	0.38	13.33	4.04
1:40	0.67	0.75	0.71	0.71	0.04	16.00	3.61
1:50	0.71	0.83	1.00	0.85	0.14	11.33	2.52
1:100	0.67	0.22	0.33	0.41	0.23	22.00	8.19
1:500	0.25	0.25	0.33	0.28	0.05	38.33	6.35

Table 6.2 Average XPS N/S ratio data of biotin-KKKKC:TEGT SAMs at different solution ratio and the number of TEGT molecule at each solution ratio.
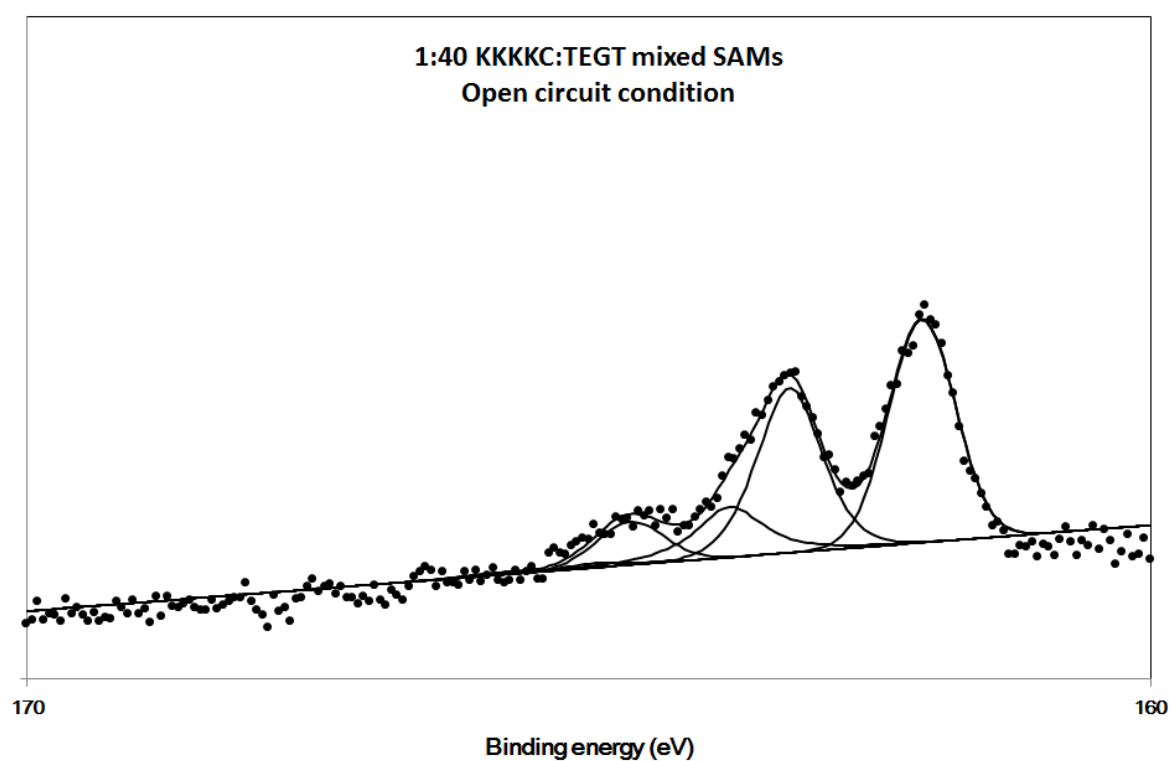
Appendix 2

Figure 6.1 XPS spectra of the S (2p) peak regions of 1:40 KKKKC:TEGT SAMs at open circuit
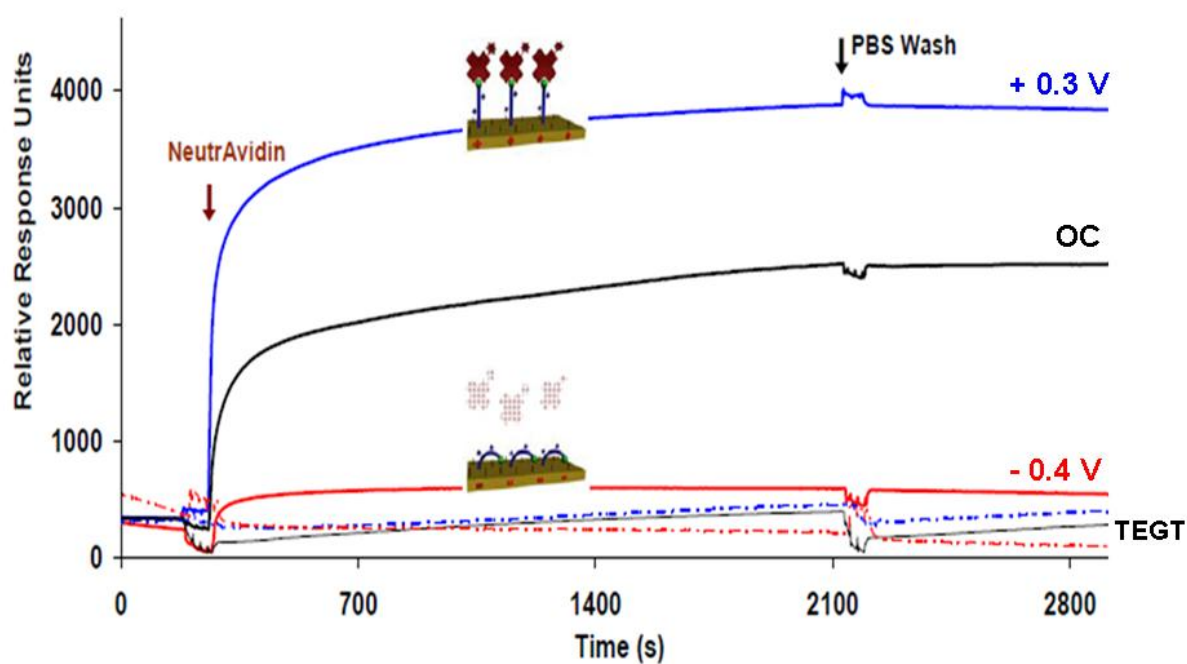
conditions.

Appendix 3

Figure 6.2 SPR sensorgram showing the binding of neutravidin to biotinKKKKC:TEGT

mixed SAMs as described in **figure 4.21**. The dash line represents pure TEGT SAMs under +

0.3 V (**blue** dash line), OC conditions (**black** dash line) and - 0.4 V (**red** dash line).

Recent Publications

List of illustrations and tables

Chapter 1

the cell and there is a strong increase in signal intensity. At time point 2, when the surface is washed with pure buffer solution, the strong signal decreases again but does not drop to the basic level that was present prior to the injection of protein, indicating an irreversible binding of the protein to this hydrophobic surface.

Figure 1.9 SA was brought in contact with an OEG-terminated surface. Unlike the CH_3-terminated SAM surface as shown in **Figure 1.8**, the signal increases when SA was flushed onto the surface as seen in time point 1, but drops back to the baseline after rinsing with the buffer solution (time point 2). These measurements prove that SA does not adsorb onto an OEG-terminated surface.

Figure 1.10 Schematic structure of the streptavidin protein consisting of four subunits. Each subunit possesses a binding pocket for the biotin molecule.

Figure 1.11 Schematic drawing illustrating the specific binding of streptavidin onto a biotinylated surface. By binding the biotin functions to the binding pockets of streptavidin, secure anchorage of streptavidin onto the gold surface is achieved.

Figure 1.12 Fluorescence microscopy image of a SAM prepared by microcontact printing. The stripes consist of a mixture of 25 mol% biotinthiol and 75 mol% OH-terminated thiol. The square is OEG-terminated thiol. The SAM has been immersed in a 100 nM fluorescence-marked SA solution. This protein only binds at the biotin-terminated parts of the surface as can be seen by the fluorescence signal.

Figure 1.13 The quantity of SA molecules anchored to a biotin-functionalized based on the mol% of biotin thiol on the surface.

Figure 1.14 A cartoon representation to demonstrate how bHRP functionalized with biotin can specifically be anchored on a surface. SA is first chemically bound onto the biotinylated surface, and subsequently, the biotin residues of the labelled bHRP can bind to the remaining vacant binding pockets on the SA.

Figure 1.15 Schematic illustration of the electrochemical conversion of NO_2 terminal group to NH_2 terminal group, which can be employed for the attachment of functional linkers and subsequently, the immobilisation of antibodies (primary (PA) and secondary (SA)) on the surface.

Figure 1.16 CV (**blue** curve) of a SAM of 4-nitrothiol phenol, the reduction of NO_2 to NH_2 groups appears as a pronounced peak at around - 0.85 V. CV (**red** curve) of the SAM of 4-nitrothiophenol after the reductive scan.

Figure 1.17 Schematic demonstrating the photolithography process (positive tone).

Figure 1.18 The microcontact printing process.

Figure 1.19 AFM tapping mode images of nanocontact printed titin multimer protein lines on a silicon surface **a)** at large scale and **b)** at high resolution with height profile cross section below.

Figure 1.20 Schematic illustration of the range of stimuli that was used to modulate bioactivity on surface based on SAMs.

Figure 1.21 The release of the RGD peptide from *O*-silyl hydroquinone monolayer (E*-RGD) by electrochemical oxidation followed by the attachment of second ligand, diene-tagged RGD peptide (RGD-Cp) via Diels Alder reaction.

Figure 1.22 Demonstration of dynamic substrates that contain 2 properties: i) the release of RGD ligand, and thus release of cells. ii) the immobilisation of a second RGD ligand leading to cell growth and migration on the surface. **a)** Swiss 3T3 fibroblast cells adhered and spread evenly over the entire substrate. **b)** An electrical potential of 550 mV was applied to the substrate for 5 min, and the substrate was incubated for 4 h. Cells were efficiently released only from the region of RGD peptide ligands that were tethered to the surface of *O*-silyl hydroquinone groups (E*-RGD). **c)** The attachment of second ligand diene-tagged RGD peptide (RGD-Cp) onto the benzoquinone region resulted in the cell migration from fibronectin (circular) regions back onto the RGD regions. After 24 hours, cells were distributed evenly across the whole surface.

Figure 1.23 Electrochemical control of cell adhesion on RGD patterned gold surface. Upon the application of an electrical potential of 650 mV, cells were released from the electroactive *O*-silyl hydroquinone regions (a→b and c→d). Whereas the application of – 650 mV released the cells from benzoquinone regions of the substrate. (a→c and b→d).

Figure 1.24 apo-GOx attached onto the FAD cofactors leading to electron transfer via the redox active rotaxanes molecular wire.

Figure 1.25 a) Schematic showing the LD-SAMs using bulky head groups to create a monolayer that can be switched between hydrophilic and hydrophobic states based on electrical potential applications.[179] **b)** An illustration of the fabrication of LD-SAMs using CD complexes, follow by the transition of anchored MHA at applied potential and subsequent protein assembly.

Figure 1.26 Illustration of LD-SAMs on microfluidic chips to control the adhesion and release of avidin and streptavidin upon the application of corresponding potentials. **a)** The application of negative potential on surface causes the carboxylate group electrostatically repelled from the surface, leading to the capture of positively charged avidin. **b)** Whereas, switching of potential from negative to positive on the surface attracted the carboxylate group towards the surface, causing the release of avidin from the surface. **c)** The application of positive potential on surface causes the ammonium group electrostatically repelled from the surface, leading to the captured of negatively charged streptavidin. **d)** The switching of potential from positive to negative causes the ammonium group attracted towards the surface, resulting the release of negatively charged streptavidin.

Figure 1.27 Alternating potentials applied on the electrically switchable DNA surface. On applying a negative potential, DNA strand repelled from the surface, causing a fluorescence response, whereas, a positive potential forces the DNA tilted towards the surface resulting the quenching of the fluorescence.

Figure 1.28 Electrical switching and hybridization of DNA layers. **a)** The alternating potential applied on the DNA surface. **b)** The fluorescence emission of the Cy3 labelled DNA layer, showing the injection of (arrow) complementary target DNA that hybridize the surface bound Cy3 labelled single stranded probe resulted in an amplified fluorescence signals. **c)** The hybridization of target DNA with the 24 completer sequence nucleotides (**red** data point) to form the 48 completer sequence nucleotides (**blue** data point) resulted in amplified fluorescence signals. 24 non-completer sequence nucleotides (**black** data point) act as a control and exhibits negligible binding affinity.[183]

Figure 1.29 Photoisomerization of azobenzene changes in SAM packing due to *trans* to *cis* isomerization.

Figure 1.30 The *trans-cis* isomerization of photoactive peptide (KRAzR) controls the binding to target RNA aptamers (Red line). The binding is caused by the hydrogen bonding to the guanidinium group and the hydrophobic interactions to azobenzene group (dash line).

Figure 1.31 Signal-off E-DNA sensor based on the surface bound DNA stem loop with a ferrocene electroactive reporter.[160] In the presence of the target DNA molecule, the distance between the ferrocene and the surface increases, causing a drop of current.

Figure 1.32 Signal-On E-DNA sensor based on the triblock molecule. In the presence of a target DNA strand, the ferrocene group move into proximity with the surface, causing an increase in electrical current.

Figure 2.13 Cyclic sweep voltammetry: The reversible sweep of an applied potential as a function of time.

Figure 2.14 Voltage-current curve (cyclic voltammogram) for a reversible electron transfer reaction. E_p^{red}- reduction redox peak potential, E_p^{ox}- oxidation redox peak potential, i_p^{red}- current at reduction redox peak potential and i_p^{ox}- current at oxidation redox peak potential.

Figure 2.15 An electrical capacitor and the potential drop between the plates.

Figure 2.16 Schematic representation of **a)** the Helmholtz electrical double layer model and the **OHP** plane **b)** the potential drop across the interface between the two charged layers (electrode and OHP) at a distance (**d**).

Figure 2.17 Schematic representation of **a)** the Guoy-Chapman model of electrical "double layer" and **b)** the potential drop across the diffusion layer.

Figure 2.18 Schematic representation of **a)** Grahame model of electrical "double layer" and **b)** the potential drop across the **IHP**, **OHP** and the **diffusion layer**.

Figure 2.19 Schematic representation of **a)** polarized light shines from the light source onto the back of the sensor chip and reflected light intensity is measured in the photodetector. **b)** At certain angle of incidence (θ_i), excitation of surface plasmon occurs inducing a reduction of the intensity of the reflected light. A change of refractive index at the gold surface causes an angle shift (θ_A to θ_B) of the intensity minimum of the reflected light.

Figure 2.20 SPR sensorgram: The angle at which the intensity minimum is observed over time.

Figure 2.21 Schematic representations of the fan-shaped beam instrument and the angle shift (θ_A to θ_B) of SPR dip followed in real time as biomolecules adsorb onto the surface.

Figure 2.22 SPR sensorgram showing the steps of an analysis cycle.

Chapter 3

Figure 3.1 A cartoon representation of the dendritic nucleation model of Arp 2/3 complex on actin filament.

Figure 3.2 Electron micrographs of the dendritic nucleation model of the actin-bound Arp2/3 complex at the branch junction combined with the 2D reconstruction of actin filament (shown in pink). The Arp 2/3 complex facilitates the branching of actin filaments. The 2D reconstruction shows that Arp2 (red) and Arp3 (green) are the first two subunits of the daughter filaments. The other five subunits of the complex, namely ARPC 1-5 (shown in pale blue, purple, yellow, green and red) are anchors across 3 actin molecules on the mother filament.

Figure 3.3 A cartoon representation of the barbed end branching model of Arp 2/3 complex on actin filament.

Figure 3.4 a) The actin cytoskeleton within the lamellipodia of a Xenopus keratinocyte. The scale bar represents 0.5 μm. **b)** Lamellipodial actin cytoskeleton at greater magnification showing the branching of actin filaments. The scale bar represents 0.1 μm.

Figure 3.5 Convergent elongation model of filopodia initiation.

Figure 3.6 A cartoon representation of hydrophobic surfaces.

Figure 3.7 Schematic representations for the formation of the ODTMS fibronectin (OF) substrate and the PDMS fibronectin (PF) substrate.

Figure 3.8 Schematic representation showing the fabrication of mixed fibronectin/BSA patterned surfaces (process 8), followed by the introduction of MEF cells on the surface (process 9) and occurrence of cell protrusion (process 10).

Figure 3.9 Schematic representations showing the experimental procedures of the ODTMS SAMs formation including the cleaning (process 1) and surface activation (process 2) of glass substrate. Solvent exchange was illustrated in process 3-7 and ODTMS SAMs formation in process 8 and process 9.

Figure 3.10 AFM images of **a)** clean glass substrate form after process 2, figure 3.9 and **b)** ODTMS modified glass surface (process 9, figure 3.9).

Figure 3.11 a) Optical image of the micropatterned (10 μm thick line x 10 μm gap) silicon master. **b)** Optical image of the micropatterned (5 μm thick line x 5 μm gap) PDMS stamp. **c)** Scanning electron microscopy image of the micropatterned (2.5 μm thick line x 0.5 μm gap) silicon master.

Figure 3.12 AFM images of non patterned microcontact printed fibronectin on ODTMS SAMs on glass. **a)** RMS value of 7.99 nm, **b)** RMS value of 17.9 nm.

Figure 3.13 Fibronectin was printed onto ODTMS SAMs on glass to fabricate bio-structures of 5 μm thick line by 5 μm gap using a patterned PDMS stamp with **a)** 30 seconds inking with cotton bud and **b)** 40 minutes inking by drop casting.

Figure 3.14 a) Fluorescence micrograph of 10 μm wide strips of fibronectin (bright line) separated by 10 μm of BSA (dark line) printed on PDMS coated glass substrate. **b)** Fluorescent micrograph of 2.5 μm wide strips of fibronectin separated by 0.5 μm of BSA printed on PDMS coated glass substrate.

Figure 3.15 MEF cell spreading on fibronectin coated glass and fixed at 5, 15 and 60 minutes. Lamellipodia protrusions were guided by filopodia attachments as seen from images taken at 5, 15 and 60 minutes.

Figure 3.16 Fluorescent micrograph showing the response of MEF cells spread on 10 μm strips of fibronectin (blue colour) and 10 μm gaps of BSA (black colour). **a)** Micrograph of fluorescently labelled actin filament of MEF cell on fibronectin strips. **b)** Micrograph of

fluorescently labelled vinculin of MEF cell on fibronectin strip. The brighter area on the fibronectin strip has a high concentration of vinculin, where focal adhesion occurs. **c)** A merge micrograph of fluorescently labelled actin filament and vinculin.

Figure 3.17 Images are single frames from a time-lapse of a MEF cell spreading on 10 μm fibronectin strips. The position of the strips is shown by the yellow overlay that was added in Adobe Photoshop. **a)** An MEF cell was attached on patterned fibronectin surface for 10 minutes. **b)** Filopodia makes contact with BSA surface within the gaps of the pattern (**solid arrows**) but did not produce persistent protrusions, like those seen on the fibronectin strips (**hollow arrows**) after 15 minutes. **c)** Filopodia continues to make contact with BSA (**solid arrows**) but did not produce protrusions. However, protrusion continues on fibronectin strips (**hollow arrows**) after 24 minutes. **d)** Cell protrusion was only observed on fibronectin strip after 30 minutes.

Figure 3.18 Arp2/3 complex localisation to filopodia is independent of adhesion. **a)** filopodia (actin filament shown in red) of MEF cell spread on 5 μm fibronectin stripes for 60 minutes. Arp2/3 complex (green dot) is present on BSA stripes (black area) as well as on the Cy3 fibronectin (blue strip). Left and middle panel scale bar is 10 μm, right panel is 5 μm. **b)** MEF cell spread on 10 μm fibronectin strip for 60 minutes. Scale bar is 10 μm. **c)** Enlargement and deconvolution of boxed area in B. Scale bar is 10 μm. We can see where filopodia forms an adhesion point to the neighbouring fibronectin strip; there is a bright response for vinculin (red circle). However, the Arp2/3 complexes do not show localise response signal on where the adhesion occurs (green circle).

Table 3.1 Summary of contact angle of ODTMS SAMs on glass compared with the contact angle of glass substrate and glass substrate after cleaning and activation.

Table 3.2 Surface thickness of ODTMS SAMs.

Table 3.3 Surface thickness of fibronectin on ODMTS SAMs.

Chapter 4

Figure 4.1 A schematic view of biotin recognition residue in the β-barrel central pocket of avidin.

Figure 4.2 Schematic representation of the attachment of neutravidin on electro-switchable oligopeptide surfaces, characterised by the fluorescence microscope and surface plasmon resonance.

Figure 4.3 Schematic representation of mixed biotin-KKKKC:TEGT SAMs formation.

Figure 4.4 A schematic representation of the stability experimental set-up using a custom design Teflon cell.

Figure 4.5 A cartoon representation showing the reversibility of biotin-KKKKC:TEGT mixed SAMs surface under OC conditions and applied potential of - 0.4 V.

Figure 4.6 Schematic representation of the area occupy by a peptide in the bent state. The maximum molecular area was calculated based on the length of the exposed part of the peptide on the mixed SAM. The calculated fully extended molecular length of the peptide and TEGT are 4.7 nm and 1.6 nm, respectively, obtained with Chem Draw 3D.

Figure 4.7 XPS spectra of the N (1s) peak regions of pure biotin-KKKKC SAMs, pure TEGT SAMs and mixed SAMs of different solution volume ratios of biotin-KKKKC and TEGT - 1:1, 1:5, 1:10, 1:20, 1:40, 1:50, 1:100 and 1:500. All graphs are displayed with the same y-scale for comparison purposes.

Figure 4.8 A graph to show the number of TEGT molecules per biotin-KKKKC peptide on surface at different solution ratios based on the XPS N:S area ratio.

Figure 4.9 A graph to show the thickness of pure TEGT SAMs and the thickness of the mixed biotin-KKKKC:TEGT monolayers at different solution ratios.

Figure 4.10 A graph to show the thickness of the mixed biotin-KKKKC:TEGT monolayers at different solution ratios after the incubation with streptavidin (brown data points) compared with the thickness of pure TEGT and mixed biotin-KKKKC:TEGT monolayers at different solution ratios (blue data points). Ellipsometry measurements were conducted by Ian Williams and Alice Pranzetti (project students) under my supervision.

Figure 4.11 A graph to show the advancing contact angle (blue data point) and receding contact angle (red data point) of pure TEGT SAMs, pure biotin-KKKKC SAMs and the mixed biotin-KKKKC:TEGT monolayers at different solution ratios.

Figure 4.12 XPS spectra of the S (2p) peak regions of 1:40 biotin-KKKKC:TEGT SAMs at various electrical potentials of - 0.6 V, - 0.3 V, - 0.1 V, open circuit, + 0.1 V, + 0.3 V, + 0.6 V, + 0.8 V and + 0.9 V. All graphs are displayed with the same y-scale for comparison purposes.

Figure 4.13 A graph to show the S/Au ratios of the biotin-KKKKC:TEGT (1:40) mixed SAMs under various electrical potentials. Due to the limitation of XPS availability, only 1 set of data was obtained for each electrical potential examined.

Figure 4.14 Cyclic voltammograms of pristine biotin-KKKKC:TEGT mixed SAMs at solution ratio of 1:40, biotin-KKKKC:TEGT mixed SAMs at a solution ratio of 1:40 after being conditioned in PBS at + 0.3 V and − 0.4 V for 30 min.

Figure 4.15 Fluorescence images of pristine gold surface and streptavidin coated biotinylated surface.

Figure 4.16 Fluorescence images of biotin-KKKKC:TEGT mixed SAMs treated with Alexa Fluor 568 neutravidin while applying **a)** + 0.3 V **b)** OC conditions and **c)** - 0.4 V.

Figure 4.17 Schematic and cartoon representation of control mixed SAMs consisting of KKKKC and TEGT

Figure 4.18 Fluorescence images of KKKKC:TEGT mixed SAMs treated with Alexa Fluor 568 neutravidin while applying **a)** + 0.3 V **b)** OC conditions and **c)** - 0.4 V.

Figure 4.19 SPR sensorgram traces showing the binding of neutravidin (37 μgml^{-1}) to the biotinKKKKC:TEGT mixed SAMs at a solution ratio of 1:40 (solid line) and KKKKC:TEGT mixed SAMs at a solution ratio of 1:40 (dash line) under + 0.3 V (**blue** line), OC conditions (**black** line) and an -0.4 V (**red** line). After neutravidin binding for 30 mins, the surfaces were washed with PBS for 20 mins to remove any non-specifically adsorbed neutravidin.

Figure 4.20 SPR sensorgram traces showing the binding of neutravidin (37 μgml^{-1}) to the biotinKKKKC:TEGT mixed SAMs at a solution ratio of 1:40 under OC conditions (**black** line), - 0.3 V (green line), and an − 0.4 V(red line). After neutravidin binding for 30 mins, the surfaces were washed with PBS for 20 mins to remove any non-specifically adsorbed neutravidin.

Figure 4.21 SPR sensorgram traces showing the response of a biotin-KKKKC:TEGT mixed SAM at a solution ratio 1:40 and KKKKC:TEGT mixed SAM at a solution ratio of 1:40 to successive OC conditions, -0.4 V for 10 min, neutravidin (37 μg ml^{-1}) for 15 min while still applying -0.4 V, OC for 25 min while the neutravidin solution was still passing through the system and PBS wash.

Figure 4.22 Cartoon representation of the overview of the switchable biological surfaces.

Chapter 5

Figure 5.1 Synthesis of TEGT